DISSERTATION

TRANSIENT PHASE MICROSCOPY USING BALANCED-DETECTION TEMPORAL INTERFEROMETRY AND A COMPACT PIEZOELECTRIC MICROSCOPE DESIGN WITH SPARSE INPAINTING

Submitted by

Cameron N. Coleal

Department of Electrical and Computer Engineering

In partial fulfillment of the requirements

For the Degree of Doctor of Philosophy

Colorado State University

Fort Collins, Colorado

Spring 2024

Doctoral Committee:

Advisor: Jesse Wilson

Randy Bartels
Nancy Levinger
Henry Adams

ABSTRACT

TRANSIENT PHASE MICROSCOPY USING BALANCED-DETECTION TEMPORAL INTERFEROMETRY AND A COMPACT PIEZOELECTRIC MICROSCOPE DESIGN WITH SPARSE INPAINTING

Transient phase detection, which measures the $\mathrm{Re}\{\Delta\mathcal{N}\}$, is the complement to transient absorption detection ($\mathrm{Im}\{\Delta\mathcal{N}\}$). This work extends transient phase detection from spectroscopy to microscopy using a fast-galvanometer point-scanning setup and compares the trade-offs in transient phase versus transient absorption microscopy for the same pump and probe wavelengths. The realization of transient phase microscopy in conjunction with transient absorption microscopy opens a new door to measure the excited-state kinetics with phase-based or absorption-based techniques; depending on the sample and the wavelengths in use, transient phase detection may provide a signal improvement over transient absorption. Up until this point, transient phase microscopy has been a neglected technique in ultrafast pump-probe imaging applications. Additionally, this work evaluates a miniature piezoelectric actuator to replace galvanometers in a compact point-scanning microscope design. Sparsity limitations present in the design are addressed by the construction of a Fourier-projections based inpainting algorithm which could enable faster imaging acquisition in future applications.

ACKNOWLEDGEMENTS

I'd like to acknowledge my two closest friends for their support throughout my degree. First, I'd like to thank Patrick Stockton for our many engaging conversations and debates about optics, physics and philosophy. His humor, support and love have given me strength throughout this five-year journey. I'd also like to thank Catherine Ellis for her constant encouragement and the laughter and joy she has brought to my life.

Finally, I thank my mentor Jesse Wilson for giving me the opportunity to step into the world of optics, and for his constant willingness to answer questions, engage in discussion, and jump into the lab to check something out. I have learned a tremendous amount under his mentorship.

The research reported in this dissertation was supported by National Institute of General Medical Sciences of the National Institutes of Health under award number 1R21GM135772, The Biophotonics Program of the Division of Chemical, Bioengineering, Environmental and Transport Systems of the National Science Foundation under award number 1943595, the Melanoma Research Alliance under award number 571635 (https://doi.org/10.48050/pc.gr.80548), and the Lisa and Desi Rhoden College Professorship in Electrical and Computer Engineering.

DEDICATION

This work is dedicated to my father, David Coleal, for his unwavering support throughout my academic career, love, and thought-provoking conversations; to my brothers Michael and Eric Coleal for their love and encouragement; and finally to my grandfather, Kenneth Craib Sr., who first put me on the path towards physics and has been an ultimate inspiration throughout my life.

TABLE OF CONTENTS

LIST OF TABLES

LIST OF FIGURES

Chapter 1

Introduction

Microscopy has opened many doors in medicine, allowing scientists to peer into the inner workings and structures of the human body. As the field of microscopy has advanced various barriers regulate the translation of technology from laboratory to clinic. These barriers include exposure limitations to mitigate laser damage during use, manufacturing costs, microscope size and bulk, slow imaging speeds and signal-to-noise limitations. One pump-probe technology, transient absorption microscopy (TAM) shows great promise for biological research with a unique contrast method that reveals molecular excited state kinetics. The wavelength of the pump pulse determines the energy transferred to the sample to create the excited-state; the probe pulse measures the change induced in the absorption spectrum of the sample at the probe wavelength. Ideally, the probe pulse wavelength can be tuned to maximize the detected signal. In practice this can be difficult and often both the pump and probe wavelengths are largely limited by the laser source. Tunability can be added to a laser in the form of an optical parametric amplifier (OPA) or through frequency-doubling, though typically only one OPA is added to a system due to cost constraints. Additionally, the OPA is usually added to the pump arm since the pump wavelength controls the type of excited-state prepared. This presents a challenge; the accessible probing wavelengths are limited and may or may not correspond to a strong change in the ground versus excited state absorption spectrum. The first project presented in this dissertation details the development of a complementary technique, transient phase microscopy, and compares the performance of transient phase versus transient absorption detection for the same pump and probe wavelengths. Instead of measuring changes in absorption, transient phase detection measures changes in refractive index, which can be stronger than absorption changes for the same probing wavelengths. This work demonstrates a path forward that could greatly improve the application of transient absorption and phase measurements in biological research by relaxing wavelength constraints. The second project presented in this dissertation explores a compact piezoelectric actuator for point-scanning

microscopes to replace bulky actuator designs such as galvanometers; this work supports the development of smaller and more compact microscope designs. The final project details a computational algorithm that can allow for faster and sparser imaging (reducing overall laser exposure) by inpainting missing data. Overall, these three projects pave the way for smaller and faster microscopes with alternative avenues for contrast generation.

This dissertation is organized as follows: Chapter 2 details the conversion of a pump-probe transient absorption microscope to a transient phase microscope with sections covering pulse compression, polarization control, and a demonstration of transient phase measurements in graphene, hemoglobin, and live red blood cells. Chapter 3 reviews the construction of a compact fiber scanning microscope, characterization and calibration procedures, and an analysis of the scan pattern and sparsity constraints. Finally, Chapter 4 presents an inpainting algorithm to address the sparsity limitations of the fiber scanner, extending the usable field of view and creating opportunities for future use in sparse imaging. The appendix chapters cover laboratory protocols, background measurements, and the usage of custom software programs made publicly available in [1].

Galvo-scanning transient phase microscopy with balanced detection and arbitrary pump polarization

Transient absorption microscopy is able to measure excited state kinetics based on the imaginary part of the pump-induced perturbation to the complex refractive index, i.e. $\mathrm{Im}\{\Delta\mathcal{N}\}$, with applications in both materials and biomedical sciences. Its complement, transient *phase* microscopy, enabled by stable inline birefringent interferometry, measures $\mathrm{Re}\{\Delta\mathcal{N}\}$, but has been limited to slow stage-scanning microscopes and materials science applications. Both real and imaginary parts of $\Delta\mathcal{N}$ are needed for complete characterization, but in some scenarios, one may have clear advantages, e.g. the Kramers-Kronig relations imply that both probe phase ($\mathrm{Re}\{\Delta\mathcal{N}\}$) and absorption ($\mathrm{Im}\{\Delta\mathcal{N}\}$) will experience a change following pump excitation; depending on the wavelength one signal may be stronger than the other. This research demonstrates transient *phase* microscopy in a fast galvo-scanning microscope with balanced detection, comparing amplitude and phase measurements in graphene, hemoglobin, and red blood cells. We examine the impacts and limitations of

galvo scanning in addition to relocation of the pump-probe combining dichroic to permit arbitrary polarization of the pump. Our results suggest that transient phase microscopy combined with two-photon pumping may enable label-free imaging of endogenous pigments with higher SNR than TAM in some scenarios. Ultimately, there appears to be a significant advantage to being able to measure both transient absorption and transient phase.

Initially pioneered by Nobel laureate Ahmed Zewail [2], pump-probe transient absorption spectroscopy (TAS) has become a valuable tool for probing femtosecond chemical reactions and excited-state molecular relaxation pathways. When coupled with a laser-scanning microscope, transient absorption microscopy (TAM) [3] generates contrast from absorptive materials through pump-induced changes in the complex refractive index, $\Delta\mathcal{N}$ (e.g. excited state absorption, ground state depletion, stimulated emission, transient changes in Franck-Condon broadening, and transient photoproducts) and associated relaxation pathways and kinetics (e.g. spontaneous emission, vibrational cooling, and photodissociated ligand recombination). The differences in excited-state lifetimes can provide stark contrast between materials that have very similar absorption spectra, such as melanins [4, 5, 6]. Other applications include hemoglobin spectroscopy and imaging [7, 8] and emerging techniques to evaluate mitochondrial redox through the cytochrome electron transport hemeproteins [9, 10], along with numerous applications in materials sciences [11, 12, 13, 14] and cultural heritage [15, 16].

With precious few exceptions, TAM operates by measuring pump-induced changes to detected probe intensity, after a time delay i.e. $S_{\mathrm{TAM}} \propto \mathrm{Im}\{\Delta\mathcal{N}(\tau)\}$. The complementary measurement by transient *phase* microscopy (TΦM), senses $S_{\mathrm{T\Phi M}} \propto \mathrm{Re}\{\Delta\mathcal{N}(\tau)\}$ through interference between the probe and a reference pulse. In pump-probe spectroscopy, such phase measurements are most often associated with impulsive Raman scattering, where molecular bond deformations are directly coupled to $\mathrm{Re}\{\Delta\mathcal{N}(\tau)\}$ via the differential polarizability [17] and can be measured through interferometry [18, 19] or spectral shifting [20]. A similar situation is found with pump-induced molecular rotational motion [21]. On the other hand, in pump-probe imaging and spectroscopy of absorptive pigments, $\mathrm{Re}\{\Delta\mathcal{N}(\tau)\}$ is mostly neglected, owing to the simplicity of measuring

$\mathrm{Im}\{\Delta\mathcal{N}(\tau)\}$, which does not require stable probe-reference interference. However, full characterization of $\Delta\mathcal{N}$ requires both real and imaginary parts, and there may be some scenarios where it is advantageous to measure TΦM instead of TAM.

Various techniques have been developed to measure $\mathrm{Re}\{\Delta\mathcal{N}\}$ through its modulation of probe pulse phase. The simplest measurement detects spectral shifting proportional to the time derivative of the modulation, as has been done in cross-phase modulation (XPM) imaging of biological samples [22] and is frequently employed in impulsive Raman scattering (ISRS) spectroscopy and imaging [20]. A more direct measurement of probe phase can be done by interference with a reference pulse. Early work in ISRS focused on spectral interferometry, where the time-delayed probe and reference pulses produce interference fringes on a spectrometer. The fringe spacing is inversely proportional to probe-reference delay, and pump-induced $\mathrm{Re}\{\Delta\mathcal{N}\}$ causes the fringes to shift. Alternatively, probe and reference pulses can be re-timed and overlapped on a single-element detector. Such measurements are spoiled by any relative phase instability between probe and reference, and high stability is achieved in geometries where probe and reference pulses trace the same path from the point where they are split from a common initial pulse to the point where their interference is measured after interaction with the sample.

The challenge in common-path interferometry is to ensure the probe interacts with the pump-induced perturbations to the sample, while the reference does not. This can be done in a Sagnac interferometer in which counter-propagating probe and reference pulses arrive at different times in the sample [23], or by propagating probe and reference along slightly different paths so that the pump overlaps spatially only with the probe [19], or using group delay differences in bulk birefringent media to create a probe-reference pair, which arrive at different times in the sample [24]. (It should be noted that for short probe-reference delays, these methods measure a finite difference $\mathrm{Re}\{\Delta\mathcal{N}(\tau_{\mathrm{pr}}) - \Delta\mathcal{N}(\tau_{\mathrm{ref}})\}$ rather than $\mathrm{Re}\{\Delta\mathcal{N}(\tau_{\mathrm{pr}})\}$ directly [18].) Of these, the birefringent common path interferometer provides a simple means of re-timing probe and reference, enabling measurement with a single-element detector rather than a spectrometer, and has been employed for microscopic spectroscopy. In a transmission setup with a pair of separation and re-timing calcites,

[25] measured both the real and imaginary components of the perturbed optical transmission coefficient for gold nanoparticles. Similarly, [26] made complex measurements of the perturbed optical reflection coefficient for a tungsten thin film. In their setup, the probe and reference are split on their way to the sample by a birefringent crystal, then after reflection from the sample re-timed by propagating in the reverse direction through the same crystal. A half-wave plate can shift the measurement from phase to amplitude in both studies, permitting measurement of the complex $\Delta\mathcal{N}$. This approach to TΦM has yet to be implemented on biological samples or adapted for imaging. In addition, the placement of the pump-combining dichroic before the birefringent splitter precludes rotation of pump polarization angle, which can have a large effect on time-resolved spectroscopy of biological pigments such as melanin [27].

This research extends TΦM with birefringent inline interferometry to a fast galvanometer-scanning microscope, measuring samples in a transmission geometry. In contrast to previous works [25, 26], we place the pump combining dichroic after the probe-reference birefringent splitter, allowing for the freedom to arbitrarily rotate the pump polarization. We evaluate the impact that galvanometer scanning has on probe-reference retiming and field of view, in addition to the signal-to-noise impact of polarization effects from placing the dichroic after the birefringent probe-reference splitter [28]. Furthermore, we provide a calibration procedure for the nonlinear phase measurements and add in a balanced detection scheme that doubles the TΦM signal while canceling relative intensity noise (RIN) from the laser. We demonstrate imaging applications on graphene and red blood cells (using 2-photon absorption for pumping), comparing the relative signal to noise ratio (SNR) achievable between TAM and TΦM. Our results demonstrate the feasibility of galvo-scan imaging using transient phase detection and show that TΦM is an excellent complement to TAM. Overall, TΦM provides an alternative method of measuring pump-induced excited-state kinetics.

Sparse Lissajous-scanning reflectance confocal microscope with an adjustable field-of-view and fast iterative Fourier filtering reconstruction

The work presented in Chapters 3 and 4 is motivated by the need for next-generation handheld reflectance confocal microscopes to support broader clinical adoption, with adjustable fields-of-view at faster frame rates while retaining a small form factor. Size, weight, and portability considerations have continued to push the development of smaller, lighter, and more versatile form factors of traditionally large medical imaging devices. In dermatology, for example, the decision for whether or not to biopsy a lesion is determined by visual inspection. The use of reflectance confocal microscopy [29] has only recently been introduced into the field for additional disease screening following its grant of medical insurance reimbursement codes in 2017, and provides a non-invasive way to screen for malignant melanoma that can potentially reduce the number of unnecessary biopsies [30]. Despite this significant milestone, there are few options for purchasing commercial-grade reflectance confocal microscopes for dermatology in the USA (i.e. VivaScope [31]) and these product offerings are both expensive and large in form factor. There remains a need for "smaller, lower-cost and easier-to-use microscopes" to achieve broader dissemination into the dermatology community than what has been achieved thus far [30].

Chapter 3 presents a characterization and analysis of a compact reflectance confocal microscope we have constructed followed by the presentation of an iterative sparse reconstruction algorithm capable of extending the usable field of view in Chapter 4. This work lays the procedural foundation for characterizing a range of mechanical responses associated with an adjustable piezoelectric actuator and the subsequent optimization of scanning parameters to best achieve a high frame rate, fill factor, and field-of-view. The reconstruction algorithm provides a platform that can be used with any sparse-sampling imaging situation.

Reflectance confocal microscopes deliver focused light to a sample and collect back-reflected light from the focal spot through a pinhole [32]. Images are formed by either scanning the sample or the focal spot. The most common type of actuator design for focal spot scanning uses a pair of (resonant) galvanometer-mounted mirrors which are able to achieve high frame rates [33] with

precise positioning; however, galvanometers are large, bulky, and not suited for small, compact, point-scanning designs. For our intended application field of handheld microscopes, a smaller and more compact form of actuation is required.

Two popular ways to construct a compact and lightweight scanner are by either a) replacing the galvanometers with micro-electrical-mechanical (MEMS) scan mirrors or b) scanning the tip of an optical fiber with a piezoelectric tube actuator. MEMS actuators are very compact and lightweight devices with good robustness to handheld movement or perturbation [34]. MEMS, however, can be expensive and complex to fabricate [35] and can have limited actuation displacement. Electrostatic MEMS actuators can achieve a larger displacement (which is more desirable for applications in dermatology), however, they tend to have higher working temperatures and low working frequencies (which places an upper limit on frame rate) [36], additionally, they suffer from optical losses on reflectivity [37]. Similar to galvanometers, the reflective geometry of MEMS scanners requires the incident beam to enter at an angle (typically $90°$) to the optic axis of the imaging lenses, adding bulk to the design. Piezoelectric fiber scanners tend to be more compact and the imaging optics are coaxial with the fiber tip to the sample plane [38], making them popular for smaller endoscopic designs [36]. Additional advantages of piezoelectric fiber scanners include 1) low cost of components and ease of fabrication, 2) large fiber tip displacement near resonance (corresponding to a large field of view) [36], and 3) no optical losses from mirrors [37]. However, piezoelectric fiber scanners suffer from two major mechanical drawbacks that limit their practical application, namely cross-coupling between fiber cantilever modes and harmonic distortions when driven at large-amplitude displacement.

For the most part, piezoelectric fiber scanner designs in the literature avoid these problems by operating on resonance with a low framerate spiral scan pattern or when a high framerate Lissajous pattern is used, optimizing for a single, small FOV with dense sampling and at a driving amplitude where harmonic distortions are not prominent. We provide a characterization of these mechanical non-idealities and describe strategies for mitigating these drawbacks by eigenaxis calibration, real-

time position sensing detection, and image reconstruction algorithms. The unique contributions of this body of research include:

- Characterization of optical fiber cantilever eigenaxes under semi-resonant conditions that support Lissajous scanning, and a procedure for rotating driving waveform to minimize cross-coupling.

- Compensation of distortions in the fiber cantilever trajectory with the use of a real-time position sensitive detector and identification of amplitude-dependent mechanical harmonics and resonance blue shift.

- Introduction of a novel reconstruction algorithm based on the physical constraint that a finite numerical aperture imposes in the Fourier domain and comparison to a related inpainting algorithm used in reconstructing images from Lissajous scan patterns.

Taken together, these characterizations and improvements will open opportunities for more widespread usage of coaxial piezoelectric fiber scanning designs by allowing for more accurate image reconstruction, higher framerates, and larger fields-of-view, in a manner robust against mechanical distortions.

Bibliography

[1] cncoleal. Dissertation. https://github.com/cncoleal/Dissertation, 2023. Accessed: 2023-09-19.

[2] Ahmed H. Zewail. Laser femtochemistry. *Science*, 242(4886):1645–1653, Dec 1988.

[3] Martin C. Fischer, Jesse W. Wilson, Francisco E. Robles, and Warren S. Warren. Invited review article: Pump-probe microscopy. 87:031101, Mar 2016.

[4] Francisco E. Robles, Sanghamitra Deb, Jesse W. Wilson, Christina S. Gainey, M. Angelica Selim, Paul J. Mosca, Douglas S. Tyler, Martin C. Fischer, and Warren S. Warren. Pump-probe imaging of pigmented cutaneous melanoma primary lesions gives insight into metastatic potential. *Biomedical Optics Express*, 6(9):3631, September 2015.

[5] Andrew Thompson, Francisco E. Robles, Jesse W. Wilson, Sanghamitra Deb, Robert Calderbank, and Warren S. Warren. Dual-wavelength pump-probe microscopy analysis of melanin composition. *Scientific Reports*, 6(1):36871, November 2016.

[6] Kuk-Youn Ju, Simone Degan, Martin C. Fischer, Kevin C. Zhou, Xiaomeng Jia, Jin Yu, and Warren S. Warren. Unraveling the molecular nature of melanin changes in metastatic cancer. *Journal of Biomedical Optics*, 24(05):1, April 2019.

[7] Andrew T. Francis, Kyla Berry, Elena C. Thomas, Andrew H. Hill, and Dan Fu. In vitro quantification of single red blood cell oxygen saturation by femtosecond transient absorption microscopy. *The Journal of Physical Chemistry Letters*, 10(12):3312–3317, June 2019.

[8] Andrew T. Francis, Melanie J. Shears, Sean C. Murphy, and Dan Fu. Direct quantification of single red blood cell hemoglobin concentration with multiphoton microscopy. *Analytical Chemistry*, 92(18):12235–12241, September 2020.

[9] Erkang Wang, Kalyn S. Specht, Adam J. Chicco, and Jesse W. Wilson. High-repetition-rate transient absorption spectroscopy of respiratory supercomplexes. *The Journal of Physical Chemistry B*, 126(7):1404–1412, February 2022.

[10] Erkang Wang, Luke A. Whitcomb, Adam J. Chicco, and Jesse W. Wilson. Transient absorption spectroscopy and imaging of redox in muscle mitochondria. *Biomedical Optics Express*, 13(4):2103, April 2022.

[11] Yuan Zhang, Junfeng Dai, Xiangli Zhong, Dongwen Zhang, Gaokuo Zhong, and Jiangyu Li. Probing ultrafast dynamics of ferroelectrics by time-resolved pump-probe spectroscopy. *Advanced Science*, 8(22):2102488, November 2021.

[12] Ying Yu, Xiankun Zhang, Zhangkai Zhou, Zheng Zhang, Yanjun Bao, Haofei Xu, Limin Lin, Yue Zhang, and Xuehua Wang. Microscopic pump-probe optical technique to characterize the defect of monolayer transition metal dichalcogenides. *Photonics Research*, 7(7):711, July 2019.

[13] Yang Lu, Xin Tan, Yanzheng Du, Donglin Ma, and Weigang Ma. Direct observation of ultrafast carrier coupling dynamics in monolayer graphene/metal system. *International Journal of Heat and Mass Transfer*, 197:123322, November 2022.

[14] Arjun Ashoka, Ronnie R. Tamming, Aswathy V. Girija, Hope Bretscher, Sachin Dev Verma, Shang-Da Yang, Chih-Hsuan Lu, Justin M. Hodgkiss, David Ritchie, Chong Chen, Charles G. Smith, Christoph Schnedermann, Michael B. Price, Kai Chen, and Akshay Rao. Extracting quantitative dielectric properties from pump-probe spectroscopy. *Nature Communications*, 13(1):1437, March 2022.

[15] Tana Elizabeth Villafana, William P. Brown, John K. Delaney, Michael Palmer, Warren S. Warren, and Martin C. Fischer. Femtosecond pump-probe microscopy generates virtual cross-sections in historic artwork. *Proceedings of the National Academy of Sciences*, 111(5):1708–1713, February 2014.

[16] Yaxin Chen, Rong Wang, and Minbiao Ji. Nondestructive nonlinear optical microscopy revealed the blackening mechanism of ancient chinese jades. *Research*, 6:0266, January 2023.

[17] Jesse W. Wilson and Randy A. Bartels. Coherence-modulated third harmonic generation for vibrational spectroscopy: a theoretical treatment. *Journal of the Optical Society of America B*, 29(8):1875, August 2012.

[18] Jesse W. Wilson, Philip Schlup, and Randy A. Bartels. Synthetic temporal aperture coherent molecular phase spectroscopy. *Chemical Physics Letters*, 463(4–6):300–304, October 2008.

[19] C. D. Cruz, J. C. Stephenson, S. Engmann, E. G. Bittle, and J. K. Wahlstrand. Pump-probe phase spectroscopy with submilliradian sensitivity and nanosecond time delay using michelson interferometers. *Optics Express*, 31(9):14299, April 2023.

[20] David R. Smith, Jeffrey J. Field, David G. Winters, Scott R. Domingue, Frauke Rininsland, Daniel J. Kane, Jesse W. Wilson, and Randy A. Bartels. Phase noise limited frequency shift impulsive raman spectroscopy. *APL Photonics*, 6(2):026107, February 2021.

[21] Francisco E. Robles, Prathyush Samineni, Jesse W. Wilson, and Warren S. Warren. Pump-probe nonlinear phase dispersion spectroscopy. *Optics Express*, 21(8):9353, April 2013.

[22] Jesse W. Wilson, Prathyush Samineni, Warren S. Warren, and Martin C. Fischer. Cross-phase modulation spectral shifting: nonlinear phase contrast in a pump-probe microscope. *Biomedical Optics Express*, 3(5):854, May 2012.

[23] Kazuhiko Misawa and Takayoshi Kobayashi. Femtosecond sagnac interferometer for phase spectroscopy. *Optics Letters*, 20(14):1550, July 1995.

[24] Philip Schlup, Jesse Wilson, Klaus Hartinger, and Randy A. Bartels. Dispersion balancing of variable-delay monolithic pulse splitters. *Appl. Opt.*, 46(23):5967–5973, Aug 2007.

[25] Meindert A. Van Dijk, Markus Lippitz, Daniel Stolwijk, and Michel Orrit. A common-path interferometer for time-resolved and shot-noise-limited detection of single nanoparticles. *Optics Express*, 15(5):2273, 2007.

[26] J. Chandezon, J.-M. Rampnoux, S. Dilhaire, B. Audoin, and Y. Guillet. In-line femtosecond common-path interferometer in reflection mode. *Optics Express*, 23(21):27011, October 2015.

[27] David Grass, Georgia M. Beasley, Martin C. Fischer, M. Angelica Selim, Yue Zhou, and Warren S. Warren. Contrast mechanisms in pump-probe microscopy of melanin. *Optics Express*, 30(18):31852, August 2022.

[28] James Heath, Meredith Kupinski, Ewan Douglas, Kira Hart, and James Breckinridge. Mueller matrix maps of dichroic filters reveal polarization aberrations. In *Space Telescopes and Instrumentation 2020: Optical, Infrared, and Millimeter Wave*, page 275, December 2020. arXiv:2012.12301 [astro-ph].

[29] Minsky Marvin. Microscopy apparatus, December 1961. U.S. Patent 3 013 467.

[30] Milind Rajadhyaksha, Ashfaq Marghoob, Anthony Rossi, Allan C. Halpern, and Kishwer S. Nehal. Reflectance confocal microscopy of skin in vivo: From bench to bedside: REFLECTANCE CONFOCAL MICROSCOPY OF SKIN IN VIVO. *Lasers in Surgery and Medicine*, 49(1):7–19, January 2017.

[31] Vivascope. VivaScope Products, 03 2022.

[32] Robert H Webb. Confocal optical microscopy. *Reports on Progress in Physics*, 59(3):427–471, Mar 1996.

[33] John P. Giannini, Andrew G. York, and Hari Shroff. Anticipating, measuring, and minimizing mems mirror scan error to improve laser scanning microscopy's speed and accuracy. *PLOS ONE*, 12(10):e0185849, Oct 2017.

[34] Xiyu Duan, Haijun Li, Zhen Qiu, Bishnu P. Joshi, Asha Pant, Arlene Smith, Katsuo Kurabayashi, Kenn R. Oldham, and Thomas D. Wang. Mems-based multiphoton endomicroscope for repetitive imaging of mouse colon. *Biomedical Optics Express*, 6(8):3074, Aug 2015.

[35] Tong Wu, Zhihua Ding, Kai Wang, Minghui Chen, and Chuan Wang. Two-dimensional scanning realized by an asymmetry fiber cantilever driven by single piezo bender actuator for optical coherence tomography. *Optics Express*, 17(16):13819, August 2009.

[36] Mandeep Kaur, Pierre M. Lane, and Carlo Menon. Scanning and actuation techniques for cantilever-based fiber optic endoscopic scanners—a review. *Sensors*, 21(1), 2021.

[37] Hyun-Joon Shin, Mark C. Pierce, Daesung Lee, Hyejun Ra, Olav Solgaard, and Rebecca Richards-Kortum. Fiber-optic confocal microscope using a mems scanner and miniature objective lens. *Optics Express*, 15(15):9113, Jul 2007.

[38] Daniel Youngsuk Kim, Kyungmin Hwang, Jinhyo Ahn, Yeong-Hyeon Seo, Jae-Beom Kim, Soyoung Lee, Jin-Hui Yoon, Eunji Kong, Yong Jeong, Sangyong Jon, Pilhan Kim, and Ki-Hun Jeong. Lissajous scanning two-photon endomicroscope for in vivo tissue imaging. *Scientific Reports*, 9(1):3560, Dec 2019.

Chapter 2

Transient Phase Microscopy

2.1 Background

Pump-probe microscopy is a nonlinear imaging technique that uses a pair of time-delayed ultrafast light pulses to probe the excited-state kinetics of a sample [1]. One way to measure this is through transient absorption microscopy (TAM); first a sample is excited with the pump pulse and then absorption changes of a successive probe pulse are measured [2]. The absorption of the probe pulse will be different when it is measured directly after excitation than when it is measured at longer delay times. The change in the probe absorption following excitation is specific to the probe wavelength and can be used as a contrast mechanism to differentiate samples with similar linear absorption spectra. However, the wavelengths accessible by a particular laser system may not always align with a peak in the absorption spectrum of the sample; this can limit which samples can be examined.

A related pump-probe technique, transient phase spectroscopy, is able to measure the transient *phase* changes in an excited sample [3, 4, 5]; we propose an extension of this method to imaging called transient phase microscopy (TΦM). Phase changes arise from variations to the real part of the complex refractive index of a sample. The complex refractive index $\mathcal{N}$ is a summation of real and imaginary components; the real component governs dispersion and the imaginary component governs absorption [6]. The real and imaginary components of the complex refractive index are linked through the Kramer's-Kronig relations [6] which results in a corresponding change to one component with an induced change in the other. Thus, for an induced change in the absorption of a sample $\mathrm{Im}\{\Delta\mathcal{N}\}$, a corresponding change is expected in the phase of a sample $\mathrm{Re}\{\Delta\mathcal{N}\}$. This correspondence ties together the pump-probe techniques of transient absorption microscopy and transient phase microscopy. So long as a resonant pump pulse induces a change in the complex re-

fractive index $\Delta\mathcal{N}$, we can measure changes to the imaginary component with transient absorption ($S_{\mathrm{TAM}} \propto \mathrm{Im}\{\Delta\mathcal{N}\}$) and changes to the real component with transient phase ($S_{\mathrm{T\Phi M}} \propto \mathrm{Re}\{\Delta\mathcal{N}\}$).

For a particular probing wavelength, $\mathrm{T\Phi M}$ may provide a stronger signal than TAM, so the ability to measure both a transient phase and transient absorption signal may increase the accessibility of a wider variety of samples. In biological samples, off-resonant probing with TAM has been demonstrated [7] but can result in a weaker signal. With the additional option of measuring $\mathrm{T\Phi M}$, off-resonant probing may become a more attractive option for some samples when $S_{\mathrm{T\Phi M}} > S_{\mathrm{TAM}}$ conferring the benefits of reduced photodamage. This chapter describes the work taken to extend transient phase detection to microscopy and evaluate the feasibility and trade-offs of TΦM and TAM for the same pump and probe wavelengths.

The direction of this research was governed by four primary goals:

1. to adapt a transient absorption microscope for phase measurements
2. to calibrate the units for transient phase measurements
3. to demonstrate the successful measurement of transient phase with an off-resonant probe wavelength
4. to extend the measurements to imaging applications

Each of these goals was met throughout the duration of the research by the following: First, the microscope was designed to employ similar polarization-based phase detection as shown in [4, 5] by utilizing an inline birefringent calcite crystal pair for time-resolved interferometry. Then, a calibration technique was developed which capitalized on the adjustable phase compensation of the calcite crystal pair. Finally, comparative measurements were made between TΦM and TAM; these measurements included both pump-probe temporal delay scans and imaging. In addition to these actions, polarization modeling of the system uncovered that diattenuation and polarization aberration may be contributing to a TΦM signal reduction.

This chapter steps through several of these stages (and others) related to the development of a transient phase microscope for off-resonant phase detection. Section 2.2 presents the underlying

theory relating transient absorption and phase measurements. Section 2.3 discusses pulse compression and sections 2.4 and 2.5 step through system design, construction and evaluation. Sections 2.6 and 2.7 present modeling efforts used to quantify signal reduction effects from diattenuation and polarization aberration, calibrate the phase measurements, and determine the spatial phase effects of galvanometer-based imaging. Finally, section 2.8 presents transient phase measurements compared to transient absorption measurements in borosilicate glass, a graphene monolayer and in hemoglobin. The findings of this research corroborate that neither TAM nor TΦM requires a resonant probe pulse; as long as $S_{\mathrm{TAM}} \propto \mathrm{Im}\{\Delta\mathcal{N}\}$ or $S_{\mathrm{T\Phi M}} \propto \mathrm{Re}\{\Delta\mathcal{N}\}$, related to the *change* in probe absorption or refractive index properties, is greater than the noise floor then a signal can be measured. The decision on whether to use TAM versus TΦM can be complicated and sample dependent; in some scenarios TAM might present the stronger signal but perhaps it is more important to see structural detail in the image that cross-phase modulation can detect, so TΦM could be used instead. In this work we have presented an approach to upgrade a transient absorption microscope so that both TAM and TΦM measurements can be made and compared the two detection techniques in material and biological applications. The limitations for TΦM with point-scan imaging are addressed and future research will be able to select which measurement is most desirable and begin to map out more fully the wavelength dependent benefits of the two techniques for biological microscopy. TΦM shows great promise as a complement to TAM.

2.2 Theory

This section introduces a light theoretical derivation of the mathematics used to model light-matter interactions and the related absorption and refractive index properties coupled through Kramers-Kronig relations.

2.2.1 Overview of Light-Matter Interactions

At a base level, atoms are made up of protons, neutrons, and electrons. The protons and neutrons create the atomic nucleus and electrons are externally bound; a group of atoms bonded

together can create a molecule. When light is incident upon a molecule, the frequency of the light will dictate the molecular response according to the molecule's inherent properties of absorption and refractive index; these properties arise from the atomic, electronic and vibrational structures of the molecule. From the Bohr frequency condition, the frequency of incident light can be related to an energy transition in a molecule from energy state E_1 to energy state E_2, where $E_2 - E_1 = \Delta E = hf = \hbar\omega$ [8]; if the incident frequency f_i corresponds to an energy transition ΔE then absorption can take place. If the incident frequency does not correspond to an energy transition and the intensity of the laser is such that only linear interactions are able to occur, then the light will simply undergo dispersion upon incidence. Dispersion occurs when different frequencies of light experience a different phase velocity (defined as $\nu = \frac{c}{n(\omega)}$) due to the frequency dependence of the refractive index [6]. At an interface, light will bend in order to maintain the phase relationship of the incident and transmitted waveforms in a process called refraction; the angle of bend is related to the incident frequency, angle, index of refraction [6]. This relationship is captured by Snell's law, where the refracted angle of light θ_e in a material can be calculated by the incident angle θ_i and the incident n_i and material n_e refractive indices: $n_i \sin\theta_1 = n_e \sin\theta_e$ [6].

We can break down light-matter interactions to encompass several components: the incident light, the material response, and the exiting light. Light is an electromagnetic wave with three important vectors: the electric field vector, the magnetic field vector, and the phase propagation vector. All three of these vectors are orthogonal in space, allowing light to be modelled as a transverse wave that propagates in direction $\hat{z}$ with an oscillatory electric field along one axis ($\hat{x}$) and an out-of-phase oscillatory magnetic field along the other axis ($\hat{y}$). We can model an electromagnetic wave $E(t)$ as

$$E(t) = A(t)e^{i\omega t} + A(t)e^{-i\omega t} \tag{2.1}$$

where $A(t)$ is the temporal amplitude envelope of the waveform oscillating at the optical frequency ω. Note that $E(t)$ is a summation over both positive and negative frequencies; for the sake of simplicity we will show only the positive frequency component of the electric field hereafter with the

implication that the derivations apply also to the complex conjugate. The material properties and response can be encoded by the *susceptibility* $\chi(\omega)$ which is the expected bulk material perturbation in an electromagnetic field of a certain intensity and wavelength. Note that $\chi(\omega)$ is a function of frequency. When light interacts with a material the resulting material response is referred to as the electric dipole polarization $P(t)$ in time and $P(\omega)$ in frequency where

$$P(\omega) = \epsilon_0 \chi(\omega) E(\omega) \tag{2.2}$$

This is known as the constitutive relation for a linear interaction [6]. $E(\omega)$ and $P(\omega)$ are the Fourier transforms of $E(t)$ and $P(t)$, respectively.

The molecular susceptibility contains the interesting aspects of the material that we want to study; the next section of this discussion focuses on the properties of this term. It was mentioned earlier that a molecule can be described in terms of its absorption and dispersion properties, both of which are functions of frequency. From the molecular susceptibility (a complex quantity), we can extract the frequency-dependent absorption and dispersion properties through the complex index of refraction $\mathcal{N}$, where

$$\mathcal{N}(\omega) = \sqrt{1 + \chi(\omega)} = n(\omega) + i\kappa(\omega) \tag{2.3}$$

The real part of the index of refraction $n(\omega)$ is responsible for dispersion (which governs events of refraction) while the imaginary part $\kappa(\omega)$ is responsible for absorption. The susceptibility can be modeled to the first order as a damped linear oscillator (Lorentz oscillator) after interaction with an electric field

$$\chi(\omega) = \frac{\omega_p^2}{\omega_0^2 - i\omega\gamma - \omega^2} \tag{2.4}$$

where ω is the frequency of the incident driving field, γ is the damping coefficient responsible for absorption, ω_0 is the harmonic frequency responsible for absorption and ω_p is the plasma frequency defining the contributing electron cloud at certain incident frequencies [6]. The plasma frequency

can be described by

$$\omega_p = \sqrt{\frac{Nq_e^2}{\epsilon_0 m_e}} \tag{2.5}$$

2.2.2 Kramers-Kronig Relations

The Kramers-Kronig relations are a set of equations that relate the real and imaginary parts of the complex refractive index [9]. While the imaginary component is easily measured (ie. this is an absorption spectrum) for linear interactions, measuring the real component can be more challenging. One major utility of the Kramers-Kronig relations is that they can allow one to estimate the the real component from the imaginary component (or vice versa) if only one frequency-dependent component has been measured. The Kramers-Kronig relations can be derived from the constitutive relation shown in Equation 2.2 subject to causality, where the polarization of a molecule cannot occur before the incidence of the electric field; a consequence of this derivation (which can be found in [6]) is that the following expression must be true

$$\chi(\omega) = \frac{1}{i\pi}\int_{-\infty}^{\infty}\frac{\chi(\omega')}{\omega' - \omega}d\omega' \tag{2.6}$$

which is equivalently stated as

$$\text{Re}\{\chi(\omega)\} + \text{Im}\{\chi(\omega)\} = \int_{-\infty}^{\infty}\frac{\text{Re}\{\chi(\omega')\} + \text{Im}\{\chi(\omega')\}}{\omega' - \omega}d\omega' \tag{2.7}$$

After separately equating the imaginary and real parts in Equation 2.7, the final expression for the Kramers-Kronig relations for susceptibility can be shown as

$$\text{Re}\{\chi(\omega)\} = \frac{1}{\pi}\int_{-\infty}^{\infty}\frac{\text{Im}\{\chi(\omega')\}}{\omega' - \omega}d\omega' \tag{2.8}$$

$$\text{Im}\{\chi(\omega)\} = -\frac{1}{\pi}\int_{-\infty}^{\infty}\frac{\text{Re}\{\chi(\omega')\}}{\omega' - \omega}d\omega' \tag{2.9}$$

These expressions can be further used to relate the real and imaginary parts of the complex index of refraction

$$n(\omega) - 1 = \frac{1}{\pi} \int_{-\infty}^{\infty} \frac{\kappa(\omega')}{\omega' - \omega} d\omega' \tag{2.10}$$

$$\kappa(\omega) = -\frac{1}{\pi} \int_{-\infty}^{\infty} \frac{n(\omega) - 1}{\omega' - \omega} d\omega' \tag{2.11}$$

Where Equation 2.10 is the real part and Equation 2.11 is the imaginary part. Figure 2.1 shows an example of the real and imaginary components of $\mathcal{N}$ for susceptibility modeled as a Lorentz oscillator (Equation 2.4). Importantly, since transient absorption measures a *change* in the absorption of the probe following excitation with a pump, it is actually measuring $\text{Im}\{\Delta\mathcal{N}(\omega_{pr})\}$, where $\Delta\mathcal{N} = \mathcal{N}_e - N_g$ and $\mathcal{N}_e$ and $\mathcal{N}_g$ are the excited state and ground state complex refractive indices, respectively. In comparison, transient phase measures $\text{Re}\{\Delta\mathcal{N}(\omega_{pr})\}$. Thus, in order for off-resonant TΦM to provide a stronger signal than TAM, the change in excited vs. ground state probe phase must be greater than the change in excited vs. ground state probe absorption for the probing wavelength (ie. $\text{Re}\{\Delta\mathcal{N}(\omega_{pr})\} > \text{Im}\{\Delta\mathcal{N}(\omega_{pr})\}$). The opposite is true for TAM to be stronger than TΦM.

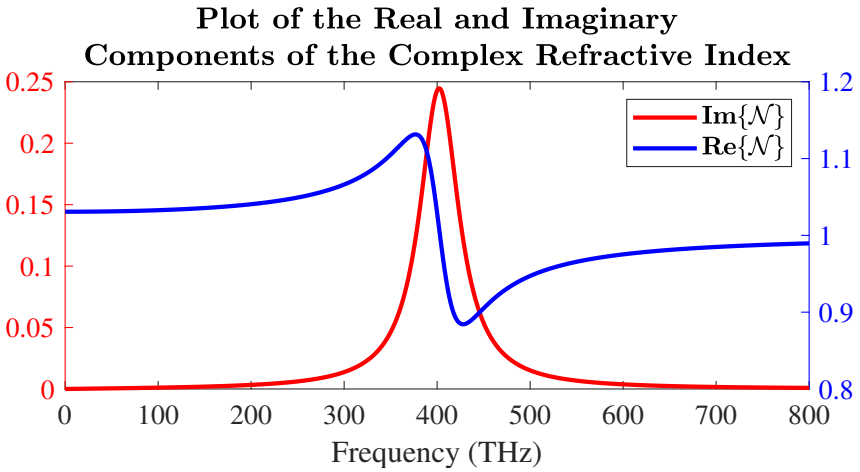

Figure 2.1: A plot of the real and imaginary components of the complex refractive index for the susceptibility modeled as a Lorentz oscillator (Equation 2.4).

In order to build intuition into the factors that might make TΦM more favorable to measure than TAM, two simulations are presented. The shape of the excited state spectrum is related to the ground state spectrum, but distinct changes can occur as a result of the molecular dynamics induced by the pump. Earlier we discussed that the absorption properties of a molecule are frequency dependent and showed that frequency has a direct relation to an energy transition. The pump wavelength in our setup is 1035 nm with the ability to excite two-photon absorption at 517 nm; thus the pump wavelength falls into the category of near-infrared (NIR) or visible (VIS) excitation. The types of molecular transitions that can be induced by VIS and NIR wavelengths include electronic transitions. Once excited, a molecule can relax through either a radiative or a non-radiative pathway. Examples of radiative pathways include fluorescence and phosphorescense, where light is emitted from the sample after excitation. Techniques such as transient absorption and transient phase are also able to probe non-radiative decay pathways, of which there are many. After exciting an electronic transition, the non-radiative decay pathway can result in vibrational and rotational motions which can occur on the order of tens to hundreds of femtoseconds. The particular molecular environment will dictate through which pathways energy will be transferred in non-radiative decay; one common vibrational phenomenon that can occur when there is good overlap between two electronic states is known as Franck-Condon broadening. Franck-Condon broadening is a type of homogeneous broadening that depends upon the Franck-Condon factors influenced by the geometry of the molecule under investigation [8]. The Franck-Condon principle says that electronic transitions occur so quickly that the internuclear distance effectively remains the same [10]; the Franck-Condon factors relate the intensity of a vibronic transition to the overlap integral of two vibrational wavefunctions [11]. Other contributing factors to the vibronic transition intensity includes the bond length between the ground and excited-state manifolds and population of the vibrational levels [11, 8]. In pump-probe spectroscopy, the pump pulse serves to place a molecule in an excited state. For non-radiative decay processes after the pump pulse excites, energy can be redistributed through the molecule as heat. This results in "hot" ground states (vibrationally excited ground-states); when the probe pulse interacts with the molecule in this state, the occupation

of higher (ground-state) vibrational levels can contribute to a spectral red shift and broadening of the absorption spectrum.

With the development TΦM, we want to understand how differences in the excited-state spectrum versus ground-state spectrum can influence the measurable signal levels and the decision for whether to measure TAM or TΦM. The first simulation presented looks at how vibrational factors (spectral broadening and red-shifting) in an excited-state spectrum could affect a simple Lorentzian absorption lineshape (the imaginary component of a Lorentz oscillator model). The second simulation seeks to take this a step further by analyzing a more spectrally complex example, myoglobin, using a time-correlator approach. The time-correlator approach depends on Franck-Condon coefficients (related to temperature-dependent vibrationally hot-ground state effects) to estimate what the excited-state spectrum might look like. Typically this model is used to evaluate the imaginary component of the complex susceptibility (proportional to absorption), but by taking the real component a relative comparison of TAM and TΦM can be made.

Simulating a Comparison of $S_{\mathrm{T\Phi M}}$ vs. S_{TAM} for a Lorentz Oscillator

Figures 2.2 and 2.3 show a simple simulation of what the real and imaginary components of a Lorentz oscillator model for an electronic excitation of $\Delta\mathcal{N}$ might look like under different circumstances. The goal of these figures is to convey some intuition into how broadening and spectral shift factors can affect $S_{\mathrm{T\Phi M}}$ vs. S_{TAM}.

Figure 2.2 compares two excited state broadening factors for a smaller excited state red shift (25 THz or ∼50 nm), while Figure 2.3 compares two excited state broadening factors for a larger excited state red shift (85 THz or ∼200 nm). The bottom row of both figures provides the most insight by comparing the relative change in $\Delta\mathcal{N}$ for $S_{\mathrm{T\Phi M}}$ vs. S_{TAM}. When the black line plotting $|\mathrm{Re}\{\Delta\mathcal{N}\}| - |\mathrm{Im}\{\Delta\mathcal{N}\}|$ is positive $S_{\mathrm{T\Phi M}} > S_{\mathrm{TAM}}$, and when the black line is negative $S_{\mathrm{T\Phi M}} < S_{\mathrm{TAM}}$. In Figure 2.2, with the smaller red-shift value (25 THz), we can see that the spectral coverage for both $S_{\mathrm{T\Phi M}}$ and S_{TAM} generally increases with broadening (col. a, row 3 versus col. b, row 3). Also of note; both TΦM and TAM indicate a signal ($\mathrm{Im}\{\Delta\mathcal{N}\}$ and $\mathrm{Re}\{\Delta\mathcal{N}\}$) off of the resonant peak (row 2).

With a larger red-shift (85 THz), these results are emphasized (row 3, Figure 2.3). Comparing Figure 2.2 to Figure 2.3, two observations can be made: (1) larger broadening factors result in increased spectral coverage for both $S_{\mathrm{T\Phi M}}$ and S_{TAM} and (2) larger spectral-shifts result in stronger signals for both $S_{\mathrm{T\Phi M}}$ and S_{TAM}. The peak signals and thus optimal probing wavelengths for TAM and TΦM occur slightly offset from the resonance peak. To further investigate the relationship between $S_{\mathrm{T\Phi M}}$ and S_{TAM}, a similar simulation but for myoglobin is presented next.

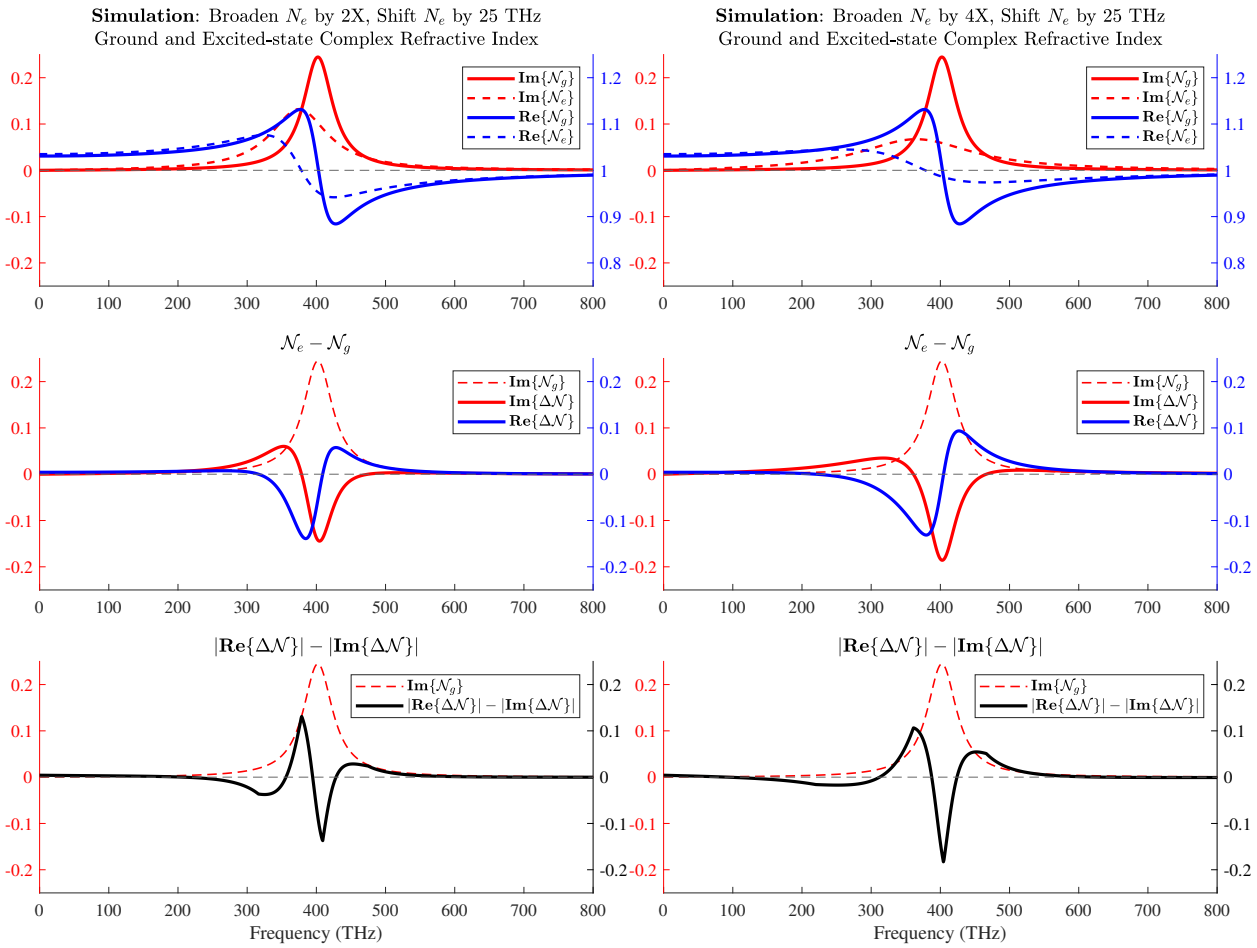

Figure 2.2: This figure compares the effects of different broadening factors on the excited state complex refractive with a red shift of 25 THz. $\mathcal{N}_g$ is the simulated ground state complex refractive index and $\mathcal{N}_e$ is the simulated excited state complex refractive index. Column (a) has an excited state broadening factor of 2X compared to the spectral width of $\mathrm{Im}\{\mathcal{N}_g\}$, while column (b) has an excited state broadening factor of 4X. Row 1 shows the real and imaginary components of $\mathcal{N}_g$ and the real and imaginary components of $\mathcal{N}_e$. Row 2 shows the real and imaginary spectral components corresponding to $\Delta\mathcal{N} = \mathcal{N}_e - \mathcal{N}_g$, with a trace of the ground state absorption spectrum shown for comparison. Finally, Row 3 shows the absolute difference between the real and imaginary components of $\Delta\mathcal{N}$, again with a trace of the ground state absorption spectrum for comparison. This row can be interpreted as a positive component corresponding to a stronger TΦM than TAM signal, and a negative component corresponding to a stronger TAM than TΦM signal for the specified wavelength.

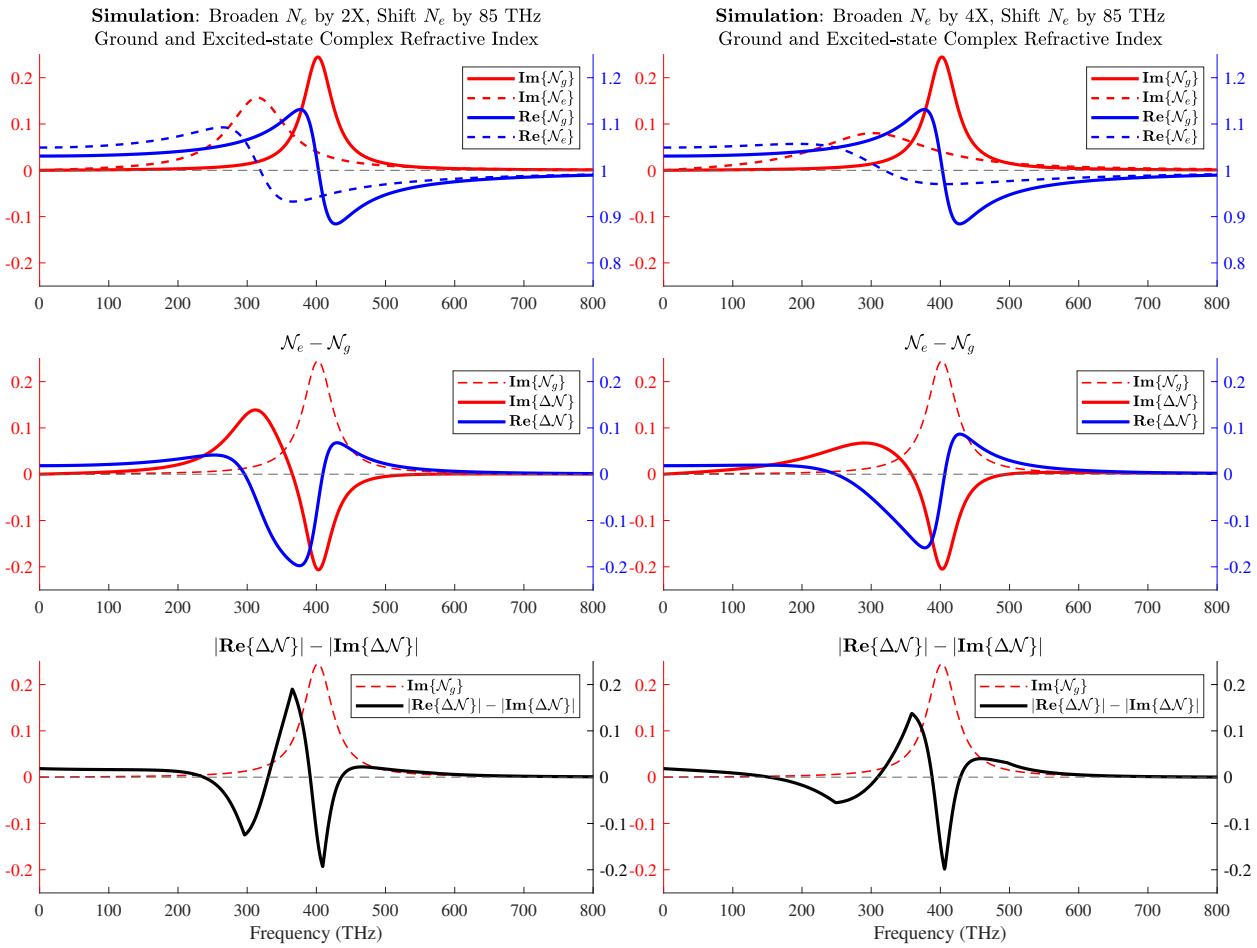

Figure 2.3: This figure compares the effects of different broadening factors on the excited state complex refractive with a red shift of 85 THz. $\mathcal{N}_g$ is the simulated ground state complex refractive index and $\mathcal{N}_e$ is the simulated excited state complex refractive index. Column (a) has an excited state broadening factor of 2X compared to the spectral width of $\mathrm{Im}\{\mathcal{N}_g\}$, while column (b) has an excited state broadening factor of 4X. Row 1 shows the real and imaginary components of $\mathcal{N}_g$ and the real and imaginary components of $\mathcal{N}_e$. Row 2 shows the real and imaginary spectral components corresponding to $\Delta\mathcal{N} = \mathcal{N}_e - \mathcal{N}_g$, with a trace of the ground state absorption spectrum shown for comparison. Finally, Row 3 shows the absolute difference between the real and imaginary components of $\Delta\mathcal{N}$, again with a trace of the ground state absorption spectrum for comparison. This row can be interpreted as a positive component corresponding to a stronger TΦM than TAM signal, and a negative component corresponding to a stronger TAM than TΦM signal for the specified wavelength.

Simulating a Comparison of $\Delta\mathcal{X}_{\mathrm{T\Phi M}}$ vs. $\Delta\mathcal{X}_{\mathrm{TAM}}$ for Deoxymyoglobin

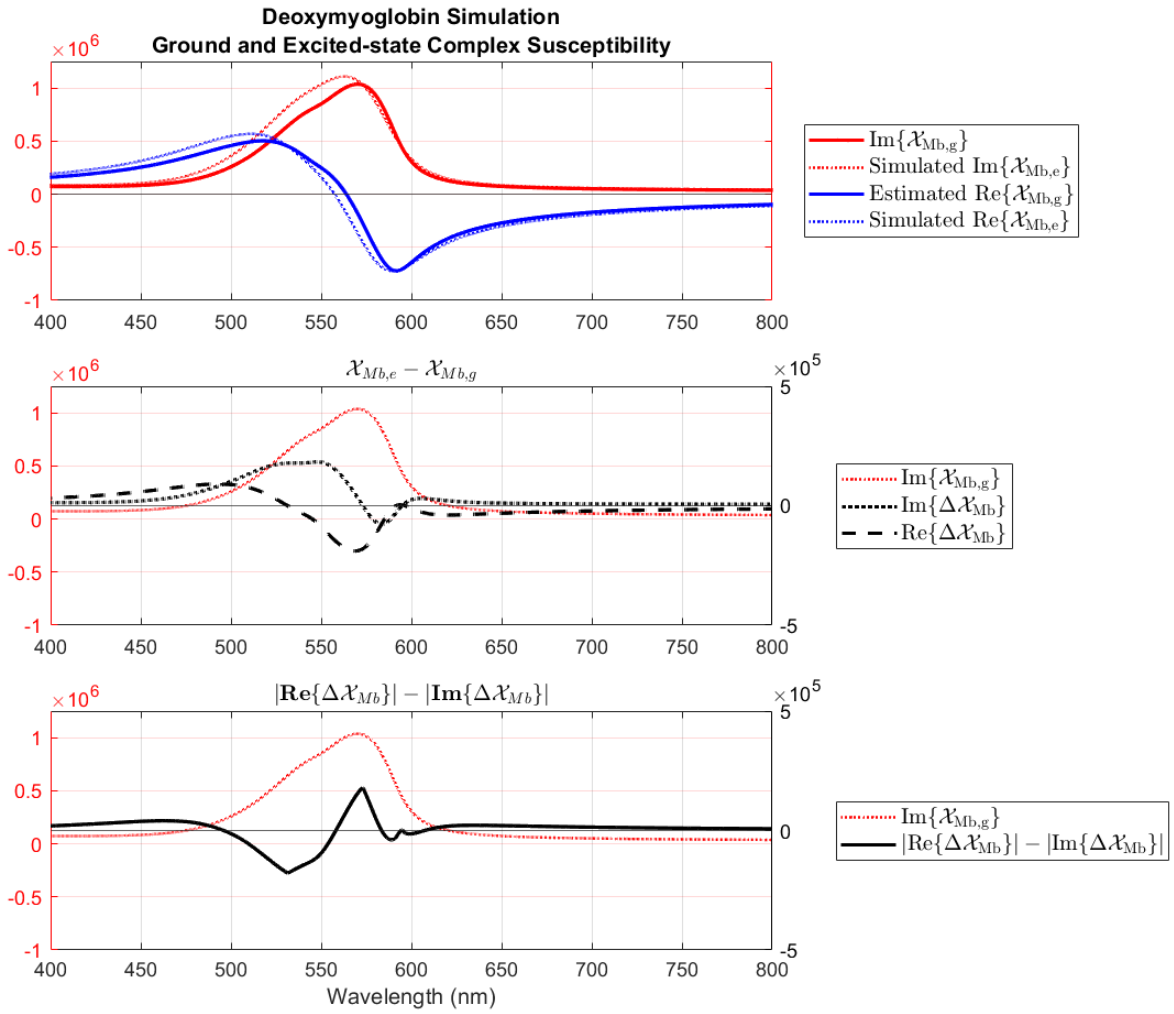

Figure 2.4: Row 1 shows a simulation of the (proportional) ground-state absorption spectrum for deoxymyoglobin in red and the associated phase spectrum in blue for 293 K; the excited-state absorption spectrum is shown as a red dashed line and the associated excited-state phase spectrum is shown as a blue dashed line for 1400 K (simulation courtesy of Dr. Jesse Wilson). Row 2 shows $\Delta\mathcal{X}$ for both absorption and phase. Row 3 shows the difference of the absolute value for each spectrum; again, positive components correspond to a stronger TΦM than TAM signal, and negative components correspond to a stronger TAM than TΦM signal for the specified wavelength. (Note that $\mathcal{N} = \sqrt{1 + \mathcal{X}}$)

Myoglobin is a heme protein, a trait linked to the porphyrin structure in the molecule which binds iron; other heme proteins include hemoglobin and cytochromes [12]. Using a time-correlator approach, [13] modelled the temperature-dependent energy relaxation processes for deoxymyo-

globin. In their report, [13] only showed the imaginary component of the complex susceptibility; here we show the real and imaginary components of their model for the complex susceptibility. Figure 2.4 shows the modelled ground and excited-state real and imaginary components of the complex susceptibility (courtesy of code provided by Dr. Jesse Wilson). Similar to the process shown above, row 2 shows the difference spectrums for both the imaginary and real components and row 3 compares the overall change in ground versus excited spectrums for the real and imaginary components. When the black line plotting $|\mathrm{Re}\{\Delta\mathcal{X}\}| - |\mathrm{Im}\{\Delta\mathcal{X}\}|$ is positive $S_{\mathrm{T\Phi M}} > S_{\mathrm{TAM}}$, and when the black line is negative $S_{\mathrm{T\Phi M}} < S_{\mathrm{TAM}}$. This approach can help to estimate what wavelengths might provide a stronger TΦM signal versus TAM signal, but require the use of documented Frank-Condon and Herzberg-Teller coefficients in the literature; sometimes this can be difficult to find for a particular sample or the coefficients may not be recorded. Additional approaches to estimate the excited-state spectra include time-independent [14] frameworks and Frank-Condon displaced-harmonic-oscillator models [15]. The example shown for deoxymyoglobin indicates that TAM might provide a stronger signal between 500-555 nm and 575-620 nm, and TΦM might provide a stronger signal between 400-500 nm, 555-575 nm, and 620-800 nm. Determining which is better to measure for a particular probe wavelength would be difficult without knowing exactly the ground and excited-state absorption spectra for the pump wavelength in use. Depending on the molecule in question, TΦM may be more advantageous to probe, but without accurate ground and excited state spectral measurements, it would be prudent to measure both TAM and TΦM.

2.3 Pulse Compression

For pump-probe experiments, the temporal pulse width $\Delta\tau$ of the pump and probe pulses dictate the maximum temporal resolution of the measurement [16]. Thus, in order to uncover faster temporal dynamics of a molecule, shorter pulses need to be used. For a specific bandwidth $\Delta\omega$, the time-bandwidth product relation for a Gaussian pulse [17]

$$\Delta\omega\Delta\tau \geq 0.441 \tag{2.12}$$

can be used to determine the transform-limit. The transform-limit is the shortest pulse of light that can be constructed with a specified bandwidth [17]. In this experiment our laser source supplies a pump beam with a center wavelength of 1035 nm and a bandwidth of ∼8.25 nm; the associated transform-limit for the pump is $\tau \sim 191$ fs. For the probe center wavelength of 800 nm with a bandwidth around 12 nm, the estimated transform limit is $\tau \sim 78$ fs.

In order to achieve a transform-limit pulse, all of the frequencies in the bandwidth must coherently overlap in time. This level of coherence can be accounted for in the spectral phase profile of the pulse; a *flat* spectral phase means that all of the frequencies overlap in time to maximally constructively interfere. However, when light passes through any medium (other than a vacuum) it experiences material dispersion. As discussed earlier, with dispersion different frequencies of light will see different indices of refraction resulting in a frequency-dependent phase velocity (i.e. some frequencies advance faster through the medium than others). Thus, from the time the laser pulse is generated to when it reaches the sample at the focal plane of the microscope, material dispersion can accumulate causing the temporal pulse width to broaden significantly and the spectral phase function to be curved. However, this unwanted dispersion can be corrected for with the use of prism and grating compressors. Compressors are able to apply spectral phase of the opposite sign to that of material dispersion, allowing the two to cancel out and minimize the pulse-broadening effects.

This section will first discuss the laser source utilized in this research and then will move into a discussion of how the temporal profile of the pump and probe pulses were measured and optimized. For these experiments a minimum pulse width of 350 fs will provide sufficient resolution between the reference and probe pulses (separated by 1.2 ps), meaning we do not need to be transform-limited.

2.3.1 Laser Source

The laser used in this experiment supplies two outputs: a pump line centered at $\lambda = 1035$ nm and a tunable probe line set to $\lambda = 800$ nm. Figure 2.5 shows a diagram of the laser source.

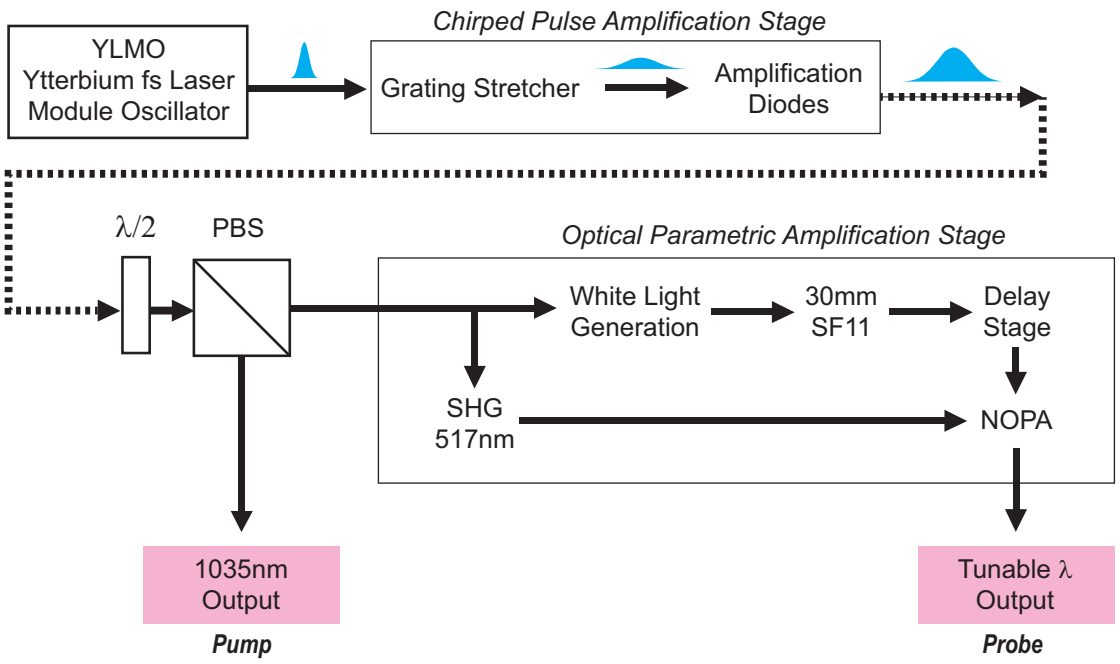

Figure 2.5: The laser oscillator seeds a fiber chirped pulse amplifier and produces pulses at $f_{\text{rep}} = 5$ MHz centered at $\lambda = 1035$ nm with a bandwidth of ~ 8.25 nm. A half-wave plate ($\lambda/2$) controls the power split between the pump output and light directed into a non-collinear optical parametric amplifier which produces the probe output. A delay stage following the white light generation controls the tunable wavelength for the probe.

Our laser source is generated by a Ytterbium-doped fiber laser oscillator (Menlo YLMO) which seeds a fiber chirped pulse amplifier to provide pulses at $f_{\text{rep}} = 5$ MHz centered at $\lambda = 1035$ nm with a bandwidth of ~ 8.25 nm. This output is split into a pump pulse train for the experiments, and another portion feeds a non-collinear optical parametric amplifier to generate the probe pulse train at $\lambda = 800$ nm. In the optical parametric amplification stage, part of the light is frequency doubled through second harmonic generation to create green light at 517 nm. Figure 2.6 shows the Jablonski diagrams for second harmonic generation on the left side; for second harmonic generation to occur two photons of the same frequency ω must arrive simultaneously in a birefringent crystal to create one photon at twice the frequency 2ω [18]. Crystals such as Beta Barium Borate (BBO) can be utilized for second harmonic generation and optical parametric amplification [19][20]. Following SHG, this beam is focused into another crystal for non-collinear optical parametric amplification. The light not split off for SHG at the PBS is sent through a sapphire crystal for white light generation, which creates a broadband pulse. A 30 mm rod of SF11 follows the

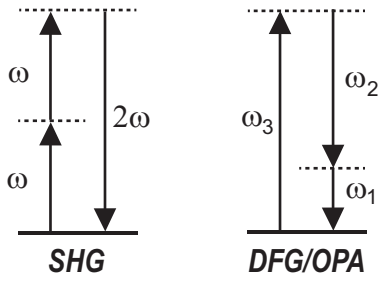

Figure 2.6: Jablonski diagrams for second harmonic generation (SHG) and difference frequency generation (DFG)/optical parametric amplification (OPA) [18]. The dashed lines represent virtual states which implies that these interactions are instantaneous.

white light generation to chirp the broadband pulse in time (ie. separating the frequencies in time). This beam line proceeds through a delay stage before being focused into the NOPA crystal. The white light and the green light must be spatially overlapped inside of the crystal for difference frequency generation to occur; difference frequency generation is the process by which optical parametric amplification occurs. This process is shown on the right side of Figure 2.6, where $\omega_3 > \omega_2 > \omega_1$; a high frequency photon at ω_3 divides into two lower frequency photons at ω_2 and ω_1. One of the photons (ω_2 or ω_1) must be present alongside ω_3 and will experience gain while the remaining photon is created. At the current delay stage position, ω_3 is the green light at 517 nm (pump), ω_2 is a photon at 800 nm (signal) supplied from the white light bandwidth that experiences gain and light at $\omega_3 = 1233$ nm is generated (idler). By changing the delay stage position, ω_2 will change causing a corresponding change in ω_1 to satisfy the expression $\hbar\omega_3 = \hbar\omega_2 + \hbar\omega_1$ [18]. At the output of the laser the pulses should be near transform-limited; the optics between the laser output and the sample focus will add material dispersion to these pulses, the effects of which will be discussed next.

2.3.2 Dispersion and Dispersion Compensation

Dispersion

Material dispersion has the effect of broadening short pulses of light; this is problematic since the temporal resolution of pump-probe spectroscopy depends on the temporal pulse width [16].

Thus, longer pulses result in a poorer temporal resolution. This broadening occurs because of the frequency dependence of the real part of the complex refractive index; as a reminder from before, materials can supply either normal or anomalous dispersion effects. In normal dispersion, higher frequencies see a higher index of refraction and thus travel slower than their lower frequency counterparts (i.e. blue light will travel slower than red). In anomalous dispersion, the opposite is true.

From a mathematical standpoint, spectral phase can capture the effects of temporal dispersion; the following discussion relates the material properties of refractive index to the imparted spectral phase on a pulse. In the frequency domain, the equation for a Gaussian light pulse is

$$E(\Omega) = A(\Omega)e^{i\phi(\Omega)} \tag{2.13}$$

where $\phi(\Omega)$ is the variable for spectral phase, ie phase as a function of frequency. We can expand the spectral phase term using a Taylor series expansion order to get a look at the impacts of first, second and third order spectral phase [21].

$$\begin{aligned}\phi(\Omega) = \phi(\Omega_0) + \frac{d\phi}{d\Omega}(\Omega-\omega_0) + \frac{1}{2}\frac{d^2\phi}{d\Omega^2}(\Omega-\omega_0)^2 + \frac{1}{6}\frac{d^3\phi}{d\Omega^3}(\Omega-\omega_0)^3 \\ = \phi_0 + \phi_1(\Omega-\omega_0) + \frac{\phi_2}{2}(\Omega-\omega_0)^2 + \frac{\phi_3}{6}(\Omega-\omega_0)^3\end{aligned} \tag{2.14}$$

The zero order term ϕ_0 is a phase offset term at the center frequency ω_0. The first order term $\phi_1(\Omega-\omega_0)$ is linear spectral phase which results in a shift in the time domain. The second order term $\frac{\phi_2}{2}(\Omega-\omega_0)^2$ is quadratic spectral phase which causes frequencies at the edge of the bandwidth to travel at different speeds (phase velocity) than those in the center; this term results in temporal pulse broadening. The third order term $\frac{\phi_3}{6}(\Omega-\omega_0)^3$ is cubic spectral phase and can cause asymmetric changes to the temporal profile. From a pulse broadening standpoint, second order dispersion is typically the dominant contributor.

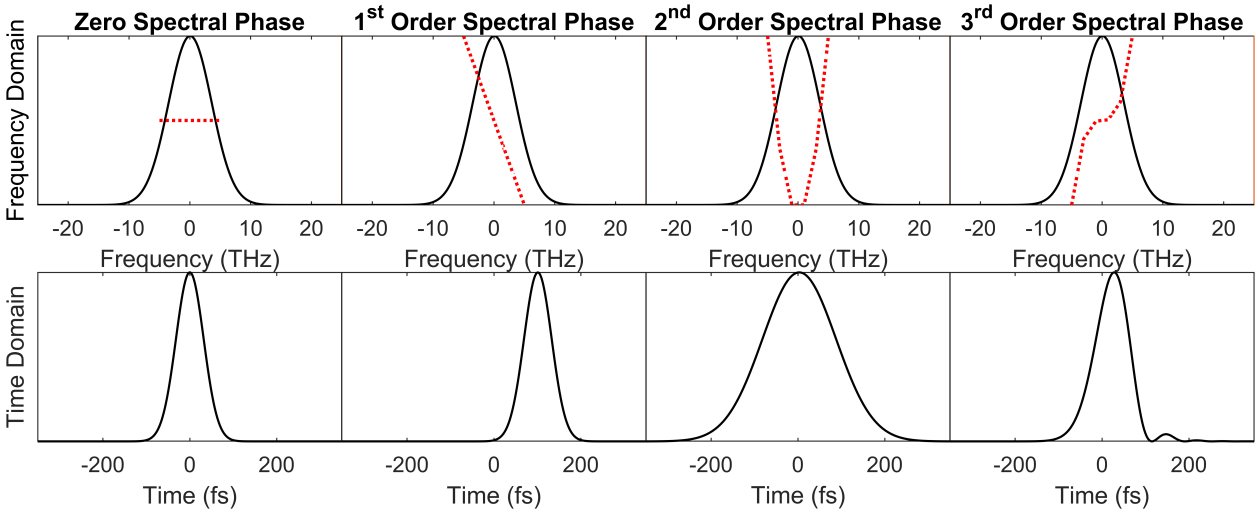

Figure 2.7: Impacts of spectral phase on a 75 fs transform-limited Gaussian pulse. Row 1 shows the frequency domain pulse envelope (black) and the applied spectral phase function (red dotted), row 2 shows the corresponding time domain pulse after taking the Fourier transform. Column 1 is the transform-limited pulse; the spectral phase function is flat. Column 2 has 100 fs of linear spectral phase applied, a corresponding 100 fs temporal shift can be seen in the time domain pulse. Column 3 has 5000 fs^2 of quadratic spectral phase applied, the corresponding time domain pulse has broadened from 75 fs to 199 fs. Column 4 has 90000 fs^3 of cubic spectral phase applied, the corresponding time domain pulse causes the temporal profile to become asymmetric with an oscillatory tail to one side [21].

Figure 2.7 demonstrates the impact of each order of spectral phase on a transform limited pulse. The top row shows a Gaussian pulse in the frequency domain (black) with the spectral phase function overlaid (dotted red). The bottom row shows the Fourier-transform associated with the top row function. When there is zero spectral phase $\phi(\Omega) = 0$, the spectral phase function is a flat line. The time domain corollary is a transform-limited pulse. When linear spectral phase is applied (second column, $\phi_1 = 100$ fs), a corresponding shift occurs in the time domain. However, there is no change to the pulse width, it is still transform-limited. When quadratic spectral phase is applied (third column, $\phi_2 = 5000$ fs^2), pulse broadening occurs in the time domain. Finally, when cubic spectral phase is applied (fourth column, $\phi_2 = 90000$ fs^3), the pulse profile experiences an asymmetric distortion with an oscillatory structure on one side [21].

When an optical pulse travels through a material of length L, material dispersion gives rise to a non-zero spectral phase through

$$\phi(\Omega) = -k(\Omega)L \tag{2.15}$$

where $k(\Omega) = \frac{n(\Omega)\omega}{c}$ is the propagation constant in the medium with refractive index $n(\Omega)$. Similar to the spectral phase function, we can also express the propagation constant as a Taylor series expansion and draw insights from its higher order terms.

$$\begin{aligned} k(\Omega) = k(\Omega_0) + \frac{dk}{d\Omega}(\Omega - \omega_0) + \frac{1}{2}\frac{d^2k}{d\Omega^2}(\Omega - \omega_0)^2 + \frac{1}{6}\frac{d^3k}{d\Omega^3}(\Omega - \omega_0)^3 \\ = k_0 + k_1(\Omega - \omega_0) + \frac{k_2}{2}(\Omega - \omega_0)^2 + \frac{k_3}{6}(\Omega - \omega_0)^3 \end{aligned} \tag{2.16}$$

Each of these terms can be directly related to refractive index in terms of frequency or wavelength (equations from [17])

$$\frac{dk}{d\Omega} = \frac{n}{c} + \frac{\Omega}{c}\frac{dn}{d\Omega} = \frac{1}{c}\left(n - \lambda\frac{dn}{d\lambda}\right) \tag{2.17}$$

$$\frac{d^2k}{d\Omega^2} = \frac{2}{c}\frac{dn}{d\Omega} + \frac{\Omega}{c}\frac{d^2n}{d\Omega^2} = \left(\frac{\lambda}{2\pi c}\right)\frac{1}{c}\left(\lambda^2\frac{d^2n}{d\lambda^2}\right) \tag{2.18}$$

$$\frac{d^3k}{d\Omega^3} = \frac{3}{c}\frac{d^2n}{d\Omega^2} + \frac{\Omega}{c}\frac{d^3n}{d\Omega^3} = -\left(\frac{\lambda}{2\pi c}\right)^2\frac{1}{c}\left(3\lambda^2\frac{d^2n}{d\lambda^2} + \lambda^3\frac{d^3n}{d\lambda^3}\right) \tag{2.19}$$

The second order dispersion term k_2 is referred to as Group Velocity Dispersion (GVD), but once it is multiplied by the material pathlength k_2L it is referred to as Group Delay Dispersion (GDD). The dispersion parameters $\frac{dn}{d\Omega}$, $\frac{d^2n}{d\Omega^2}$, and $\frac{d^3n}{d\Omega^3}$ are material properties that can be looked up for many common materials; Table 2.1 shows the dispersion parameters for glass, dense flint and fused silica.

Table 2.1: This table was adapted from [17] and provides a list of the dispersion parameters for glass (BK7), dense flint (SF10) and fused silica (SQ1).

Material	λ_c [nm]	$n(\omega_c)$	$\frac{dn}{d\Omega}$ [fs] 10^{-2}	$\frac{d^2n}{d\Omega^2}$ [fs^2] 10^{-3}	$\frac{d^3n}{d\Omega^3}$ [fs^3] 10^{-4}	$\frac{dn}{d\lambda}$ [μm^{-1}] 10^{-2}	$\frac{d^2n}{d\lambda^2}$ [μm^{-2}]	$\frac{d^3n}{d\lambda^3}$ [μm^{-3}]
BK7	800	1.5106	0.67	0.06	39	-2	0.05	-0.29
	1000	1.5074	0.73	-3.2	114	-1.4	0.016	-0.09
SF10	800	1.7112	1.7	6	58	-5	0.17	-1
	1000	1.7038	1.5	2	132	-2.8	0.06	-0.3
SQ1	800	1.4533	0.58	-0.4	41	-1.7	0.04	-0.24
	1000	1.4504	0.67	-3.8	121	-1.3	0.012	-0.08

Material dispersion is the dominant contributor to spectral phase that can cause pulse broadening, however, angular dispersion can be utilized to undo these effects and shorten pulses. This can be achieved through the incorporation of a prism and/or grating compressor.

Prism and Grating Compressors

While material imparts a *positive* second and third order spectral phase component to a light pulse, prism compressors are able to impart *negative* second and third order spectral phase. Interestingly, grating compressors are able to impart *negative* second order but *positive* third order spectral phase [17]. Table 2.2 shows the comparison of spectral phase signs for these three scenarios.

Table 2.2: Sign of the second and third order spectral phase imparted by material dispersion, a grating compressor, and a prism compressor [17]

	Material	Gratings	Prisms
GDD	+	-	-
TOD	+	+	-

Prism and grating compressors can be utilized separately or in tandem. Figure 2.8 shows an example of a double-pass prism compressor on the left and a double-pass grating compressor on the right. Grating compressors can be constructed much more compactly than prism compressors

and only provide one tuning knob: the separation between a pair of gratings. They are great for compensating for large amounts of GDD, but cannot be used to compensate for TOD simultaneously [21]. Prism compressors, however, provide two tuning knobs: the separation between a pair of prisms and the material pathlength through the prisms. They can add negative GDD with increased prism separation and can independently tune the amount of TOD by changing the prism insertion. However, they provide low angular dispersion in comparison to grating compressors. In tandem, a grating and prism compressor can account for large amounts of GDD while independently tuning for TOD compensation.

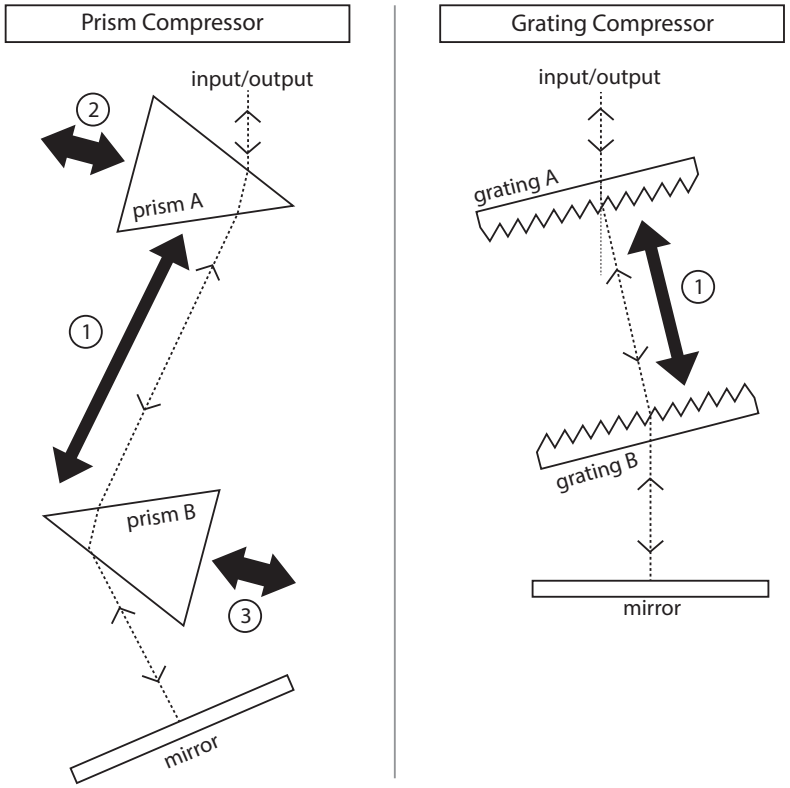

Figure 2.8: Example diagrams for a double-pass prism compressor (left) and a double-pass grating compressor (right). In a prism compressor, the separation between the two prisms can be adjusted (1) and the insertion of each prism into the beam line can be adjusted (2) and (3). In a grating compressor, only the separation between the gratings can be adjusted (1).

Prism Compressor Spectral Phase Equations Changing the insertion of a prism alters the amount of material dispersion experienced, while increasing the distance between the two prisms increases the amount of angular dispersion.

Equations 2.20 and 2.21 show spectral phase terms for a double-pass prism compressor configuration. L is the separation between the two prisms which controls angular dispersion and L_g is the pathlength through the prisms on a single pass. These equations are from [17].

$$\frac{d^2\phi}{d\Omega^2} = 2\left\{\frac{L_g}{c}\left[2\frac{dn}{d\Omega} + \omega_c\frac{d^2n}{d\Omega^2}\right] - \frac{\omega_c}{c}\left(4L + \frac{L_g}{n^3}\right)\left(\frac{dn}{d\Omega}\right)^2\right\} \tag{2.20}$$

$$\frac{d^3\phi}{d\Omega^3} = 2\left\{\frac{\lambda_c^4}{(2\pi c)^2 c}\left[12L\left(\frac{dn}{d\lambda}^2\left[1 - \lambda_c\frac{dn}{d\lambda}\left(\frac{1}{n^3} - 2n\right)\right] + \lambda_c\frac{dn}{d\lambda}\frac{d^2n}{d\lambda^2}\right)\right] - L_g\left(3\frac{d^2n}{d\lambda^2} + \lambda_c\frac{dn^3}{d\lambda_c^3}\right)\right\} \tag{2.21}$$

Grating Compressor Spectral Phase Equations In a grating compressor, the first grating refracts the spectral components of a light pulse at different angles. This causes different frequencies of light to experience different pathlengths through air before the second grating spatially recombines the beam. The second order dispersion applied by a pair of gratings can be computed with

$$\frac{d^2\phi}{d\Omega^2} = -2\left\{\frac{\lambda_c}{2\pi c^2}\left(\frac{\lambda_c}{d}\right)^2\frac{1}{cos^2\beta'(\omega_c)}\right\}L \tag{2.22}$$

where d is the width of one line (equal to 1 over the groove density), L is the grating separation and β is the angle of incidence. This equation is taken from [17].

As we have seen, angular dispersion is a critical tool in the pulse compression toolbox. It allows compressors built using prisms and gratings to compensate for second and third order spectral phase effects that would otherwise make short pulses longer. However, in order to determine how

much GDD and TOD exists on an optical pulse, and thus how much needs to be compensated for, we turn to a technique known as Frequency Resolved Optical Gating (FROG).

2.3.3 Measuring the Spectral Phase with FROG

In 1991 a technique known as Frequency Resolved Optical Gating (FROG) was proposed by Daniel Kane and Rick Trebino [22] as a way to measure the spectral phase on an optical pulse. This is the technique employed here to determine the spectral phase on the pump and probe pulses after they have passed through the majority of optical elements (but before they are focused by the objective onto the sample plane). FROG requires an indirect measurement of the pulse paired with an iterative algorithm to back out the associated spectral phase. The measurement is a spectrogram of the pulses (frequency versus delay); typically a second harmonic (SHG) spectrogram is utilized though other types of spectrograms can be used. The iterative algorithm has seen many variations over the years; the algorithm employed in this work is the Principal Component Generalized Projections Algorithm (PCGPA) [23].

In order to measure the SHG spectrogram of a pulse, two identical copies of the pulse must be made and then focused (non-collinearly) into a second harmonic crystal like KDP. Each pulse will generate a second harmonic pulse, but the two pulses will also together generate a sum frequency pulse (SFG) at the second harmonic wavelength. It is this SFG pulse that needs to be measured by a spectrometer as a function of delay between the two pulses. After running a delay scan an array like the one shown in (a) of Figure 2.9 will be generated.

The measured spectrogram is utilized as an intensity constraint as the algorithm iterates between the time and frequency domain to reconstruct the pulse. Following the steps shown in Figure 2.9 (b), first a guess is made for the probe $P(t)$ and gating functions $G(t)$. Then the outer product of the two functions is taken to create an array followed by a row-rotation and the Fourier transform (FFT) along the columns. At this point, an estimated spectrogram is created. The phase of the estimated spectrogram is retained, but the intensity is replaced by the modulus of the measured spectrogram. Then the inverse Fourier transform (iFFT) is taken followed by an inverse

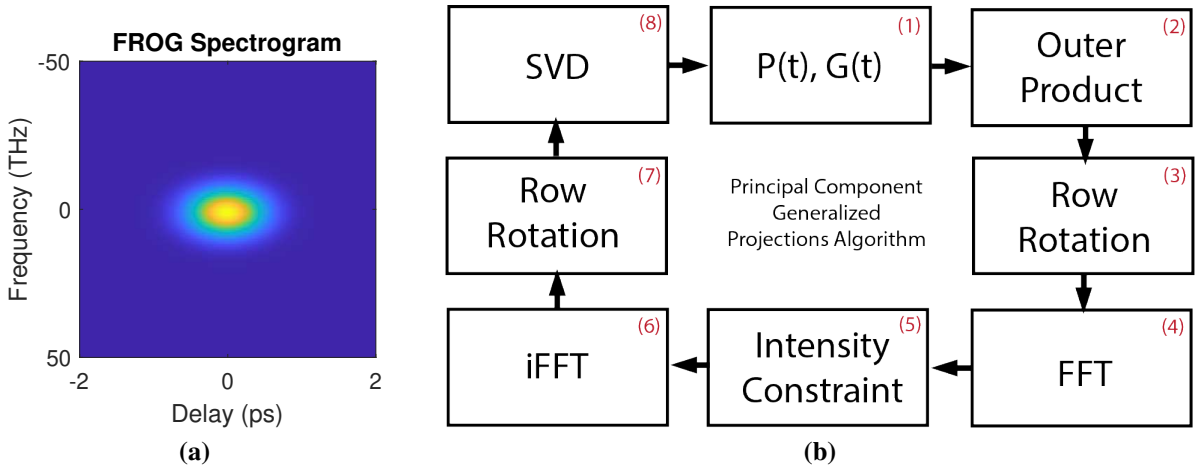

Figure 2.9: (a) An example of a SHG spectrogram. (b) The process for the iterative algorithm to solve for spectral phase from the measured spectrogram, adapted from [24] (FFT: Fast Fourier Transform, iFFT: inverse Fast Fourier Transform, SVD: Singular Value Decomposition, P(t): Probe function, G(t): Gate function)

row-rotation. Application of a singular value decomposition (SVD) to the array will then produce estimates of the probe and gate functions. For SHG FROG, the gating function is set equal to the probe and the process repeats itself until the estimated spectrogram is a match for the measured spectrogram.

One drawback of the SHG FROG technique is that suffers from a time reversal ambiguity [21]. In order to use the spectral phase estimates from SHG FROG, a secondary spectrogram must also be processed where an object of known dispersion has been added to the beam line. This allows the proper sign to be applied to the phase estimates; recall that this is important for knowing whether to add or subtract positive versus negative GDD and TOD with the compressors.

Measurements

A pre-constructed optical setup was utilized for acquiring the spectrogram traces on the pump and probe lines; a diagram of this setup is shown in Figure 2.10. The pump and probe pulses were measured separately with only one beam line entering the FROG apparatus, which is split by a beam-splitter. One copy encouters a motorized delay stage, the other proceeds directly to the second harmonic crystal, KDP. Importantly, the pulse pair is crossed in a non-collinear geometry through the KDP, allowing the SFG component to easily be selected by the spectrometer for

measurement when it appears between the two SHG components. The spectrogram measurements made for both the pump and probe were acquired as far downstream in the optical setup as possible; ideally the FROG measurement would be taken at the focal plane of the objective but for practical purposes this is not possible. Thus, while the majority of the system dispersion is captured in the FROG measurements, dispersion from the objective was not included. In order to compensate for this, the FROG measurements were acquired with a rod of BK7 placed in the beam line to add similar amount of GDD as was expected by the objective. A secondary advantage of doing this is that it allowed the sign of the spectral phase estimates to be determined between spectrograms acquired with and without the rod.

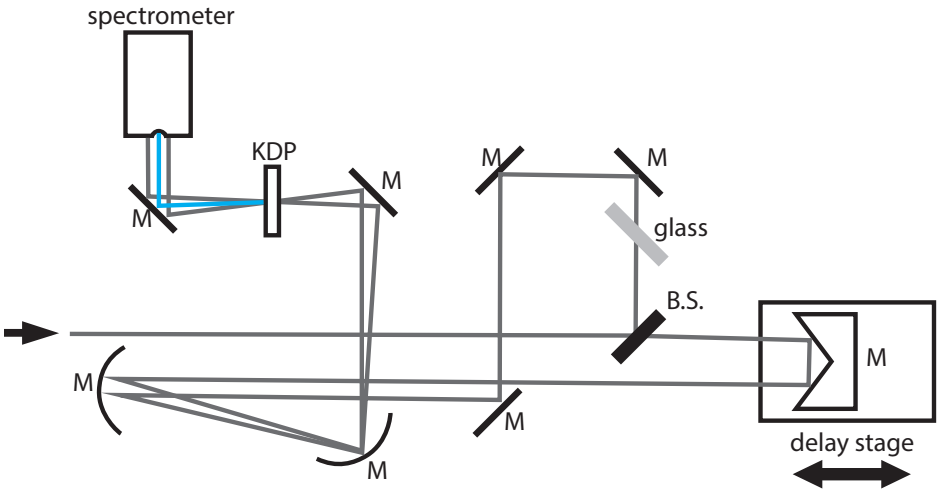

Figure 2.10: Diagram of the SHG FROG setup used. This setup was built by one of Dr. Bartel's previous students. The setup is self-contained on a breadboard and preferentially accepts p-polarized light. The incident beam is split by a neutral density beamsplitter; a beam copy proceeds to a roof mirror on a motorized delay stage and a copy proceeds through a piece of glass to account for dispersion obtained by the other beam before the two bounce off two curved mirrors and are focused into a KDP crystal in a non-collinear geometry. The sum-frequency component generated in the nonlinear crystal appears between two second harmonic components which continue along either beam propagation direction. (M: Mirror, B.S.: Beamsplitter)

The GDD applied from a piece of BK7 can be estimated from the equation

$$\frac{d^2\phi}{d\Omega^2} = \frac{L_g}{c}\left[2\frac{dn}{d\Omega} + \omega_c\frac{d^2n}{d\Omega^2}\right] \tag{2.23}$$

where L_g is the pathlength through the material, c is the speed of light, and ω_c is the center wavelength. The dispersion parameters for BK7 can be found for the pump and probe wavelengths in Table 2.1. According to [25], our current objective in use (Nikon Plan Apo λ, 20X/0.75 NA) adds a GDD of approximately 4150 fs^2. By inserting a 9 cm rod of BK7 into either beam line prior to the FROG apparatus, approximately 4062 fs^2 of GDD was added to the probe beam and 2631 fs^2 of GDD to the pump beam. This provided a closer approximation to what the pulse width would look like at the focal plane for either pulse.

Initially, only a prism compressor existed on the probe arm and a grating compressor on the pump arm (from the adopted setup). However, third order dispersion was found to be a limiting factor in the pump pulse so a prism compressor was added to complement the grating compressor. It is hypothesized that this third order dispersion is tied to self-phase modulation occurring during the chirped pulse amplification stage of the laser source. The pump and probe compressors were tuned alongside various FROG measurements until the pulse width for each was reduced to at least 350 fs (which provides good resolution between the 1.2 ps separated probe and reference pulses).

Final Probe Dispersion The final FROG measurement after tuning the prism compressor on the probe arm placed the estimated pulse width around 167 fs. As a reminder, the transform limit for the probe is ~ 78 fs meaning additional compression could occur, however, this is well below the necessary 350 fs pulse width needed in this project. Figure 2.11 shows the final measured and reconstructed FROG spectrogram after running the iterative PCGPA algorithm. The 9 cm rod of BK7 was included in this FROG measurement, so the pulse width should be more similar to what it would be after passing through the objective.

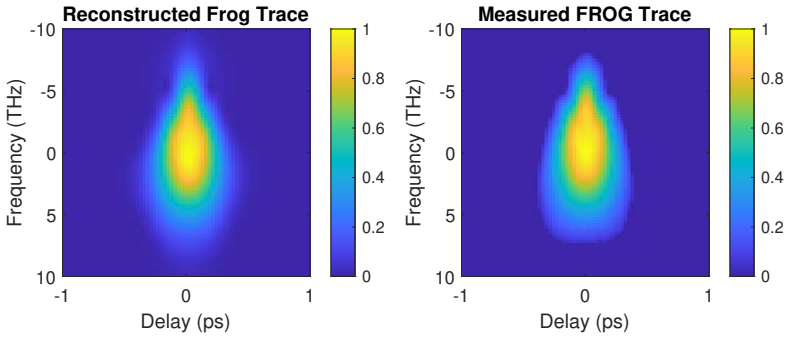

Figure 2.11: Reconstructed (left) and measured (right) FROG traces for the final prism compressor position on the probe arm.

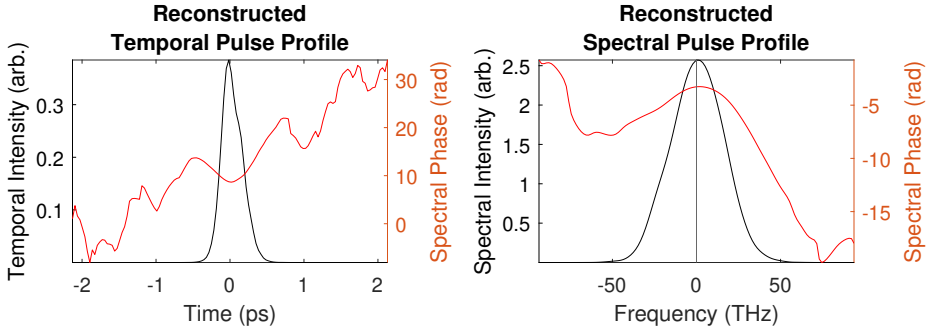

Figure 2.12: Reconstructed probe pulse after running the FROG algorithm for the time domain (left) and frequency domain (right).

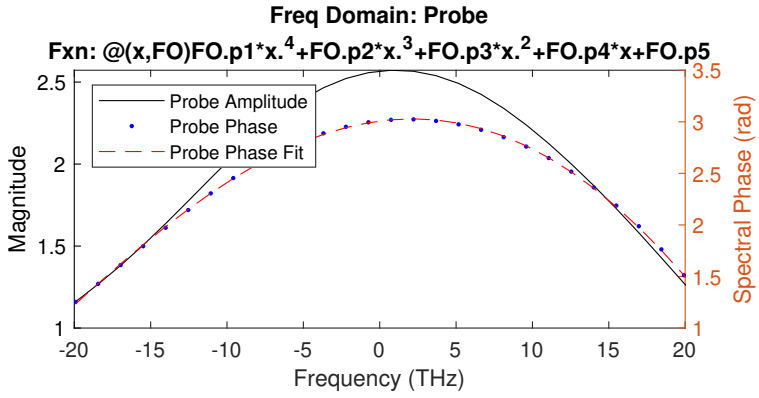

(a)

	Values
p1	7.2287e-07
p2	-3.1183e-05
p3	-0.0044
p4	0.0194
p5	3.0076
GD (ps)	0.0194
GDD (fs^2)	-440.7003
TOD (fs^3)	-3.1183e+03

(b)

Figure 2.13: (a) shows the reconstructed spectral pulse for the probe with a fit polynomial function to the reconstructed spectral phase. (b) displays the fit parameters for the polynomial (p1 - p5) and the resulting extraction of the GD, GDD, and TOD parameters from the fit.

Figure 2.12 shows the reconstructed temporal and spectral pulse profiles and Figure 2.13 shows the polynomial fit to the spectral phase function (a) and the extracted dispersion values (b). The function was fit to a fourth order polynomial (variables p1 - p5) and the first, second and third order polynomials were converted to group delay (GD), group delay dispersion (GDD) and third order dispersion (TOD) values. Note that about $\sim$440 fs^2 of GDD still exists on the pulse as well as $\sim$3118 fs^3 of TOD.

Final Pump Dispersion Before the addition of a prism compressor to the pump line, the grating compressor was first optimized. It was found that the minimum cross-correlation between the pump and probe achievable at this point was 400 fs, approximately 50 fs greater than desired, and that TOD dispersion on the order of 8000 fs^3 remained on the pump pulse. A prism compressor was added to the pump line in order to add independent TOD compensation from the grating compressor and further reduce the pump pulse width. Figure 2.14 shows the before and after designs for the addition of a prism compressor to the pump arm. Careful note was taken of pathlengths in the initial setup before the prism compressor was constructed. This made it easier to re-acquire time-overlap after the prism compressor was complete.

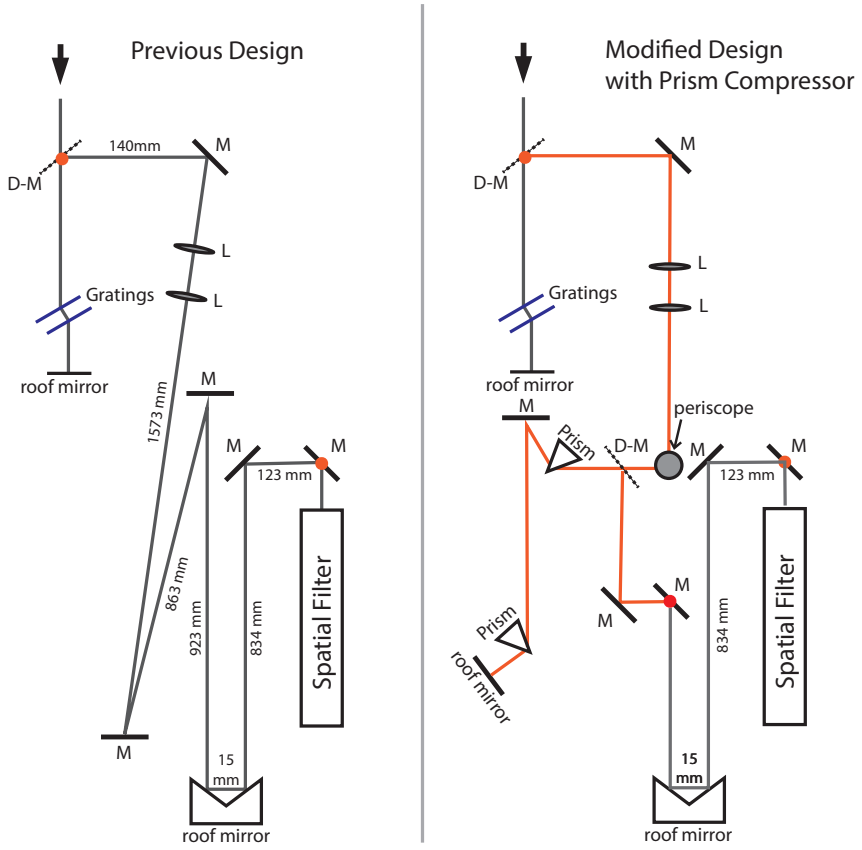

Figure 2.14: (left) Previous beam path on the pump arm from the gratings to the spatial filter. (b) Modified beam path (in orange) with the addition of a prism compressor after the grating compressor. In order to minimize the impact on time overlap, the pathlengths were measured on the previous design. (M: Mirror, D-M: D-Mirror,

The prism compressor shows a folded design, where the pump beam double passes through each prism but at a different height on the return path. In the design of the prism compressor, Equations 2.20 and 2.21 were used to determine what prism separation and insertion values could make a SF10 prism pair GDD neutral. Ideally, the grating compressor could be set to maximally compensate for GDD and the prism compressor could be set to maximally compensate for TOD.

Table 2.3 shows several starting configurations for the prism compressor where GDD is neutral and primarily TOD is compensated. This table was utilized in determining how to initially setup the prism pair.

Table 2.3: Estimation of prism configurations that would minimize GDD compensation.

Material Pathlength (per prism) [cm]	Material Pathlength (total) [cm]	Prism Separation [mm]	GDD [fs^2]	TOD [fs^3]
1.225	2.45	500	3.50	6297
1.345	2.69	550	7.26	6941
1.470	2.94	600	4.28	7557
1.590	3.18	650	6.55	8201
1.715	3.43	700	4.99	8817
1.835	3.67	750	5.34	9446

After the prism compressor was built and set to the estimated position, the cross-correlation pulse width was found to be $\sim$ 350 fs achieving enough pulse compression to continue with experiments. A final FROG taken at this position is shown in Figure 2.15. The reconstructed pulses (Figure 2.16) and the fit spectral phase function (Figure 2.17) places the remaining GDD on the pump pulse ~ 111 fs^2 and the remaining TOD ~ 1872 fs^3.

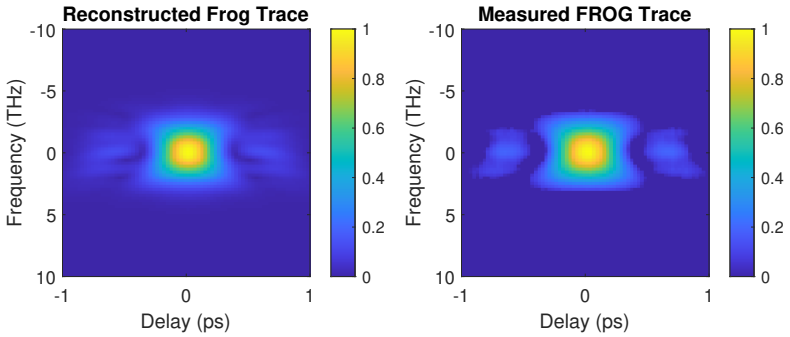

Figure 2.15: Reconstructed (left) and measured (right) FROG traces *after* the addition of a prism compressor following the grating compressor on the pump arm.

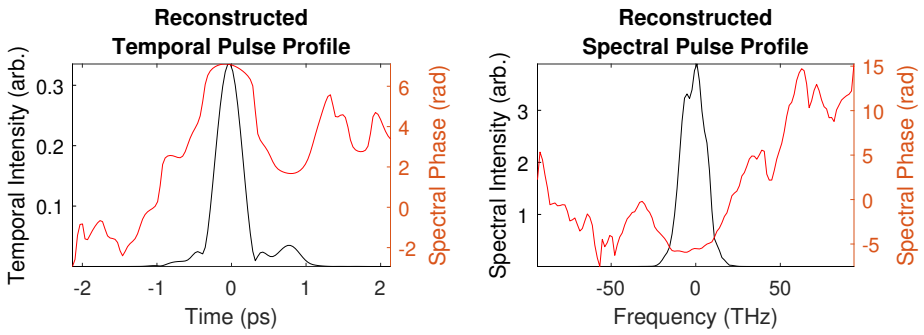

Figure 2.16: Reconstructed pump pulse after running the FROG algorithm for the time domain (left) and frequency domain (right). This FROG was taken after a prism compressor was added to the pump line. The FWHM of the reconstructed temporal pulse is $\sim$ 350 fs.

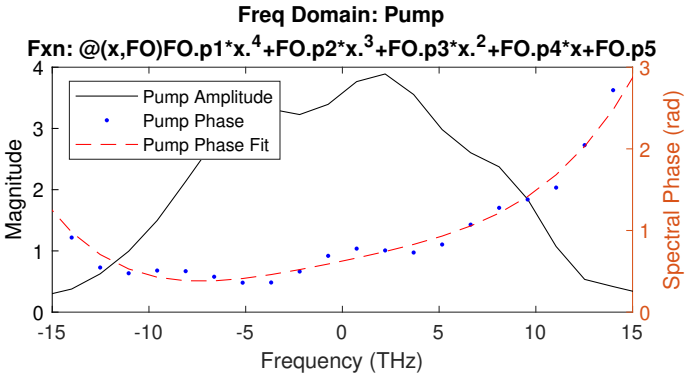

(a)

	Values
p1	2.3046e-05
p2	1.8720e-05
p3	0.0011
p4	0.0499
p5	0.6256
GD (ps)	0.0499
GDD (fs^2)	111.8774
TOD (fs^3)	1.8720e+03

(b)

Figure 2.17: (a) shows the reconstructed spectral pulse for the pump after the prism compressor addition with a fit polynomial function to the reconstructed spectral phase. (b) displays the fit parameters and the resulting extraction of the GD, GDD, and TOD parameters from the fit.

In summary, the addition of the prism compressor to the grating compressor on the pump arm was able to reduce the overall pulse width by $\sim$50 fs. The transform-limit for the pump is $\sim$ 191 fs, meaning there is room for a 160 fs improvement still in the pump compression if future research requires it. In the next section, we will turn our attention to the microscope design required to carry out the transient phase and transient absorption measurements.

2.4 Microscope Design

2.4.1 Changes to the Original Microscope

The microscope adopted for this project was originally setup as a transient absorption microscope by previous graduate student, Dr. Patrick Stockton. Figure 2.18 shows the layout of this microscope; a delay stage on the probe arm controlled the pump-probe delay τ_1, spatial filters present on both arms helped clean up the spatial beam modes, and an acoustic optic modulator (AOM) on the pump line imparted an amplitude modulation to the pump pulse train for downstream lock-in detection. A dichroic beam combiner (Thorlabs DMLP900) was used to combine the pump and probe beams before they were relayed onto a set of x/y scanning galvonometer mirrors conjugated to the back focal plane of a microscope objective, focused onto the sample plane and followed by a condenser. The light exiting the condenser was then relayed to a detector which sent a voltage signal to a preamplifier and lock-in amplifier (LIA) before being processed by the data acquisition device (DAQ).

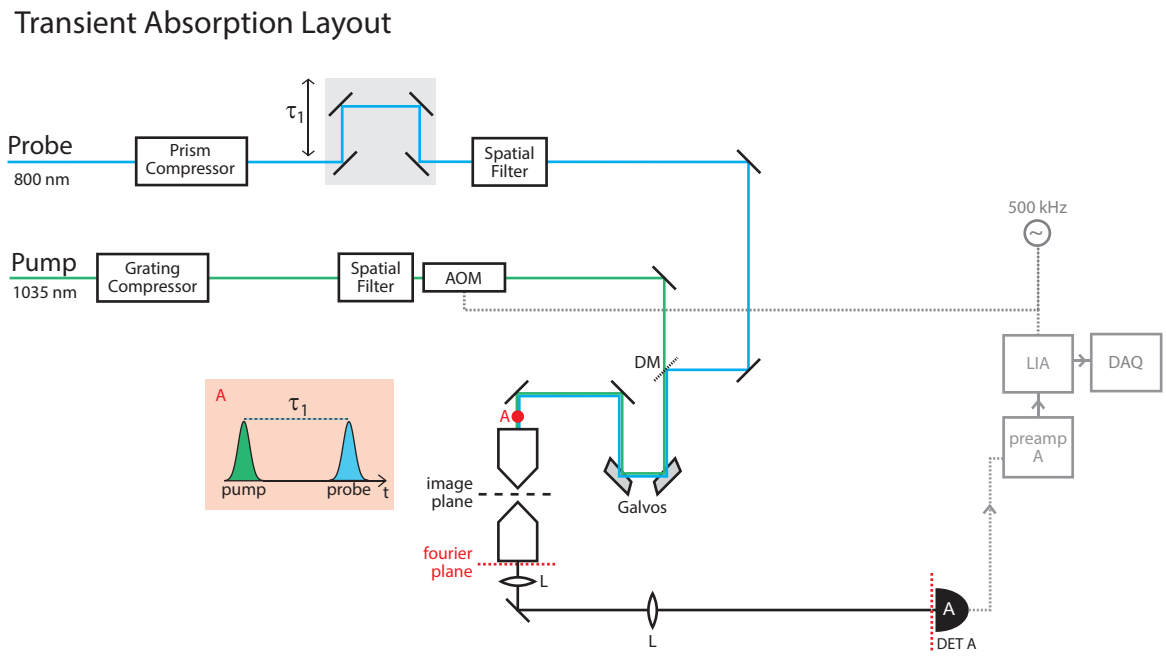

Figure 2.18: The original transient absorption microscope. (HWP: half-wave plate, POL: polarizer, CAL: calcite, DM: dichroic mirror, L: lens, DET: detector, LIA: lock-in amplifier, DAQ: data acquisition device)

The modifications to this microscope design for transient phase include three primary differences: a prism compressor added to the pump line, polarization optics added to both beam lines, and the addition of a second detector for balanced detection.

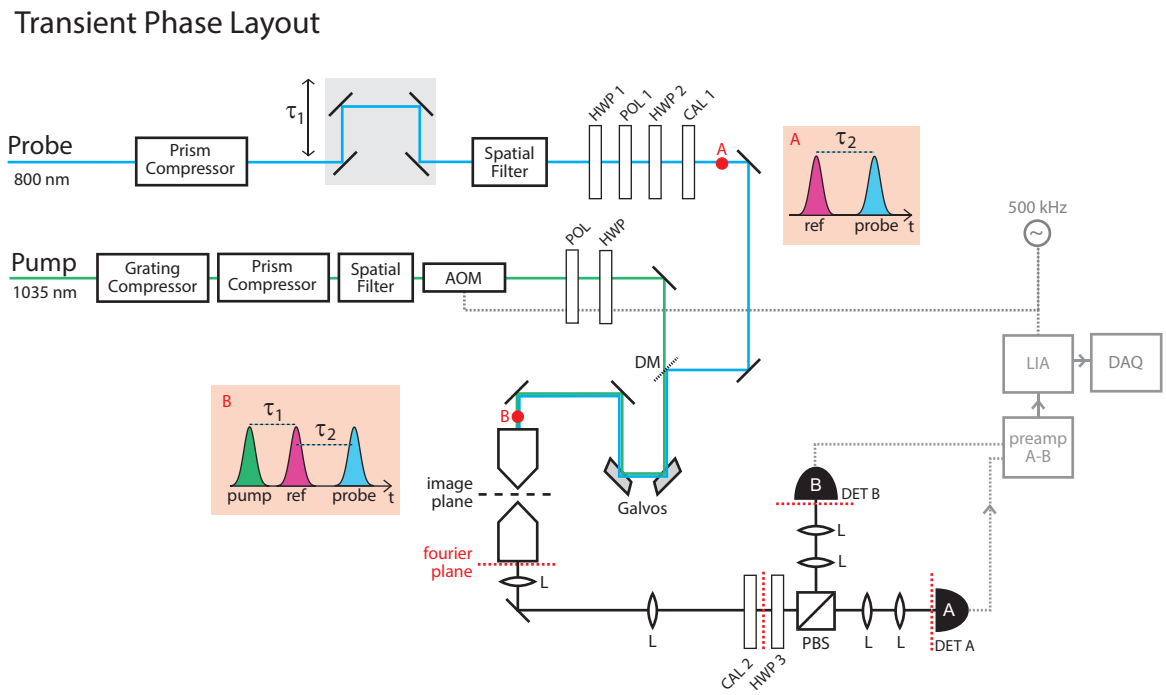

Figure 2.19: Modifications to the transient absorption microscope for transient phase. The probe pulse is split into a reference and probe pulse with the first calcite crystal (CAL 1) separated by a time delay of τ_2 $\sim$1.2ps (see Label A). The delay stage in the probe beam controls the temporal separation of the pump and reference pulses τ_1(see Label B). We utilize a Nikon Plan-Apo λ 20X objective (0.75 NA) and a Zeiss LD Epiplan 50X condenser (0.50 NA). The Fourier plane on the back aperture of the condenser is relayed to the plane between the re-timing calcite (CAL 2) and half-wave plate (HWP 3), as well as to the detector planes. (HWP: half-wave plate, POL: polarizer, CAL: calcite, DM: dichroic mirror, L: lens, DET: detector, LIA: lock-in amplifier, DAQ: data acquisition device)

Figure 2.19 shows the comparative modifications made to the original microscope. Following the AOM on the pump arm, polarization control was added in the form of a polarizer (POL) and a half-wave plate (HWP). On the probe arm several polarization optics were added: first a half-wave plate (HWP 1) and polarizer (POL 1) combination to clean up and maximize linearly polarized light. Then another half-wave plate (HWP 2) was utilized to change the rotation angle of the polarization before incidence on a 2 mm thick calcite crystal (CAL 1). CAL 1 creates a reference-

probe pulse pair with a separation τ_2 determined by the calcite thickness and angle of incidence. Finally in the detection another calcite crystal (CAL 2) for re-timing and half-wave plate (HWP 3) for polarization control were added. A polarizing beam splitter with two detectors (DET A and DET B) in a balanced detection configuration were also added. Also note the relay lenses of the detection arm are setup such that the Fourier plane appears between CAL 2 and HWP 3 (where these are placed as close together as possible) and at each detector plane; optimally minimizing translation through both of them when point scanning. The objective utilized in the transient phase setup was a Nikon Plan Apo λ (20X/0.75 NA) and the condenser a Zeiss LD Epiplan (50X/0.50 NA). The two detectors are both amplified photodiodes (Thorlabs PDA36A2) with the gain setting at 0 dB.

2.4.2 Polarization Optics

The polarization optics on the probe arm and in the detection tree allow phase measurements to be made by converting phase changes into interference effects which are then time-integrated into amplitude changes by the detectors. If the polarization optics are set incorrectly or if the microscope optics between CAL 1 and CAL 2 add polarization aberrations, then proper pulse splitting and re-timing might not occur and decreases in the achievable signal-to-noise ratio (SNR) can arise.

Figure 2.20 shows a closer inspection of the role for each polarization optic used for phase detection. POL 1 is set to allow p-polarized light to transmit, where p-polarization is defined parallel to the plane of the optical table (step 1). HWP 1 is rotated to maximize the amount of light that transmits through POL 1. HWP 2 is used to rotate the linearly polarized light to 45 degrees (step 2). CAL 1 is 2 mm thick piece of calcite cut so that the optic axis runs along the front face of the crystal (a-cut). It is oriented so that the extraordinary axis coincides with p-polarized light and the ordinary axis coincides with s-polarized light. When the probe beam is incident on CAL 1 at 45 degrees it is projected onto the ordinary ($n_o = 1.6514, n_{g,o} = 1.673$) and extraordinary axes ($n_e = 1.4826, n_{g,e} = 1.4920$). Two pulses exit CAL 1 (step 3) orthogonally polarized;

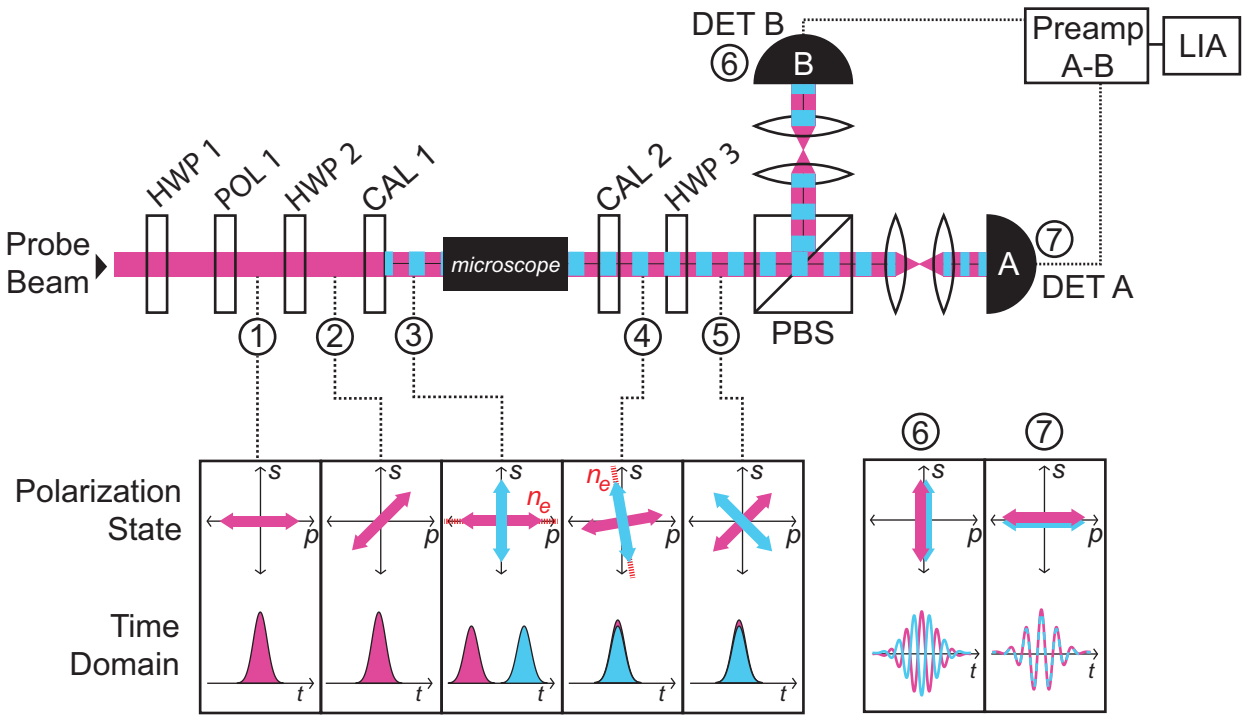

Figure 2.20: Overview of the polarization and detection optics and their impact on the reference and probe pulses. The (HWP: half-wave plate, POL: polarizer, CAL: calcite, DET: detector, LIA: lock-in amplifier)

the reference pulse is advanced and p-polarized, the probe pulse is delayed and s-polarized. The probe pulse pair proceeds through the microscope before encountering CAL 2. CAL 2 is oriented opposite to CAL 1; the ordinary (slow) axis is rotated to coincide with the advanced reference pulse and the extraordinary (fast) axis coincides with the delayed probe pulse. The result is a re-timing of the two pulses (step 4). Note that the axes of CAL 2 may not align with s- and p- polarization as referenced to the table surface, but is instead set based on the axes of the reference and probe polarizations after going through the microscope. HWP 3 is used to rotate the re-timed reference and probe polarizations such that they are 45 degrees to the s- and p- axes of the polarizing beam splitter (PBS), so that both the reference and probe pulses send a copy of themselves to DET A and DET B (step 5). The pulse pair copy on DET B (step 6) will be π out of phase from the pulse pair on DET A (step 7). Thus, if one detector measures destructive interference between the reference-probe pair then the other detector will measure constructive interference.

With each sample, the initial offset phase Φ_0 between the probe and reference pulses is set to a balanced position such that $V_A - V_B = 0$, where V_A is the voltage on DET A and V_B is the voltage

on DET B. The offset phase can be set by adjusting the angle-of-incidence (α_{ext}) of CAL 1 with p-polarized light. This angle is set with the pump pulse blocked so that the offset phase accounts for any residual phase imparted to the reference and probe pulses by the microscope and sample. When the pump pulse is unblocked, a phase advance imparted to the probe pulse from an excited sample will cause an increase in V_A and a decrease in V_B and the overall balanced detection signal $V_A - V_B$ will swing positive. Similarly, a phase delay imparted to the probe pulse will cause a decrease in V_A and an increase in V_B and the overall signal $V_A - V_B$ will swing negative. Figure 2.21 shows an example of the temporal interference between the reference (pink) and probe (blue) pulses on detector A and B for these scenarios.

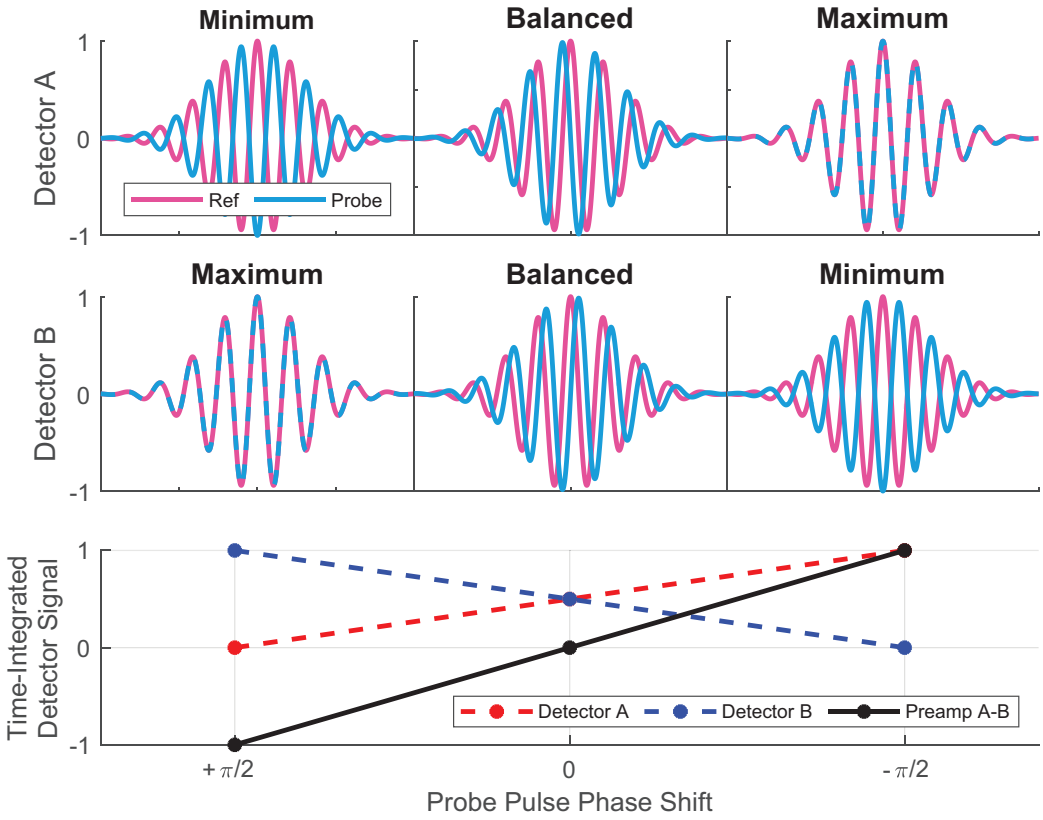

Figure 2.21: Visual of the interference signals present on Detector A and B with different phase shifts imparted to the probe pulse.

Ultimately our setup is capable of measuring an excited state phase change of $\pm\frac{\pi}{2}$ from the initial offset point. The voltage measured on each detector is the time integrated interference between the reference and probe; since our final signal is $V_A - V_B$ we end up with a 2X increase in measurable signal than if we were conducting our measurements with only one detector. The preamplifier (SR 560) measures $V_A - V_B$ and applies a voltage gain before the difference signal is sent into a lock-in amplifier (Liquid Instruments Moku:Lab). The lock-in amplifier measures amplitude changes of $V_A - V_B$ that coincide with the 500 kHz modulation frequency of the pump train; these measurements correspond to pump-induced phase changes $\mathrm{Re}\{\Delta\mathcal{N}\}$.

Setting up the Calcite Crystals

When setting up the pulse splitting and re-timing calcites there are a few measurements that can be made to verify proper orientation. These measurements are described next.

Calcite 1 The first calcite controls two parameters: the time delay τ_2 between the reference and probe pulses and the phase offset Φ_0 between the reference and probe pulses. The temporal pulse separation τ_2 at normal incidence is governed by the group indices for the extraordinary and ordinary axes and the thickness d of the calcite;

$$\tau_2 = \frac{n_{g,o} - n_{g,e}}{c} d = \frac{1.6737 - 1.4920}{3 \times 10^8 \text{ m/s}} 2 \text{ mm} \approx 1.21 \text{ ps} \tag{2.24}$$

The anticipated pulse separation with a 2 mm thick piece of calcite is 1.21 ps. In order to verify this, a half-wave plate was placed directly after CAL 1 to rotate the polarization back to 45 degrees before passing both pulses into a polarizing beam splitter. The interference spectrum was then measured at the output of the transmitted (p-polarized) light. Figure 2.22 shows the measured spectral fringes and the corresponding Fourier transform; as expected the fringes correspond to a temporal separation of $\sim$1.2 ps.

From the way that CAL 1 is mounted, two angles can be rotated. Figure 2.23 provides a visual of this mount. θ_{CAL1} controls the relative angle of the optic axis (which is coincident with

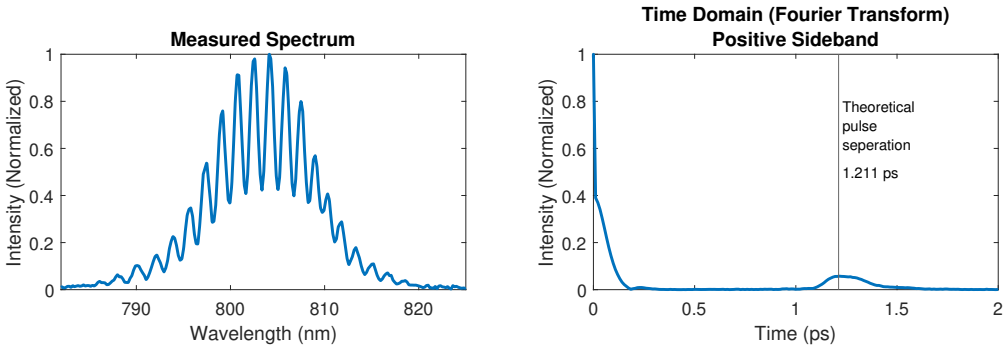

Figure 2.22: A Fourier transform of the spectral interference fringes measured after the first calcite reveal the expected reference-probe temporal pulse separation of 1.2 picoseconds.

the extraordinary axis n_e) with the polarization of incident light. As a reminder, the polarization incident on CAL 1 has been set to 45 degrees where p-polarization is defined as parallel to the optical table. When θ_{CAL1} is correctly set an equal projection of the incident pulse will be split to the extraordinary and ordinary axes. α_{ext} controls the angle-of-incidence between the propagation vector of the incident light and the front plane of the calcite crystal; α_{ext} is what changes the phase offset Φ_0 between the reference and probe pulses.

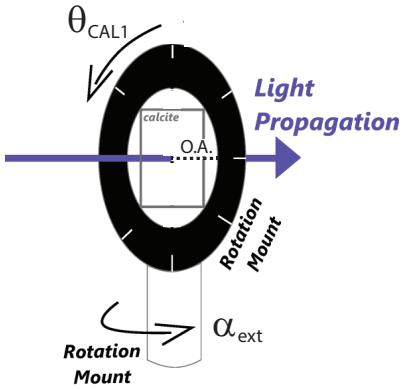

Figure 2.23: Diagram of calcite 1 mount. θ_{CAL1} controls the orientation of the optic axis (O.A.) and α_{ext} controls the angle-of-incidence which changes the offset phase ϕ_0 between the probe and reference.

Calcite 2 The second calcite is responsible for proper re-timing of the reference and probe pulses. This is critical for temporal interference to occur and thus phase measurements to be made. Similar

to CAL 1, there is an angle θ_{CAL2} that controls the relative alignment of the optic axis (O.A.). Figure 2.24 demonstrates three possible scenarios that can occur to the reference-probe pair depending on the orientation of CAL 2.

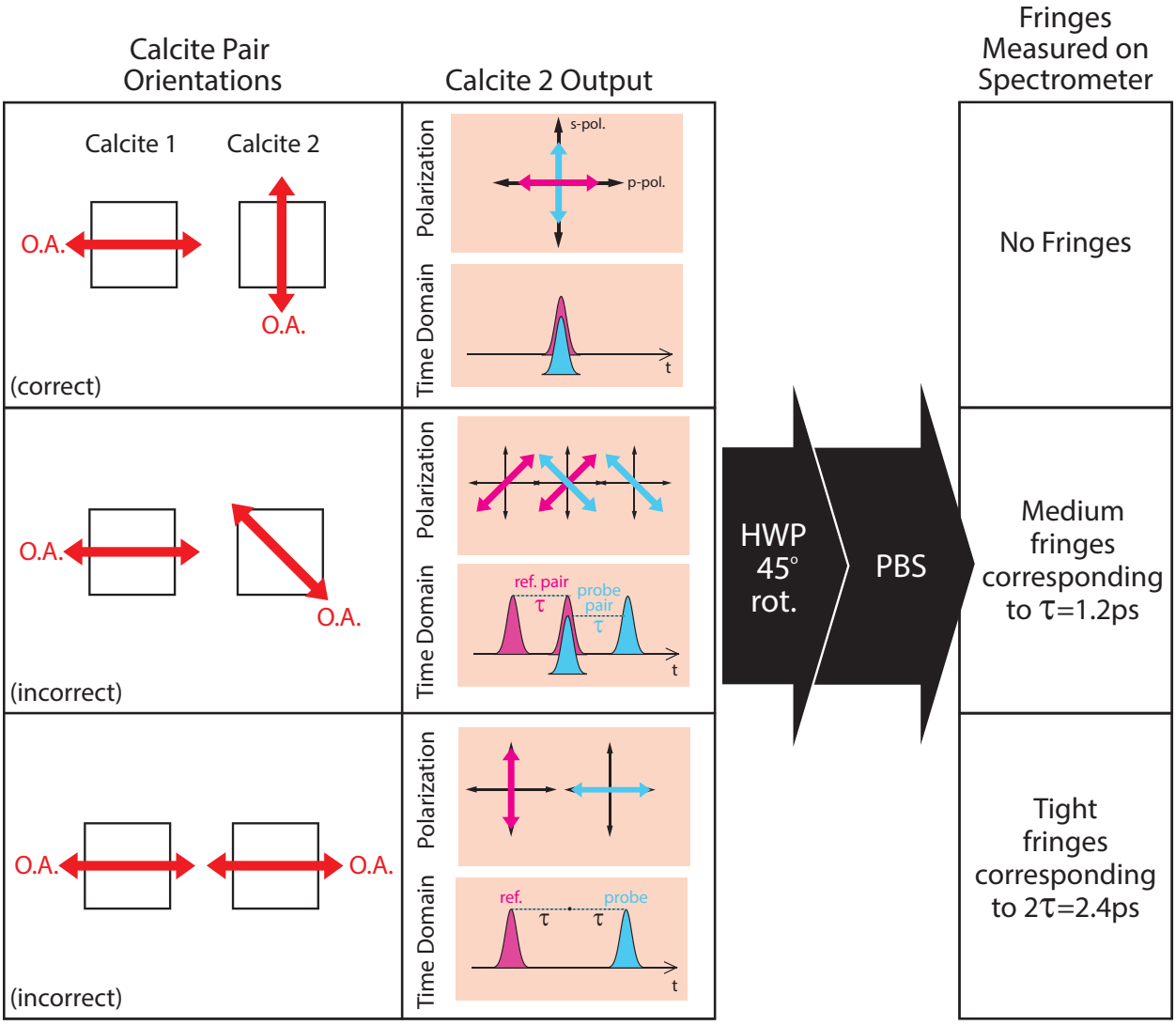

Figure 2.24: The effects of calcite 2 on the reference and probe pulses for different optic axis orientations. Row 1 shows the proper re-timing scenario where the optic axes of calcite 1 and calcite 2 are orthogonal. In this case no spectral fringes would be measured on a spectrometer. Row 2 shows the scenario with the optic axis of calcite 2 rotated 45 degrees to calcite 1; in this case each the reference and probe pulses are re-split. From the orientation of the HWP 3 though, the pair that proceeds to the spectrometer is only $\sim$1.2 ps apart. Finally, row 3 shows the scenario where the reference and probe pulses are further separated, resulting in spectral fringes $\propto$2.4 ps.

The ideal scenario occurs in the top row of Figure 2.24 where the O.A. of CAL 2 is perpendicular to that of CAL 1; in this case the reference and probe are properly re-timed. A confirmation of re-timing can be made by placing a spectrometer in place of one of the detectors in the scheme outlined in Figure 2.20. When the pulses are overlapped in time, no spectral fringes will be visible on the spectrometer; column 1 in Figure 2.25 shows an example of a measured spectrum corresponding to this scenario.

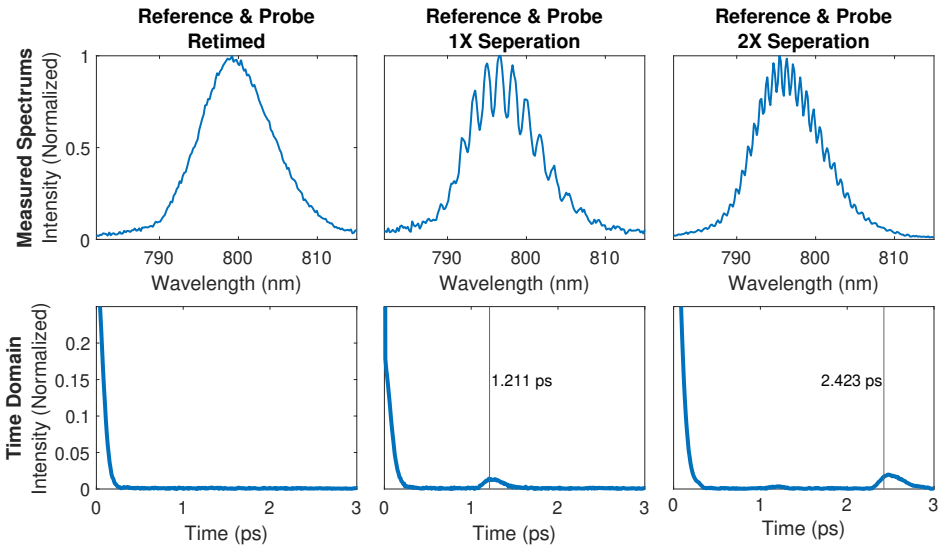

Figure 2.25: The interference spectrums measured for different rotation angles of the re-timing calcite. The bottom row depicts the Fourier transform of each spectrum where the positive sideband is shown. Peaks can be seen for the bottom center and bottom right image corresponding to $\tau_2 = 1.2$ ps and $2\tau_2$.

Two other undesirable scenarios can occur. One is shown in the second row of Figure 2.24 where the axes of the second calcite are rotated 45 degrees from the axes of the first crystal. The result is that both the advanced reference pulse and the delayed probe pulse are re-projected onto the slow and fast axes of the second calcite crystal splitting into two more pulses and ultimately creating four probe pulses. After HWP 3 rotates these pulses 45 degrees, the reference pulse pair is sent to one detector and the probe pulse pair to the other detector. Thus at the spectrometer spectral fringes corresponding to a 1.2 ps separation are measured; column 2 in Figure 2.25 shows an example of a measured spectrum corresponding to this scenario.

The final scenario that can occur is when axes of the second calcite align with the axes of the first calcite, further delaying the probe pulse and advancing the reference pulse. This results in two pulses which are separated by $2\tau_2$ manifesting as spectral fringes on the spectrometer that are twice the frequency as seen in the most recent scenario; column 3 in Figure 2.25 shows an example of a measured spectrum corresponding to this scenario.

2.4.3 Controlling the Measurement of $\mathrm{Re}\{\Delta\mathcal{N}\}$ vs $\mathrm{Im}\{\Delta\mathcal{N}\}$

One advantage of this detection configuration is the ability to switch between measuring transient absorption ($\mathrm{Im}\{\Delta\mathcal{N}\}$) and transient phase ($\mathrm{Re}\{\Delta\mathcal{N}\}$) simply by changing the projection of the probe and reference pulses on the PBS axes. This projection angle is controlled by HWP 3; Figure 2.26 shows three projection scenarios of the reference-probe pair polarization axes onto the PBS. If HWP 3 is oriented such that the reference-probe pair polarization axes are 45 degrees to the s- and p- axes of the PBS (left image), then there is an equal amplitude projection of both pulses to the two detectors. This setting is for making purely a *phase* measurement since any changes to the amplitudes of either pulse will cancel in the balanced detection scheme; only changes to the temporal interference on either detector caused by changes in $\mathrm{Re}\{\Delta\mathcal{N}\}$ will result in $V_A - V_B \neq 0$.

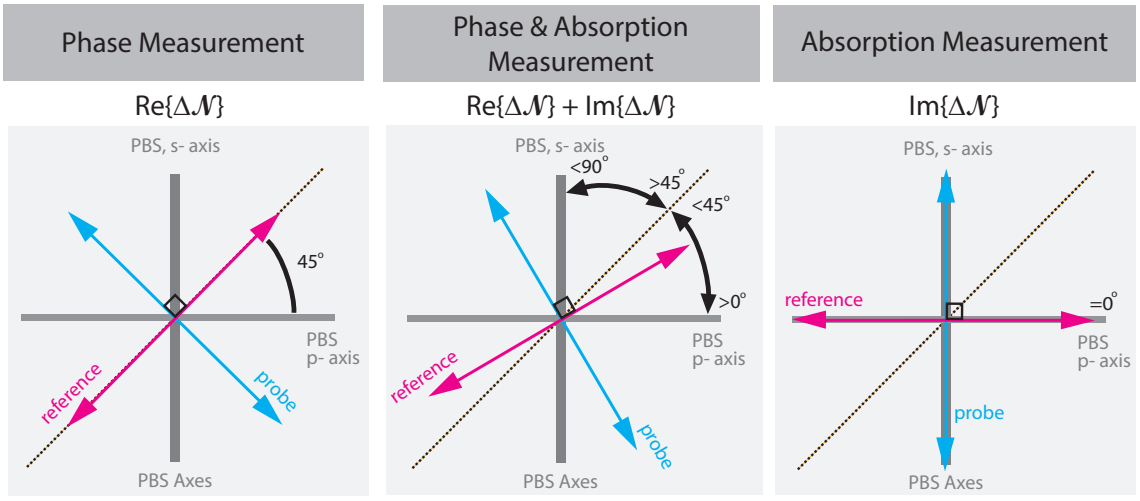

Figure 2.26: Polarization angle with respect to PBS axes determines if the measurement will be a phase measurement, an absorption measurement, or a combination of the two.

If HWP 3 is oriented such that the reference-probe pair polarization axes are aligned to the s- and p- axes of the PBS (right image), then DET A will measure amplitude changes to the reference pulse and DET B wil measure amplitude changes to the probe pulse. This setting is for making purely an *absorption* measurement since any changes to the phase of either pulse will have no bearing on the integrated intensity measured by the detector; only changes to the amplitude of either pulse caused by changes in $\mathrm{Im}\{\Delta\mathcal{N}\}$ will result in $V_A - V_B \neq 0$.

Finally, if HWP 3 is oriented for any other projection (middle image), then a combination of a phase and absorption measurement will be made.

2.5 Sources of Signal Degradation

Signal degradation can occur with either a decrease in signal or an increase in noise, both resulting in a smaller signal-to-noise ratio (SNR). In this setup, the dichroic mirror was found to spoil the maximum signal levels by decreasing the fringe contrast of the interferometric signals integrated by the detectors. One way by which this occurred was due to the creation of polarization-dependent spectral phase on the reference and probe (which were orthogonally polarized at the dichroic mirror interface). This is discussed below. Measurements of the noise floor found that the system is limited by the electronic noise floor of the preamplifier, approximately 40 dB above the shot noise floor.

2.5.1 Dichroic Mirror Polarization-dependent Spectral Phase

The existence of polarization-dependent spectral phase was confirmed after measuring the interference spectrum of the reference-probe pulses with and without the pump-combining dichroic mirror. Figure 2.27 shows the experimental setup that was used to test this.

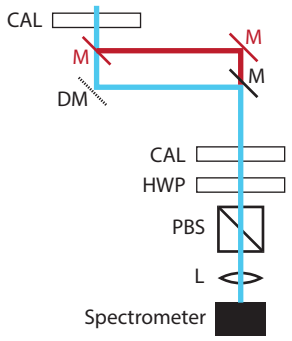

Figure 2.27: Setup used to measure the existence of spectral phase effects due to the dichroic beam combiner. The maroon path shows the setup for measurements bypassing the dichroic and the turquoise path shows the setup for measurements with the dichroic. (CAL: calcite, M: mirror, DM: dichroic mirror, HWP: half-wave plate, PBS: polarizing beam splitter, L:lens)

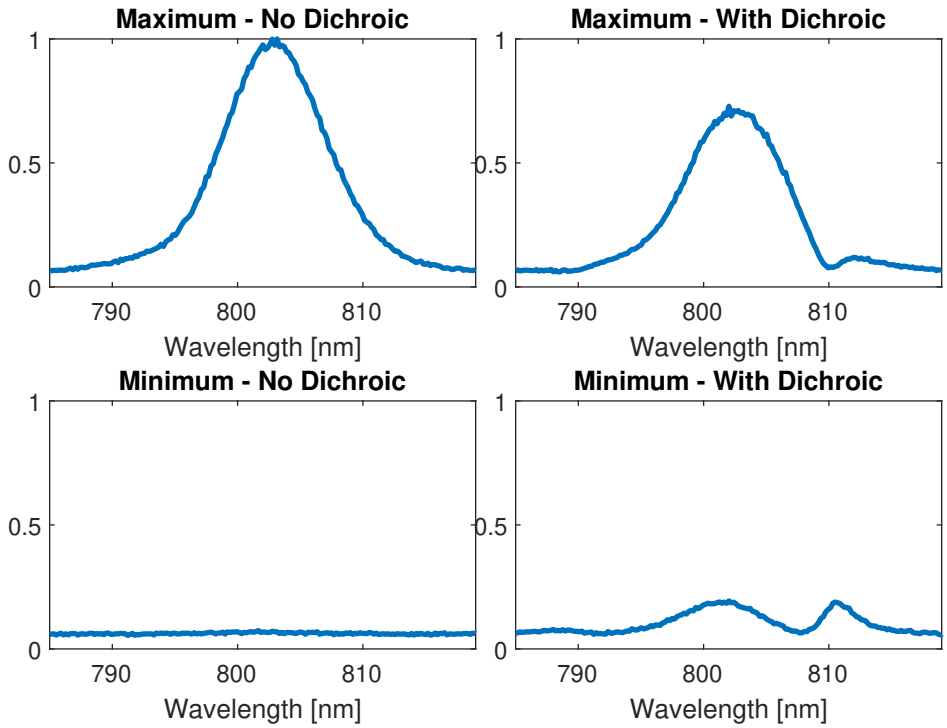

Figure 2.28: An overall comparison of the maximum constructive and destructive interference measured by tuning the phase relationship of the reference and probe pulse with and without the dichroic beam-combiner in the beam path.

With CAL 2 set for re-timing of the probe and reference, spectra were measured for the different offset phases Φ_0 imparted by changing α_{ext} of CAL 1 corresponding to maximum and minimum

interference. When the dichroic is bypassed the spectrogram is able to show fully constructive and fully destructive interactions as seen in the left column of Figure 2.28. However, the maximally constructive and destructive measurements with the dichroic show that only some wavelengths are constructive while others are destructive (and vice versa). The overall decrease in swing (integrated maximum constructive interference spectrum minus integrated minimum constructive interference spectrum) is close to 2X with the dichroic versus without the dichroic. One benefit of leaving the dichroic in its current position is the ability to freely change the pump polarization, however, this is at the expense of a decreased TΦM signal.

2.5.2 Noise Floor

Figure 2.29 shows the spectral noise measurements made for the detection system. The top left image shows the measured electronic noise floor at four different configurations: from the MOKU with no inputs attached, with the pre-amplifier connected but turned off, with the pre-amplifier connected and turned on (no input connections), and finally with the detectors turned off but connected to the pre-amplifier. The top right image shows the noise floor with the detectors blocked but turned on (i.e. measuring the dark current of the photodetectors). The bottom left image shows the noise floor with one detector blocked and 0.22 mW of laser power on the other detector. This demonstrates the noise floor in the absence of balanced detection where RIN can be seen. Adding in the balanced detection configuration with 0.28 mW of laser power on the other detector returns the noise floor back to the electronic noise floor of the pre-amplifier. Thus we are not yet at the shot noise limit (this still lies beneath the electronic noise floor by $\sim$40 dB) but rather by the electronic noise floor of the pre-amplifier. The addition of balanced detection affords a RIN reduction of ~ 6 dB at a pre-amplifier gain of 1.

In order to calculate the expected shot noise we can use the equation

$$I_{\mathrm{shot}} = \sqrt{2qI_{\mathrm{dc}}} \tag{2.25}$$

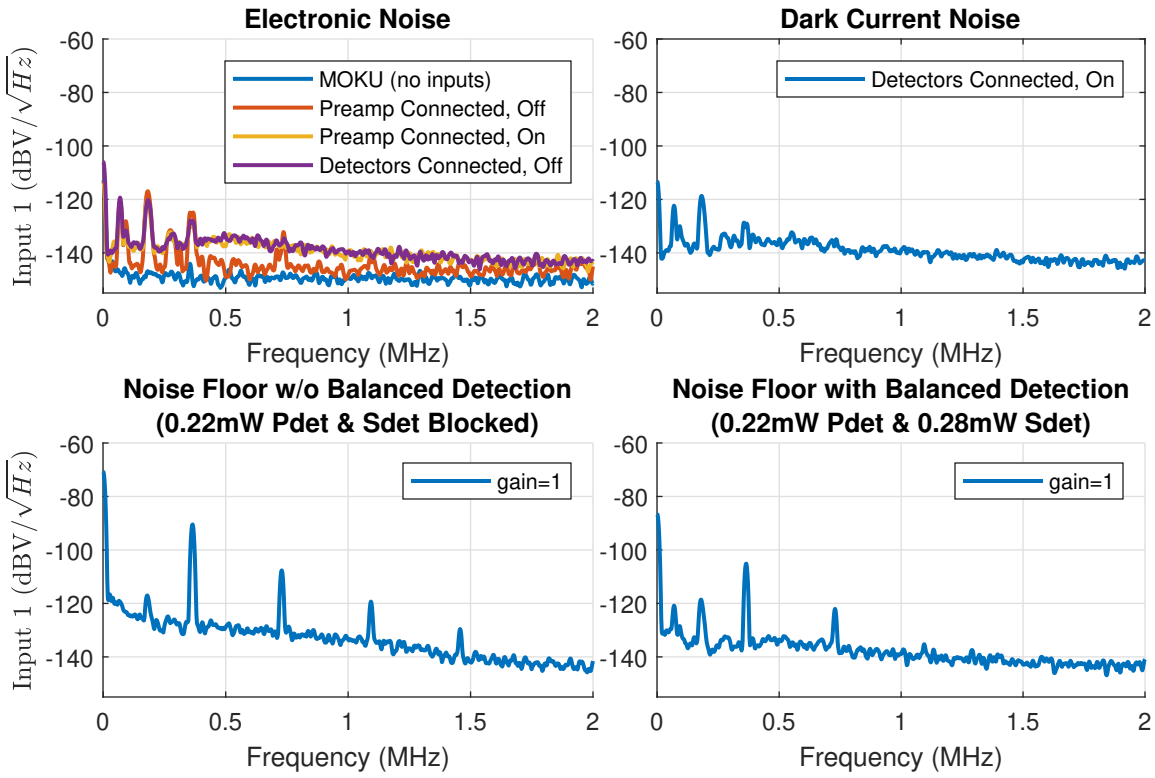

Figure 2.29: Spectral noise measurements

where I_{shot} is the shot noise current [A], q is the charge of an electron [C], and $I_{\text{dc}} = P_{\text{in}}R$ is the current [A] generated by an input power P_{in} [W] at the detector responsivity R for the wavelength of light incident. The gain setting for the photodetectors used (Thorlabs PDA36A2) was set to 0 dB but with a specified gain G of $1.51 \times 10^3 \, \frac{V}{A}$. The shot noise [V] can then be calculated from

$$V_{\text{shot}} = GI_{\text{shot}} \tag{2.26}$$

and converted to units of dBV with $\text{dBV}_{\text{shot}} = 20\log_{10}(\text{V}_{\text{shot}})$. For a power of 0.22 mW, the expected shot noise is -160.9 [dBV]. However, we utilize 20 dB attenuators inline on both detectors leading into the pre-amplifier to avoid saturation. The 20 dB attenuator results in a $V_{\text{shot,attn}} = 0.1V_{\text{shot}}$ such that the actual expected shot noise for our setup is -180.9 [dBV]; well below the electronic noise floor measured.

For future improvements to the SNR of this system, the first calcite crystal could be moved to after the dichroic mirror as is done in [4, 5]. This would avoid the effects of polarization-

dependent spectral phase but would require the pump polarization to lie either along the ordinary or extraordinary axes of the calcite crystal. However, doing so should increase the signal levels for phase measurements by close to 2X. Alternatively, the beam-joining dichroic could be replaced by a 50:50 beam splitter; while this would cut the power in half it would also eliminate the polarization-dependent spectral phase effects and retain the freedom of selecting the pump polarization. Another option that would increase the signal level would be to remove the 20 dB attenuators. The use of 20 dB attenuators was required to prevent saturation in the preamp (which has a 1 VDC input range); if a future preamplifier had a larger DC input range, then a 20 dB improvement could be added to the signal levels by removing the attenuators but without changing the noise floor (since the shot noise would then be close to -160 dB which is still 20 dB below the preamp electronic noise floor). Past that, improvements to decrease the noise floor down to the shot noise limit would increase the SNR.

2.6 Polarization Modeling

In order to calibrate the phase measurements the first calcite AOI (α_{ext}) was rotated to impart various phases $\Phi_{\mathrm{CAL1}}(\theta')$ to the reference-probe pulse pair while $V_{\mathrm{A}} - V_{\mathrm{B}}$ was measured from the preamplifier. By creating a model that connects α_{ext} to $\Phi_{\mathrm{CAL1}}(\theta')$ to accompany the voltage measurements, an overall calibration map can be created that ties a change in phase (here that is $\Phi_{\mathrm{CAL1}}(\theta')$ but in real TPM measurements the phase change would be due to $\Delta\Phi_{\mathrm{tpm}}$) to $V_{\mathrm{A}} - V_{\mathrm{B}}$. Figure 2.30 shows a measurement made for α_{ext} from -1.2 to 6 degrees passing through normal incidence at zero degrees.

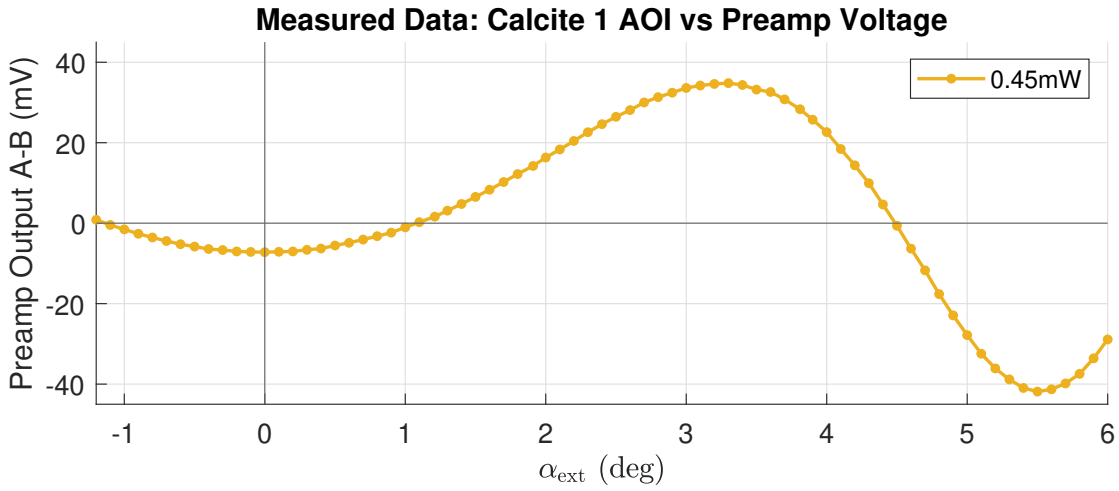

Figure 2.30: Measured preamp output for a range of α_{ext} passing through normal incidence (0 deg). The power measured on detector A with calcite 2 removed was 0.45 mW; the power levels are required for backing out a power-dependent calibration map shown on page 84.

The next section describes in detail various model components and then compares a complete model to the measured data. Mismatch between the model and measured data is addressed through the addition of diattenuation and polarization aberration terms to the model which indicate that our setup is operating at 55% of its achievable signal level (without amplitude or polarization defects).

2.6.1 Model Components

There are several components that need to be accounted for in this model: the phase imparted by CAL 1, the phase imparted by CAL 2, and the angle of HWP 3 which controls the amplitude projection from the polarizing beam splitter onto detectors A and B.

Calcite Model

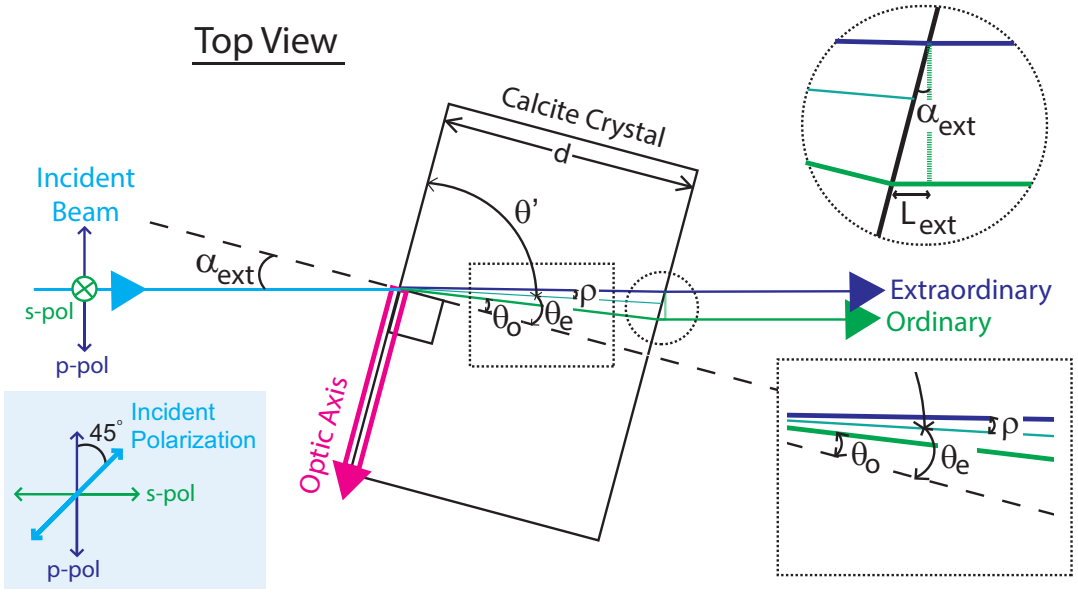

Figure 2.31: Diagram of the first calcite crystal (based on the diagram in [26] and adapted for our setup). α_{ext} is the external angle of incidence, θ_0 is the internal refraction angle for the ordinary ray, θ_e is the internal refraction angle for the extraordinary ray, ρ is the walk-off angle and $\theta' = 90 - \theta_e$.

Figure 2.31 shows a diagram of the calcite crystals used in this setup. The optic axis is cut along the front face of the crystal (a-cut) and creates an angle dependent extraordinary axis index of refraction $n_e(\theta')$. The calcite is $d = 2$ mm thick. Snell's law determines the relationship between incident and transmitted angles at an interface with $n_i \sin\theta_{\text{i}} = \text{n}_{\text{t}} \sin\theta_{\text{t}}$ [6]. This relationship holds simply for the ordinary ray of light which sees the ordinary refractive index. Since the extraordinary axis is angle dependent an extra step is needed to determine the refractive index value as a function of the internal refracted angle θ_e measured relative to the optic axis by θ'. Figure 2.32 shows the extraordinary index of refraction n_e as a function of external angle of incidence α_{ext}. The range of refractive index values for the extraordinary axis is from 1.4819 to 1.5454.

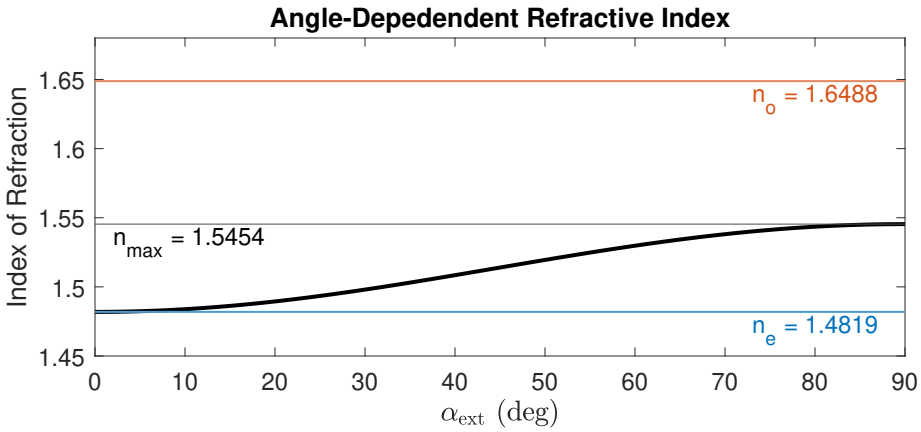

Figure 2.32: Angle-dependent index of refraction.

The propagation vector of the incident light is normal to the crystal face when $\alpha_{\text{ext}} = 0$ and polarized at 45 degrees; the 45 degree polarization splits at the air-crystal interface into a polarization component parallel to the optic axis (p-polarized) which sees an extraordinary index of refraction and a polarization component perpendicular to the optic axis (s-polarized) which sees the ordinary index of refraction. Calcite is a negative uniaxial crystal where $n_e - n_o < 0$ and $n_e < n_o$. This means that the polarization component with the lower refractive index (p-polarized) will travel faster through the calcite than the component with the higher refractive index (s-polarized). This results in an advanced **reference** pulse that is p-polarized and a delayed **probe** pulse that is s-polarized.

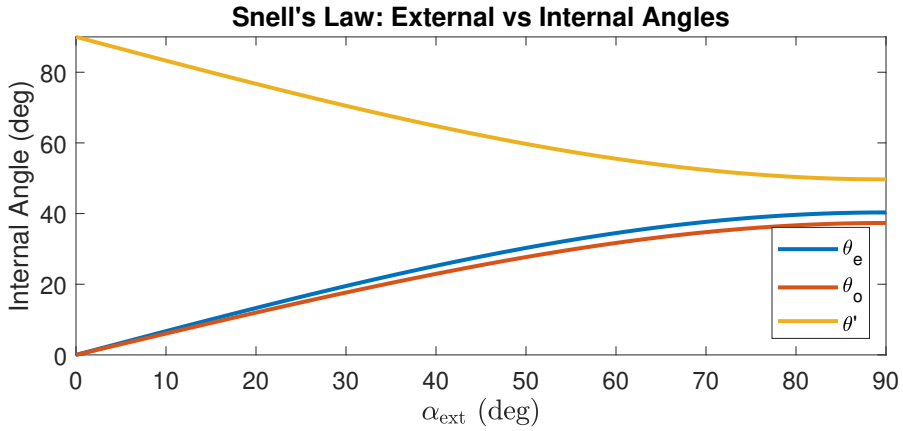

Figure 2.33: A simulation of the internal refracted angles as a function of external angle of incidence α_{ext}

Figure 2.33 shows the internal refracted angles for the ordinary (θ_o) and extraordinary (θ_e) axes as a function of external angle of incidence. Theoretically, as the propagation vector rotates from perpendicular to the optic axis (θ' = 90) to parallel to the optic axis (θ' = 0), the extraordinary index of refraction should collapse back to the value of the ordinary index of refraction [27][6]. However, in our configuration since the optic axis is cut along the front face of the crystal (and we cannot set the propagation vector to lie along this axis), the maximum refracted angle θ_e that can be achieved is 40.3 degrees and the corresponding minimum angle θ' is 49.7 degrees.

Temporal Pulse Separation The pulse separation imparted between the probe and reference pulses is a function of the external angle-of-incidence since the extraordinary refractive index is a function of angle. Figure 2.34 shows the calculated pulse separation as a function of α_{ext} where the maximum pulse separation occurs at normal incidence with $\tau_2 = 1.21$ ps.

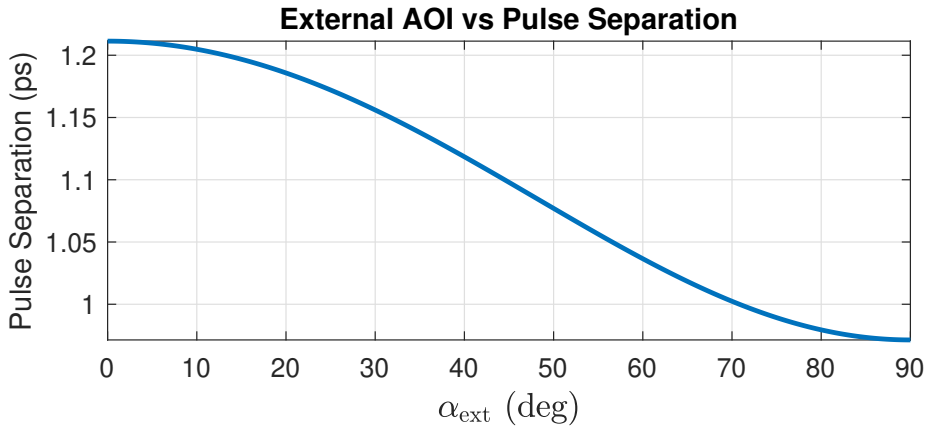

Figure 2.34: The simulated maximum pulse separation between the ordinary and extraordinary pulses is 1.21 picoseconds

At a wavelength of 800 nm the group refractive indices for calcite are $n_{g,o} = 1.6737$ and $n_{g,e} = 1.4920$; from [26] the equation to calculate total pulse delay is

$$T = \frac{1}{c}\left[L_o n_g^o + L_{\text{ext}} - L_e n_g^e(\theta')\right] \tag{2.27}$$

where c is the speed of light in a vacuum. $L_o + L_{\text{ext}}$ is the pathlength of the ordinary ray and L_e is the pathlength of the extraordinary ray. We can utilize Snell's law to find the pathlength of the ordinary ray in the calcite with

$$L_o = \frac{d}{\cos(\theta_o)} = \frac{n_o d}{\sqrt{n_o^2 - \sin^2(\alpha_{\text{ext}})}} \tag{2.28}$$

To determine the pathlengths L_{ext} and L_e, we first must find θ_e and $n_g^e(\theta')$ of the extraordinary ray. Using Snell's law again and accounting for the a-cut of the crystal we can solve for θ_e by substituting Equation 2.30 into Equation 2.29,

$$n_g^e(\theta') \sin\theta_e = \sin\alpha_{\text{ext}} \tag{2.29}$$

where $\theta' = \frac{\pi}{2} - \theta_e$. The angle dependent refractive index [26][27][6] is found with

$$n_g^e(\theta') = \frac{n_{g,o} n_{g,e}}{\sqrt{n_{g,e}^2 \cos^2(\theta') + n_{o,e}^2 \sin^2(\theta')}} \tag{2.30}$$

where the substitution of $\cos(\frac{\pi}{2} - \theta_e) = \sin(\theta_e)$ and $\sin(\frac{\pi}{2} - \theta_e) = \cos(\theta_e)$ can be utilized. Note, θ' in the equation above is specifically measured from the $\hat{z}$ principal axis of the calcite crystal [28]; by convention however for uniaxial crystals $n_x = n_y = n_o$ and $n_z = n_e \neq n_o$ [27], meaning the principal $\hat{z}$ axis aligns with the optic axis. After some rearranging this results in the expression

$$\theta_e = \tan^{-1}\left(\frac{n_{g,o}}{\sqrt{(\frac{n_{g,o} n_{g,e}}{\sin\alpha_{ext}})^2 - n_{g,e}^2}}\right) \tag{2.31}$$

Neglecting Poynting walkoff, we can finally find the extraordinary ray pathlength with

$$L_e = \frac{d}{\cos\theta_e} \tag{2.32}$$

and the external ordinary pathlength

$$L_{ext} = [\tan(\theta_e) - \tan(\theta_o)]\, d \sin(\alpha_{\text{ext}}) \tag{2.33}$$

Phase Difference between Pulses In order to find the phase difference between the ordinary and extraordinary rays imparted by the first calcite we can use the same equations except with strictly the phase refractive indices n_o and n_e instead of the group refractive indices. This means that the equation for the angle of refraction of the extraordinary ray becomes

$$\theta_e = \tan^{-1}\left(\frac{n_o}{\sqrt{(\frac{n_o n_e}{\sin\alpha_{ext}})^2 - n_e^2}}\right) \tag{2.34}$$

the extraordinary refractive index becomes

$$n_e(\theta') = \frac{n_o n_e}{\sqrt{n_e^2\cos^2(\theta') + n_o^2\sin^2(\theta')}} \tag{2.35}$$

The phase on the reference pulse from the first calcite is

$$\Phi_{\text{ref},1}(\theta') = (\frac{L_e n_e(\theta')}{c})\omega \tag{2.36}$$

and the phase on the probe pulse from the first calcite is

$$\Phi_{\text{pr},1} = (\frac{L_o n_o + L_{ext}}{c})\omega \tag{2.37}$$

where L_{ext} is recalculated using the new θ_e.

At the second (retiming) calcite the phase on the reference pulse from the ordinary axis is

$$\Phi_{\text{ref},2} = (\frac{L_o n_o}{c})\omega \tag{2.38}$$

and the phase on the probe pulse from the extraordinary axis at normal incidence is

$$\Phi_{\mathrm{pr},2} = (\frac{L_e n_e}{c})\omega \tag{2.39}$$

As a reminder, the CAL 1 and CAL 2 axes are orthogonal so that the reference pulse sees the extraordinary axis for CAL 1 and the ordinary axis for CAL 2. Likewise, the probe pulse sees the ordinary axis for CAL 1 and the extraordinary axis at normal incidence for CAL 2. Thus, the total phase imparted to the reference pulse from calcite 1 and 2 is

$$\Phi_{\mathrm{ref}} = \Phi_{\mathrm{ref},1}(\theta') + \Phi_{\mathrm{ref},2} = (\frac{L_e n_e(\theta')}{c})\omega + (\frac{L_o n_o}{c})\omega \tag{2.40}$$

and the phase on the probe pulse is

$$\Phi_{\mathrm{pr}} = \Phi_{\mathrm{pr},1} + \Phi_{\mathrm{pr},2} = (\frac{L_o n_o + L_{ext}}{c})\omega + (\frac{L_e n_e}{c})\omega \tag{2.41}$$

Figure 2.35 shows the phase difference imparted to the probe and reference pulses just from rotating the angle-of-incidence on the first calcite.

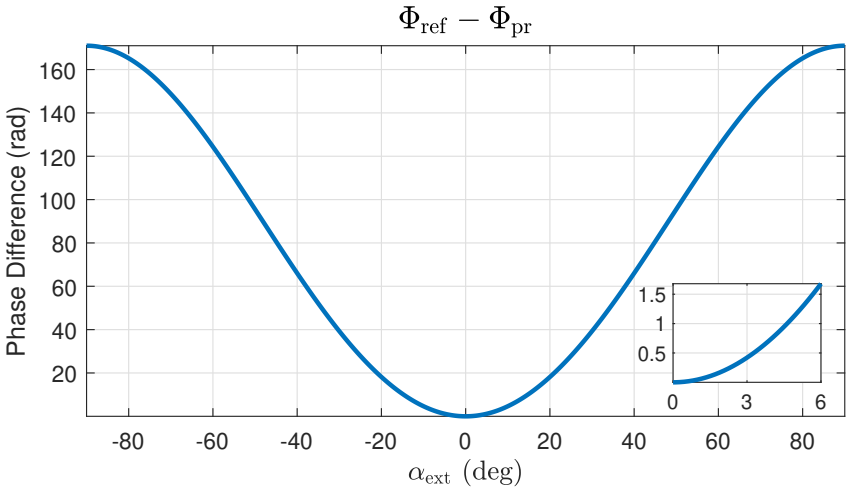

Figure 2.35: Total phase imparted after the second calcite crystal. The external incidence angle refers to the incidence angle on the first calcite only; the second calcite is oriented at normal incidence.

HWP 3 Model

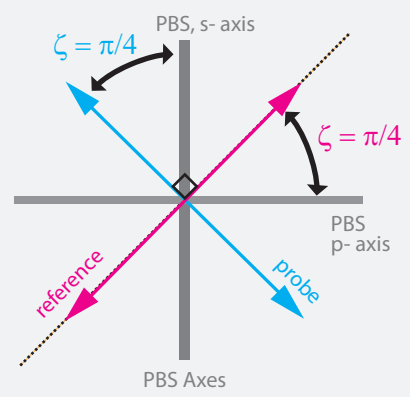

Figure 2.36: For the reference pulse, the cosine term of ζ proceeds to detector A and the sine term to detector B. For the probe pulse, the sine term of ζ proceeds to detector A and the cosine term to detector B.

HWP 3 is used to rotate the polarization axes of the reference and probe pulses after they exit calcite 2. The polarization axes are set to 45 degrees relative to the PBS axes so that both the reference and probe pulses equally project onto the s- and p- axes. Detector A measures the waveforms that transmit on the p- axis and detector B measures the waveforms that reflect on the s- axis. Figure 2.36 shows a diagram relating the polarization axes of the reference and probe pulses to the axes of the PBS. When $\zeta = \frac{\pi}{4}$ the amplitude of each pulse is split equally to either detector. If ζ is any other value, the amplitude projection of the reference pulse to the two detectors will be related by

$$E^A_{\text{ref}} \propto \left(\frac{\cos(\zeta)}{\cos(\zeta) + \sin(\zeta)} \right) \tag{2.42}$$

$$E^B_{\text{ref}} \propto \left(\frac{\sin(\zeta)}{\cos(\zeta) + \sin(\zeta)} \right) \tag{2.43}$$

and the amplitude of the probe projection will be swapped (ie. the cosine term will correspond to s- polarization and the sine term to p- polarization)

$$E^A_{\text{pr}} \propto \left(\frac{\sin(\zeta)}{\cos(\zeta) + \sin(\zeta)} \right) \tag{2.44}$$

$$E_{\mathrm{pr}}^{B} \propto \left(\frac{\cos(\zeta)}{\cos(\zeta) + \sin(\zeta)} \right) \tag{2.45}$$

Where E_{ref}^{A} and E_{ref}^{B} are the electric fields incident on the A and B detectors from the reference pulse, respectively, and E_{pr}^{A} and E_{pr}^{B} are the electric fields incident on the A and B detectors from the probe pulse.

2.6.2 Modeling the Balanced Detection Signal

Figure 2.37 (row 2) shows a comparison of the modelled balanced detection signal versus measured data. There is a mismatch in the position of the valley around 5.5 degrees between the model and the measurement; the measured data extends lower than the model and has a minimum $\sim$0.2 degrees to the left. The working range of the system is from 3.2 to 5.6 degrees, so the model vs measurement mismatch at 0 degrees can be ignored. Figure 2.38 shows a closer comparison of the model vs. measurement for the working range. The balance point $V_A - V_B = 0$ occurs where the dashed line intercepts the data.

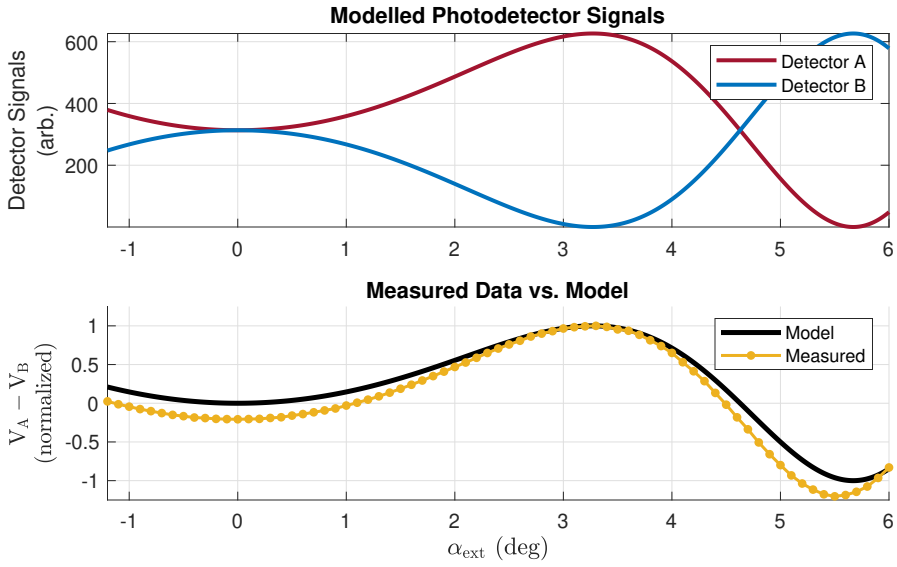

Figure 2.37: Modelled photodetector signals (row 1) and a comparison of the modelled signal $V_A - V_B$ to measured data (row 2) for 0.55 mW incident on detector A (power measured with the retiming calcite removed); $\Phi_0 = 3\pi/2$

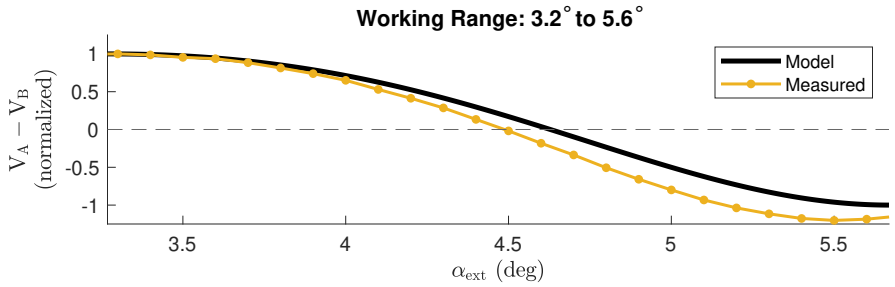

Figure 2.38: The working range for the system is from 3.2 to 5.6 degrees. The dashed line indicates the setting corresponding to a balanced point where $V_A - V_B = 0$. This is the balance point that all the TPM measurements start at; a phase advance in the probe will cause the signal to swing positive and a phase delay will cause the signal to swing negative. An overall phase shift of $-\frac{\pi}{2} : \frac{\pi}{2}$ can be measured from the balance point.

We can create a model for the balanced detection signal in the absence of the pump pulse by starting with the reference and probe waveforms estimated as Gaussian envelopes with a carrier frequency ω, then adding in phase terms picked up between the first and second calcites. The reference waveforms measured on DET A and DET B are

$$E_{\text{ref}}^{A} = Ae^{-(t^2/\sigma^2)}e^{i\omega t}e^{i\Phi_{\text{ref},1}(\theta')}e^{i\Phi_{\text{ref},2}}\left(\frac{\cos(\zeta)}{\cos(\zeta)+\sin(\zeta)}\right) \tag{2.46}$$

$$E_{\text{ref}}^{B} = Ae^{-(t^2/\sigma^2)}e^{i\omega t}e^{i\Phi_{\text{ref},1}(\theta')}e^{i\Phi_{\text{ref},2}}\left(\frac{\sin(\zeta)}{\cos(\zeta)+\sin(\zeta)}\right) \tag{2.47}$$

and the two probe waveforms measured are

$$E_{\text{pr}}^{A} = -A(e^{-((t-t_o)^2/\sigma^2)}e^{i\omega t}e^{i\Phi_{\text{pr},1}}e^{i\Phi_{\text{pr},2}}\left(\frac{\sin(\zeta)}{\cos(\zeta)+\sin(\zeta)}\right)e^{i\Phi_0} \tag{2.48}$$

$$E_{\text{pr}}^{B} = Ae^{-((t-t_o)^2/\sigma^2)}e^{i\omega t}e^{i\Phi_{\text{pr},1}}e^{i\Phi_{\text{pr},2}}\left(\frac{\cos(\zeta)}{\cos(\zeta)+\sin(\zeta)}\right)e^{i\Phi_0} \tag{2.49}$$

where Φ_0 is an offset phase is an picked up during travel through the microscope, A is an amplitude term, and ζ measures the angle between ref-probe polarization axes and the s- and p- polarization axes of the PBS; in the ideal scenario $\zeta = \frac{\pi}{4}$ for a phase measurement. Note the negative sign in

Eqn. 2.73; this accounts for the π phase shift between the probe and reference pulses incident on detector A.

The waveforms on detectors A and B are then

$$E^A = E^A_{ref} + E^A_{pr} \tag{2.50}$$

$$E^B = E^B_{ref} + E^B_{pr} \tag{2.51}$$

Since the detectors are slow compared with the optical carrier frequency and the pulse duration, the signal measured on each detector is the time-integrated intensity of the waveforms,

$$V_A \propto \int dt I^A = \int dt E^A E^{A*} \tag{2.52}$$

$$V_B \propto \int dt I^B = \int dt E^B E^{B*} \tag{2.53}$$

where V_A and V_B are the voltage signals measured on detector A and B, respectively. Finally, for balanced detection the ultimate signal we are measuring ΔV is

$$\Delta V = V_A - V_B \propto -A^2 \cos(\Phi_0 + \Phi_{\mathrm{pr},1} + \Phi_{\mathrm{pr},2} - \Phi_{\mathrm{ref},1}(\theta') - \Phi_{\mathrm{ref},2}) \tag{2.54}$$

where ΔV is dominated by a cosine that is a function of the phase terms. The phase offset Φ_0 shifts the relative location of the calibration model fringes and the associated DC offset at normal incidence as shown for a variety of phase values in Figure 2.39.

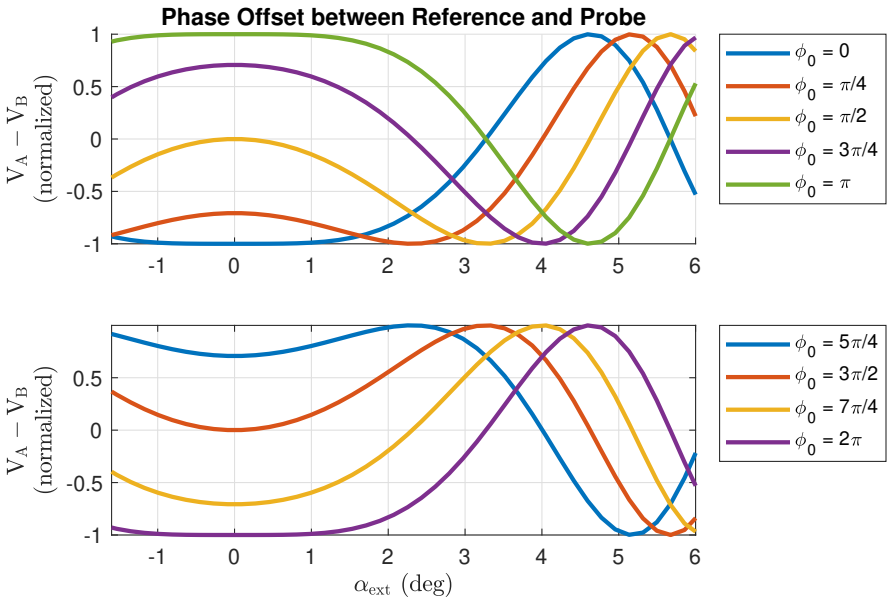

Figure 2.39: The impact of changing Φ_0 on the signal ΔV.

There are two effects that could be contributing to the model-measurement mismatch shown in Figures 2.37 and 2.38; diattenuation and polarization aberration. Diattenuation is related to the unequal absorption of a material based on the incident polarization state; the result of this would be an unequal amplitude of the reference and probe pulses $A_{\text{ref}} \neq A_{\text{pr}}$. Polarization aberrations can result in a change to initial polarization state of a pulse; in our setup likely the linear polarization states of the reference and probe pulses are picking up some ellipticity. If we add in terms for diattenuation and polarization aberration to the model it is able to match the measured data very well; however, this only occurs if **both** of these effects are present. If only diattenuation or only polarization aberration is present, the model does not match the measured data any better than the model without these terms.

Diattenuation

In order to account for diattenuation in the model we can add amplitude terms to the reference and probe pulses, A_{ref} and A_{pr} where $A_{\text{ref}} \neq A_{\text{pr}}$. The waveforms on the two detectors thus become

$$E_{\text{ref}}^{A} = A_{\text{ref}} e^{-(t^2/\sigma^2)} e^{i\omega t} e^{i\Phi_{\text{ref},1}(\theta')} e^{i\Phi_{\text{ref},2}} \left(\frac{\cos(\zeta)}{\cos(\zeta) + \sin(\zeta)} \right) \tag{2.55}$$

$$E_{\text{ref}}^{B} = A_{\text{ref}} e^{-(t^2/\sigma^2)} e^{i\omega t} e^{i\Phi_{\text{ref},1}(\theta')} e^{i\Phi_{\text{ref},2}} \left(\frac{\sin(\zeta)}{\cos(\zeta) + \sin(\zeta)} \right) \tag{2.56}$$

$$E_{\text{pr}}^{A} = -A_{\text{pr}} (e^{-((t-t_o)^2/\sigma^2)} e^{i\omega t} e^{i\Phi_{\text{pr},1}} e^{i\Phi_{\text{pr},2}} \left(\frac{\sin(\zeta)}{\cos(\zeta) + \sin(\zeta)} \right) e^{i\Phi_0} \tag{2.57}$$

$$E_{\text{pr}}^{B} = A_{\text{pr}} e^{-((t-t_o)^2/\sigma^2)} e^{i\omega t} e^{i\Phi_{\text{pr},1}} e^{i\Phi_{\text{pr},2}} \left(\frac{\cos(\zeta)}{\cos(\zeta) + \sin(\zeta)} \right) e^{i\Phi_0} \tag{2.58}$$

and the overall balanced detection signal reduces to

$$\Delta V = V_A - V_B \propto -A_{\text{pr}} A_{\text{ref}} \cos(\Phi_0 + \Phi_{\text{pr},1} + \Phi_{\text{pr},2} - \Phi_{\text{ref},1}(\theta') - \Phi_{\text{ref},2}) \tag{2.59}$$

If Equation 2.59 is compared to equation 2.54 for different values of A_{ref} versus A_{pr}, a comparative SNR can be calculated. Figure 2.40 shows the trade-offs in maximum signal level available for different ratios of amplitude inequality. Interestingly, diattenuation amounts to an SNR decrease that is linear with respect to the ratio of reference to probe pulse amplitude (or vice versa if $A_{\text{ref}} > A_{\text{pr}}$).

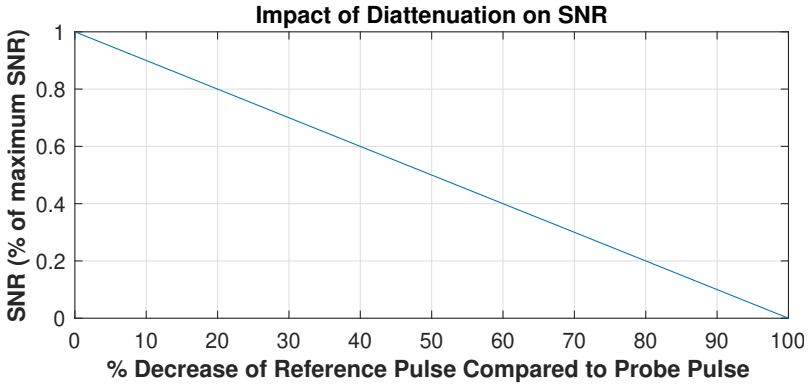

Figure 2.40: A comparative SNR analysis for diattenuation; here SNR is plotted as a percent of the maximum SNR when $A_{\text{ref}} = A_{\text{pr}}$. The X axis denotes the percent decrease of A_{ref} as compared to A_{pr} (i.e. $A_{\text{ref}} = 0.8A_{\text{pr}}$ is a 20% decrease)

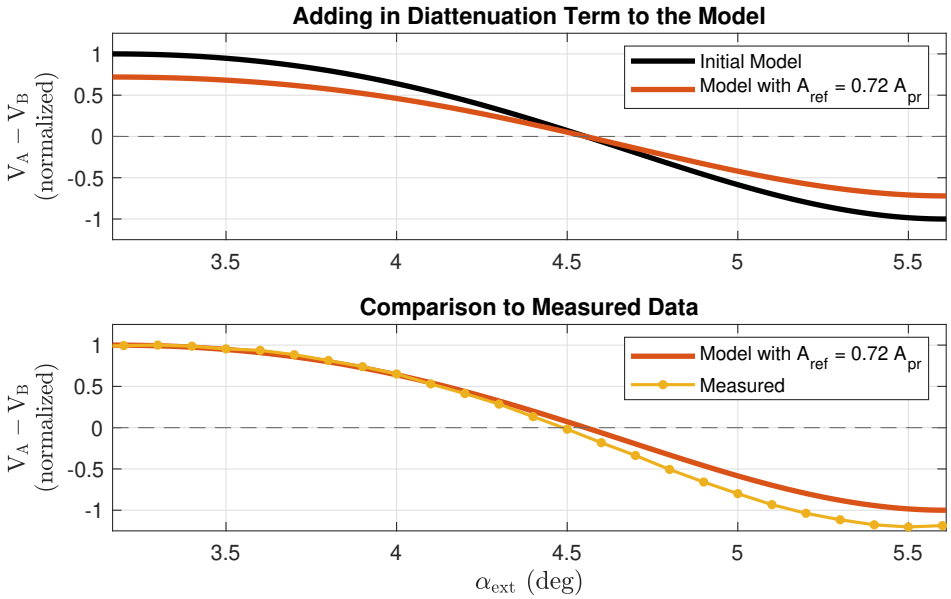

Figure 2.41: The top figure compares the diattenuation model with $A_{ref} = 0.72A_{pr}$ to the initial model (normalized to the initial model). The diattenuation model shows a symmetrically reduced swing. The bottom figure compares the diattenuation model with $A_{ref} = 0.72A_{pr}$ to the measured data (each normalized independently). The diattenuation model is unable to match the asymmetric signal swing present on the measured data.

Figure 2.41 (row 1) shows a comparison of the original model to a model with a diattenuation term of $A_{\text{ref}} = 0.72A_{\text{pr}}$ (normalized to the original model); The diattenaution model shows a symmetric reduction in the signal swing versus the original model. When compared to the measured data, the model is still unable to match the asymmetric signal swing that extends further negative than positive (row 2).

Polarization Aberration

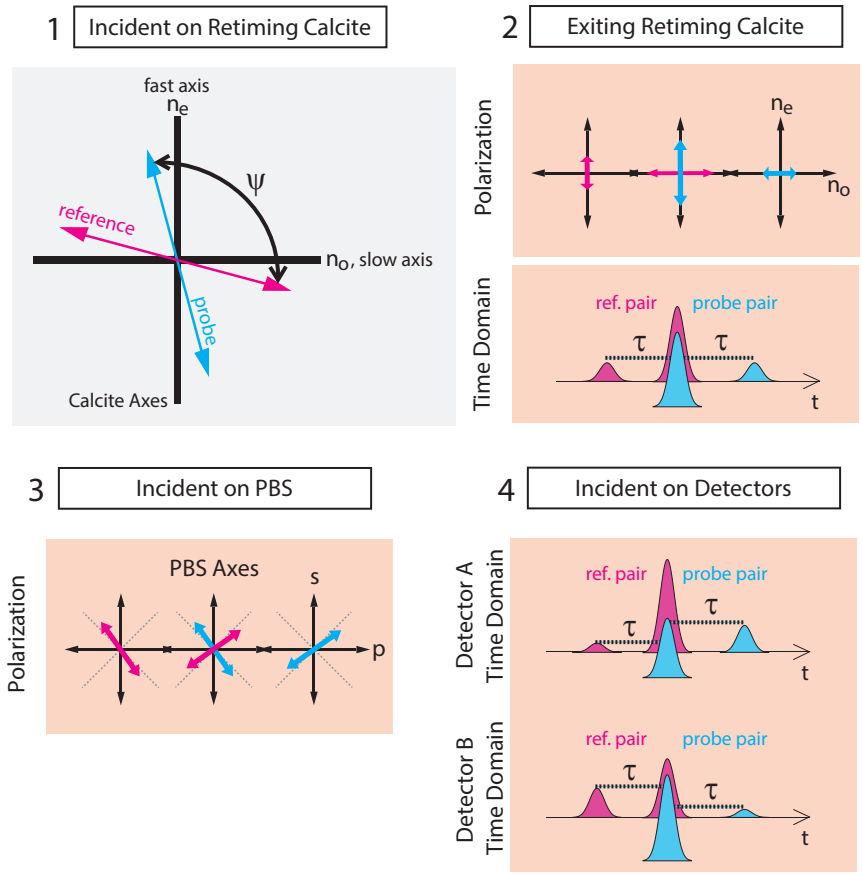

Figure 2.42: 1) The probe and reference pulses incident on the retiming calcite for $\Psi > 90°$. 2) The output of the retiming calcite is a pair of reference pulses orthogonally polarized (one advanced and one retimed) and a pair of probe pulses orthogonally polarized (one retimed and one delayed). 3) Since the angle of HWP 3 is set with the probe pulse blocked and the retiming calcite removed, the pulses are offset from 45 degrees on the PBS axes by $\frac{\Psi-90°}{2}$. 4) Four pulses proceed to detector A and four pulses to detector B. The DC offset created by the advanced and delayed pulses cancel out between the two detectors since the amplitudes $A_{\text{ref}} = A_{\text{pr}}$ so only the retimed pulses contribute to a signal.

If the reference and probe pulses pick up ellipticity as they travel through the microscope, then the way they interact with the retiming calcite will change and a decrease in SNR will occur. We can define an angle Ψ that is a proxy measurement of ellipticity of the probe and reference polarizations (shown in Figure 2.42), where $\Psi = 90° + \theta_{\text{ref}} + \theta_{\text{pr}}$.

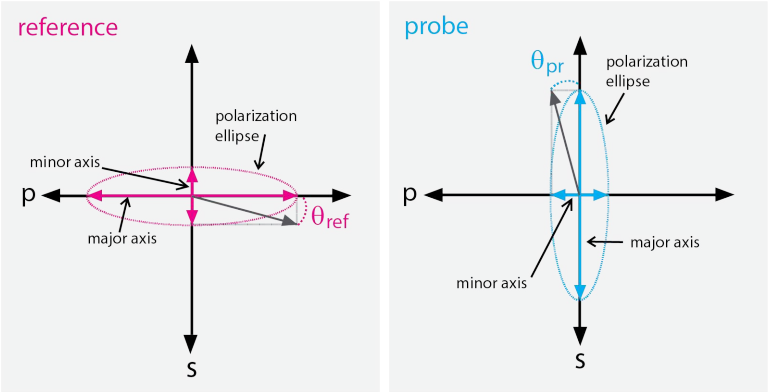

Figure 2.43: θ_{ref} (left) and θ_{pr} (right) are measures of ellipticity that result in polarization components on the orthogonal axes.

For normal conditions where the probe and reference are linearly polarized and orthogonal, $\Psi = 90°$. If the p-polarized reference pulse picks up ellipticity, then an orthogonal polarization component is present along the s-polarization axis. We can define an angle θ_{ref} that measures the amount of power projected onto the s-component versus the p-component of polarization for the ellipticity present (see Figure 2.43). Similarly, we can define a term θ_{pr} for the probe pulse. A formal measure of ellipticity is defined as $e = \frac{E_{\text{min}}}{E_{\text{max}}}$ where E_{min} is the the minor axis field and E_{max} is the major axis field [6]. e ranges from 0 to 1 where 0 corresponds to linear polarization and 1 corresponds to circular polarization. The angle θ_{ref} is related to the ellipticity factor by $\theta_{\text{ref}} = \tan^{-1}(e^2_{\text{ref}}) = \tan^{-1}(\frac{I_{\text{min}}}{I_{\text{max}}})$, where an elliptical or circular polarization state is measured when $\theta_{\text{ref}} > 0$.

When the retiming calcite angle θ_{CAL2} is set the assumption is that the 45 degree axis between n_e and n_o on the crystal face aligns with $\frac{\Psi}{2}$. Since $\Psi > 90°$ the reference pulse splits into an advanced and retimed pulse pair orthogonally polarized and the probe pulse splits into a retimed and delayed pulse pair orthogonally polarized. Figure 2.42 shows an example of the angle $\Psi \neq 90°$ and the resulting double pulse pair. HWP 3 is set so that the reference pulse aligns with the 45 degree axis of the PBS *when the retiming calcite is removed*; once the retiming calcite is replaced the angle $\zeta = \frac{\pi}{4} - \frac{\beta}{2}$ where $\beta = \Psi - 90°$ resulting in an uneven amplitude distribution on two

detectors for each pulse. The reference pulse that is *advanced* in time sends a larger amplitude copy to detector B than detector A and thus there is a DC offset on detector B after balanced detection from the reference. The *retimed* reference and probe pulses are also split in unequal amplitude to the two detectors where they both interfere. The *delayed* probe pulse, similarly to the advanced reference pulse, will create a DC offset on detector A. Since the amplitude of the two pulses is equal in this scenario ($A_{\mathrm{ref}} = A_{\mathrm{pr}} = A$), the retimed waveforms are

$$E^{A}_{\mathrm{ref,ret.}} = Ae^{-(t^2/\sigma^2)}e^{i\omega t}e^{i\Phi_{\mathrm{ref},1}(\theta')}\frac{\cos(\frac{\beta}{2})}{\cos(\frac{\beta}{2})+\sin(\frac{\beta}{2})}e^{i\Phi_{\mathrm{ref},2}}\left(\frac{\cos(\zeta)}{\cos(\zeta)+\sin(\zeta)}\right) \tag{2.60}$$

$$E^{B}_{\mathrm{ref,ret.}} = Ae^{-(t^2/\sigma^2)}e^{i\omega t}e^{i\Phi_{\mathrm{ref},1}(\theta')}\frac{\cos(\frac{\beta}{2})}{\cos(\frac{\beta}{2})+\sin(\frac{\beta}{2})}e^{i\Phi_{\mathrm{ref},2}}\left(\frac{\sin(\zeta)}{\cos(\zeta)+\sin(\zeta)}\right) \tag{2.61}$$

$$E^{A}_{\mathrm{pr,ret.}} = -A(e^{-((t-t_o)^2/\sigma^2)}e^{i\omega t}e^{i\Phi_{\mathrm{pr},1}}\frac{\cos(\frac{\beta}{2})}{\cos(\frac{\beta}{2})+\sin(\frac{\beta}{2})}e^{i\Phi_{\mathrm{pr},2}}\left(\frac{\sin(\zeta)}{\cos(\zeta)+\sin(\zeta)}\right)e^{i\Phi_0} \tag{2.62}$$

$$E^{B}_{\mathrm{pr,ret.}} = Ae^{-((t-t_o)^2/\sigma^2)}e^{i\omega t}e^{i\Phi_{\mathrm{pr},1}}\frac{\cos(\frac{\beta}{2})}{\cos(\frac{\beta}{2})+\sin(\frac{\beta}{2})}e^{i\Phi_{\mathrm{pr},2}}\left(\frac{\cos(\zeta)}{\cos(\zeta)+\sin(\zeta)}\right)e^{i\Phi_0} \tag{2.63}$$

On detector A the non-retimed waveforms are

$$E^{A}_{\mathrm{ref,adv.}} = e^{-((t-1.2\mathrm{ps})^2/\sigma^2)}e^{i\omega t}\frac{\sin(\frac{\beta}{2})}{\cos(\frac{\beta}{2})+\sin(\frac{\beta}{2})}\frac{\sin(\zeta)}{\cos(\zeta)+\sin(\zeta)} \tag{2.64}$$

$$E^{A}_{\mathrm{pr,dly}} = e^{-((t+1.2ps)^2/\sigma^2)}e^{i\omega t}\frac{\sin(\frac{\beta}{2})}{\cos(\frac{\beta}{2})+\sin(\frac{\beta}{2})}\frac{\cos(\zeta)}{\cos(\zeta)+\sin(\zeta)} \tag{2.65}$$

On detector B the non-retimed waveforms are

$$E^{B}_{\mathrm{ref,adv.}} = e^{-((t-1.2\mathrm{ps})^2/\sigma^2)}e^{i\omega t}\frac{\sin(\frac{\beta}{2})}{\cos(\frac{\beta}{2})+\sin(\frac{\beta}{2})}\frac{\cos(\zeta)}{\cos(\zeta)+\sin(\zeta)} \tag{2.66}$$

$$E^{B}_{\mathrm{pr,dly}} = e^{-((t+1.2\mathrm{ps})^2/\sigma^2)}e^{i\omega t}\frac{\sin(\frac{\beta}{2})}{\cos(\frac{\beta}{2})+\sin(\frac{\beta}{2})}\frac{\sin(\zeta)}{\cos(\zeta)+\sin(\zeta)} \tag{2.67}$$

Thus the total intensity measured on detectors A and B is

$$I^A = I^A_{\text{ref,adv.}} + (E^A_{\text{pr,ret.}} + E^A_{\text{ref,ret.}})(E^A_{\text{pr,ret.}} + E^A_{\text{ref,ret.}})^* + I^A_{\text{pr,dly}} \tag{2.68}$$

$$I^B = I^B_{\text{ref,adv.}} + (E^B_{\text{pr,ret.}} + E^B_{\text{ref,ret.}})(E^B_{\text{pr,ret.}} + E^B_{\text{ref,ret.}})^* + I^B_{\text{pr,dly}} \tag{2.69}$$

and the overall balanced detection signal reduces to

$$\Delta V = V_A - V_B \propto \frac{4A^2 \cos(\frac{\beta}{2})^2 \sin(\beta)}{\cos(2\beta) - 4\sin(\beta) - 3} \cos(\Phi_0 + \Phi_{\text{pr},1} + \Phi_{\text{pr},2} - \Phi_{\text{ref},1}(\theta') - \Phi_{\text{ref},2}) \tag{2.70}$$

Note that for the advanced reference pulse and the delayed probe pulse, the pulse phases do not need to be tracked since there will be no interference when those pulses hit either detector.

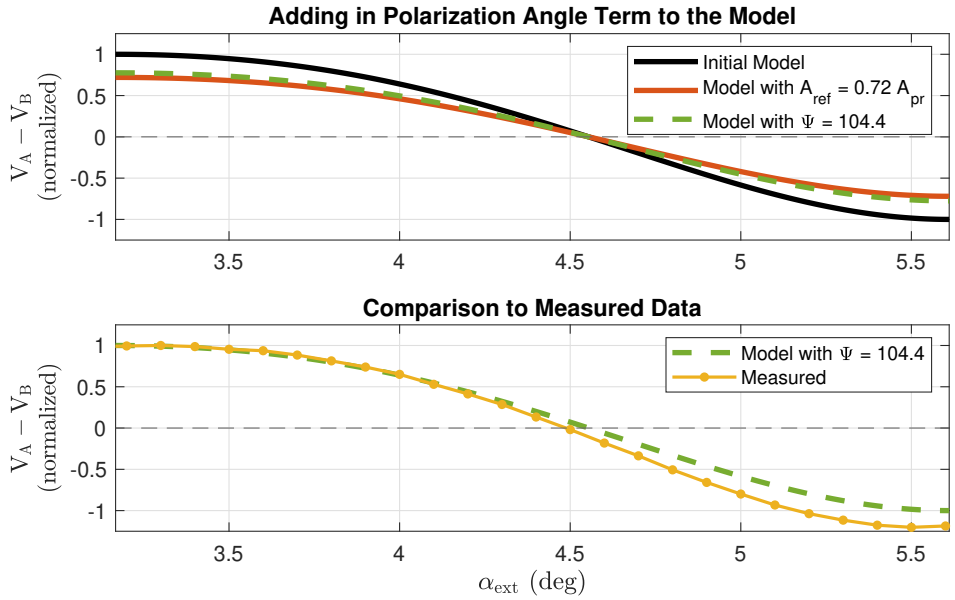

Figure 2.44: The top figure compares the polarization aberration model with the diattenuation model and the initial model (all normalized to the initial model). The polarization aberration shows a symmetrically reduced swing compared to the initial model. The bottom figure compares the polarization aberration model with $\Psi = 104.4°$ to the measured data (each normalized independently). The polarization aberration model is unable to match the assymmetric signal swing present on the measured data.

Figure 2.44 shows the addition of a model with a polarization aberration term compared to the initial model and the diattenuation model (row 1). Similar to the diattenuation model, the

polarization aberration model sees a symmetric decrease in the positive and negative signal levels. When compared to the measured data (row 2), again the updated model is not able to match the asymmetric signal swing present in the measurement.

An important observation of the advanced reference and delayed probe pulses is that as long as $A_{\text{ref}} = A_{\text{pr}} = A$ then Eqn. 2.64 cancels with Eqn. 2.67 and Eqn. 2.65 cancels with Eqn. 2.66 in the balanced detection scheme. Therefore, only the retimed pulses contribute to the measured signal and any elliptical polarization components due to $\Psi > 90°$ simply cause an SNR decrease. Figure 2.45 shows the comparative SNR decrease as a function of Ψ for the polarization aberration model compared to the initial model.

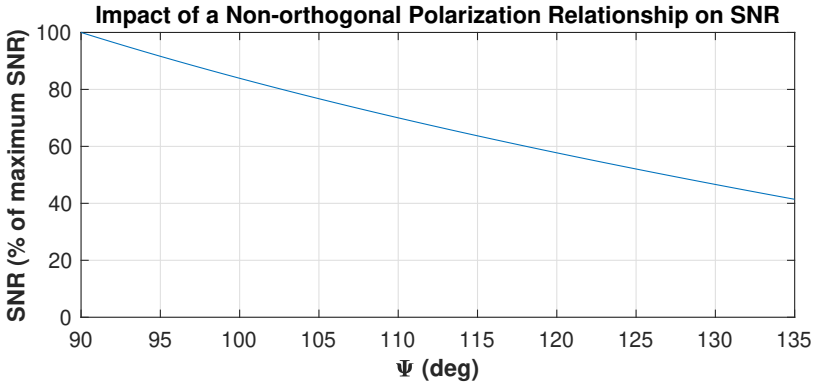

Figure 2.45: SNR decrease due to a change in the polarization relationship between the reference and probe pulse captured in angles of Ψ

Diattenuation & Polarization Aberration

In the event that both diattenuation and polarization aberration have occurred, the asymmetric swing in the measured data can be matched by the model. Figure 2.46 shows a comparison of this model with the measured data (row 2) for $A_{\text{ref}} = 0.72A_{\text{pr}}$ and $\Psi = 104.4°$. From the equations for the retimed, advanced and delayed pulses shown below we can see that with $A_{\text{ref}} \neq A_{\text{pr}}$ Equations 2.75 and 2.78 and Equations 2.76 and 2.77 no longer cancel which contribute to the unequal swing seen in the measured data. The retimed waveforms are

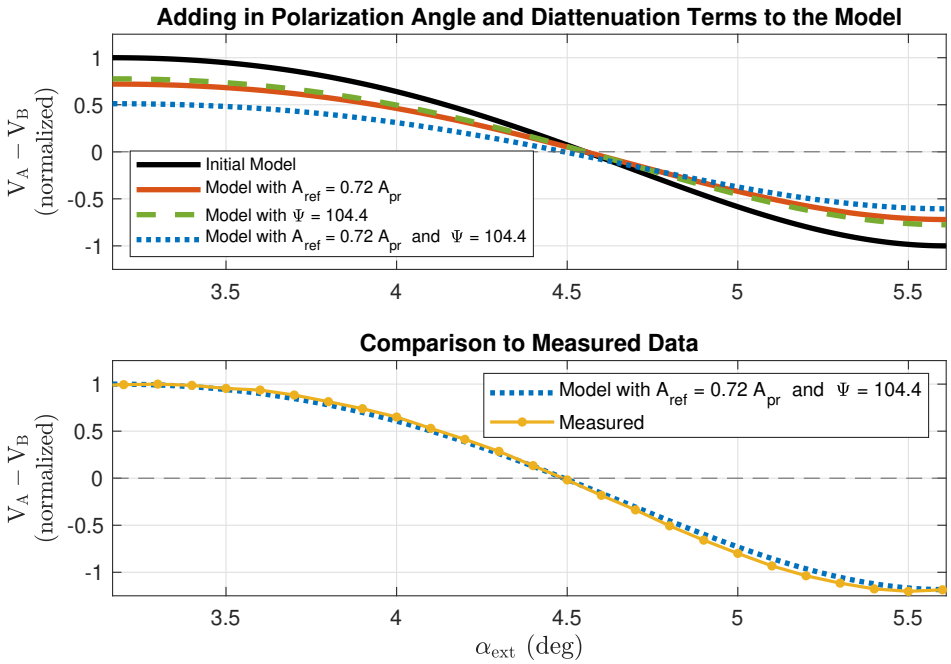

Figure 2.46: The top figure compares all four model modifications to the initial model: the diattenuation & polarization aberration model ($A_{\text{ref}} = 0.72A_{\text{pr}}$ and $\Psi = 104.4°$), the polarization aberration model ($A_{\text{ref}} = A_{\text{pr}}$ and $\Psi = 104.4°$), the diattenuation model ($A_{\text{ref}} = 0.72A_{\text{pr}}$ and $\Psi = 90°$) and the initial model ($A_{\text{ref}} = A_{\text{pr}}$ and $\Psi = 90°$). The diattenuation & polarization aberration model is able to match the asymmetric swing that is present in the measured data (bottom figure), while the other three models could not.

$$E^A_{\text{ref}} = A_{\text{ref}} e^{-(t^2/\sigma^2)} e^{i\omega t} e^{i\Phi_{\text{ref},1}(\theta')} \frac{\cos(\frac{\beta}{2})}{\cos(\frac{\beta}{2}) + \sin(\frac{\beta}{2})} e^{i\Phi_{\text{ref},2}} \left(\frac{\cos(\zeta)}{\cos(\zeta) + \sin(\zeta)} \right) \tag{2.71}$$

$$E^B_{\text{ref}} = A_{\text{ref}} e^{-(t^2/\sigma^2)} e^{i\omega t} e^{i\Phi_{\text{ref},1}(\theta')} \frac{\cos(\frac{\beta}{2})}{\cos(\frac{\beta}{2}) + \sin(\frac{\beta}{2})} e^{i\Phi_{\text{ref},2}} \left(\frac{\sin(\zeta)}{\cos(\zeta) + \sin(\zeta)} \right) \tag{2.72}$$

$$E^A_{\text{pr}} = -A_{\text{pr}} (e^{-((t-t_o)^2/\sigma^2)} e^{i\omega t} e^{i\Phi_{\text{pr},1}} \frac{\cos(\frac{\beta}{2})}{\cos(\frac{\beta}{2}) + \sin(\frac{\beta}{2})} e^{i\Phi_{\text{pr},2}} \left(\frac{\sin(\zeta)}{\cos(\zeta) + \sin(\zeta)} \right) e^{i\Phi_0} \tag{2.73}$$

$$E^B_{\text{pr}} = A_{\text{pr}} e^{-((t-t_o)^2/\sigma^2)} e^{i\omega t} e^{i\Phi_{\text{pr},1}} \frac{\cos(\frac{\beta}{2})}{\cos(\frac{\beta}{2}) + \sin(\frac{\beta}{2})} e^{i\Phi_{\text{pr},2}} \left(\frac{\cos(\zeta)}{\cos(\zeta) + \sin(\zeta)} \right) e^{i\Phi_0} \tag{2.74}$$

On detector A the non-retimed waveforms are

$$E^A_{\text{ref,adv.}} = A_{\text{ref}} e^{-((t-1.2\text{ps})^2/\sigma^2)} e^{i\omega t} \frac{\sin(\frac{\beta}{2})}{\cos(\frac{\beta}{2}) + \sin(\frac{\beta}{2})} \frac{\sin(\zeta)}{\cos(\zeta) + \sin(\zeta)} \tag{2.75}$$

$$E^A_{\text{pr,dly}} = A_{\text{pr}} e^{-((t+1.2ps)^2/\sigma^2)} e^{i\omega t} \frac{\sin(\frac{\beta}{2})}{\cos(\frac{\beta}{2}) + \sin(\frac{\beta}{2})} \frac{\cos(\zeta)}{\cos(\zeta) + \sin(\zeta)} \tag{2.76}$$

and on detector B the non-retimed waveforms are

$$E^B_{\text{ref,adv.}} = A_{\text{ref}} e^{-((t-1.2\text{ps})^2/\sigma^2)} e^{i\omega t} \frac{\sin(\frac{\beta}{2})}{\cos(\frac{\beta}{2}) + \sin(\frac{\beta}{2})} \frac{\cos(\zeta)}{\cos(\zeta) + \sin(\zeta)} \tag{2.77}$$

$$E^B_{\text{pr,dly}} = A_{\text{pr}} e^{-((t+1.2\text{ps})^2/\sigma^2)} e^{i\omega t} \frac{\sin(\frac{\beta}{2})}{\cos(\frac{\beta}{2}) + \sin(\frac{\beta}{2})} \frac{\sin(\zeta)}{\cos(\zeta) + \sin(\zeta)} \tag{2.78}$$

The total intensity measured on detectors A and B is

$$I^A = I^A_{\text{ref,adv.}} + (E^A_{\text{pr,ret.}} + E^A_{\text{ref,ret.}})(E^A_{\text{pr,ret.}} + E^A_{\text{ref,ret.}})^* + I^A_{\text{pr,dly}} \tag{2.79}$$

$$I^B = I^B_{\text{ref,adv.}} + (E^B_{\text{pr,ret.}} + E^B_{\text{ref,ret.}})(E^B_{\text{pr,ret.}} + E^B_{\text{ref,ret.}})^* + I^B_{\text{pr,dly}} \tag{2.80}$$

and the overall balanced detection signal reduces to

$$\Delta V = V_A - V_B \propto \frac{2\cos(\beta)^2(A_{\text{pr}}^2 - A_{\text{ref}}^2)}{\cos(2\beta) - 4\sin(\beta) - 3} + \frac{8A_{\text{pr}}A_{\text{ref}}\cos\left(\frac{\beta}{2}\right)^3 \sin\left(\frac{\beta}{2}\right)}{\cos(2\beta) - 4\sin(\beta) - 3}\cos(\Phi_0 + \Phi_{\text{pr},1} + \Phi_{\text{pr},2} - \Phi_{\text{ref},1}(\theta') - \Phi_{\text{ref},2}) \quad (2.81)$$

Figure 2.47 shows several curves comparing the SNR for various Ψ values at different amplitude relationships to the initial model. For the values of $A_{\text{ref}} = 0.72A_{\text{pr}}$ and $\Psi = 104.4°$, the SNR decrease compared to the original model is $\sim 55.84\%$ (Figure 2.48).

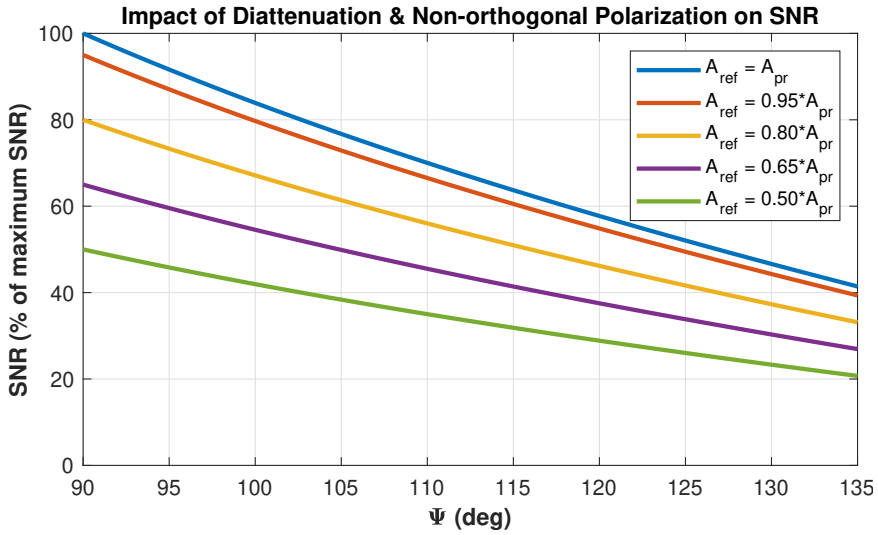

Figure 2.47: Evaluation of SNR with both diattenuation and a change in the polarization relationship between the reference and probe pulse captured in angles of Ψ

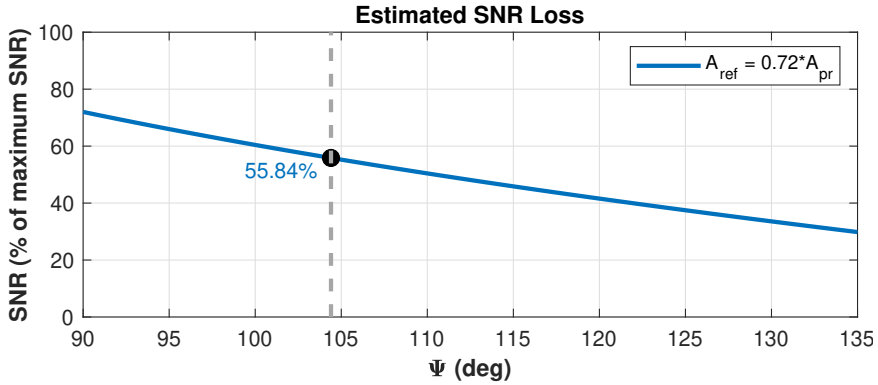

Figure 2.48: The SNR decrease for the diattenuation & polarization model ($A_{\mathrm{ref}} = 0.72A_{\mathrm{pr}}$ and $\Psi = 104.4°$) compared to the initial model ($A_{\mathrm{ref}} = A_{\mathrm{pr}}$ and $\Psi = 90°$).

By adding additional diattenuation and polarization aberration terms to the model we have been able to show good agreement with the measured data. For more details on the selection of the model terms $A_{\mathrm{ref}} = 0.72A_{\mathrm{pr}}$ and $\Psi = 104.4°$ see the appendix page 158. It was earlier discussed that the dichroic beam combiner was contributing polarization-dependent spectral phase to the reference and probe pulse. It is possible that the dichroic is also the source of the diattenuation and polarization aberration suspected in our system; it is known that dichroic beam combiners can be sources of diattenuation and polarization aberration [29]. If this is the case, then swapping out the dichroic beam combiner for a regular 50/50 beam combiner could increase the attainable SNR for the system. This would of course be at the expense of tossing 50% of the power before the focus, but since the system operates at very low power (several mW) for analyzing biological samples this would not be an issue.

2.7 Phase Calibration

2.7.1 Generating a Voltage to Phase Conversion Map

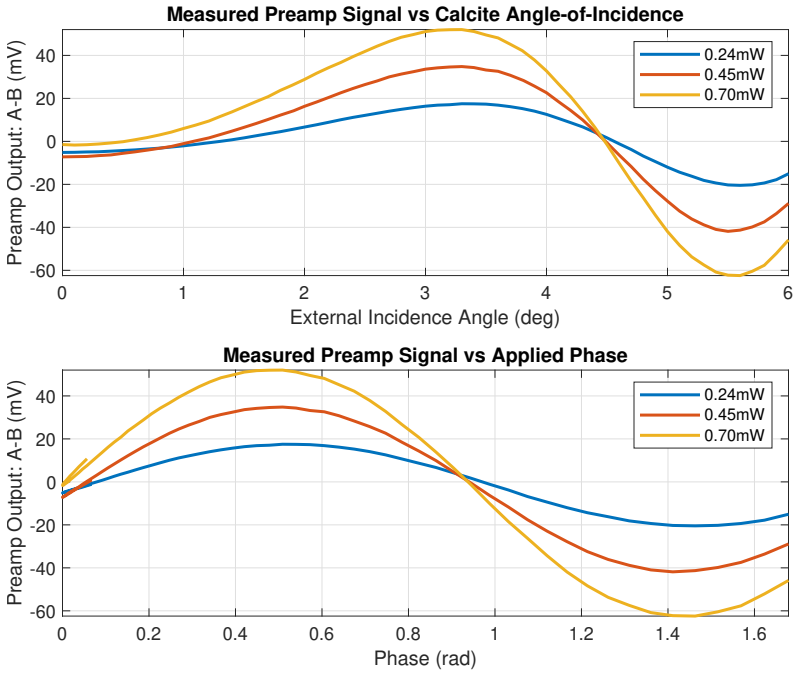

Figure 2.49: Mapping measured voltage data to phase, the power levels for each curve denote the power measured on the s- detector with the re-timing calcite removed

Finally, we can utilize our **model** of α_{ext} versus Φ_{CAL1} in conjunction with the **measured** α_{ext} vs balanced detection signal (ΔV) to create a phase to voltage (Φ_{CAL1} to ΔV) mapping. This calibration mapping will allow us to convert all future measurements from voltage to units of phase shift (mRad).

For data collection, the "balance" point that the system is set to is where the curve passes through 0V between the maxima and minima (row 2, Figure 2.49). At that balance point the power on the s- detector is measured with each sample so a corresponding calibration curve can be scaled. A $\pm\pi/2$ positive phase shift results in a voltage swing from the minima to the maxima of this curve. Confining our window to only the minimum and maximum of this curve and zero centering the phase shift we are able to formally create our voltage to phase calibration curve shown in Figure 2.50.

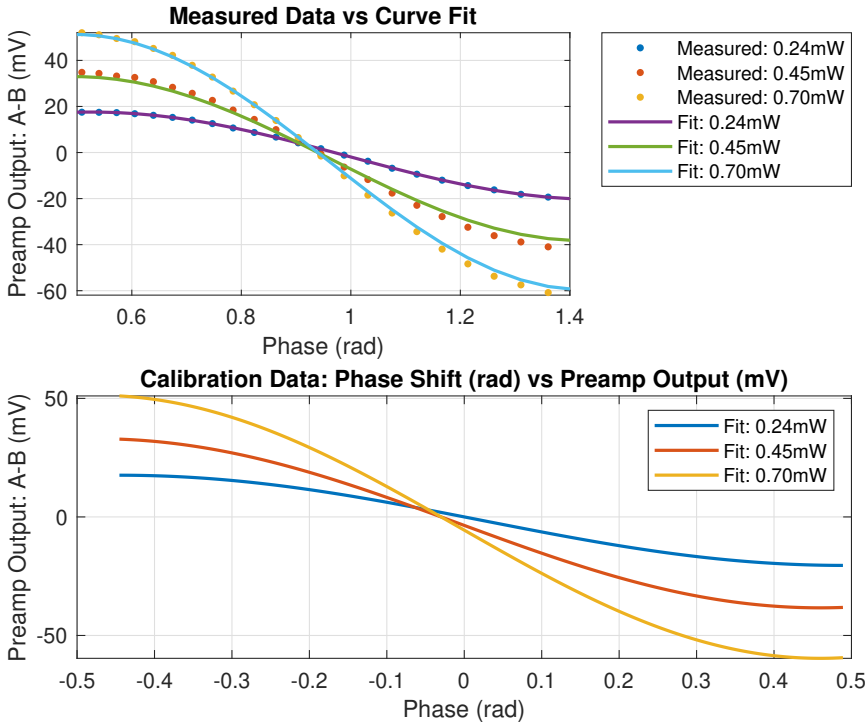

Figure 2.50: Voltage to Phase Calibration Curve.

Note the x-axis is now in units of radians; we are expecting a π phase shift between the minimum and maximum values of our curve.

Utilizing Figure 2.50, we curve fit the 0.24 mW curve with a sinusoid function and scaled the line of best fit by the power levels. The line of best fit ultimately has the form

$$Y = 19.02\, a\, \sin(3.363X - 0.1946) - 1.429 \tag{2.82}$$

where a is a scaling factor compared to 0.24 mW (i.e. for the 0.70 mW curve $a = \frac{0.7}{0.24} = 2.9167$). X is the phase axis in units of radians and Y is the signal out of the preamp in millivolts. For the 0.24 mW curve that was fit the SSE is 1.134, the R-square value is 0.9999, and the RMSE = 0.1282. The final calculated phase will need to have the phase for Y=0V subtracted from it (Thus, $X_{\text{final}} = X(Y) - X(0)$). Note, this assumes a constant transmissivity through the sample.

2.7.2 Impact of Galvanometer Scan Angle on Re-timing Phase

Modelling the Impact of Scan Angle

Galvo-scanning microscopy is a new development in TΦM and comes at the price of a limited FOV based on angle-dependent retiming phase. As a larger FOV is scanned the angle-of-incidence at calcite 2 ($a_{\text{ext},2}$) impacts the phase imparted to the retimed reference and probe pulse; this angle is equivalent to θ_5 in Figure 2.51 and can be solved for in terms of the displacement x_3 of the laser spot in the object plane.

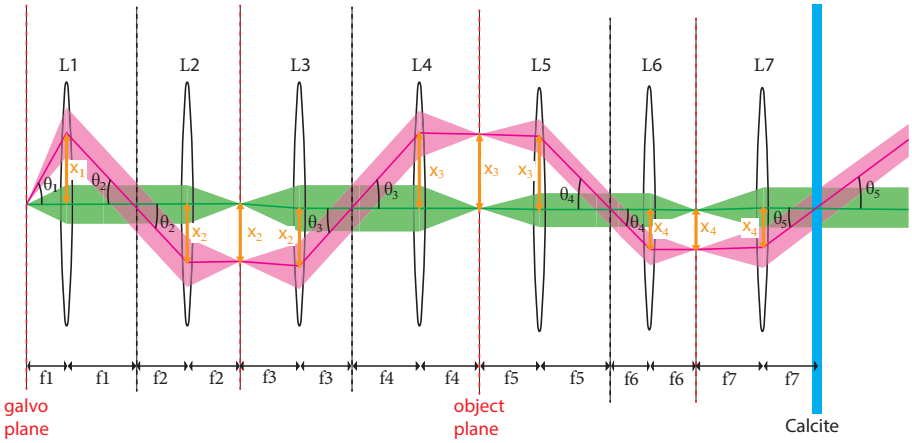

Figure 2.51: A map of the galvonometer angle through the microscope system to the retiming calcite plane.

Equation 2.83 shows the relationship between θ_5 and x_3

$$\theta_5 = \tan^{-1}(\frac{x_4}{f_7}) = \tan^{-1}(\frac{f_6 \tan(\theta_4)}{f_7}) = \tan^{-1}(\frac{f_6 \tan(\tan^{-1}(\frac{x_3}{f_5}))}{f_7}) = \tan^{-1}(\frac{f_6 x_3}{f_5 f_7}) \tag{2.83}$$

Thus,

$$\alpha_{\text{ext},2} = \theta_5 = \tan^{-1}(\frac{f_6 x_3}{f_5 f_7}) \tag{2.84}$$

Note that x_3 is the projection onto the extraordinary axis of the crystal since only the extraordinary axis is angle-dependent. Thus,

$$x_3 = \sqrt{x^2 + y^2}\cos(\eta) \tag{2.85}$$

where η is the angle between the extraordinary axis of the crystal and the axis defined by a chord through (0,0) and the (x,y) location of the pixel being scanned (Figure 2.52).

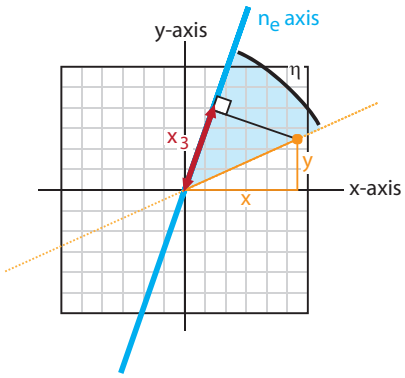

Figure 2.52: Determining the projection onto the re-timing calcite extraordinary axis, x_3, from the pixel location in the object scan plane

The phase accumulated as a function of external angle of incidence then becomes

$$\Phi_{\text{galvo}}(\alpha_{\text{ext},2}) = \Phi_{\text{galvo,e}}(\alpha_{\text{ext},2}) - \Phi_{\text{galvo,o}} = \frac{L_e n_e(\alpha_{\text{ext},2})\omega}{c} - \frac{(L_o n_o + L_{\text{ext}})\omega}{c} \tag{2.86}$$

using equations 2.28, 2.32, and 2.33 to solve for the length vectors as a function of the galvo-based external angle of incidence $\alpha_{\text{ext},2}$ in place of α_{ext}. From Equation 2.84 it can be easily seen that the retiming phase is proportional to the field-of-view (x_3) and f_6 and inversely proportional to f_5 and f_7. Thus, decreasing the FOV and/or increasing the magnification of the beam at the calcite plane would minimize retiming phase effects. This can be seen from the magnification relationship of $\frac{f_7}{f_6}$ where increasing f_7 or decreasing f_6 causes the beam size to increase and θ_5 to decrease.

Scan Data through Glass

Galvo-scanning microscopy is a new development in TΦM and comes at the price of an angle-dependent retiming phase present across the scanned field-of-view. In order to determine how big an impact galvo dependent re-timing phase has on this system, a cross-phase modulation (XPM) image was taken in a glass slide at different fields-of-view. Since glass is homogenous and has

no transient signal, a flat signal would be expected across the entire FOV in the absence of galvo dependent re-timing phase. The measured data shown in Figure 2.53 indicates a phase shift of 80 μRad and 96 μRad across a 30 μm FOV due to scan angle for XPM images taken at the pump-reference overlap (row 1, column 1) and pump-probe overlap (row 1, column 2), and a phase shift of 342 μRad and 406 μRad across a 225 μm FOV due to scan angle for the pump-reference (row 2, column 1) and pump-probe (row 2, column 2) XPM images, respectively. The images shown in Figure 2.53 have had the on-axis phase shift DC subtracted so only the spatially-dependent phase shift is portrayed.

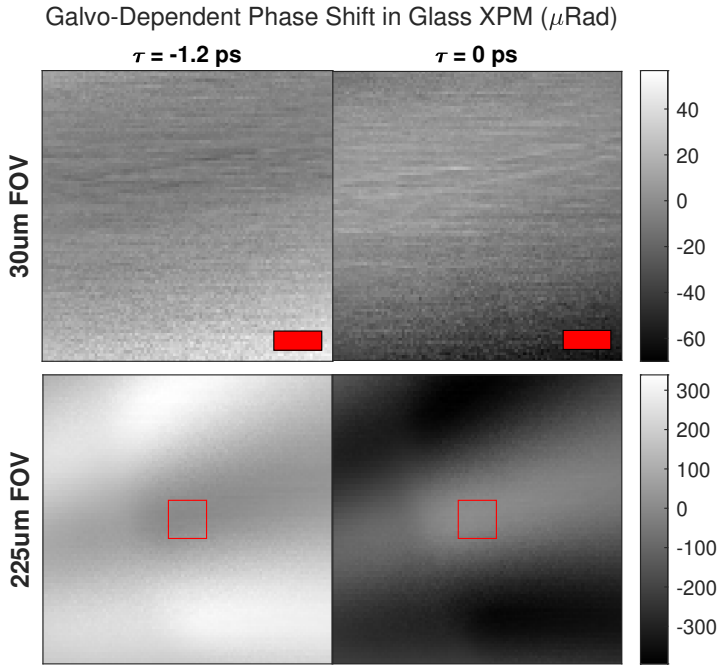

Figure 2.53: The top row shows the XPM images in glass measured at the pump-reference and pump-probe overlap peaks for a 30 μm x 30 μm FOV. The red scale bar is 5 μm wide. The bottom row shows the XPM images measured at the pump-reference and pump-probe overlap peaks for a 225 μm x 225 μm FOV. The square box in the center of each image outlines the FOV for the top row images. The scale for all images is the same and shows phase shift as a function of position with units of μRad, where the on-axis phase shift has been DC subtracted.

Clearly, the larger field of view sees a stronger galvo-dependent phase shift Φ_{galvo}. One possible way to completely mitigate this effect could be to add in de-scanning prior to the retiming calcite.

2.8 Results

This section presents the results of measuring transient absorption and transient phase in glass, a graphene monolayer, bovine hemoglobin in solution and in live human red blood cells. The probe wavelength of 800 nm is considered off-resonance for the hemoglobin and red blood cell samples.

2.8.1 Cross-phase Modulation Measurement in Glass

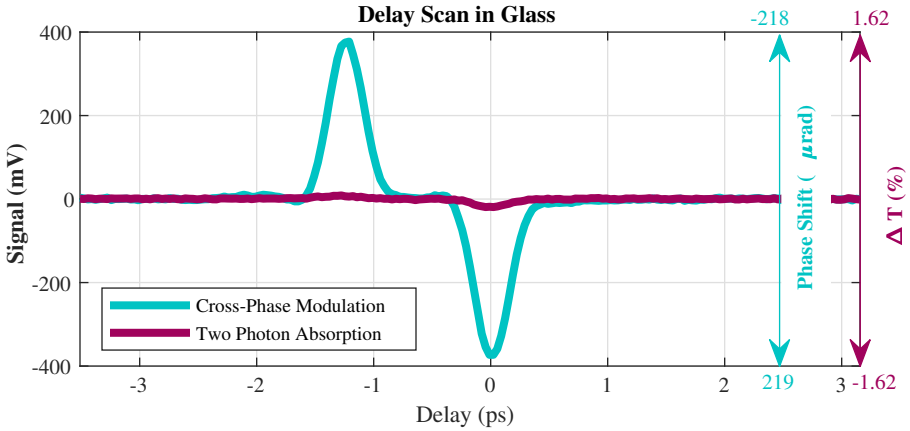

Figure 2.54: An initial delay scan in borosilicate glass revealed a cross-phase modulation detectable by transient phase, and a very small two photon signal measured with transient absorption. At the focus, the pump power is 3.9 mW and the probe power is 0.78 mW. The pump-induced phase shift $\Phi_{\mathrm{T\Phi M}} = \{-206 : 204\}\ \mu\mathrm{Rad}$.

First we acquired a delay scan in a glass microscope slide (Figure 2.54). Glass has a minimal absorption at the probe wavelength of 800 nm and the interaction that occurs between the sample and the pump pulse is instantaneous. Thus, the width of the cross phase modulation pulses gives us an estimate of pulse duration for our reference and probe pulses as they overlap with the pump pulse in time; these pulses are ∼350 fs in duration. The pump-induced phase shift $\Phi_{\mathrm{T\Phi M}} = \{-206 : 204\}\ \mu\mathrm{Rad}$ after converting the measured voltage to phase.

2.8.2 Graphene Monolayer

Next we explored the 2D and 3D nonlinear response of a graphene monolayer on a 0.5 mm quartz substrate placed on top of a 1 mm glass microscope slide. Previous works looking at

graphene have utilized transient absorption to analyze graphene carrier dynamics [30, 31]. It is a material that shows promise for use in various applications including electronics and drug delivery making it a popular research target [32]. Here, graphene serves as a control material to compare TAM with TΦM since it has a strong transient absorption response at our pump and probe wavelengths.

Time-Domain Spectroscopy

An initial delay scan taken in the center of the sample revealed a stronger transient absorption vs transient phase response with a decay time of $\sim$2 picoseconds.

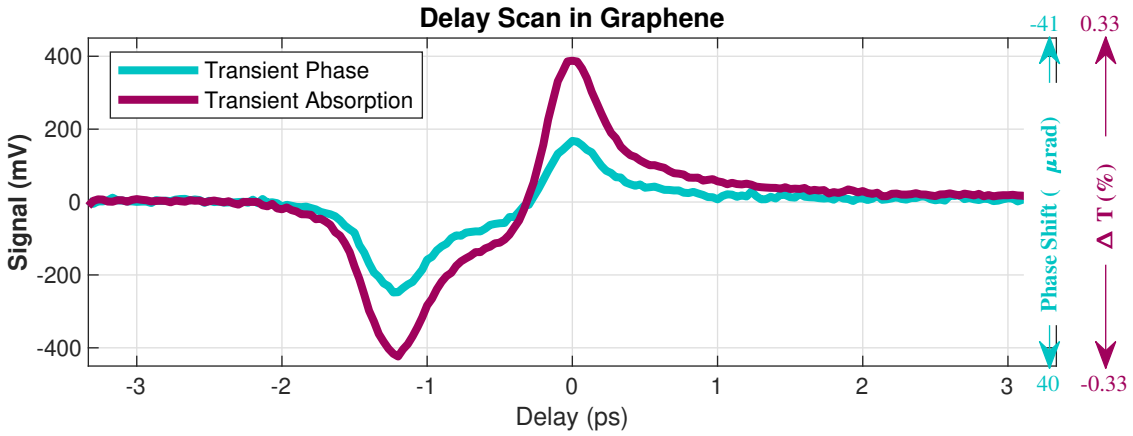

Figure 2.55: A transient absorption versus transient phase delay scan in monolayer graphene. At the focus, the pump power is 7.8 mW and the probe power is 0.97 mW. The transient phase signal ranges from -15 μRad to 22 μRad.

The first peak at $\tau = -1.2$ ps corresponds to the pump-reference overlap and has a maximum phase shift of $\Phi_{\mathrm{T\Phi M}} = 22$ μRad and the second peak at $\tau = 0$ ps corresponds to the pump-probe overlap with a maximum phase shift of $\Phi_{\mathrm{T\Phi M}} = -15$ μRad.

Imaging

Image stacks were acquired at the edge of the graphene sample where we expected to see some variation in the deposition of graphene on the quartz substrate. A calibration image was acquired after setting the half-waveplate for phase measurements and the angle of incidence for the first

calcite for a "balanced" state (i.e. $V_A - V_B = 0$) with the pump blocked. Utilizing the power measured on one of the photodetectors after setting the balance, the acquired calibration image can be used to back out a map of ground-state (in the absence of the pump) phase changes which can change the starting "balance state" $V_A - V_B$ spatially. Stated differently, the calibration image accounts for ground refractive index changes that alter the spatially-dependent starting voltage, where the on-axis starting voltage is set to zero indicating a "balanced state". This allows the units of the measured transient phase image to be converted to μRad. From Figure 2.56 the edge of the sample can be seen and give context to interpreting the image stack in Figure 2.57.

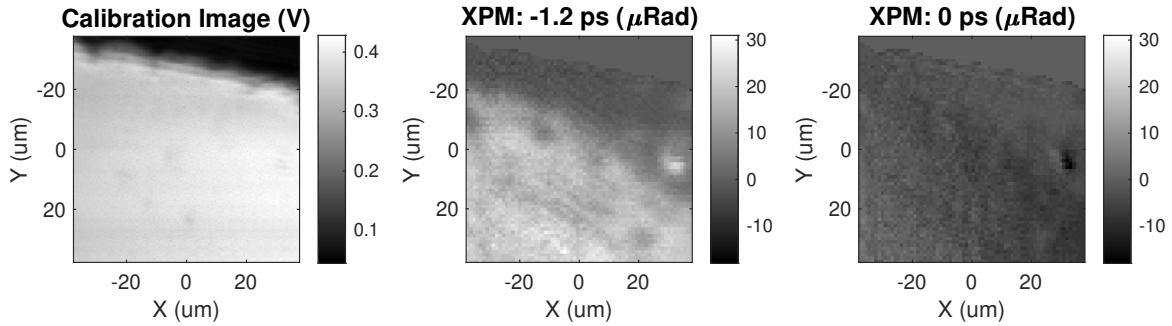

Figure 2.56: Graphene phase calibration image and the peak XPM images with calibrated units of phase (μRad). The phase shift in the XPM image at -1.2 ps ranges from {-2.16 : 11.59} μRad and the phase shift in XPM at 0 ps ranges from {-7.07 : 2.18} μRad.

An image stack was acquired for both transient phase and transient absorption at the edge of the graphene and are compared with output from the lock-in amplifier (V) (Figure 2.57). The transient absorption measurements still provide better SNR, but similar structural information can be seen in both techniques.

2.8.3 Hemoglobin and Red Blood Cells

Next we moved onto a biological sample. First we looked at the spectroscopy of a hemoglobin sample prepared with 9 mM of bovine hemoglobin lyophilized powder (Sigma-Aldrich H2500) in phosphate buffer solution. Then we imaged a droplet of whole blood placed on a Poly-L-Lysine coated microscope slide with a glass coverslip. The whole blood used was acquired from healthy

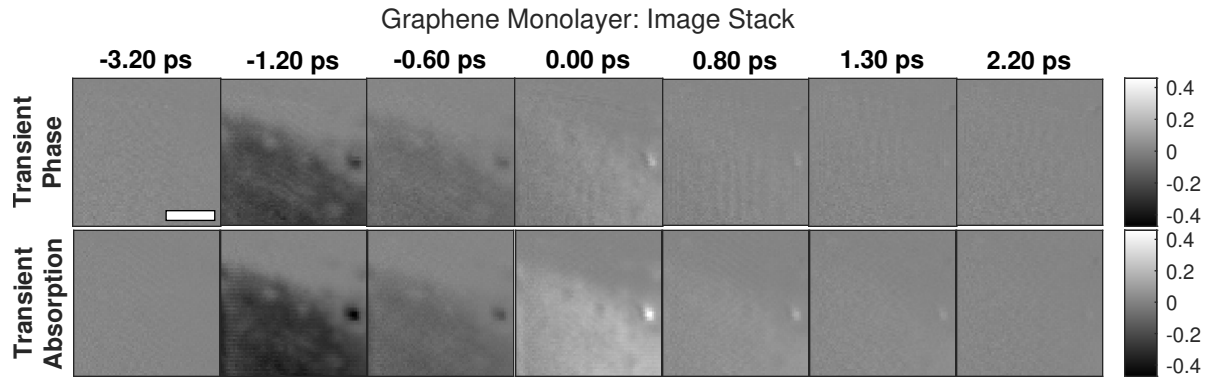

Figure 2.57: Intensity is measured in voltage from the lock-in amplifier output. The scale bar is 25 μm wide. At the focus, the pump power is 7.8 mW and the probe power is 0.97 mW.

donors by venipuncture by Dr. Liszt Madruga of the Department of Chemical Engineering (CSU) working under Prof. Matt Kipper of the Departments of Chemical & Biological Engineering CSU) and Prof. Ketul Popat of the Department of Mechanical Engineering (CSU). The protocol followed was approved by the Colorado State University Institutional Review Board.

Time-Domain Spectroscopy of Hemoglobin

The hemoglobin sample showed a ~ 2.5 ps decay curve (top row in Figure 2.58). Interestingly, hemoglobin demonstrated a pump polarization dependent signal with differences between the polarization sensitivity of the transient absorption vs transient phase measurements (bottom row of Figure 2.58), which would be impossible to observe if the pump combining dichroic was placed before the probe-reference splitting calcite like in [4, 5]. With transient absorption the pump-reference overlap showed a polarization dependence while the pump-probe overlap did not. For the pump-reference overlap, the strongest signal occurred with an s-polarized pump. With transient phase both overlaps demonstrated a polarization dependence; the pump-reference overlap shows the largest signal for the s- polarized pump and the pump-probe overlap shows the largest signal for the p- polarized pump. With a 45°pump, the transient phase signal ranges from {21.9 : 26.35} μRad. With an s-polarized pump, the transient phase signal ranges from {-25.55 : 17.55 } μRad. Finally, with a p-polarized pump, the transient phase signal ranges from {-16.15 : 38.45} μRad.

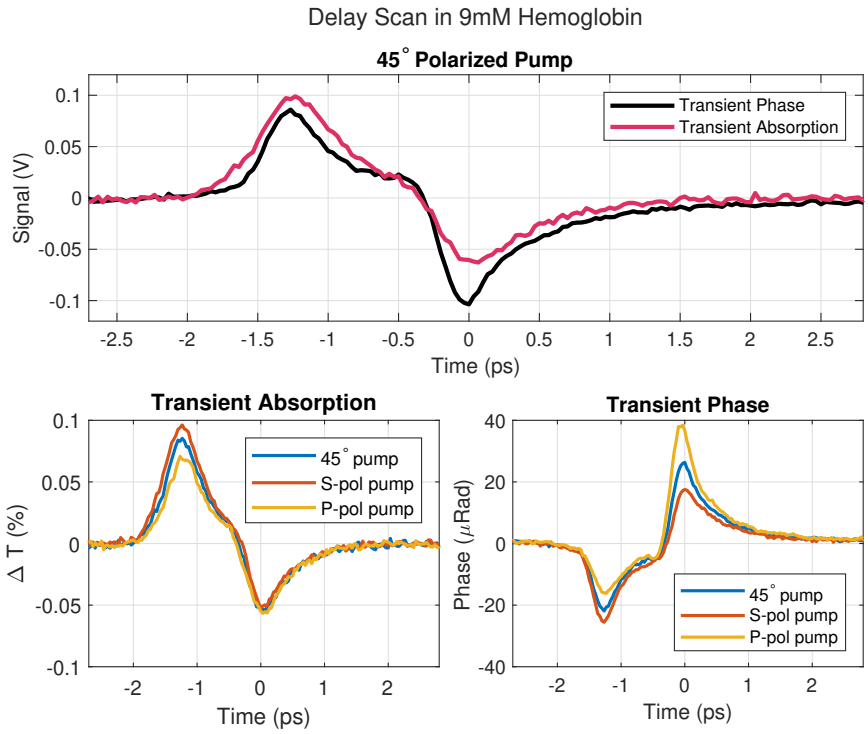

Figure 2.58: Delay scans in 9 mM bovine hemoglobin powder in phosphate buffer solution; the pump power at the focus is 0.81 mW and the probe power at the focus is 0.73 mW. The top row shows a comparison (in V) of the measured transient phase (black) and transient absorption (pink) delay scans for a $45°$ polarized pump beam. The first peak occurs with overlap of the pump-reference pulses at $\tau = -1.2$ ps and the second peak occurs with overlap of the pump-probe pulses at $\tau = 0$ ps. The bottom left image compares three transient absorption delay scans for different pump polarizations and the bottom right image compares three transient phase delay scans for different pump polarizations.

Red Blood Cell Imaging

Imaging human red blood cells we expected to see a predominant signal from hemoglobin and a similar SNR from the two techniques (based on the results from the delay scans), however transient phase demonstrated a stronger signal than transient absorption in this case with clearer structural details due to XPM. Figure 2.59 shows a comparison of TΦM and TAM for imaging the transient decay in RBC. All of the images are shown on the same intensity scale; the overlaps with the pump-reference at $\tau = -1.20$ ps and with the pump-probe at $\tau = 0$ ps show the strongest signals and good structural detail for TΦM.

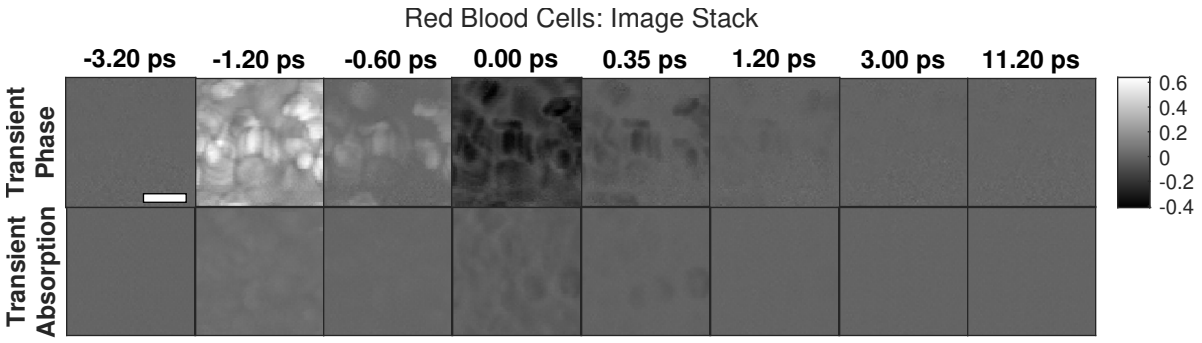

Figure 2.59: Image delay stack of live red blood cells. The scale bar is 10um wide; the intensity axis denotes voltage.

These cells were suspended in plasma beneath a coverslip on a Poly-L-Lysine slide but it was observed that the cells did not adhere to the slide. During the time it took to acquire image stacks the cells migrated significantly. Figure 2.60 shows a calibration image acquired before the imaging session (left) and after the imaging session (right). Clearly the images are not the same; thus a spatial mapping connecting $\Phi_0(x, y)$ to the transmitted power measured at ($x = 0$,$y = 0$) cannot be made in correspondence with the measured transient phase images since the power scaling factor a in Equation 2.82 is not known spatially.

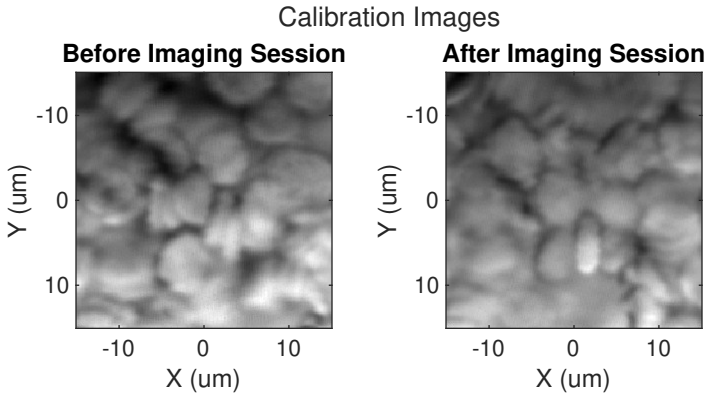

Figure 2.60: Comparison of a transient phase calibration image taken before the imaging session (left) vs after the imaging session (right). The red blood cells have drifted position during the length of the imaging session.

2.9 Conclusion

The purpose of this research was to evaluate TΦM as a complement to TAM for constrained probing wavelengths. If the TAM and TΦM spectra are not known for a particular sample, measuring both TAM and TΦM may uncover that one technique is advantageous to measure over the other. Conveniently, the microscope design presented here allows for an easy transition between TAM and TΦM measurements. In the future two changes to the microscope design here could be made to improve the utility for TΦM; first, the dichroic beam combiner could be swapped for a 50/50 beamsplitter. While this would cut the power at the combiner by half, it would also eliminate the polarization-dependent effects that we have shown negatively impact the SNR of TΦM. Additionally, descanning could be added prior to the retiming calcite to remove the spatial dependence on retiming phase. Another interesting route forward would be to swap the pump and probe arms of this microscope and place the tunability on the pump. Then the impact of pump excitation wavelength could be evaluated in conjunction with a NIR probe wavelength for TAM and TΦM.

Bibliography

[1] Martin C. Fischer, Jesse W. Wilson, Francisco E. Robles, and Warren S. Warren. Invited review article: Pump-probe microscopy. 87:031101, Mar 2016.

[2] Yifan Zhu and Ji-Xin Cheng. Transient absorption microscopy: Technological innovations and applications in materials science and life science. *The Journal of Chemical Physics*, 152(2):020901, Jan 2020.

[3] E. Tokunaga, T. Kobayashi, and A. Terasaki. Frequency-domain interferometer for femtosecond time-resolved phase spectroscopy. *Optics Letters*, 17(16):1131, August 1992.

[4] Meindert A. Van Dijk, Markus Lippitz, Daniel Stolwijk, and Michel Orrit. A common-path interferometer for time-resolved and shot-noise-limited detection of single nanoparticles. *Optics Express*, 15(5):2273, 2007.

[5] J. Chandezon, J.-M. Rampnoux, S. Dilhaire, B. Audoin, and Y. Guillet. In-line femtosecond common-path interferometer in reflection mode. *Optics Express*, 23(21):27011, October 2015.

[6] Justin Peatross and Michael Ware. *Physics of light and optics*. Brigham Young University, Department of Physics, Provo, Utah, 2015 edition, june 25, 2020 edition, 2020.

[7] Andrew T. Francis, Kyla Berry, Elena C. Thomas, Andrew H. Hill, and Dan Fu. In vitro quantification of single red blood cell oxygen saturation by femtosecond transient absorption microscopy. *The Journal of Physical Chemistry Letters*, 10(12):3312–3317, June 2019.

[8] Jeanne L. McHale. *Molecular spectroscopy*. CRC Press, Boca Raton, 2nd ed edition, 2017.

[9] Robert Boyd. *Nonlinear Optics*. Nikki Levy, fourth edition edition, 2020.

[10] Suresh Chandra. *Molecular spectroscopy*. Alpha science international ltd, Oxford, 2009.

[11] Peter F. Bernath. *Spectra of atoms and molecules*. Oxford University Press, New York, 2nd ed edition, 2005.

[12] Yilin Xing, Shanxing Gao, Xinyu Zhang, and Jiachen Zang. Dietary heme-containing proteins: Structures, applications, and challenges. *Foods*, 11(22):3594, November 2022.

[13] Y. Kholodenko, M. Volk, E. Gooding, and R.M. Hochstrasser. Energy dissipation and relaxation processes in deoxy myoglobin after photoexcitation in the soret region. *Chemical Physics*, 259(1):71–87, September 2000.

[14] Fabrizio Santoro, Alessandro Lami, Roberto Improta, Julien Bloino, and Vincenzo Barone. Effective method for the computation of optical spectra of large molecules at finite temperature including the duschinsky and herzberg–teller effect: The qx band of porphyrin as a case study. *The Journal of Chemical Physics*, 128(22):224311, June 2008.

[15] Shaohong L. Li and Donald G. Truhlar. Franck–condon models for simulating the band shape of electronic absorption spectra. *Journal of Chemical Theory and Computation*, 13(6):2823–2830, June 2017.

[16] John A. Moon. Optimization of signal-to-noise ratios in pump-probe spectroscopy. *Review of Scientific Instruments*, 64(7):1775–1778, July 1993.

[17] Jean-Claude Diels and Wolfgang Rudolph. *Ultrashort laser pulse phenomena: fundamentals, techniques, and applications on a femtosecond time scale*. Optics and photonics. Elsevier / Academic Press, Amsterdam; Boston, 2nd ed edition, 2006.

[18] Geoffrey New. *Introduction to Nonlinear Optics*. Cambridge University Press, United States of America, 2011.

[19] Hang Liu, Jianguan Yao, and Ashok Puri. Second and third harmonic generation in bbo by femtosecond ti: sapphire laser pulses. *Optics Communications*, 109(1–2):139–144, June 1994.

[20] V. Krylov, J. Gallus, U.P. Wild, A. Kalintsev, and A. Rebane. Femtosecond noncollinear and collinear parametric generation and amplification in bbo crystal. *Applied Physics B: Lasers and Optics*, 70(2):163–168, February 2000.

[21] Andrew Marc Weiner. *Ultrafast optics*. Wiley series in pure and applied optics. Wiley, Hoboken, N.J, 2009.

[22] Rick Trebino. *Frequency-Resolved Optical Gating: The Measurement of Ultrashort Laser Pulses*. Springer US, Boston, MA, 2000.

[23] Daniel J. Kane. Principal components generalized projections: a review [invited]. *Journal of the Optical Society of America B*, 25(6):A120, June 2008.

[24] Daniel J. Kane, G. Rodriguez, A. J. Taylor, and Tracy Sharp Clement. Simultaneous measurement of two ultrashort laser pulses from a single spectrogram in a single shot. *Journal of the Optical Society of America B*, 14(4):935, Apr 1997.

[25] David L. Wokosin. Pulse duration spectra and measurements for laser scanning microscope systems. In *Multiphoton Microscopy in the Biomedical Sciences V*, volume 5700, page 1–13. SPIE, Mar 2005.

[26] Philip Schlup, Jesse Wilson, Klaus Hartinger, and Randy A. Bartels. Dispersion balancing of variable-delay monolithic pulse splitters. *Appl. Opt.*, 46(23):5967–5973, Aug 2007.

[27] Geoffrey New. *Introduction to Nonlinear Optics*. Cambridge University Press, Cambridge; New York, 2011.

[28] Grant R. Fowles. *Introduction to modern optics*. Dover Publications, New York, 2nd ed., dover ed edition, 1989.

[29] Sawyer Miller, Linan Jiang, and Stanley Pau. Birefringent coating to remove polarization aberrations. *Opt. Express*, 30(12):20629–20646, Jun 2022.

[30] Felice Gesuele. Ultrafast hyperspectral transient absorption spectroscopy: Application to single layer graphene. *Photonics*, 6(3):95, August 2019.

[31] Yang Lu, Xin Tan, Yanzheng Du, Donglin Ma, and Weigang Ma. Direct observation of ultrafast carrier coupling dynamics in monolayer graphene/metal system. *International Journal of Heat and Mass Transfer*, 197:123322, November 2022.

[32] Junjie Li, Weixia Zhang, Ting-Fung Chung, Mikhail N. Slipchenko, Yong P. Chen, Ji-Xin Cheng, and Chen Yang. Highly sensitive transient absorption imaging of graphene and graphene oxide in living cells and circulating blood. *Scientific Reports*, 5(1):12394, July 2015.

Chapter 3

The Development of a Compact Reflectance Confocal Fiber Scanning Microscope

In the previous chapter the microscope utilized a point-scan imaging technique controlled by fast scanning mirror galvanometers. Galvanometers are commonly used actuators that can achieve high frame rates [1] with precise positioning, but they are large, bulky, and not suited for small, compact, point scanning designs. In this chapter, we present the development of a compact fiber scanning microscope that uses an alternative actuator: a miniature piezoelectric tube. Actuation influences important parameters of an imaging device such as size, weight, frame rate, field-of-view (FOV) and image reconstruction for point-scanning techniques. Current literature around piezoelectric actuators focuses on device optimization with a fixed FOV but neglects adjustability. Here we introduce an adjustable FOV piezoelectric fiber-cantilever microscope and provide a characterization and optimization procedure. To overcome calibration challenges we utilized a Position Sensitive Detector (PSD) and address trade-offs between FOV and sparsity with a novel inpainting technique (Chapter 4). Overall, this work furthers optimization research into compact actuation designs to support the future development of smaller medical imaging devices, helping to bridge the gap between laboratory and clinic.

This chapter is structured to first introduce the light source and system design followed by an in-depth review of the design and construction process. The remaining sections describe the characterization and calibration of the final microscope build (Version 3.3) and present an evaluation of the system imaging performance and limitations.

3.1 Background

In this project, we are measuring the reflected and back-scattered light from a sample with a technique known as reflectance confocal microscopy (RCM). Confocal microscopy is a simple

imaging technique that requires few optical components; the hallmark attribute of a confocal system is the use of a spatial filter (a pinhole) placed at a specific plane to prevent out of focus light from being collected by the detector. The only requirement for the light source is that it interacts with the sample and is collected by the detector in either a transmission or reflection geometry. Figure 3.1 shows an example of a reflection confocal geometry; a typical setup has an illumination source which is focused onto the object and separated from back-reflected light using a beam-splitter. The detector and pinhole are placed 1-f away from the closest relay lens that is focusing the light. In order to scan different axial planes, the sample can be raised or lowered through the focus. Note the majority of the light emitted from planes below and above the focus is blocked by the pinhole. Due to the pinhole configuration, this technique typically uses a single pixel detector which records light intensity as a function of time. Additionally, the extension of this technique to imaging applications typically requires point-scan imaging. In point-scanning the focal point is swept across the object and the beam position is recorded in time in conjunction with the reflected intensity.

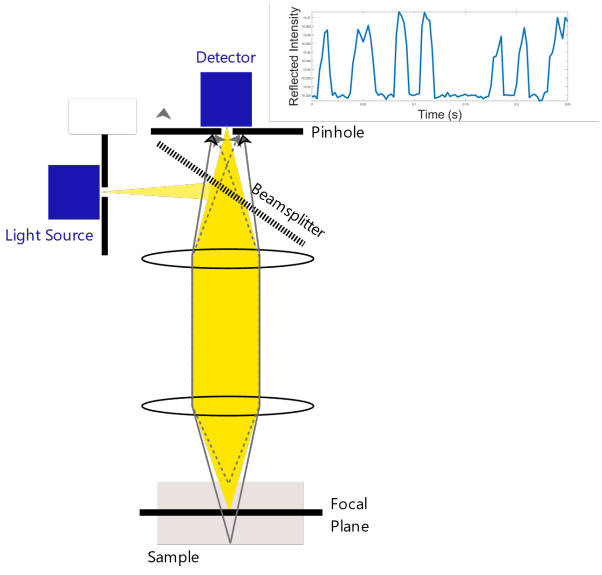

Figure 3.1: Reflection setup for confocal microscopy

Light incident upon a sample will either be transmitted, absorbed, scattered, or reflected [2]. The signal being measured in this system is related to the reflected light intensity which is in turn related to the refractive index of a sample. The Fresnel equations calculate the amplitudes of the reflected and transmitted light, which are reliant upon the angle of incidence, polarization, and refractive indices of the incident and object medium [2]. Snell's law $n_i \sin\theta_i = n_t \sin\theta_t$ allows us to determine the angle of refraction for the transmitted light, and the law of reflection informs us that the reflected angle equals the incident angle [3]. The Fresnel reflection coefficients are

$$r_s = \frac{\sin(\theta_t - \theta_i)}{\sin(\theta_t + \theta_i)} \tag{3.1}$$

$$r_p = \frac{\tan(\theta_t - \theta_i)}{\tan(\theta_t + \theta_i)} \tag{3.2}$$

Note the subscripts s and p denote s- versus p- polarized light incident on a medium. Clearly the amount of reflected light we measure ($I \propto r_s + r_p$) varies as a function of the refractive index of a material when Snell's law is plugged in. If a material has a complex refractive index (ie $\mathcal{N} = n + i\kappa$), then $\mathcal{N}$ replaces n. Thus for materials with a complex refractive index (i.te. non-transparent materials for visible light), the reflected light contains information about the refractive index and the absorption properties of a material [3].

3.1.1 Light Source

In our system light is supplied from a 10 mW 785 nm CW laser diode (Thorlabs LPS-785-FC) and diode driver (Thorlabs CLD1010). The output of the laser diode is connected to a non-polarization maintaining fiber optic cable. At the output of the fiber optic the light is likely a mix of polarization states even though the light exiting the laser diode is linearly polarized; it has been shown that birefringence can occur in single mode optical fibers due to imperfections in the core geometry (deviating from a circular cross-section) as well as compressive stress when the fiber is bent [4], which would alter the input polarization state. Next, the light exits the fiber optic with a numerical aperture (NA) of 0.13 and is relayed by two plano-convex lenses in a 4-f configuration

to the imaging plane. Light is collected in the reflection geometry and the fiber optic core and cladding act as a pinhole, rejecting out of focus background light. Due to this confocal geometry our initial point spread function dictating our lateral resolution at the imaging plane is multiplied by itself upon collection, providing an increased lateral resolution than would be possible without a confocal measurement. The next section describes a derivation for the lateral and axial point spread functions used to determine the resolution of scanner version 3.3.

Derivation of Lateral and Axial Point-Spread Functions

Optical resolution is dictated by the lateral and axial point spread functions (PSFs). Here we define resolution as the full-width at half maximum (FWHM) of the fitted PSFs. Mode Field Diameter (MFD), the $\frac{1}{e^2}$ beam width, is related to FWHM and beam radius, w_0, by $\mathrm{MFD} = 2\mathrm{w}_0 = 1.699 \times \mathrm{FWHM}$.

In reflectance confocal microscopy the point spread function of the system is convolved with the object being imaged then multiplied by itself on the return path back through the confocal pinhole [5]. Assuming a standard Gaussian laser beam at the sample plane with the intensity distribution,

$$I(r,z) = I_0 \left(\frac{\mathrm{w}_0}{\mathrm{w(z)}}\right)^2 e^{-2r^2/\mathrm{w(z)}^2}, \tag{3.3}$$

where the z-dependent spot size is $\mathrm{w(z)} = \mathrm{w}_0\sqrt{1+(\mathrm{z}/\mathrm{z}_\mathrm{R})^2}$, the PSF for both illumination and collection is multiplied leaving us with the square of the intensity:

$$\mathrm{PSF}(r,z)^2 = I(r,z)^2 = I_0^2 \left(\frac{\mathrm{w}_0}{\mathrm{w(z)}}\right)^4 e^{-4r^2/\mathrm{w(z)}^2}. \tag{3.4}$$

To determine lateral resolution, we utilized the "knife edge" method [6][7][8], where we translate a reflective sharp edge across the beam at the focal plane. This measures reflected power, P, as a

function of x-position of the knife edge,

$$P(x_b) = \int_{x_b}^{\infty} \int_{-\infty}^{\infty} \mathrm{G}(x,y)^2 \mathrm{d}y\mathrm{d}x \tag{3.5}$$

where the coordinate $x_b = (x, y)$ is where the measurement is made and the cross-sectional intensity profile of a Gaussian ($\mathrm{TEM}_{0,0}$) mode is

$$G(x,y) = \mathrm{PSF}(r, z=0) = I_0 e^{-2(x^2+y^2)/\mathrm{w}_0^2} \tag{3.6}$$

The response measured by the photodetector when only translating the knife edge along the x-axis can then be written by

$$P(x_b) = \int_{x_b}^{\infty} \int_{-\infty}^{\infty} I_0^2 e^{-4(x^2+y^2)/\mathrm{w}_0^2} \mathrm{d}y\mathrm{d}x. \tag{3.7}$$

Utilizing u-substitution we can simplify this further to

$$P(x_b) = I_0^2 \frac{\mathrm{w}_0}{2} \sqrt{\pi} \int_{x_b}^{\infty} e^{-4x^2/\mathrm{w}_0^2} \mathrm{d}x. \tag{3.8}$$

From [8] we can cast this measurement in terms of the complementary error function,

$$\mathrm{erfc}(x) = \frac{1}{\sqrt{2\pi}} \int_{x}^{\infty} e^{-u^2/2} \mathrm{d}u \tag{3.9}$$

such that

$$P(x_b) = I_0^2 \mathrm{w}_0 \pi \frac{\sqrt{2}}{2} \mathrm{erfc}\left(\frac{\mathrm{x}\sqrt{8}}{\mathrm{w}_0}\right), \tag{3.10}$$

where $u = x\sqrt{8}/\mathrm{w}_0$. We can directly fit the complementary error function to the data and determine the beam radius, w_0.

Likewise, the axial PSF can be measured by detected power from a reflective surface that is scanned in z:

$$P(z) = \int_{-\infty}^{\infty}\int_{-\infty}^{\infty} \mathrm{PSF}(r,z)^2 \mathrm{d}x\ \mathrm{d}y = I(z)^2 = I_0^2\left(\frac{\mathrm{w}_0}{\mathrm{w(z)}}\right)^4 = I_o^2\left(\frac{1}{1+\frac{2z^2}{z_R^2}+\frac{z^4}{z_R^4}}\right) \quad (3.11)$$

3.1.2 Microscope Overview

Actuation

In order to create an image our scanner utilizes the mechanical resonance of a cantilever, translating micrometers of displacement of a piezoelectric tube into hundreds of micrometers of displacement of a cantilevered optical fiber.

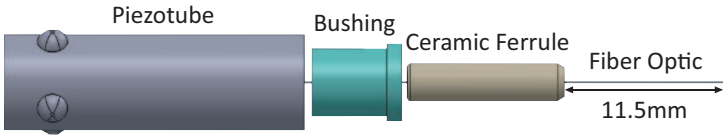

Figure 3.2: Exploded view of the cantilever components. The solder balls on the piezotube are visible but the quadrant electrodes are not shown. The optical fiber is seated inside a ceramic ferrule which press-fits into the bushing. The bushing is glued to the inside of the piezotube.

The actuator assembly consists of four components: the piezoelectric tube, a bushing, a ceramic ferrule and an optical fiber (shown in Figure 3.2). The optical fiber is a single mode fiber (Thorlabs 780HP) and is held concentric to the four-quadrant cylindrical piezotube. 11.5 cm of the fiber optic extends past the ceramic ferrule, and the base of the fiber is secured as it enters the ferrule creating a cantilever geometry. The piezotube itself is also a cantilever with the free end facing the fiber optic. A distinct benefit of utilizing a piezotube to drive fiber motion is that the actuator size is small, though it does require a high-voltage control scheme. Competing micro-actuation techniques include electromagnetic, electrothermal, and shape memory alloys, among others (see [9] for a thorough review of actuation techniques). In addition to the small convenient form factor, by utilizing piezoelectric actuation we are able to take advantage of a wide driving frequency range, which accommodates flexibility in various fiber resonances.

System Design

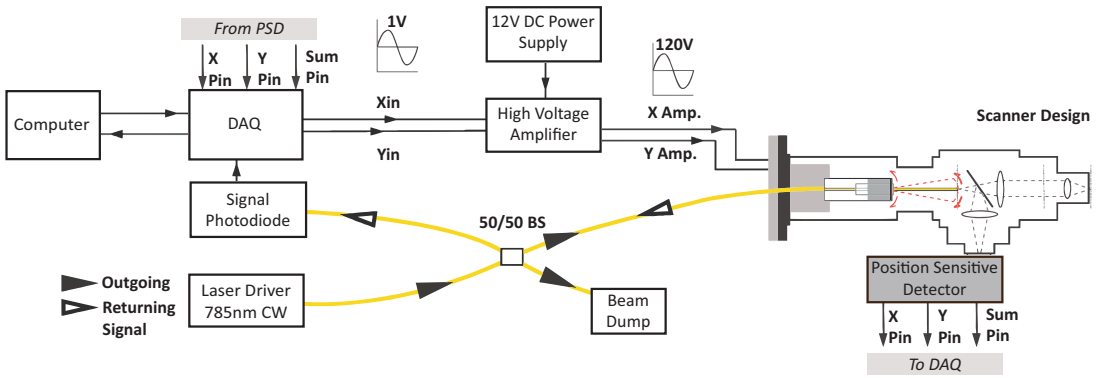

Figure 3.3: High-level system design. DAQ-Data Acquisition, Xin/Yin - Input waveforms to the High Voltage Amplifier (bounded 0-1V), X Amp./Y Amp. - Output High Voltage Waveforms, BS - Beam Splitter, CW - Continuous Wave Laser Source

As previously stated, the fiber optic acts as a confocal pinhole for imaging in the reflection geometry which rejects out-of-focus reflections and enables optical sectioning [10, 11]. Additionally, in the cantilever design, we can take advantage of an adjustable field of view which is dependent on the applied driving voltage. Figure 3.3 displays the entire system diagram.

The optical fiber cantilever is created by cutting a patch cable in half and cleaving the free end. The glass fiber optic (Thorlabs 780HP) has a 0.13 NA, 125 μm diameter cladding, 4.4 μm diameter core, and 5.0 μm nominal mode field diameter. The optical fiber is threaded through a 2.5 mm diameter ceramic ferrule, which is press fit into a custom made bushing so that half of its length is inside the bushing. Finally the bushing is slid into the front of the piezotube. This assembly places the fiber cantilever at the end of the base piezotube cantilever. Small deflections by the base cantilever will amplify into larger deflections by mechanical resonance in the fiber optic cantilever.

We use a computer controlled data acquisition (DAQ) module (National Instruments USB 6211) to send sinusoidal driving waveforms to the homebuilt high voltage amplifier. The high voltage differential output is applied to opposite electrodes on the four-quadrant piezotube (see Figure 3.4) at frequencies near the resonant frequency of the fiber cantilever.

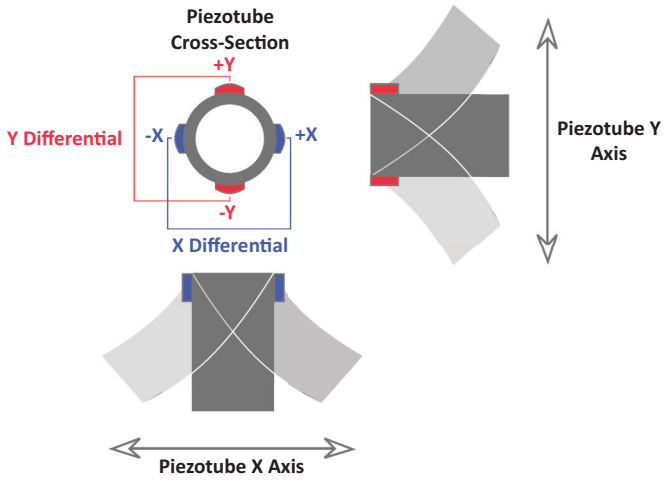

Figure 3.4: Driving axes of the piezotube. The cross-section shows a front view of the tube and locations for the X and Y axis high-voltage electrode contacts. Application of a sinusoidal voltage across the +/- Y electrodes drives a vertical cantilevered response of the free end of the piezotube. A sinusoidal voltage across the +/- X electrodes drives a horizontal cantilevered response of the free end of the piezotube.

Light from the fiber tip is relayed to the object focal plane with a 4-f lens system; and then recollected in the reflection geometry. We use a thin glass coverslip to pick off $\sim 4\%$ of the excitation beam before L1, which is redirected onto a 9mm square position sensitive detector (PSD) (see Figure 3.5).

The PSD tracks the beam position during scanning and has two outputs to track position, Δx and Δy, and a normalization reference, SUM. The beam positions are calculated $\{x, y\} = L_{\{x,y\}}\Delta\{x, y\}/2\ \mathrm{SUM}$, where L_x and L_y are the X and Y dimensions of the PSD active area, respectively. We use a 10mW 785nm CW laser diode (Thorlabs LPS-785-FC) and diode driver (Thorlabs CLD1010) as the light source which passes through a 50:50 fiber optic coupler (Thorlabs TN785R5F2). Backreflections from the sample pass back through the coupler to an amplified photodetector (Thorlabs PDA36A2). During scanning, the DAQ synchronously collects this signal along with all three PSD pins at a rate of 62.5kHz. This low sampling rate compounds issues of sparsity that we encounter at larger driving voltages.

Details of the custom piezo driver are posted in a GitHub repository [12]. In brief, the high-voltage amplifier is a power op-amp (LM675) driving a step-up transformer (Talema 62020, toroidal power transformer, 5.0 VA, 7V/14V secondary, 115V/230V primary). It has a gain of 120, an out-

put range of 6V to 240V and relies on a 12V DC power supply. This arrangement provides several high-voltage safety features: There is no need for a high-voltage power supply to power the amplifier, no high-voltage is present when there is no input signal, and the transformer provides intrinsic electrical isolation. A minor disadvantage is it cannot provide high-voltage DC and the frequency range is limited at 50 Hz to 2 kHz.

Tracking the fiber position in real-time is important for accurate image reconstruction, especially with resonant actuation where the fiber-optic cantilever is sensitive to handheld motion, mechanical perturbation, and general nonlinearities. Various approaches have been taken to address fiber-tip tracking such as recording an initial calibration scan before continued use [13], constructing a two-headed scanner with a lock-in to determine phase [14], implementing a control loop [15] [16], using a maximum image correlation algorithm in post-processing [17], utilizing a CCD which collects segments of a trace over many cycles to build up an image [18], and sensing coils which are calibrated during the ring-down of a scan [11]. All of these methods are comparatively complicated, slower, or not able to capture subtleties of motion blur and short-lived nonlinearities in frame to frame changes of a scan pattern compared to an integrated PSD in the scan head. We believe this technique has been significantly overlooked in the literature, having found only one paper making use of an integrated PSD [19]. PSDs are available as off-the-shelf components, are very easy to implement and calibrate, and provide continuous, beam tracking data for robust image reconstruction. A limitation we have found while utilizing the PSD is related to a strain-induced birefringence in the non-polarization-maintaining fiber optic cable. When the cable is moved, we have found that the front and back polarization-dependent surface reflections on the PSD from the coverslip can differ in intensity. Since the PSD takes the centroid of the intensity distribution incident upon it, differences in intensity between the two beam spots on the PSD make the beam appear to be moving when it is physically stable. This limitation can be mitigated with a polarization-maintaining fiber or by using a non-polarizing beam splitter in lieu of a coverslip.

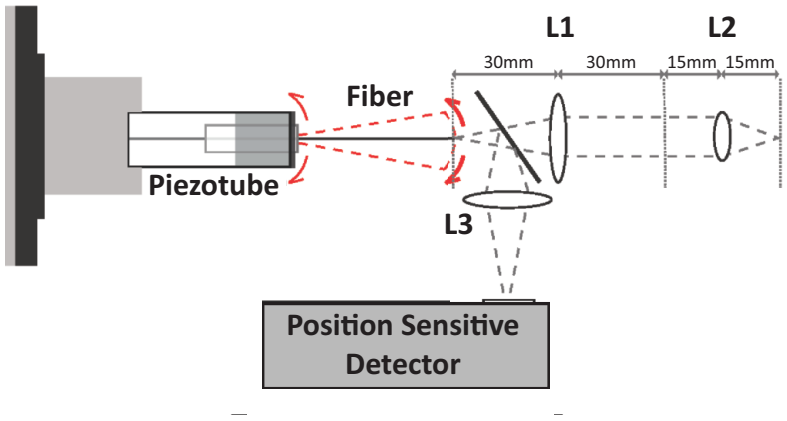

Figure 3.5: 4-f imaging design with a PSD. The main light path is imaged from the fiber tip through Lens 1 (L1) and 2 (L2) to the focal plane and reflected light retraces this path to be captured by the fiber tip. A secondary light path is picked using a glass coverslip prior to L1 which sends approximately 4% of the main light towards Lens 3 (L3) and the PSD due to the backreflection off the coverslip surface.

3.2 Construction

Three versions of this scanner were constructed, moving the scanner from a state of exposed parts to an enclosed and portable system mounted to an optical breadboard. Throughout the iterations of design and construction the two primary challenges were to design a concentric, replaceable and repeatable fiber mounting assembly and to design a cheap, enclosed, and portable microscope housing.

Figure 3.6 shows the evolution of the fiber mount and housing assemblies. The next two sections provide details on the upgrades made with each version.

3.2.1 Fiber Mounting Assembly

The fiber mounting assembly connects the optical fiber as a cantilever to the piezotube actuator. Three important aspects drove the design changes between versions 1 and 3. First, the fiber optic needed to be mounted concentric to the axis of the piezotube. This was important to ensure that when the assembly was enclosed with lens tubing that the light from the fiber optic was on axis with the relay lenses. Off-axis tilt of the fiber cantilever would result in imaging aberrations. Second, the base of the fiber cantilever needed to be secure within the piezotube. The piezotube is hollow

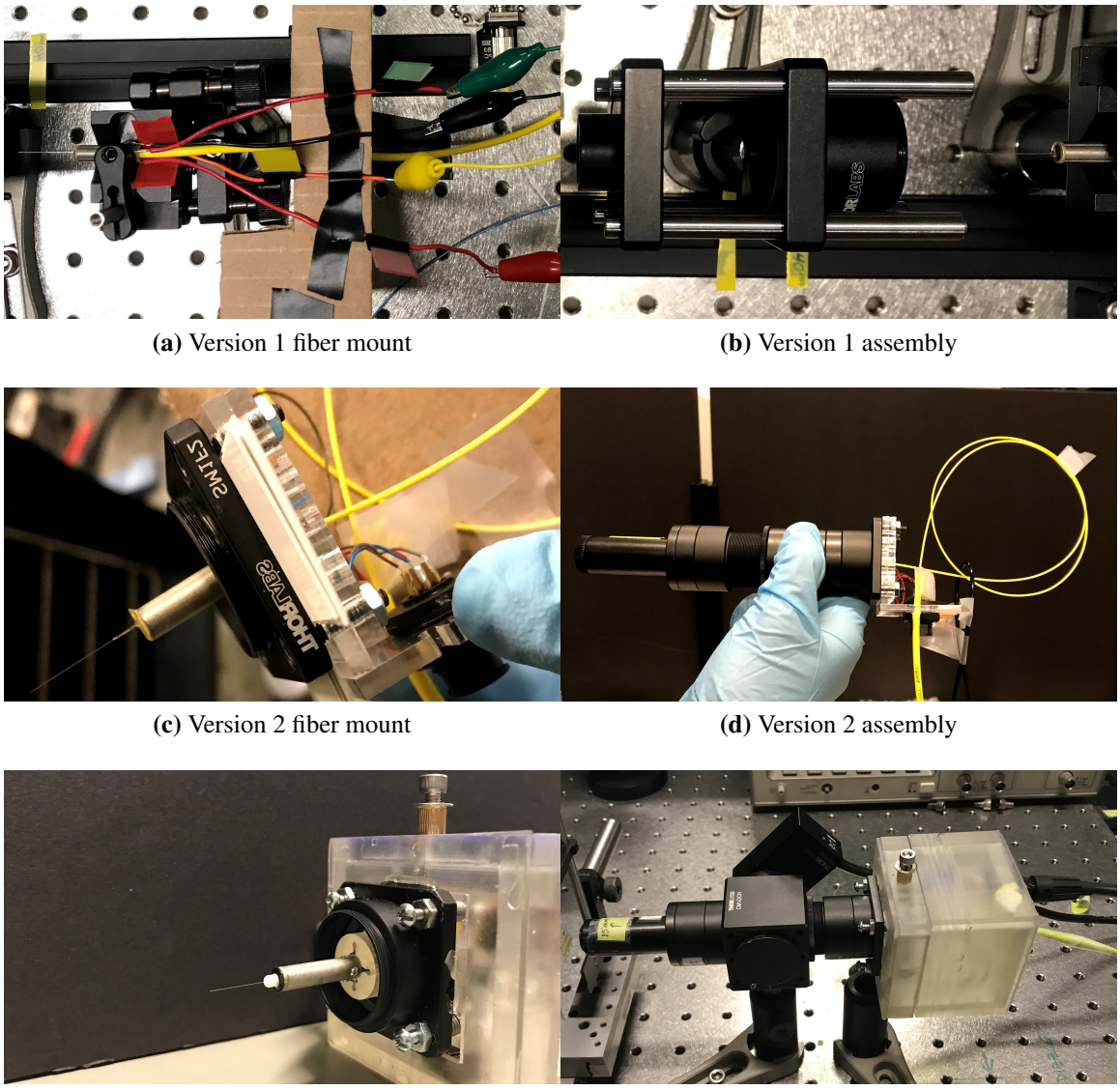

(a) Version 1 fiber mount

(b) Version 1 assembly

(c) Version 2 fiber mount

(d) Version 2 assembly

(e) Version 3 fiber mount

(f) Version 3 assembly

Figure 3.6: Various fiber scanner constructions and fiber mounting mechanisms.

with an internal diameter of $\sim$3.7 mm and the fiber optic has an outer diameter of 2.5 mm. This leaves a gap of about 1.2 mm between the fiber optic and internal wall of the piezotube where the fiber optic needs to be securely fastened. Poor fastening can cause increased dampening of the fiber optic cantilever (meaning a smaller scan range/field-of-view) and a transfer of downstream fiber optic motion to the cantilever (which would add unwanted distortions to the scan pattern). Finally, in the event that the fiber optic breaks, it would be ideal for the fiber to be able to be replaced without having to also replace the piezotube.

Figure 3.7 shows a visual of the various mounting approaches taken. In version 1 of the scanner (created by previous graduate student Erkang Wang), the optic fiber was UV glued into the piezotube. He centered the fiber by eye and then used UV light to cure the glue. Several problems arise with this approach: first the room for variation in the distribution of UV glue make it a difficult process to repeat. Second, the concentricity of the fiber within the piezotube is not precise since it is centered visually. Thirdly, if the fiber were to break in this setup the entire piezotube would need to be replaced; ideally our setup would allow for the fiber to be re-cleaved and mounted without discarding components were it to break.

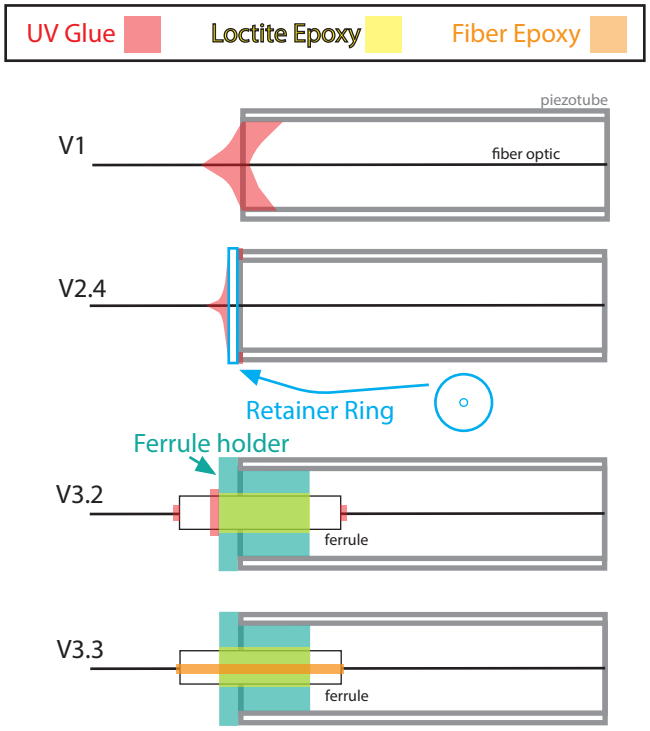

Figure 3.7: Different methods of fiber gluing explored

Version 2 iterated on this design with the addition of a thin acrylic alignment ring (row 2). This ring sat on top of the end lip of the piezotube and the fiber passed through the center hole, however since the acrylic ring sits outside of the piezotube it still needs to be visually centered. Additionally, this design would still require a piezotube replacement in the event of fiber breakage.

Version 3 utilized a two part assembly: a plastic bushing and an off-the-shelf fiber optic ferrule. I machined the plastic bushing (the ferrule holder) to slip fit *over* the Thorlabs ferrule (CF128) and *inside* of the piezotube (see Figure 3.8). The lip on the ferrule holder acts as a stopper on the edge of the piezotube. This mounting style better secures the fiber inside of the ferrule and creates a stronger cantilever base. The buffer holder (a 1" long plastic tube) acts as a stabilizer to rigidly hold the fiber optic seated inside additional furcation tubing (buffer) right after it exits the backside

of the piezotube. This helps keep the fiber and piezotube concentric and reduces the chance of angular strain at the backside of the ferrule.

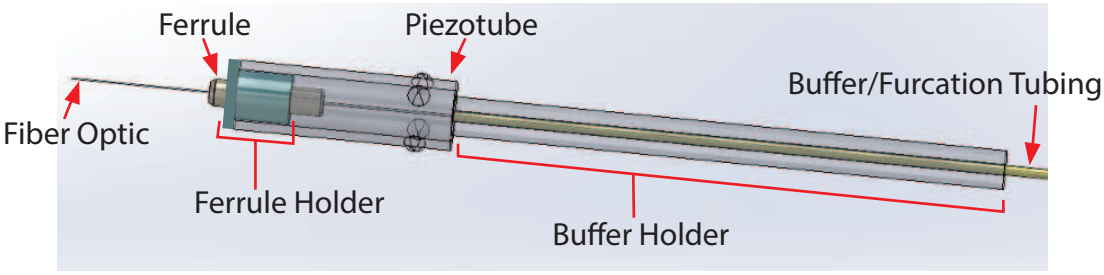

Figure 3.8: Fiber mount assembly V3.3: the optical fiber is glued to the inside of a Thorlabs ferrule which press-fits inside of a machined plastic ferrule holder. The external diameter of the ferrule holder matches the internal diameter of the piezotube with a lip added to secure the holder in place. A machined buffer holder backs up to the end of the piezotube to reduce strain on the fiber optic.

For Version 3.2 Loctite epoxy EA E-00CL was used to glue the bushing to the inside of the piezotube and UV glue was used to anchor the ferrule to the bushing and the fiber to the ferrule (row 3, Figure 3.7). In this setup if the fiber breaks, the ferrule can be removed from the bushing by carefully chipping away the UV glue holding the ferrule to the bushing. Then the fiber can be mounted into a new ferrule and re-cleaved before the ferrule is reattached to the bushing; this task can be cumbersome though. In Version 3.3, Loctite epoxy was still used to anchor the bushing into the piezotube, but a Thorlabs fiber connector epoxy F120 was used to secure the fiber optic inside of the ferrule instead of the UV glue (row 4, Figure 3.7). Additionally no glue was used to attach the ferrule to the bushing, and the press fit is the only force securing the two together. This design addresses issues of concentricity with machined precision, provides a stable cantilever base for the optical fiber, and allows the assembly to be re-used even if the fiber breaks.

3.2.2 Housing

The housing structure encloses the fiber optic/actuator assembly and the relay lenses. The design requirements for the housing included a full, portable enclosure (i.e. so the scanner can

be handheld) and a cost-effective repeatable design. The first scanner version did not include any form of enclosure; the parts were simply attached to the optics bench independently.

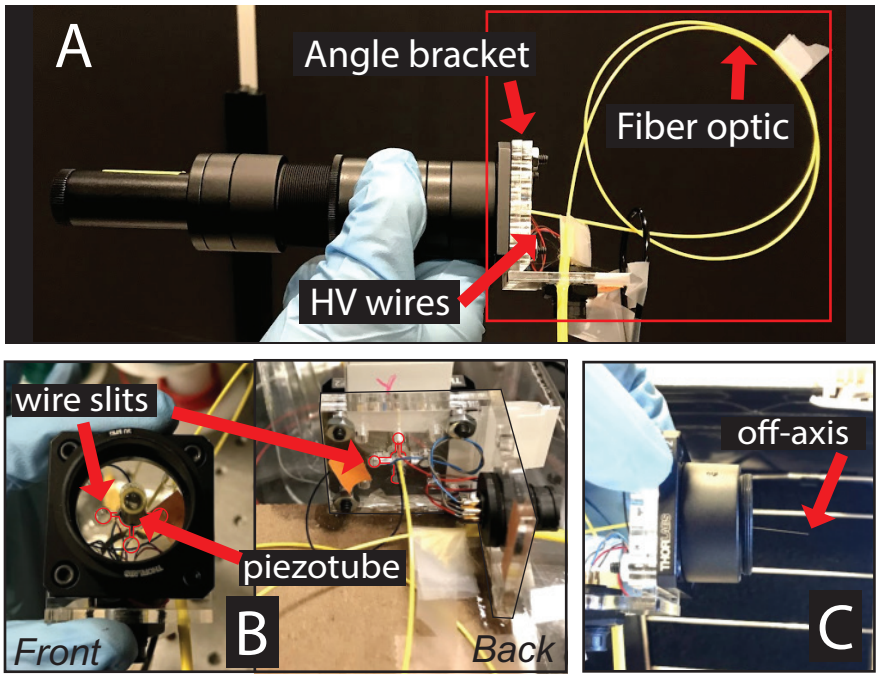

Figure 3.9: (A) photograph of the V2 scanner. An acrylic angle bracket was used to anchor the piezotube inside of the lens tubing. (B) slits cut into the acrylic allowed the high voltage (HV) wires to feed through and connect to an adapter on the opposite side of acrylic. Note the back of the angle bracket is exposed. (C) The lack of tip/tilt and lateral/vertical shift control in this version meant that if the piezotube was not seated perfectly then the fiber optic could extend off-axis to the lens tubing.

Version 2 included mounting the relay lenses inside of lens tubing and the addition of an acrylic angle bracket (courtesy of the 2020 senior design team) was installed to help with cable management for the high voltage supply to the piezotube and the fiber optic cable. Figure 3.9 (A) shows the acrylic angle bracket attached to the lens tubing and the connected fiber optic cable. The angle bracket included a depression to anchor the piezotube, however securing the piezotube so that both the tube and the fiber optic were concentric to the lens tubing was a challenge. Figure 3.9 (C) shows an example of the impact when the piezotube was not seated properly in the angle bracket. Off-axis fiber tilt could be severe with respect to the center axis of the lens tube due to the lack of tip/tilt and lateral/vertical shift control in this design. Additionally, this design did not include an

enclosure for the wire connections that provide the high voltage connection to the piezotube and the fiber optic cable experienced strain with how it was held by the angle bracket. Figure 3.9 (B) shows the front and back sides of the angle bracket where slits cut into the acrylic feed through the high voltage (HV) wires that control the piezotube. Note that the backside of the angle bracket is exposed.

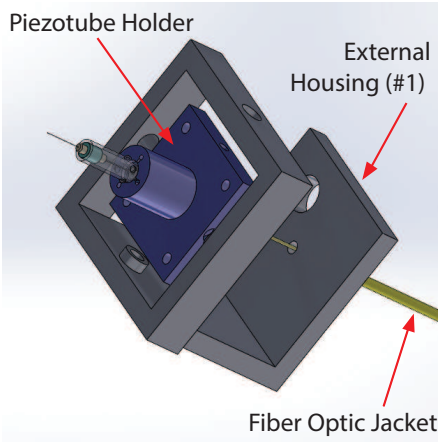

Figure 3.10: Version 3 housing changes: the piezotube was mounted into a holder with a deeper depression to seat the piezotube. The high voltage wires feed through slots next to the tube. The piezotube holder is mounted inside the first piece of a two-part external housing setup.

In version 3, the backside of the piezotube has a snug fit into the piezotube holder with slots cut so that the piezotube wires can feed through (see Figure 3.10). The buffer holder is also held in place by the piezotube holder. In order to address issues of fiber tilt once mounted into the ferrule & piezotube, a spring and screw-based tilt system was created between the interface of the piezotube holder and the Thorlabs 1" flange to lens adapter. Additional external screw holes allow for slight lateral and vertical adjustment of the fiber axis relative to the center axis of the lens tubes attached to the 1" flange to lens adapter (see Figure 3.11).

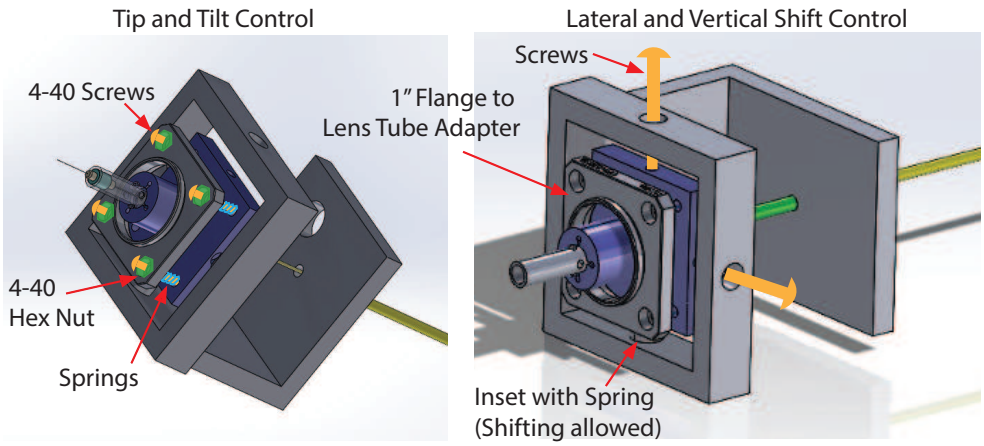

Figure 3.11: Addition of alignment control to the V3.3 housing design; tension screws were added to the four corners connecting the 1" flange to lens tube adapter to the piezotube holder providing tip and tilt control of the fiber optic with respect to the center axis of the lens tubing. A vertical and horizontal screw and spring pair additionally provided slight lateral and vertical shift control of the fiber optic.

This final housing design fully enclosed the fiber mount/actuator assembly with adjustment capability for aligning the piezotube and fiber optic down the center axis of the lens tubing. Additionally an external housing provided cable management for the high voltage wires and reduced strain on the fiber optic cable feeding into the piezotube. This setup is not attached to the optical breadboard and can be picked up. Finally, many components of this design were 3D printed (included the external housing and piezotube holder) or machined in the machine shop (plastic bushing and buffer holder) and the tip/tilt and lateral/vertical shift control was incorporated with simple screw and spring assemblies thus driving down overall design costs. Figure 3.12 shows photographs taken during the construction of V3.3. See the appendix page 178 for a build tutorial.

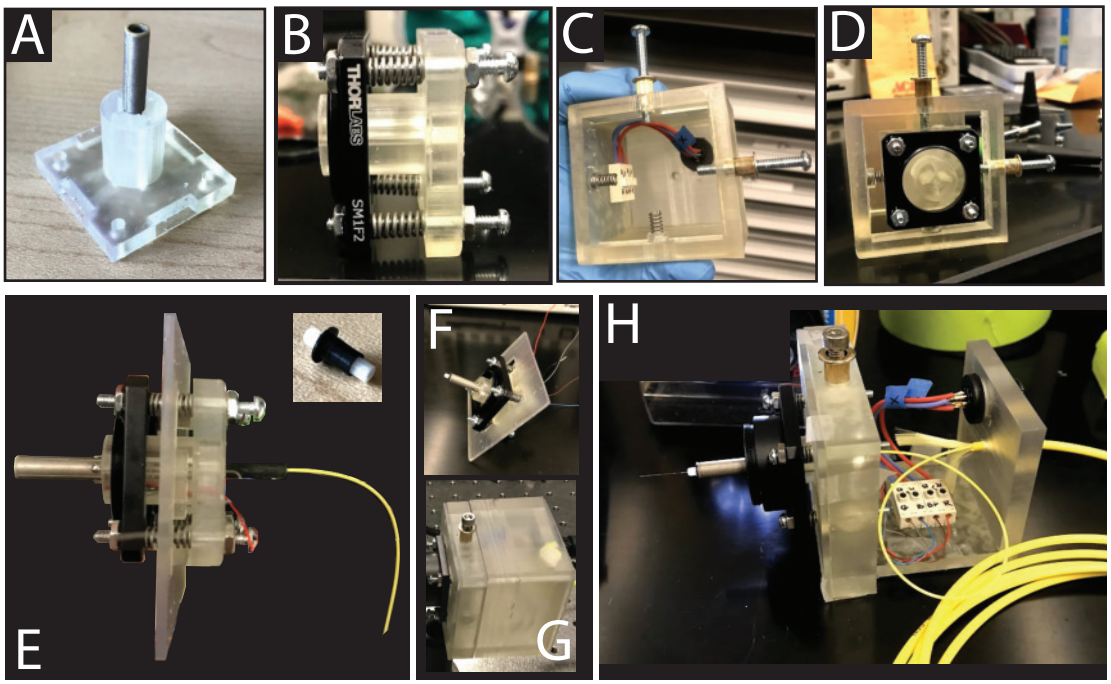

Figure 3.12: Housing build for V3.3. (A) the piezotube seated into the 3D printed piezotube holder. (B) the tip/tilt control setup between the piezotube holder and the 1" flange-to-lens tube adapter. (C) the inside of the external housing #1; screw and spring pairs for lateral/vertical shift are shown and poke-home connectors attached to high-voltage connections from the HV adapter are shown. (D) mounting of the piezotube holder into the external housing #1. (E) A side view of the piezotube holder, piezotube, tip/tilt control, and the buffer holder to fiber optic cable extending out of the back. The inset shows the Thorlabs ferrule seated inside the machined ferrule holder. (F) The ferrule/ferrule holder mounted into the end of the piezotube. (G) The two external housing pieces (#1, #2) combine to create a full enclosure. (H) The final housing assembly before adding relay lenses/tubing, the PSD, and external housing #2.

3.2.3 Major Design Changes and Observations

One major design change that occurred between versions 2 and 3 was the incorporation of a position sensitive detector (PSD) for continuous beam tracking. The initial plan for reconstructing an image with the version 2 fiber scanner was to utilize the PSD at the focal plane to capture an initial calibration scan pattern for post-processing image reconstruction. Early on it was observed that the actual fiber scanning trajectory deviated from the theoretical scan pattern. Incorporation of the PSD in version 3 meant that any changes in the scan pattern between images would be captured whether due to mechanical nonlinearities or noise.

Additional observations found that laser feedback from back-reflections at fiber-to-fiber connections when the diode was run at full power was contributing noise to the measured signal. The specifications for the laser diode (Thorlabs LPS-785-FC) place the the working drive current around 50 mA. However, a measured current vs output power curve for our laser diode unit (see Figure 3.13) found that 1) we had a measured maximum driving current of $\sim$47 mA before we hit the maximum output power of 10mW (less than the specifications) and 2) that reducing the driving current even more (down to $\sim$39 mA with an output power of $\sim$7 mW) was found to minimize the effects of back-reflections but at the expense of reducing the overall system power. With an optical loss of 83.8% this leaves only $\sim$1.13 mW to be measured at the focus for an input power of 7 mW; for a reflective sample like the resolution card enough light is reflected back to the detector to measure a signal. However, if the sample is scattering, the measured signal is not strong enough to surpass the noise floor. For a future version the installation of polarization maintaining fibers would change the fiber connections from FC to APC to help reduce back-reflections at fiber-to-fiber connections. It would also allow a polarization maintaining beamsplitter to be used which only splits the light on the return path, not both the outgoing and returning paths as the current beam splitter does. Polishing the fiber optic tip to an angle of 8 degrees [20] would also help reduce back-reflections. Additionally, a higher NA imaging system could be used to increase the collection efficiency, or an isolator could be added after the laser diode output to prevent back-reflections. Finally, a higher powered laser diode could be purchased; our diode has a specified output power of 10mW, however Thorlabs creates laser diodes that would work with our driver at output powers of 20mW (LP785-SF20) and laser diodes with powers up to 100mW (LP785-SF100), though these might require a different TEC and driver (CLD1011LP).

A final observation of version 3.3 was that when the fiber optic cable outside of the external housing experienced motion (but no voltage was applied to the piezotube), the PSD detected motion. Physically, it is highly unlikely that the fiber optic cantilever is actually moving (it is adhered to the inside of the 10 mm long ferrule and downstream motion should be decoupled). However, it is hypothesized that polarization-dependent bending loss in the optical fiber could be causing the

Figure 3.13: Measured current vs. output power curve for laser diode unit LPS-785-FC (Thorlabs).

false motion recorded on the PSD. A glass coverslip is used to direct $\sim 4\%$ of the laser to a position sensitive detector (PSD) for recording the laser position. A front and back surface reflection on the coverslip results in two points of light being focused onto the PSD and the PSD measures the centroid of these two back-reflections to determine position. If polarization-dependent bending loss occurs in the fiber optic cable when it is jostled it could cause the intensity of the polarization-dependent back-reflections to change ultimately shifting the centroid measured by the PSD. Thus, motion is detected by the PSD even when the fiber is stationary. This issue needs to be addressed before the system can be handheld; in the future, the use of polarization maintaining fibers should be able to mitigate this effect.

3.3 Characterization

The characterization procedure developed for the various version of fiber scanners built included evaluation of the cantilever resonant frequency response, an optimal selection of driving frequencies, measurement of the transformation matrices to compensate for misalignment between the cantilever eigenaxes fo the fiber and piezotube, and of optical resolution. Each of these factors is fully dependent on the fiber type, fiber length, and model-to-model variations in the epoxying and mounting of the fiber to the piezotube.

3.3.1 Resolution

We performed a "knife edge" measurement [6][7][8] utilizing the reflected intensity in order to determine the lateral resolution. The fit Gaussian complementary error function is shown in Figure 3.14, where the fit beam radius is $\mathrm{w}_0 = 4.23\mu$m leading to a FWHM of 4.98μm.

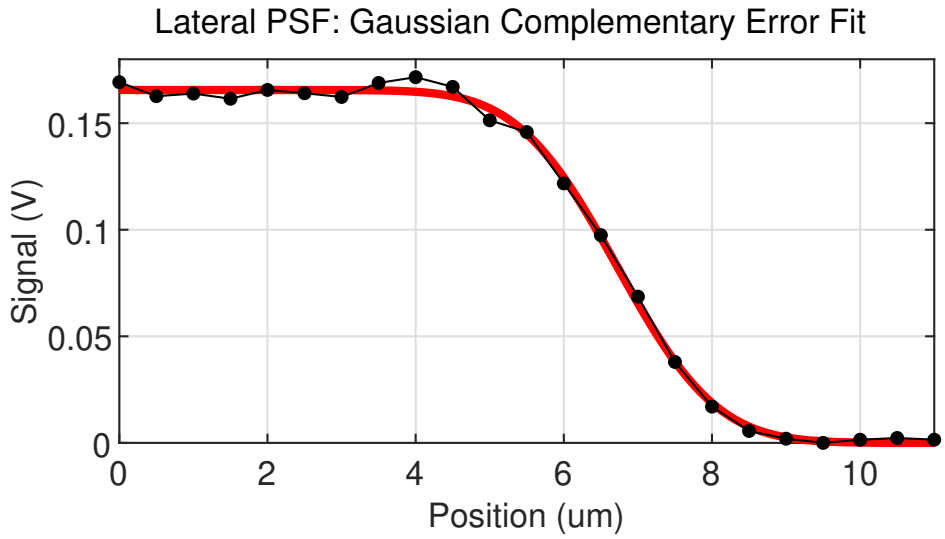

Figure 3.14: The measured knife-edge response resulting from a lateral translation of a sharp edge across a static beam path. Within a confidence interval of 95% the lower and upper estimates for w_0 are 3.87 μm and 4.59 μm, respectively, with an R^2 value of 0.998 for the estimate of $\mathrm{w}_0 = 4.23\mu$m.

The specified mode field diameter (MFD) of the fiber at 850nm is 5 ± 0.5 μm, which after de-magnification by L1 and L2 estimates a FWHM of 1.47 μm at the focal plane. Our relay optics encompass a simple 4-f configuration utilizing a 1" diameter, uncoated, f=30mm, plano-convex lens and a 1/2" diameter, uncoated, f=15mm, plano-convex lens.

From a beam radius of $\mathrm{w}_0 = 4.23$ μm we expect a Rayleigh range of $z_r = (\mathrm{w}_0^2 \pi \mathrm{n})/\lambda = 71.6$ μm, which is within the 95% confidence interval of our measured Rayleigh range. The data collected for the axial PSF measurement revealed a primary lobe with two smaller side lobes, indicative of spherical aberration [21][22], which is to be expected in the absence of corrective optics. In order to estimate the axial resolution we only fit the primary lobe in Figure 3.15, revealing a Rayleigh range of $z_R = 80.61$ μm and an axial resolution of $b = 2z_R = 161.2$ μm.

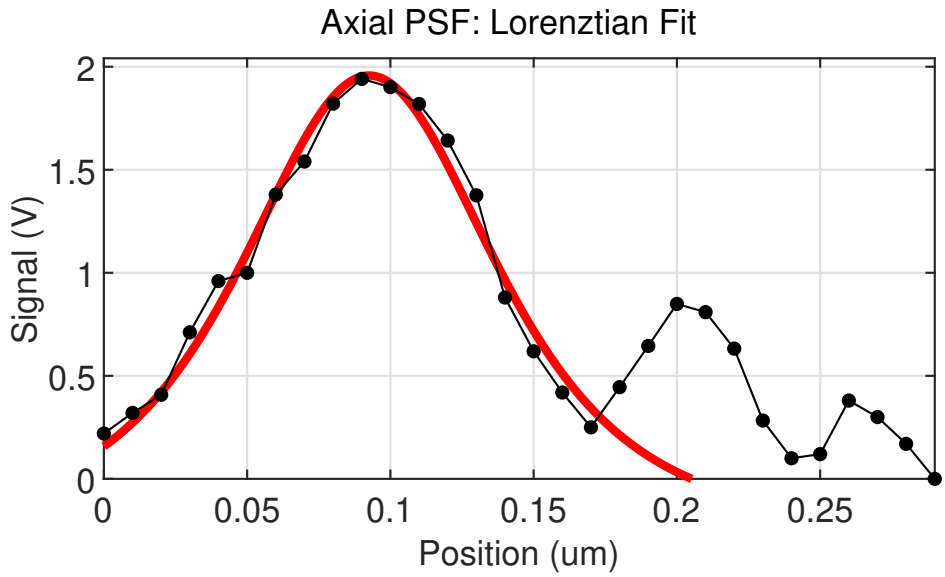

Figure 3.15: The measured axial point spread function; reflected signal was measured against position as a planar reflective target was swept through the focus. Within a confidence interval of 95%, the Rayleigh range minimum and maximum estimates are 64.9 μm and 96.2 μm, respectively, and the R^2 value for the estimate of $z_R = 80.61$ μm is 0.9807.

Our measured lateral resolution is about 2.9X the theoretical resolution of the system. We conjecture that our resolution could be improved if we increased the beam size to fill the back-aperture of the second lens (currently we are filling $\sim$62%), swapped our plano-convex lenses for aspheres, altered the tube length of the second lens or added a corrective lens [23]. The NA of the fiber and the focal length of the first lens set the beam diameter incident upon the second lens, thus with a higher NA fiber or a longer focal lens first lens we could increase the amount of coverage on the back-aperture of the second lens [10].

To see a protocol for acquiring the lateral and axial point spread function data, see page 171 and the associated code in [24].

3.3.2 Frequency Response

When driven on a single axis, the fiber tip (illuminated spot on the PSD) typically traces an ellipse oriented on some diagonal, indicating a cross-coupling between the response axes of the fiber versus the driving axis of the piezotube. Note the X-Y coordinate system of the PSD is not aligned with the piezo tube, which accounts for part of the angle of the diagonal. With no cross-

coupling the trace would be a straight line at an angle that is the relative orientation of the PSD and piezo tube. The magnitude of the response is measured as the diagonal length of the bounding box of the ellipse as shown in Figure 3.16, i.e. $R = \sqrt{\Delta X^2 + \Delta Y^2}$ where $(\Delta X, \Delta Y)$ is the peak-to-peak response on each PSD axis.

The first-order resonant frequency of the fiber is a function of the fiber cantilever length, thickness and material (see [9] for the equation). The cantilever length is 11.5mm long where the free end of the fiber extends beyond the end of the ferrule.

To determine the mechanical response of the fiber we perform independent sweeps of driving frequency along the X and Y axes (as defined by the quadrants of the piezotube) for nine different driving voltages, acquiring one second of data at each frequency in 0.5Hz steps. For this measurement, the PSD was mounted at the focal plane of lens L2, rather than L3, to directly measure beam displacement.

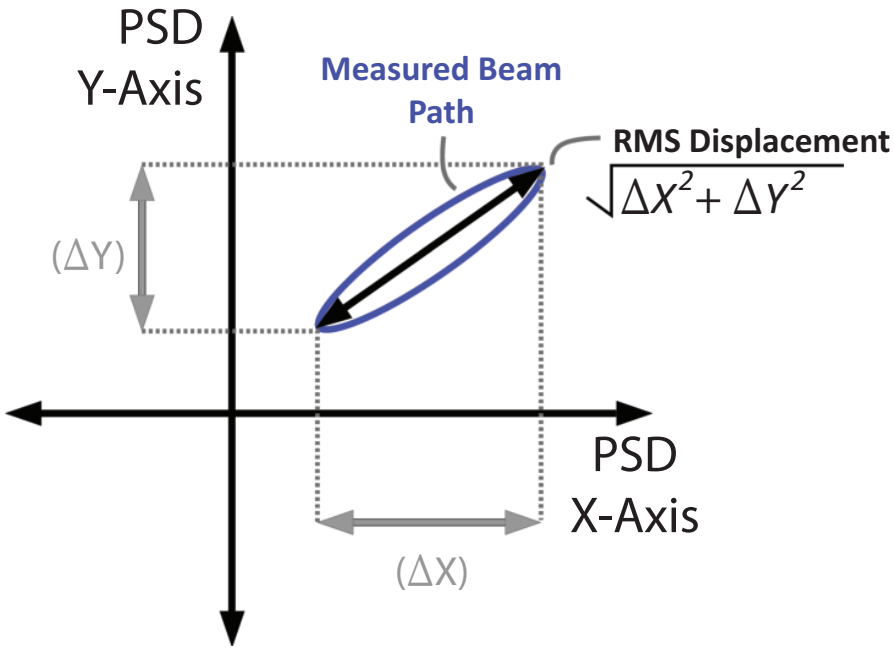

Figure 3.16: Computing the magnitude of the frequency response vector, R, from the independently measured X and Y beam positions on the position sensitive detector.

Frequency response measurements are shown in Figure 3.17; one for driving the X-axis and one for driving the Y-Axis of the piezotube. We show the measured voltage-dependent frequency

response of the fiber by plotting fiber displacement responses versus driving frequency. The resonant frequency for both drive axes hovers around 805Hz, however, it is interesting to note that with increasing drive voltage there is a slight blue shift of the resonant frequency (see the inset of Fig 3.17). This could be due to a nonlinear "hardening" spring effect such as increasing centripetal acceleration with increasing drive voltage[15]. We also report that with higher drive voltages, the path the fiber traces is more circular, indicating more cross-coupling.

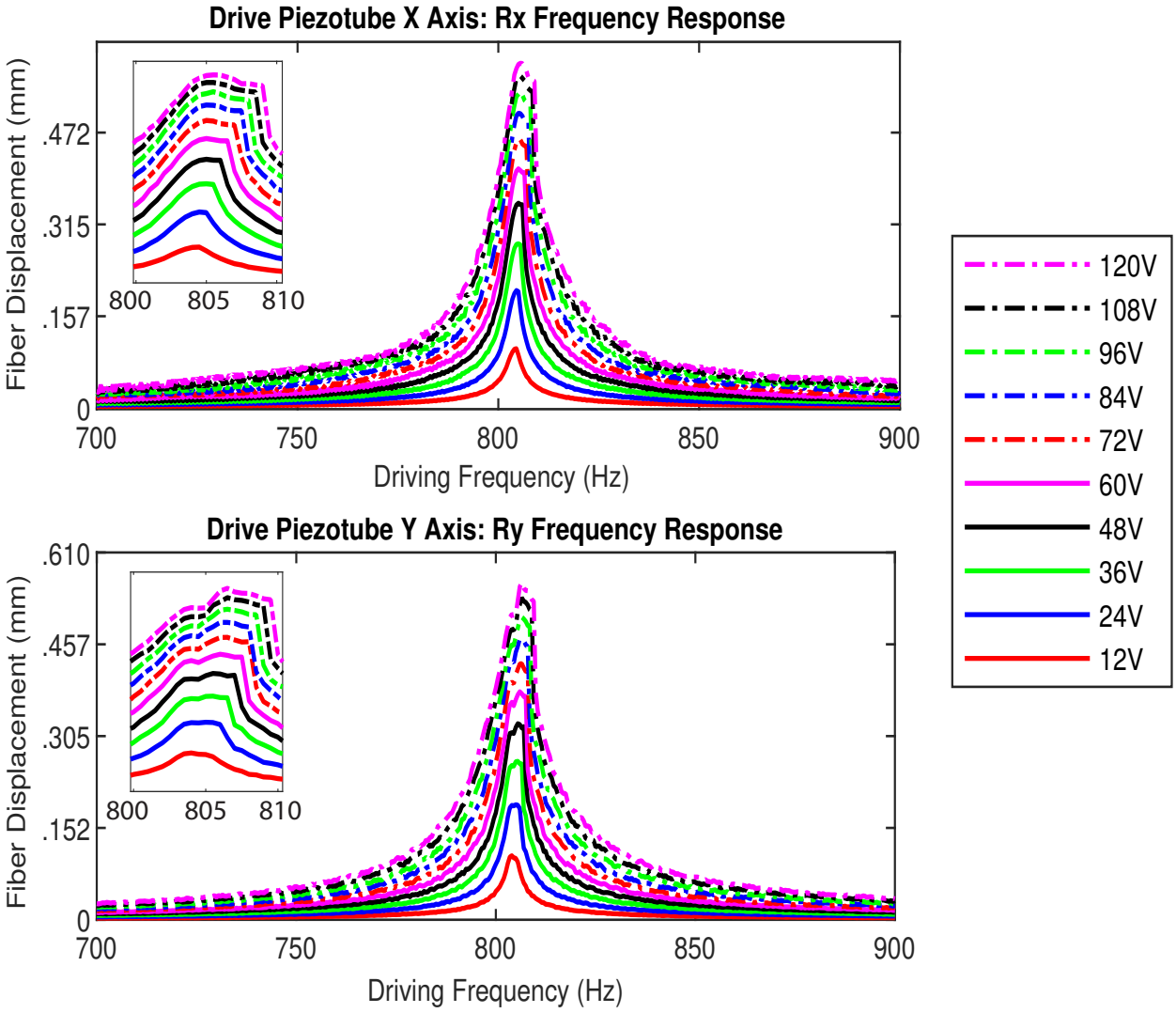

Figure 3.17: Voltage-dependent frequency response of the cantilevered optical fiber when driven only along the X axis of the piezotube (top figure) and the Y axis of the piezotube (bottom figure). The legend denotes the voltage applied to the electrode contacts of the piezotube; the larger the applied voltage the larger the peak fiber displacement. *Inset:* With increasing voltage we see increasing non-linearities and distortions, and a shift in the peak resonant frequency from a lower to higher frequency. This shift is on the order of 2Hz over a voltage range of 12V to 120V.

A protocol for measuring the frequency response can be found on page 172.

3.3.3 Selecting Driving Frequencies

We follow the method outlined by [25] to select semi-resonant driving frequencies that best manage frame rate and field of view. Typically, in Lissajous scanning the frame rate is defined as the pattern repeat time and is equal to the greatest common factor between the two driving frequencies. In a semi-resonant regime, the greater the frequency separation of the driving frequencies, the higher the frame rate. However, this places the two frequencies at a lower amplitude on the resonant curve, resulting in a smaller FOV for the same drive voltage.

As an example, our chosen frequency pair falls within 10% of the peak resonant displacement, while the best frequency pair at twice the frame rate is less than 50% of the peak resonant displacement at a drive voltage of 60V. The second row of Table 3.1 shows the fiber displacement tradeoffs for a frequency pair at 3 fps and 6 fps.

Table 3.1: Fiber Displacement vs Frame Rate Tradeoffs

	3 Frames/s	6 Frames/s
Frequency Pair (X,Y)	804 Hz, 807 Hz	810 Hz, 798 Hz
Fiber Displacement (60V)	397μm, 370μm	187μm, 172μm
Smallest FOV (6V)	0.183 mm^2	0.006 mm^2
Largest FOV (90V)	1.385 mm^2	0.409 mm^2

If we compare this frequency pair at the smallest and largest usable driving voltages (shown in the third and fourth rows of Table 3.1), we approximately find a $30\times$ increase in the area covered at lower driving voltages and about a $3.4\times$ increase in maximum area imaged when the fiber is driven at 3 fps instead of 6 fps. These are important tradeoffs to be aware of when selecting frequency

pairs. The remaining results presented in this paper will be data collected from the fiber scanner at 3 fps (frequencies 804Hz and 807Hz) to provide the larger field of view.

A protocol for selecting driving frequencies can be found on page 172.

3.3.4 Eigen Transformations

As illustrated in Figure 3.18, mismatch between the piezotube drive axes and the mechanical cantilever eigenaxes of the fiber, result in mechanical cross-couplings ("whirling"), or elliptical motion of the fiber tip when a linear driving force is applied [9][13][17] [26]. Such cross-coupling occurs with small deviations from concentricity in the draw of the fiber resulting in ovularity, as well as possible asymmetries in stiffness at the cantilever base due to uneven gluing. This results in eigenaxes of the fiber that are not exactly perpendicular, paired with overlapping resonant frequency curves that can result in a non-zero response along the axis orthogonal to the driving axis.

This undesired motion can be corrected by rotating the applied driving waveforms to match the cantilever eigenaxes of the fiber at angles θ_A and θ_B.

The transformations occurring from the driving of our piezotube to our reconstructed image are:

$$\begin{bmatrix} \cos(\theta_A) & -\sin(\theta_A) \\ \sin(\theta_A) & \cos(\theta_A) \end{bmatrix} \begin{bmatrix} X \\ 0 \end{bmatrix} = \begin{bmatrix} X_x^{'} \\ X_y^{'} \end{bmatrix} \tag{3.12}$$

$$\begin{bmatrix} \cos(\theta_B) & -\sin(\theta_B) \\ \sin(\theta_B) & \cos(\theta_B) \end{bmatrix} \begin{bmatrix} 0 \\ Y \end{bmatrix} = \begin{bmatrix} Y_x^{'} \\ Y_y^{'} \end{bmatrix} \tag{3.13}$$

$$\begin{aligned} X' &= X_x^{'} + Y_x^{'} \\ Y' &= X_y^{'} + Y_y^{'} \end{aligned} \tag{3.14}$$

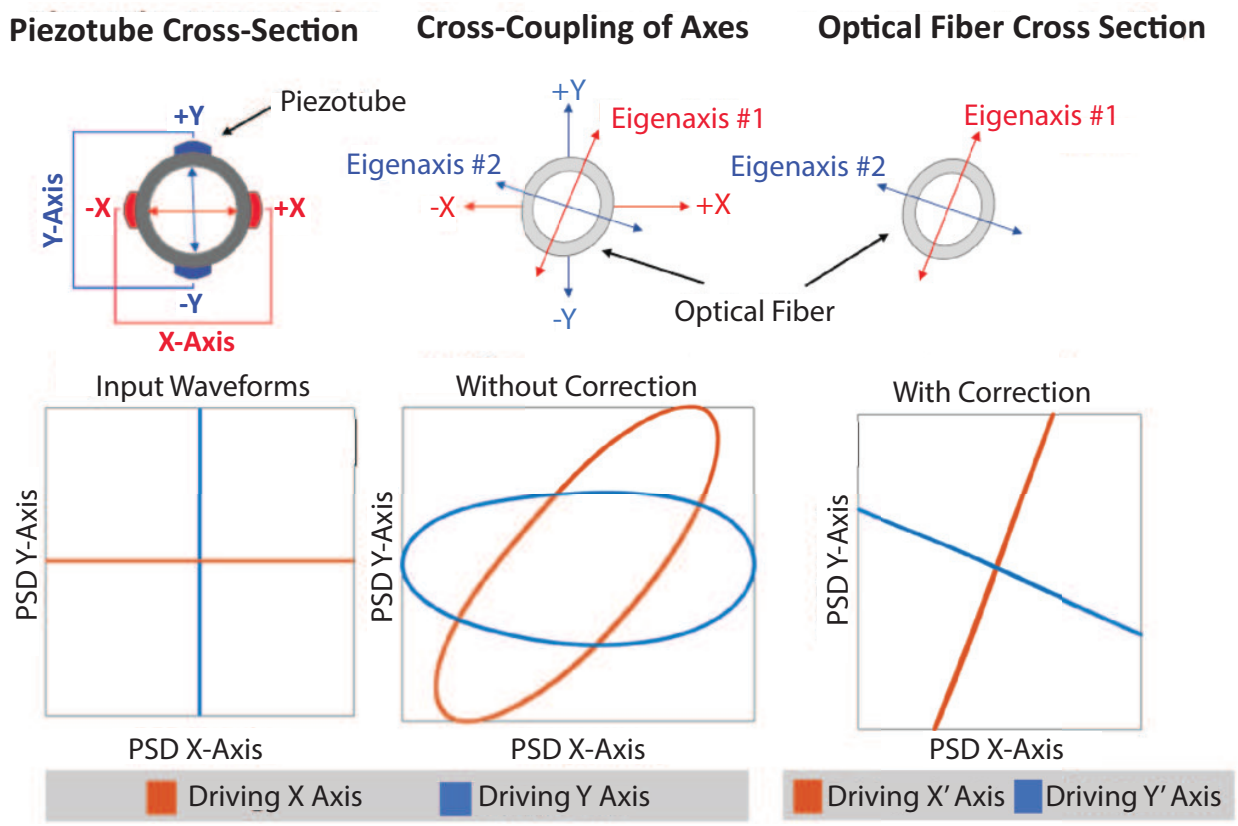

Figure 3.18: Patterns traced by the optical fiber in an ideal situation (left) when driven only along the X piezotube axis (red) or Y piezotube axis (blue), the actual measured beam path (center), and the final measured beam path after correcting for an orientation and angle mismatch between the driving axes of the piezotube and the response axes of the fiber (right).

Here X and Y are the input driving waveforms to the piezotube where $X = A_x cos(2\pi 268(3)t)$ and $Y = A_y cos(2\pi 269(3)t + \frac{2\pi}{4(268)})$ and A_x, A_y are the corresponding input voltage amplitudes. θ_A is the rotation angle from the X coordinate axis of the piezotube to the first eigenaxis of the fiber, and θ_B is the angle from the X axis to the second eigenaxis.

The driving waveforms sent to the piezotube are precompensated by these matrices so that the actual trajectory traced out by the fiber tip is (X', Y').

Shown in (3.15), we apply an additional transformation matrix to the acquired data on the PSD, which simply rotates the field of view to squarely match the plotting window.

$$\begin{bmatrix} \cos(\psi) & -\sin(\psi) \\ \sin(\psi) & \cos(\psi) \end{bmatrix} \begin{bmatrix} X' \\ Y' \end{bmatrix} = \begin{bmatrix} X_{\text{MEASURED}} \\ Y_{\text{MEASURED}} \end{bmatrix} \tag{3.15}$$

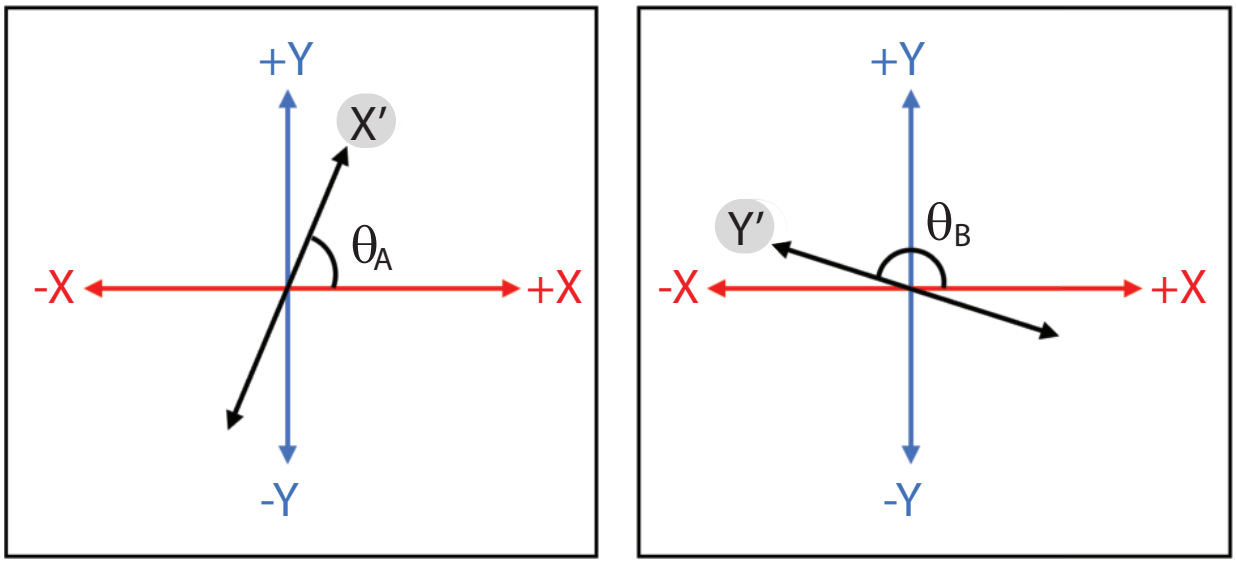

Figure 3.19: Angles between the piezotube axes and fiber response axes.

3.4 Calibration

3.4.1 Finding Eigenaxes

We measure θ_A and θ_B in Figure 3.19 by placing the position sensitive detector at the sample plane of the microscope and sending out a single driving waveform that is rotated through 180 degrees, recording the data off of the PSD for 1 second at every angle. We are able to identify the two input rotation angles which minimize the cross-coupling seen at the sample plane. Cross-coupling presents itself as an ellipse traced by the fiber when driven by a waveform that should result in a straight line. By rotating this straight line *driving* waveform we can find the angle at which the fiber minimizes cross coupling and the ellipse traced by the fiber collapses down to a straight line. Computationally, we process all of this data using Matlab to plot a recorded fiber trace at each input rotation angle, compute the approximate major and minor axes lengths of a fitted ellipse, and then plot the axes length as a function of rotation angle. We have consistently found that the fiber mechanical eigenaxes are $\sim 81 - 88°$ apart. It should be noted that angle corresponding to the eigenaxis of the fiber is both amplitude and frequency dependent, the two eigenaxes measured at the X driving frequency and the two eigenaxes measured at the Y driving frequency can differ

by several degrees which necessitates a small compromise in the selected eigenangles to minimize cross coupling as much as possible along both axes. A slight amplitude dependence also exists so we decided to select the eigenangles corresponding to 60V. The measured values θ_A and θ_B are 63° and 151° for an input X and Y driving waveform on our scanner, respectively. Note, finding the accurate eigenaxes does severely impact the Lissajous scan pattern – without this step, the scan pattern is dominated by cross-coupling and the resulting beam path deviates significantly from a Lissajous. It does not however, affect the reconstructed data since we are able to continuously track the beam position with the position sensitive detector (PSD).

A protocol for measuring a fibers eigenaxes can be found on page 175.

3.4.2 Display Rotation

After determining the appropriate input drive rotations, we need to determine the angle ψ to rotate the image reconstructed using the position sensitive detector so that the image captured is oriented optimally inside of the matlab viewing window (lines up the edges). Then we apply a correction factor determined from imaging a ronchi-ruling of known lines per millimeter to convert the measured displacement measured on the PSD into the displacement of the fiber at the focal plane.

3.5 Scan Pattern Analysis

The Lissajous scan, like the raster and spiral scan, is a commonly employed bi-axial scan pattern used for point scanning techniques [27]. The selection of the scan pattern used with a point scanning microscope becomes an integrated decision which requires careful characterization of the constructed setup. Since our scanner utilizes a resonant mechanical process to actuate the optical fiber we are limited to utilizing either a Lissajous or spiral scan. A major pitfall of spiral scanning which prompts us to pursue Lissajous scanning instead is its high sampling density at the center of its FOV. This can result in photo-damage and photo-bleaching for live specimens [28, 29]. For the future of microscopes utilized for dermatological use we believe that Lissajous scan patterns are

better suited to the imaging of live cells due to their reduced likelihood of photo-damage. Despite this benefit though, a Lissajous scan does not provide homogeneous sampling over its field of view. Typically, the center of the scan is less densely sampled than the outer edges, which can cause reduced image quality in the center of the frame depending on how sparsely sampled the image is.

The incorporation of a PSD into our scanner design eliminates the need for any calibration procedures before the scanner can be utilized. This is in contrast to many designs that require repeated calibrations in order to link driving waveforms and focal-plane position to the point-scanned reflected intensity signal. A significant advantage of continuous beam tracking is the ability to operate our scanner at a range of driving voltages and with distorted mechanical responses, since we aren't limited to a repeatable scan pattern in order to know what location in the focal-plane we are imaging. As we will discuss in the next section, at higher driving voltages these distortions to the scan pattern could be used advantageously as they provide additional sampling coverage frame-to-frame that wouldn't be acquired with a repeated scan trajectory. On a single frame basis however, our iterative sparse reconstruction algorithm is able to extend the usable field of view despite distortions and address sparsity without having to sacrifice frame rate

3.5.1 Theoretical

Here we compare theoretical and measured Lissajous patterns, both with the selected driving frequencies of $f_x = 804$Hz, $f_y = 807$Hz, a 3Hz frame rate and sampled at 62500 samples per second. The driving waveforms have the form of

$$X = A_x \cos(2\pi n_x f_0 t) \tag{3.16}$$

$$Y = A_y \cos(2\pi n_y f_0 t + \frac{k\pi}{4n_x}) \tag{3.17}$$

Where $n_x = 268$, $n_y = 269$, $f_0 = 3Hz$, and $k = 2$. Figure 3.20 below shows the expected ideal scan pattern.

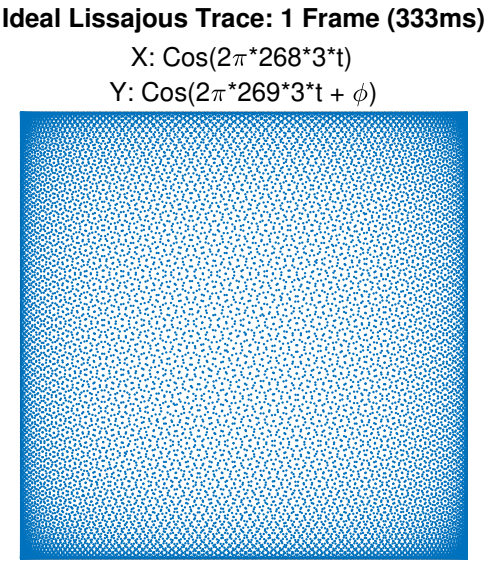

Figure 3.20: Ideal Lissajous scan patterns for a single frame.

3.5.2 Experimental

In practice we have identified that mechanical harmonics present in the fiber cantilever contribute to a distortion from rectangularity in our field of view, which increase with driving voltage. This distortion from an ideal scan or from a single calibration scan indicates the importance of having a real-time beam tracking capability for proper image reconstruction. We have also characterized how field of view and fill-factor with our setup change as a function of driving voltage.

Harmonic Distortion

Figure 3.21 shows the difference between two Lissajous traces; both driven with the same sinusoidal waveforms except that Ax,Ay = 6V for the top figure and Ax,Ay = 90V for the bottom figure. Each figure shows one frame of acquired data. With the larger driving amplitude we see a prominent increase in the harmonics present and more severe distortion from the ideal square field of view. The increased harmonic distortion with increased drive voltage is consistent with an underlying nonlinear cause.

In principle the harmonic distortions seen at higher driving voltages could be dampened by shortening the fiber length, however this would increase the drive frequency and decrease the FOV.

This trade-off is application dependent, for applications in dermatology a FOV >1mm is highly desirable.

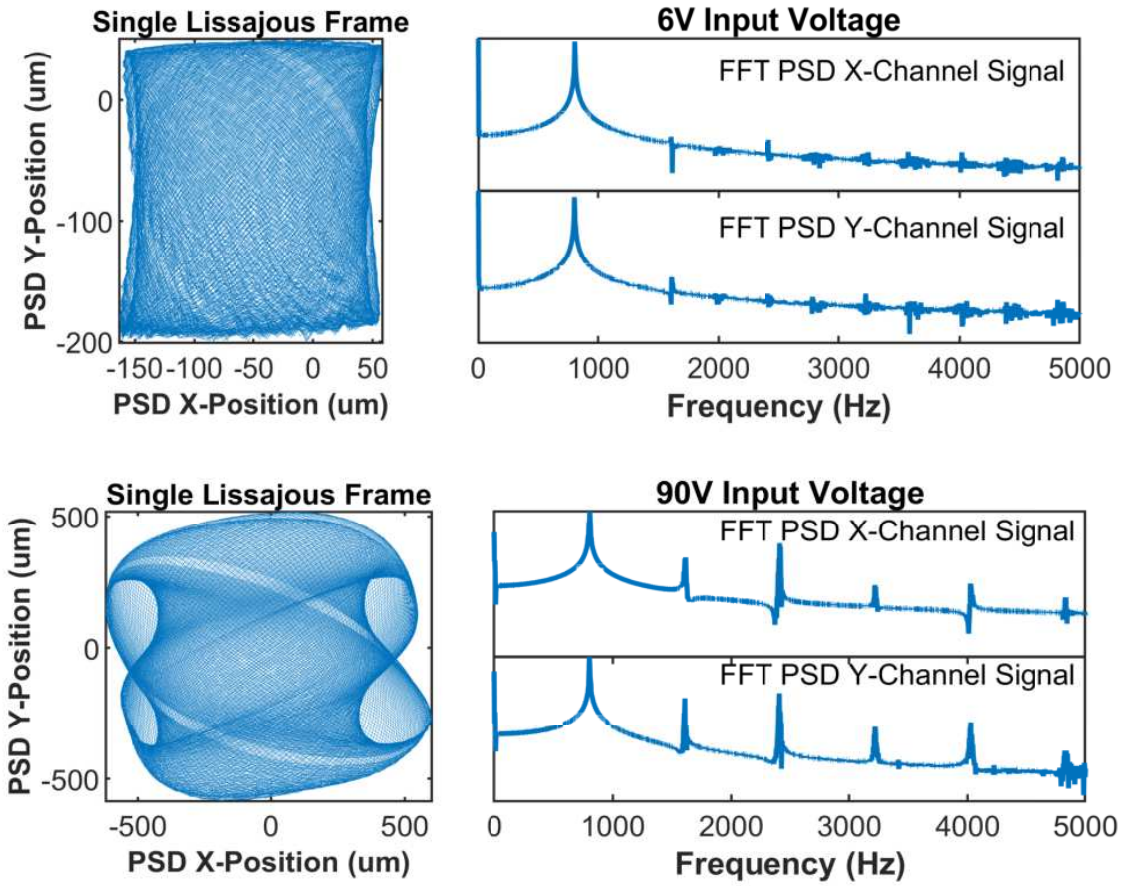

Figure 3.21: Mechanical harmonic distortion present in the measured Lissajous trace. The mechanical harmonics shown on the right side for the measured X and Y beam positions (log scale) increase in amplitude with increasing applied voltage resulting in more distortion (seen in the full Lissajous trace plotted on the left side for 6V and 90V).

3.6 Image Sampling Limitations

3.6.1 Fill-Factor

There is one fundamental limitation of the Lissajous scan when retaining a consistent frame rate: sparser sampling with an increased field of view. Due to the path that a Lissajous scan takes, this sparseness shows up in the center of the image, with higher sampling density around the edges

of the field of view. This poses an upper limit on the field of view that can be used at a particular frame rate and ADC sampling rate – a limit we can extend with the use of our reconstruction algorithm.

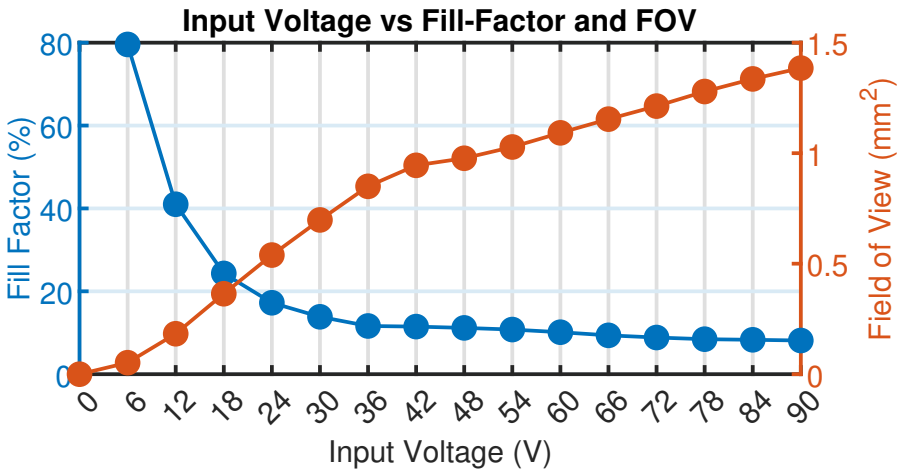

Figure 3.22: Fill-factor decreases with increasing drive voltage (blue line) at a constant frame rate and the field of view increases with increasing drive voltage (red line).

In the literature fill-factor has been used to describe two different methods of measure for sampling density *potential* of a Lissajous pattern; here we provide clarification. There is *line density* which [30] describes as "judged by the distance between two adjacent lines. . . in the center of the scan" which is a measure of resolution defined by the scan pattern. This is typically calculated from the ideal pattern that will be sent to the scanning electronics. Then there is *fill-factor* which is measured after an image is acquired and is dependent on the ratio of the lateral resolution to pixel size [30] and ADC sample rate. It can be measured as a percentage of sampled versus unsampled pixels for a given gridding [29] and highlights the sparsity of a given scan pattern after reconstruction. Here we utilize the definition for fill-factor provided by [29] and measure fill-factor as a function of input voltage.

In order to satisfy Nyquist it is required that we have two pixels per lateral PSF FWHM

$$w_{px} = \frac{\text{FWHM}}{2} = 2.49\mu m \tag{3.18}$$

where w_{px} is the largest pixel width we can utilize.

Figure 3.22 shows the experimentally-measured tradeoffs between field of view and fill-factor versus driving voltage. Ranging from 6V to 90V at 3fps, we found that we could achieve a field of view ranging from $0.183\ \mathrm{mm}^2$ to $1.385\ \mathrm{mm}^2$ over which sampling density decreased from 80% to 8%. Figure 3.23 shows the measured Lissajous patterns for several different driving voltages, where it is easier to see the increase in sparsity and impact of harmonic distortion on the scan pattern.

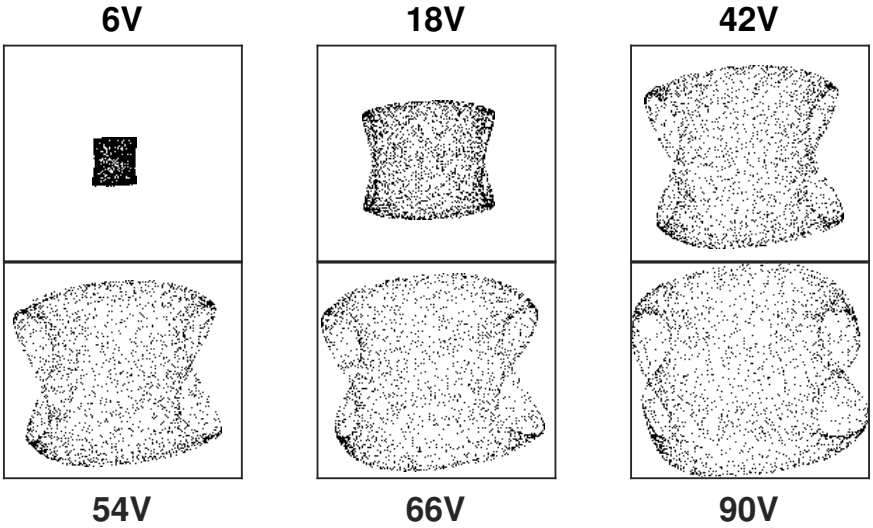

Figure 3.23: Sample Lissajous frames measured at increasing drive voltages. The black points show locations that are sampled in the field of view for a single frame. As drive voltage increases the sampling density becomes sparser (decreased fill-factor) and the field of view becomes larger and more distorted.

Chapter 4 presents some of the acquired image data for this scanner imaging a ronchi ruling reflective/transmissive target. The issues with sampling sparsity shown in this section are addressed with a custom inpainting algorithm coined Fast-Iterative Fourier Filtering Reconstruction (FIFFR).

Bibliography

[1] John P. Giannini, Andrew G. York, and Hari Shroff. Anticipating, measuring, and minimizing mems mirror scan error to improve laser scanning microscopy's speed and accuracy. *PLOS ONE*, 12(10):e0185849, Oct 2017.

[2] Jeanne L. McHale. *Molecular spectroscopy*. CRC Press, Boca Raton, 2nd ed edition, 2017.

[3] Justin Peatross and Michael Ware. *Physics of Light and Optics*. 2015 edition.

[4] R. Ulrich, S. C. Rashleigh, and W. Eickhoff. Bending-induced birefringence in single-mode fibers. *Optics Letters*, 5(6):273, June 1980.

[5] Robert H Webb. Confocal optical microscopy. *Reports on Progress in Physics*, 59(3):427–471, Mar 1996.

[6] Mario González-Cardel, Pedro Arguijo, and Rufino Díaz-Uribe. Gaussian beam radius measurement with a knife-edge: a polynomial approximation to the inverse error function. *Applied Optics*, 52(16):3849, 2013.

[7] John M. Khosrofian and Bruce A. Garetz. Measurement of a gaussian laser beam diameter through the direct inversion of knife-edge data. *Appl. Opt.*, 22(21):3406–3410, Nov 1983.

[8] G. Veshapidze, M. L. Trachy, M. H. Shah, and B. D. DePaola. Reducing the uncertainty in laser beam size measurement with a scanning edge method. *Appl. Opt.*, 45(32):8197–8199, Nov 2006.

[9] Mandeep Kaur, Pierre M. Lane, and Carlo Menon. Scanning and actuation techniques for cantilever-based fiber optic endoscopic scanners—a review. *Sensors*, 21(1), 2021.

[10] Hadi Mansoor, Haishan Zeng, Isabella T. Tai, Jianhua Zhao, and Mu Chiao. A handheld electromagnetically actuated fiber optic raster scanner for reflectance confocal imaging of

biological tissues. *IEEE Transactions on Biomedical Engineering*, 60(5):1431–1438, May 2013.

[11] Benno H. W. Hendriks, Walter C. J. Bierhoff, Jeroen J. L. Horikx, Adrien E. Desjardins, Cees A. Hezemans, Gert W. 't Hooft, Gerald W. Lucassen, and Nenad Mihajlovic. High-resolution resonant and nonresonant fiber-scanning confocal microscope. *Journal of Biomedical Optics*, 16(2):026007, 2011.

[12] William A. Hudson. Piezo ac driver project. https://github.com/wahudson/piezo_ac_drive, 2022. Accessed: 2022-10-07.

[13] I. L. Yeoh, P. G. Reinhall, M. C. Berg, and E. J. Seibel. Self-Contained Image Recalibration in a Scanning Fiber Endoscope Using Piezoelectric Sensing. *Journal of Medical Devices*, 9(1), 03 2015. 011004.

[14] Adam Harbi Shadfan, Michal Emanuel Pawlowski, and Tomasz S. Tkaczyk. Development of tunable miniature piezoelectric-based scanners validated by the combination of two scanners in a direct image relay technique. *Optical Engineering*, 55(01):1, January 2016.

[15] Quinn Y. J. Smithwick, Per G. Reinhall, Juris Vagners, and Eric J. Seibel. A Nonlinear State-Space Model of a Resonating Single Fiber Scanner for Tracking Control: Theory and Experiment. *Journal of Dynamic Systems, Measurement, and Control*, 126(1):88–101, March 2004.

[16] Miyase Tekpınar, Ramin Khayatzadeh, and Onur Ferhanoğlu. Multiple-pattern generating piezoelectric fiber scanner toward endoscopic applications. *Optical Engineering*, 58(2):1 – 6, 2019.

[17] Sucbei Moon, Sang-Won Lee, Marc Rubinstein, Brian J. Wong, and Zhongping Chen. Semi-resonant operation of a fiber-cantilever piezotube scanner for stable optical coherence tomography endoscope imaging. *Optics Express*, 18(20):21183–21197, 2010.

[18] Kartikeya Murari, Wenxuan Liang, Yuying Zhang, Jiefeng Xi, and Xingde Li. Lissajous scanning fiber-optic nonlinear endomicroscope with precise position calibration. *Biomedical Optics and 3-D Imaging*, 2012.

[19] Tong Wu, Zhihua Ding, Kai Wang, Minghui Chen, and Chuan Wang. Two-dimensional scanning realized by an asymmetry fiber cantilever driven by single piezo bender actuator for optical coherence tomography. *Optics Express*, 17(16):13819, August 2009.

[20] Pigtailed laser diodes, single mode fiber. https://www.thorlabs.com.

[21] Colin J. R. Sheppard, Min Gu, Keith Brain, and Hao Zhou. Influence of spherical aberration on axial imaging of confocal reflection microscopy. *Applied Optics*, 33(4):616, Feb 1994.

[22] C. J. R. Sheppard and Min Gu. Aberration compensation in confocal microscopy. *Applied Optics*, 30(25):3563, Sep 1991.

[23] Colin J. R. Sheppard, Min Gu, Keith Brain, and Hao Zhou. Influence of spherical aberration on axial imaging of confocal reflection microscopy. *Applied Optics*, 33(4):616, Feb 1994.

[24] cncoleal. Dissertation. https://github.com/cncoleal/Dissertation, 2023. Accessed: 2023-09-19.

[25] Junya Wang, Gaofei Zhang, and Zheng You. Design rules for dense and rapid lissajous scanning. *Microsystems & Nanoengineering*, 6(1):101, Dec 2020.

[26] Ramin Khayatzadeh, Onur Ferhanoğlu, and Fehmi Çivitci. Unwarped lissajous scanning with polarization maintaining fibers. *IEEE Photonics Technology Letters*, 29(19):1623–1626, 2017.

[27] Yik R. Teo, Yuen K. Yong, and Andrew J. Fleming. A review of scanning methods and control implications for scanning probe microscopy. In *2016 American Control Conference (ACC)*, pages 7377–7383, 2016.

[28] Kyungmin Hwang, Jae-Beon Kim, Yeong-Hyeon Seo, Jinhyo Ahn, Pilhan Kim, and Ki-Hun Jeong. Fully packaged video-rate confocal laser scanning endomicroscope using lissajous fiber scanner. In *2017 19th International Conference on Solid-State Sensors, Actuators and Microsystems (TRANSDUCERS)*, pages 143–146, 2017.

[29] Kyungmin Hwang, Yeong-Hyeon Seo, Jinhyo Ahn, Pilhan Kim, and Ki-Hun Jeong. Frequency selection rule for high definition and high frame rate lissajous scanning. *Scientific Reports*, 7(1):14075, Dec 2017.

[30] Weiqi Du, Gaofei Zhang, and Liangchen Ye. Image quality analysis and optical performance requirement for micromirror-based lissajous scanning displays. *Sensors*, 16(5), 2016.

Chapter 4

Sparse Inpainting with a Fast Iterative Fourier Filtering Algorithm

4.1 Summary

The scanner described in Chapter 3 suffered from a low DAQ sampling rate rendering images taken at larger fields-of-view very sparse. This prompted the construction of a computational solution able to supplement the sparsity problem with an inpainting approach. This section describes the outcome of this challenge: a fast iterative fourier-filtering reconstruction algorithm, coined FIFFR. Currently this algorithm is only adapted for use in post-processing but shows promise as a quick FFT-based inpainting solution for real-time processing in the future. Many different approaches to addressing the inpainting problem exist; references [1][2][3][4] provide a brief sampling of the techniques that exist in this field.

4.2 Operating Principle

The scanner detailed in the previous section can achieve large fields of view at the expense of scan pattern distortions and sampling sparsity. Both of these problems are mitigated during image reconstruction by (a) making use of the PSD readings track the fiber trajectory in real time and (b) using a fast iterative Fourier filtering reconstruction (FIFFR) method to inpaint the missing data. Unlike algorithms [5] [6] based on regularized estimation, FIFFR is based on alternating iterative Fourier projections, similar to the approach used in phase retrieval and ptychographic imaging [7][8]. The algorithm is illustrated in Figure 4.1. First, a spatial grid (x, y) is set up to cover the extent of the scan pattern with grid spacing set for Nyquist sampling (2.49 μm pixel width), i.e. two pixels across the lateral PSF FWHM. Each time-domain sample from the photodiode is assigned to a pixel based on the PSD X, Y coordinates.

Then a 2D fast Fourier Transform (FFT) transforms the image to the spatial frequency domain (κ_x, κ_y). There, a binary mask eliminates spatial frequencies outside a defined bandwidth, which is initially set to be narrow and progressively relaxed to match the physical numerical aperture (NA) of the optical imaging system. An inverse 2D FFT transforms the data back to the spatial domain (x, y), where sampled pixels are replaced with measured values. The process iterates between the Fourier bandwidth constraint and the spatial-domain measurement constraint until convergence. The sparser the acquired data, the higher the number of iterations that will be needed to reach an optimal reconstruction. Note also the time it takes per iteration increases with respect to grid size of the reconstructed image. Our final reconstructed image retains the original values of the sampled pixels and only estimates the values for the unsampled pixels.

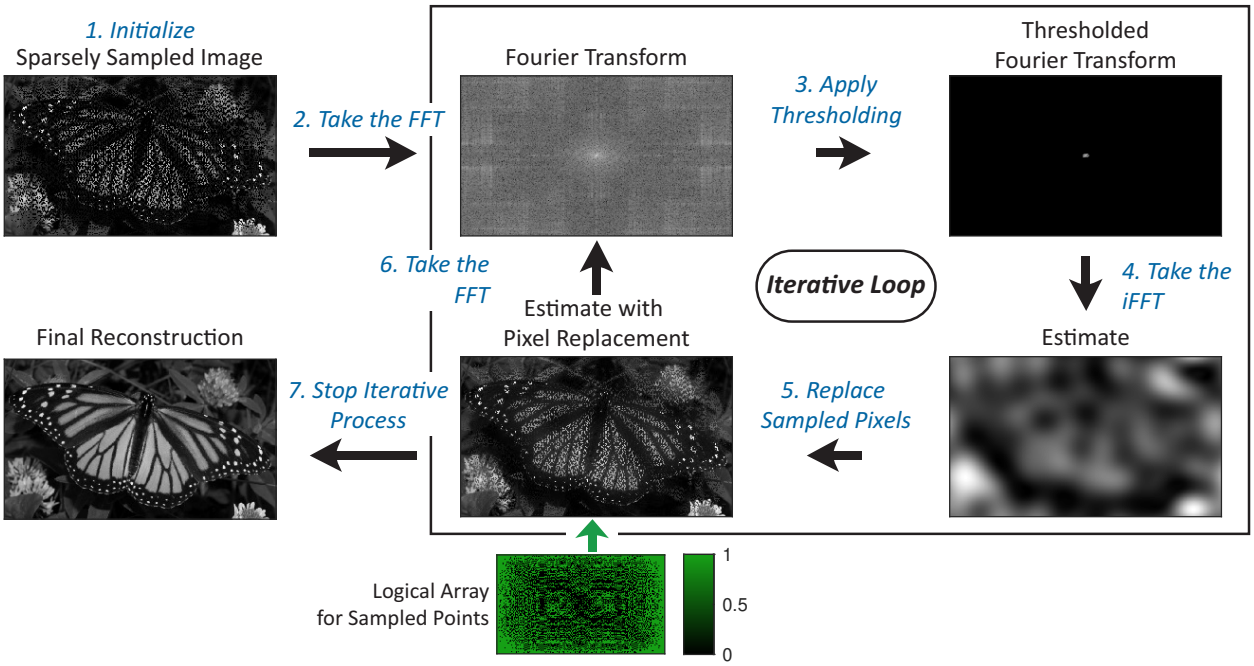

Figure 4.1: Fast iterative Fourier filtering reconstruction Loop: First the data is acquired and Fourier transformed, a binary mask is applied to clip a specific set of spatial frequencies (determined by the threshold function) and the image is inverse Fourier transformed. Then the points measured in the acquired data replace their associated estimated pixel values and the loop begins again with a Fourier transform.

The Fourier bandwidth constraint is $\kappa_c = \frac{X \cdot NA}{n\lambda}$, where κ_c is the radial cutoff frequency for the spatial frequency support in the Fourier plane, n is the index of refraction and NA is the

numerical aperture of the system, λ is the wavelength, and X is an iteration-dependent multiplier that gradually relaxes the bandwidth constraint.

4.2.1 Bandwidth Constraint

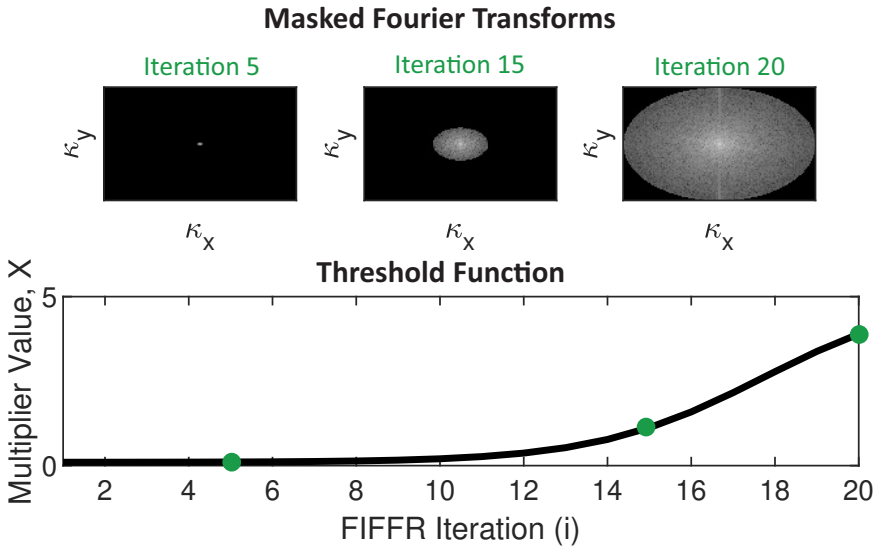

Figure 4.2: A progressive thresholding function (bottom row) creates a Fourier constraint with a cutoff frequency, $\kappa_c = \frac{X \cdot NA}{n\lambda}$, equal to some percentage of the maximum x or y spatial frequency (whichever is larger). The top row shows three examples of the masked Fourier transform after the Fourier constraint has been applied.

The need for a progressively relaxed bandwidth constraint arises from spatial frequency artifacts due to the scan pattern sampling in the spatial domain. By starting with tight lowpass filtering in the Fourier domain, unsampled pixels in the spatial domain estimate approach the value of their neighboring pixels, reducing the scan pattern artifacts in the next iteration. Allowing the filter radius to increase to the maximum spatial frequency support of the image in later iterations then allows the replacement step to fill in higher frequency information in the spatial estimate (see Figure 4.2).

Experimentally we have found that using a sigmoid function for X, to relax the bandwidth constraint, performs well, but depends on several tunable parameters. As shown in Algorithm 1, these parameters are 1) I, the number of iterations, 2) U, the upper limit (i.e. translates to the

largest κ_c), 3) L, the lower limit (i.e. translates to the smallest κ_c), 4) a, the slope of the sigmoid, and 5) s, the shift of the sigmoid.

Algorithm 1 Bandwidth constraint relaxation function

X = multiplier value
i = iteration number
U = upper limit
L = lower limit
a = sigmoid slope
s = sigmoid shift
$\mathcal{N}(x) = (x - min(x))/(max(x) - min(x))$

$$X(i) = (U - L) \cdot \mathcal{N}\left(\frac{1}{1 + exp(-a(i - s))}\right) + L$$

Often an iterative algorithm is run until some convergence criterion is met. Instead we choose the number of iterations based on time constraints, and adjust the sigmoid function for best results. This reduces the number of tuning knobs and allows the optimization of the reconstruction to be focused on just the slope and shift of the threshold function.

In this way the total number of iterations, I, can be determined simply from $I = t_{max}/t_1$, where t_{max} is the maximum time a user wants the algorithm to run, and t_1 is the time it takes for a single iteration (at a specific grid size) to process. The upper limit, U, is set so that κ_c is equal to the largest spatial frequency that will be retained in the final reconstruction. For the lower limit, L, we have found experimentally that a value of 0.1 is sufficient. The sigmoid slope and shift values are the two values that require the most tuning. Experimentally we have found the best values for a range from 0.1 to 0.5 and for s range from 83% to 100% of the number of iterations.

These values were experimentally determined with a simulated dataset where the ground truth image was known and a direct comparison could be made between the reconstructed image and the ground truth image using the Structural Similarity Index Measure (SSIM) [9]. The SSIM is measured on a scale of [-1, 1], where a score of 1 indicates a perfect match between the two

images being compared. The sigmoid slope and shift values were tuned in order to maximize the achievable SSIM, however, our approach was not exhaustive and future research should encompass a more robust approach to the parameter optimization procedure.

4.2.2 Fourier Artifacts

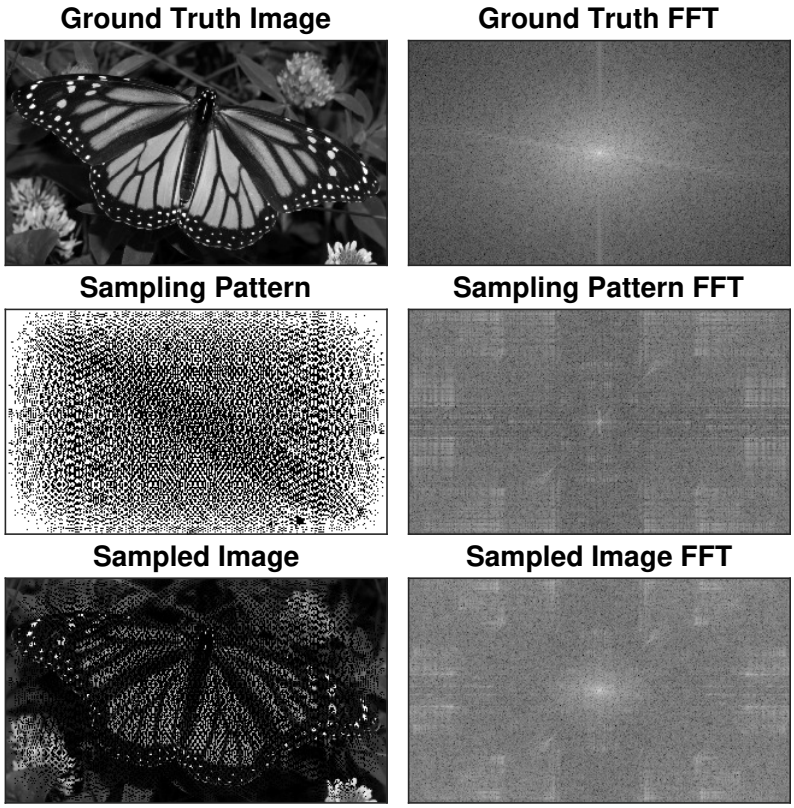

Figure 4.3: The ground truth image (top left) is multiplied with the sampling pattern (mid left) in the real domain to create the sampled image (bottom left). In the fourier domain this amounts to a convolution of the ground truth FFT (top right) and the sampling pattern FFT (mid right), such that the fourier transform of the sampled image (bottom right) contains both real information and artifacts of the sampling pattern.

When an image of interest is sampled in the spatial domain, the image is effectively multiplied by the sampling pattern. In the Fourier domain, this amounts to a convolution of the underlying image's spectrum with the sampling pattern's spectrum. Thus the Fourier transform of the sampled image contains both information on the underlying image and artifacts from the sampling pattern (see Figure 4.3). Many of these artifacts are high-frequency components and can be iteratively

removed through initial tight lowpass filtering. This is the reasoning behind a progressively relaxed bandwidth constraint that starts with a small aperture constraint for many iterations before increasing the bandwidth to match the NA of the lens system. Additionally, the tight bandwidth forces the unsampled pixels to approach an optimal initial estimate. We have found this decouples starting values used to replace unsampled Null values from the resulting reconstruction; i.e. using zero, a median-value, or a maximum value to replace NaN values prior to taking the FFT does not result in a change in the quality of the reconstruction.

4.3 Simulation Results

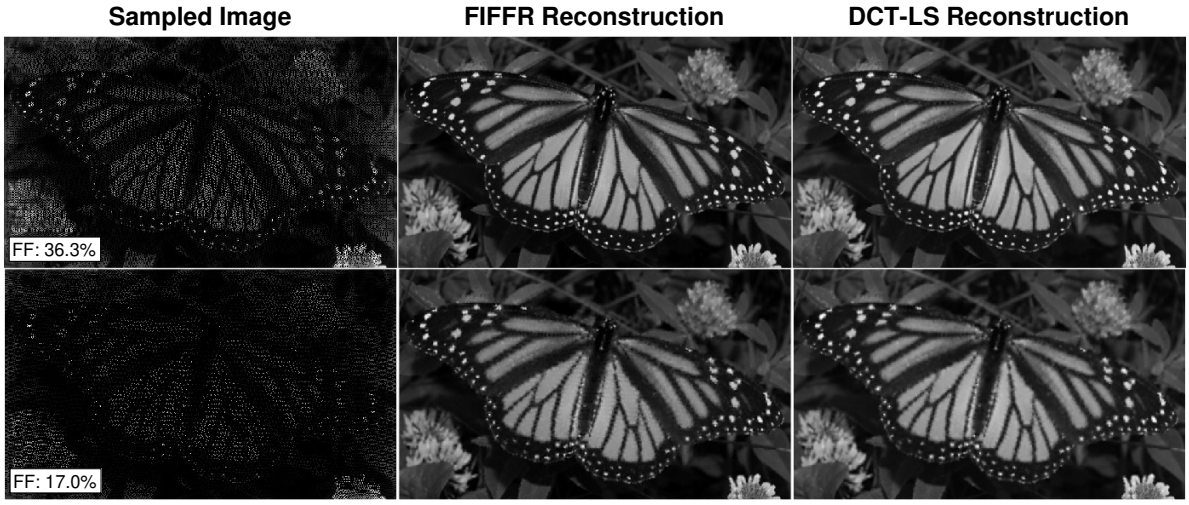

Figure 4.4: Examples of reconstruction results from FIFFR (middle column) and DCT-LS (right column) for an input image with a fill-factor of 36.3% (top row) and 17% (bottom row). Here FIFFR was run 40 iterations with an SSIM of 0.9353 (top) and 100 iterations with an SSIM of 0.8500 (bottom), and DCT-LS was run 100 iterations with an SSIM of 0.9210 (top) and 20 iterations with an SSIM of 0.8457 (bottom)

In order to benchmark the performance of FIFFR we first applied the algorithm to a simulated dataset where the ground truth image was known. Figure 4.4 shows the results of FIFFR reconstruction on a simulated test 381×647 image. Sampling was simulated with Lissajous waveforms (using the same frequencies as our experimental setup), varying the fill factor by changing the number of points sampled. We compared the performance of FIFFR to a related inpainting algorithm, Discrete Cosine Transform Least Squares (DCT-LS) [5], which has recently found use in recon-

structing images from sparsely-sampled Lissajous scan patterns [6] [10]. For DCT-LS, we used the open source code made available by its original author [11]. Like FIFFR, DCT-LS is an iterative algorithm, which alternates between spatial and frequency domain representations of the data. The key difference is that DCT-LS seeks a reconstruction that balances fit to measured datapoints with a complexity penalty in the spatial domain, while FIFFR enforces a bandwidth constraint in the Fourier domain. DCT-LS balances fit error versus complexity by searching for a regularization parameter that optimizes generalized cross-validation. FIFFR, on the other hand, alternates between applying a measured data constraint (by substitution) in the spatial domain and applying a bandwidth constraint in the Fourier domain. This bandwidth constraint is initially set extremely narrow to fill large unsampled gaps and eliminate the bulk of the sparse sampling artifacts, and is progressively relaxed to the physical numerical aperture of the optics.

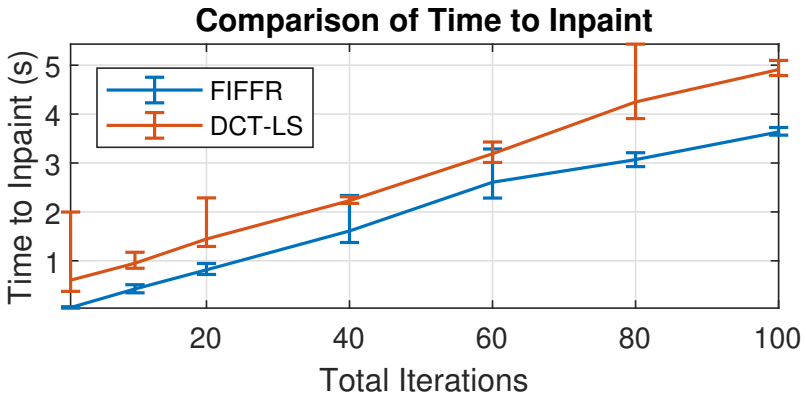

Figure 4.5: The minimum, mean, and maximum amounts of compute time to inpaint (averaged over 10 datapoints) for both FIFFR and DCT-LS run at various total iterations

For the same number of iterations, FIFFR outperforms DCT-LS in terms of speed (see Figure 4.5). This comparison of time to inpaint was conducted on a PC with an Intel Core i5-6500 CPU with 8GB of RAM. Additionally, as seen in Figure 4.6, FIFFR was able to achieve comparable SSIM scores to DCT-LS.

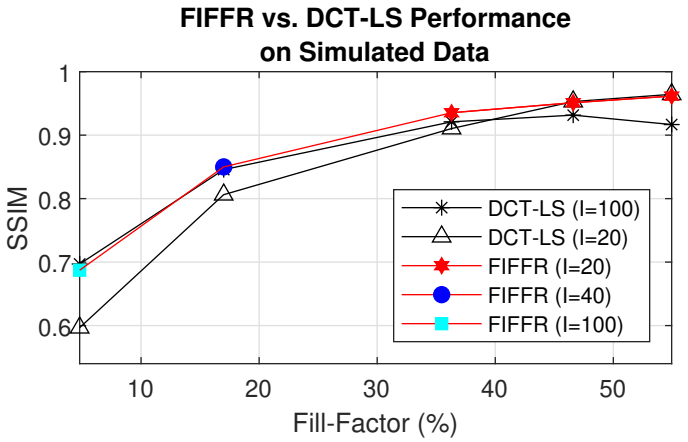

Figure 4.6: A comparison between FIFFR and DCT-LS performance at various fill-factors. The SSIM score for DCT-LS is shown for the default number of iterations (100) and for 20 iterations. A comparable SSIM score for FIFFR is shown at various iterations.

4.4 Application to RCM

4.4.1 Comparison With & Without FIFFR

Figure 4.7 shows the FIFFR results acquired from the scanner imaging a Ronchi-ruling test target having 30 lines/mm (33um pitch) at two different driving voltages. In both cases, the Lissajous pattern is driven with the same frequencies, but different voltages, showing the tradeoff between field of view and sparsity. The upper limit, U was set to equal 2 so that the maximum spatial frequency reached was $\kappa_c = \frac{2 \cdot NA}{n\lambda}$ since our system is confocal [12].

The FIFFR reconstruction effectively doubles the usable field of view in post-processing, however at FOV's larger than $0.183\ \mathrm{mm}^2$ it can be seen that the signal tapers off at the edges. This is because we are imaging a planar reflective target and the surface that the fiber traces out while scanning is spherical, meaning the axial plane sampled at the edges of the FOV is in front of the axial plane we are imaging when the fiber is at DC. However, the ronchi ruling is visible even at the higher driving voltages, allowing FOV's where the scan pattern is both sparse and distorted to be usable.

In Chapter 3 I highlighted some of the fundamental challenges arising from tradeoffs between field of view, scan pattern distortions, and sparsity. In answer to these challenges we presented a fast iterative Fourier-filtering reconstruction (FIFFR) algorithm. In tests with a Ronchi ruling

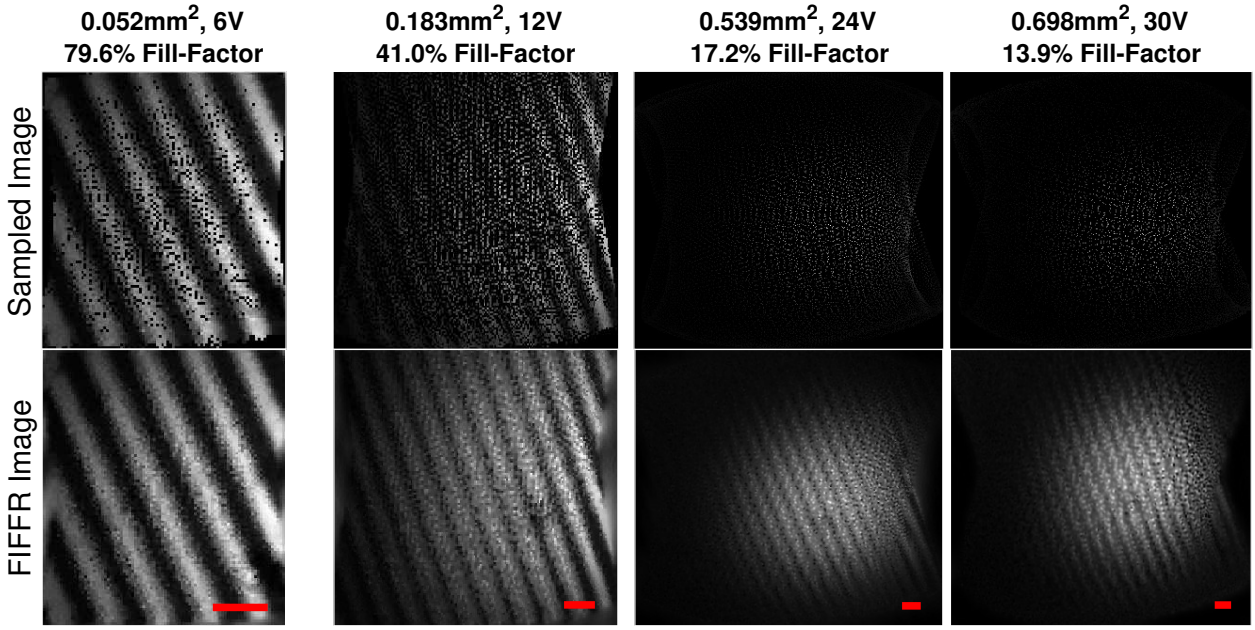

Figure 4.7: Experimental results imaging a 30 lpmm ronchi ruling target. The top row shows the input images, where unsampled pixels are black (initialized at zero), and the bottom row shows the output images of the algorithm, where unsampled pixels have been inpainted. The red line indicates $50\mu m$.

target, FIFFR was able to take advantage of scan pattern distortions and non-uniformities to increase the usable field of view from $0.052\ \mathrm{mm}^2$ up to $0.698\ \mathrm{mm}^2$. This algorithm can be utilized not only with Lissajous scan patterns, but with any point scanning method that faces problems with sparsity or in post-processing for any acquired images that are sparsely sampled. Finally, in addition to expanding the usable field of view, we anticipate that this combination of real time position sensing and fast sparse reconstruction will enable applications in scenarios where external mechanical motion perturbs the fiber scanning pattern, e.g. handheld operation in the field or in clinical settings.

While we have only explored the application of FIFFR to post-processed data, this algorithm shows great potential for utilization in real-time imaging applications. The approach shown in Figure 4.1 could be adapted for continuous estimation by adding in newly sampled data at Step 5 versus sampled pixels from the same frame. By placing a window over the number of iterations to keep in working "memory" for the current running estimate, the reconstruction could update as the FOV was panned. FIFFR in a "dynamic sampling" case would be able to keep up with the

frame rate of any instrument who's frame rate was slower than a single iteration of the algorithm, which we have seen for an image sized 381x647 pixels can take on the order of 0.03 s (or 2 kHz). Additionally, scan pattern distortion could be further exploited to help each subsequent frame to sample different regions, resulting in a clearer reconstruction. Future research will explore this application and focus on a more robust approach to parameter optimization, providing further avenues to improve scanner operation when sparsity and distortion dominate the field-of-view.

Bibliography

[1] R. Everson and L. Sirovich. Karhunen–loève procedure for gappy data. *J. Opt. Soc. Am. A*, 12(8):1657–1664, Aug 1995.

[2] Takahiro Ogawa and Miki Haseyama. Image inpainting based on sparse representations with a perceptual metric. *EURASIP Journal on Advances in Signal Processing*, 2013(1):179, December 2013.

[3] Jean-Luc Starck, Fionn Murtagh, and Jalal Fadili. *Sparse Image and Signal Processing: Wavelets and Related Geometric Multiscale Analysis, Second Edition*. Cambridge University Press, Cambridge, 2 edition, 2015.

[4] M. Elad. *Sparse and redundant representations: from theory to applications in signal and image processing*. Springer, New York, 2010.

[5] Damien Garcia. Robust smoothing of gridded data in one and higher dimensions with missing values. *Computational Statistics & Data Analysis*, 54(4):1167–1178, Apr 2010.

[6] Shane Z. Sullivan, Ryan D. Muir, Justin A. Newman, Mark S. Carlsen, Suhas Sreehari, Chris Doerge, Nathan J. Begue, R. Michael Everly, Charles A. Bouman, and Garth J. Simpson. High frame-rate multichannel beam-scanning microscopy based on lissajous trajectories. *Optics Express*, 22(20):24224, Oct 2014.

[7] Andrew M. Maiden and John M. Rodenburg. An improved ptychographical phase retrieval algorithm for diffractive imaging. *Ultramicroscopy*, 109(10):1256–1262, Sep 2009.

[8] D.J. Kane. Real-time measurement of ultrashort laser pulses using principal component generalized projections. *IEEE Journal of Selected Topics in Quantum Electronics*, 4(2):278–284, Apr 1998.

[9] Z. Wang, A.C. Bovik, H.R. Sheikh, and E.P. Simoncelli. Image quality assessment: From error visibility to structural similarity. *IEEE Transactions on Image Processing*, 13(4):600–612, Apr 2004.

[10] Andreas C. Geiger, Justin A. Newman, Suhas Sreehari, Shane Z. Sullivan, Charles A. Bouman, and Garth J. Simpson. Sparse sampling image reconstruction in lissajous trajectory beam-scanning multiphoton microscopy. page 1007606, San Francisco, California, United States, Feb 2017.

[11] Damien Garcia. Inpaint over missing data in 1-d, 2-d, 3-d,... nd arrays. https://www.mathworks.com/matlabcentral/fileexchange/27994-inpaint-over-missing-data-in-1-d-2-d-3-d-nd-arrays, 2023.

[12] Colin Sheppard. Confocal microscopy: Development of a modern microscopy. *GIT Imaging and Microscopy*, pages 41–44, 01 2008.

Chapter 5

Conclusion

Taken together the results of these projects have provided advancements towards smaller, faster, and broader microscopy applications. The research in Chapter 2 demonstrates the benefits of measuring both transient phase and transient absorption in pump-probe microscopy. Off-resonant probing in biological samples may become a more attractive method with transient phase detection to complement transient absorption detection, helping to avoid the existing limitations of sample heating and improving the applicability for future research into the biological mechanisms underlying various human diseases. The research in Chapters 3 and 4 have uncovered limitations and trade-offs with a compact piezoelectric actuator, an important step as smaller actuator designs are evaluated in the inevitable miniaturization of current reflectance confocal technologies. The sparse inpainting algorithm provides an additional route forward to work with non-ideal scan patterns and low sampling rates while allowing for faster imaging. Each of these projects were completed end-to-end requiring stages of design, construction, characterization and performance evaluation while navigating constraints of budget, software creation, laser maintenance, and experimental trial-and-error.

In Chapter 2, I discussed the Kramers-Kronig relations underlying the relationship between transient phase and transient absorption measurements. Beginning with an adopted transient absorption setup, initial pulse compression efforts were found to be tied to the self-phase modulation dispersion imparted by the chirped pulse amplification stage of the laser source. It was determined that significant third-order dispersion effects were present on the pump line after a major laser tuning, resulting in the construction of a prism compressor. Various approaches were taken to optimize the pulse compression, ending with the utilization of Frequency Resolved Optical Gating (FROG) in order to achieve a pump-probe cross-correlation pulse around 350 fs. The addition of polarization optics and a balanced detection scheme to the transient absorption microscope converted it into a transient phase setup capable of measuring both absorption and phase kinetics. A

computational model was constructed to allow for calibrated measurements and to verify the performance of the detection scheme. It was uncovered that the beam-joining dichroic located after the initial pulse-splitting on the probe line was contributing several undesired effects including polarization-dependent spectral phase and was likely cause of several SNR decreases. An extension of the initial model to include effects of diattenuation and polarization aberration was able to quantify an estimated signal-to-noise reduction present on the transient phase measurements. A successful demonstration of transient phase microscopy was made in graphene and live red-blood cells and transient absorption and phase measurements were compared. Additional measurements made in a glass microscope slide were utilized in evaluating the impact of scan-angle re-timing phase due to the point-scanning galvanometer setup for TΦM.

Compared to TAM, TΦM is able to measure the real component of the complex refractive index; this provides similar information about the excited state decay as the imaginary component, but there are trade-offs between the two techniques. Since TΦM requires a phase measurement that depends on the polarization state of the probe and reference being retained, it is sensitive to polarization aberrations. However, these effects can be minimized with a careful selection of optical components. For example, in our setup the dichroic beam combiner could be swapped for a 50/50 beam splitter to eliminate the polarization-dependent effects we uncovered. Additionally, FOV limitations in TΦM arising from the angle-dependent retiming phase on the second calcite could be mitigated by incorporating galvo de-scanning. It remains to be seen how TAM and TΦM with off-resonant probing compare for a broader range of biological targets; for a NIR probe wavelength of 800 nm, we have shown that TΦM has a stronger hemoglobin signal in human red blood cells than TAM. To map out more clearly other biological targets that could benefit from NIR probing with TΦM vs. TAM, the pump and probe arms of this microscope setup could be swapped moving the wavelength tunability to the pump.

In Chapter 3 I introduced the construction design challenges and solutions that led to the creation of the current fiber scanner version. The current design addresses obstacles in stable, concentric, and adjustable fiber optic mounting within the piezotube actuator fully enclosed in a

compact and portable housing. Aspects of the housing design incorporated 3D printed structures and simple adjustability mechanisms utilizing anchored screw and spring pairs to reduce costs. A position sensing detector was added to allow for real-time beam tracking, alleviating the repeatability requirements of single-shot calibration techniques and allowing for scan pattern distortion to be measured without jeopardizing the reconstructed image quality. Characterization of the constructed versions revealed the source of cross-coupling contributing to some of the scan pattern distortion and voltage dependent qualities such as resonant frequency, piezotube-to-fiber optic rotational eigenaxes, and mechanical harmonics. Calibration procedures were created to reduce some of the scan pattern distortion due to the cross-coupling phenomenon but the final scan pattern was found to suffer from issues of sparsity at higher driving voltages with larger fields-of-view; this was in part addressed by the development of an inpainting algorithm. However, in future versions a higher sampling DAQ would help to further reduce sparsity impacts. The use of non-polarization maintaining optical fibers resulted in a sensitivity to upstream fiber optic cable motion preventing this version from being used handheld; swapping out the current optical fiber for a polarization maintaining fiber should not only address this issue, it would also improve the low power limits. A high optical loss in part due to the double-passed 50/50 beam splitter in the current configuration places a maximum of the output power at the focus to $\sim$ 1.13 mW. With scattering samples, not enough power is measured on the return path to overcome the noise floor, limiting scanner use to reflective targets. With a polarization maintaining beam splitter, only one 50/50 split occurs on the return path increasing available signal by 2X. Additionally, a higher power diode (20 mW) could be purchased to increase the overhead power.

Finally, in Chapter 4, I presented a simple inpainting algorithm based on iterative Fourier projections with a 2D progressive bandwidth constraint and a real-space pixel replacement constraint. Compared to existing inpainting techniques this algorithm provides reconstruction results of comparable quality but with an algorithm structure that is straightforward to implement and at a faster performance time. This algorithm was developed to address the sparsity issues faced by the compact scanning microscope and ultimately extended the usable field-of-view from $0.05\ \mathrm{mm}^2$ to

$0.69\ \mathrm{mm}^2$. Currently it is only developed for post-processing usage, but adjustments could be made for real-time applications by supplying in new data each iteration.

In conclusion, this dissertation has explored a broad spectrum of technologies in microscopy. From low-power compact microscope designs to measuring excited state phase changes with an ultrafast microscope, these advances will help pave the way for future technologies in smaller, faster, and safer medical imaging devices.

Appendix A

Protocols for TΦM Microscope and Research

A.1 Operating the Laser

A.1.1 Quick Startup Procedures from Native Software

1. Open Avasoft 8 (Avantes) software to view the spectrometers
2. Open the TEC shortcut à verify at 43C
3. Open the LV15 preamp diode software
   (a) Select “reset” on the YFi box to clear the interlock, then select “clear” on the GUI
   (b) Set the current to 2.25A (right click in slider)
   (c) Turn “Laser ON”
4. Open the Digital Delay Generator (DDG) software
   (a) Open the image (.png) of boxes to fill from the open file folder:
      i. Trigger > Source > Select “External +”
      ii. Parameters:
         A. Frequency > 50,000,000
         B. 50 Ohm > Check the box
         C. Div > 10
         D. Level > 0.3
      iii. Channel A
         A. Delay > nsec > 16
         B. Width > nsec > 22
         C. Select “On”

iv. Channel B

A. Delay > nsec > 16

B. Width > nsec > 22

C. Select “On”

(b) Click “Send”

(c) Click “Refresh” and verify parameters are updated

(d) Close the dialog box

5. Switch back to the Avasoft software and verify that the Oscillator spectrum is present

6. Open the MV diode software

   (a) Select “reset” on the YFi box to clear the interlock if necessary, then select “clear” on the GUI on screen for both COM3 and COM4

7. Right click in the slider to set the current to 7.5A for both COM3 and COM4 (navigate using the “communications” tab in the upper taskbar)

8. Select “Laser On” for both COM3 and COM4

9. Switch back to the Avasoft software and verify that the NOPA spectrum is present and beginning to grow.

10. Allow the system 15-20 minutes to warm up

A.1.2 Quick Shutdown Procedures from Native Software

1. In the MV Diode software GUI à Re-select “Laser On” for **both** COM3 and COM4 to TURN THE LASER DIODES OFF. The current should drop to 0A. Close GUI

2. In the LV Diode software GUI à Re-select “Laser On” to TURN OFF THE LASER DIODE. The current should drop to 0A. Close GUI.

3. Return to the Avasoft software and verify that both spectrums have disappeared. Close the GUI.

A.2 Field-of-View Calibration

In order to calibrate the FOV a resolution card was imaged with transmitted probe light. The resolution card denotes 25 um segments with a black line in the horizontal and vertical directions. From Figure A.1 it was determined that and applied voltage of 1 V to the galvonometers (galvo) results in a deflection of ± 150 um with a total span of 300 um.

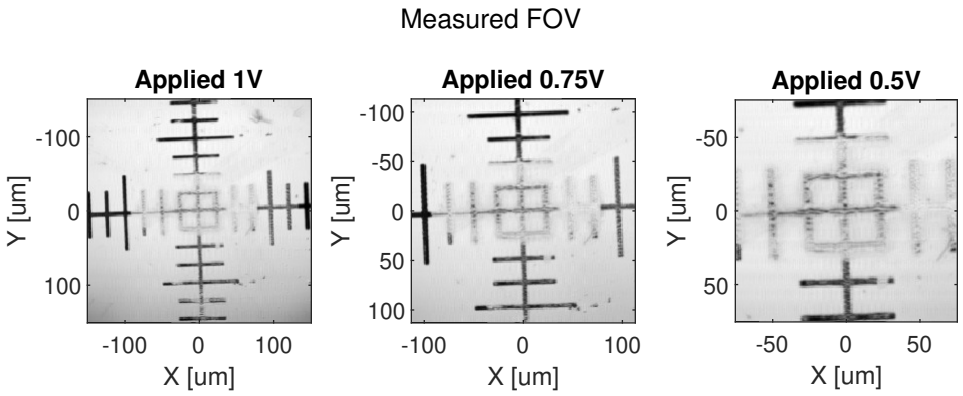

Figure A.1: Resolution card images for calibration the galvo driving voltage to FOV in the sample plane. (Note: The loss of contrast at the center of target is due to surface damage on the resolution card).

A.3 Resolution Estimate

In order to estimate the resolution for the pump-probe measurements, the transmission point-spread function (PSF) was measured and then squared. Since pump-probe techniques are a nonlinear interaction, the resolution is actually proportional to the PSF^2. For the purposes of this research an estimate of resolution is

An initial resolution measurement was made using the transmission light of the probe beam through a resolution target with periodic absorptive and transmissive lines.

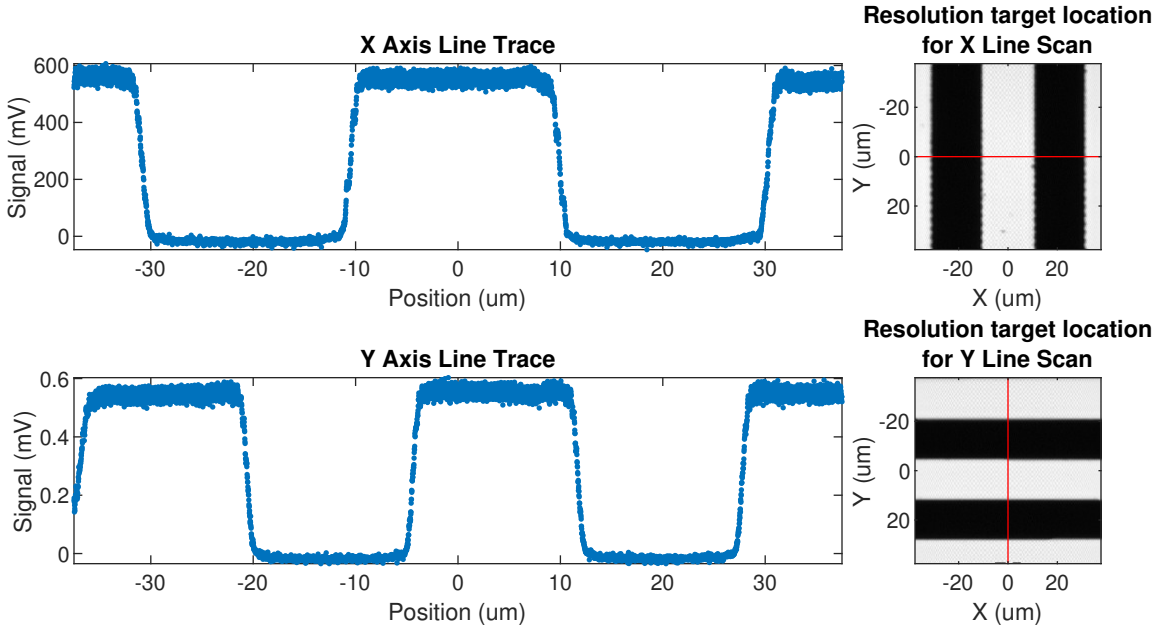

Figure A.2

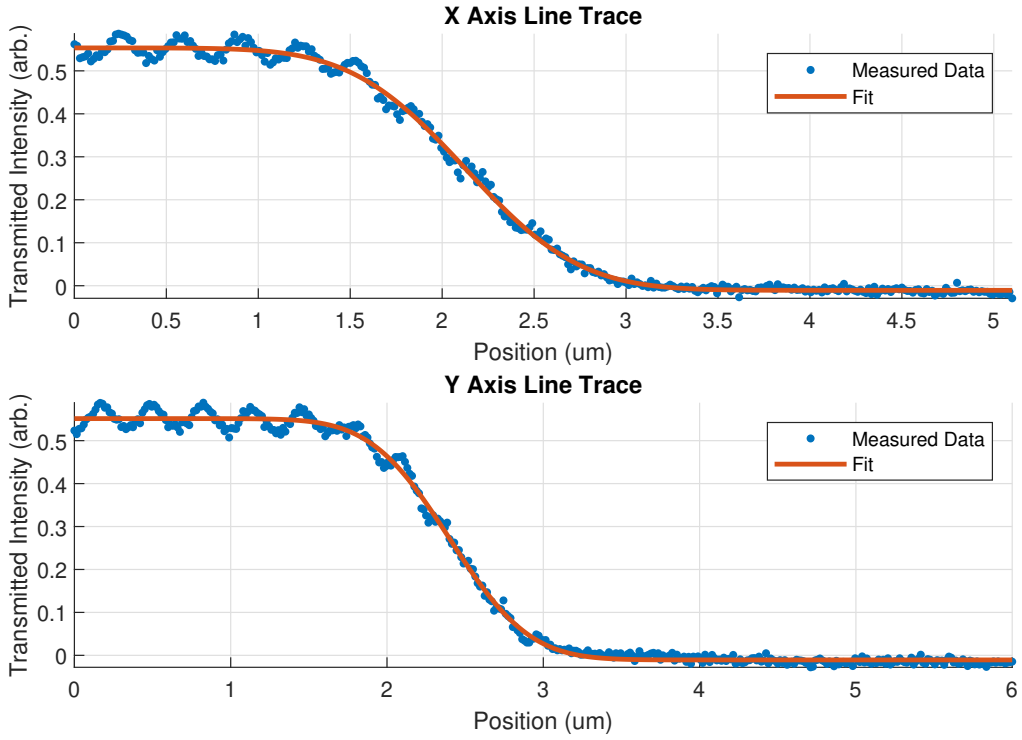

Figure A.3: Line fits overlaid on top of measured data

Table A.1: Resolution fit paramters for the probe beam

	X	Y
w_0	0.9821 um	0.7976 um
FWHM	1.1561 um	0.9389 um

The lineouts passing over a sharp edge can be fit with the function

$$P_0 + \frac{P}{2}(1 - \mathrm{erf}(\frac{\sqrt{2}(\mathrm{x} - \mathrm{x}_0)}{\mathrm{w}_0})) \tag{A.1}$$

where P_0 is an offset for background power, P is the maximum transmitted laser power, x is the position of the laser, w_0 is the Gaussian beam radius [1]. Note the full-width half-max (FWHM) of a fit Gaussian point-spread function (PSF) is $2\mathrm{w}_0$.

The theoretical resolution based on the objective and condenser numerical aperture (NA) can be estimated with the equation $\frac{\lambda}{2NA}$. Using this equation the theoretical resolution of the objective is 0.53um and the the theoretical resolution of the condenser is 0.82 um. From the fit parameters shown in Figure A.3 the estimated probe pulse resolution parameters are shown in Table A.1.

This provides the resolution measurements for all of the transmission data collected by the probe pulse. The resolution of the pump-probe setup was not measured, however as a multiphoton process, the pump and probe pulses will multiply resulting in a point-spread function that is similar to the PSF^2, achieving a better resolution than is available with simply transmission imaging.

A.4 Selection of Diattenuation & Polarization Aberration Model Parameters (Ψ,A_{ref},A_{pr})

For the diattenuation & polarization aberration model ($A_{\mathrm{ref}} = 0.72A_{\mathrm{pr}}$ and $\Psi = 104.4°$), the value for Ψ was measured and the value $A_{\mathrm{ref}} = 0.72A_{\mathrm{pr}}$ was qualitatively determined by sweeping through amplitude values until the model matched the measured data. Interestingly, the **measured** power differences between the probe and reference pulses placed the amplitude relationship at $A_{\mathrm{ref}} = 0.93A_{\mathrm{pr}}$, but the model does not match the measurement as well with these parameters. A

possible source of this discrepancy could lie in the polarization-dependent spectral phase imparted by the dichroic. A difference in spectral phase on the probe versus the reference pulse would impact the integrated wavelength-dependent constructive versus destructive interference measured by the photodetectors, but not the overall power measured on the individual reference and probe pulses.

As a reminder, $\Psi = 90^\circ + \theta_{\mathrm{ref}} + \theta_{\mathrm{pr}}$. In order to measure θ_{ref}, first a power measurement was made at the detector planes with only the reference pulse ($P_{\mathrm{ref,A}}$ and $P_{\mathrm{ref,B}}$); a PBS was placed directly after CAL 1 but before the dichroic mirror to redirect the s- polarized probe pulse into a beam block. Figure A.4 (A) diagrams the setup for this measurement. CAL 2 was removed and HWP 3 was oriented to *maximize* the signal on detector A, but a small amount of power was still measurable on detector B. The measured power values were $P_{\mathrm{ref,A}} = 0.37\ \mathrm{mW}$ and $P_{\mathrm{ref,B}} = 0.02\ \mathrm{mW}$ for setup A.

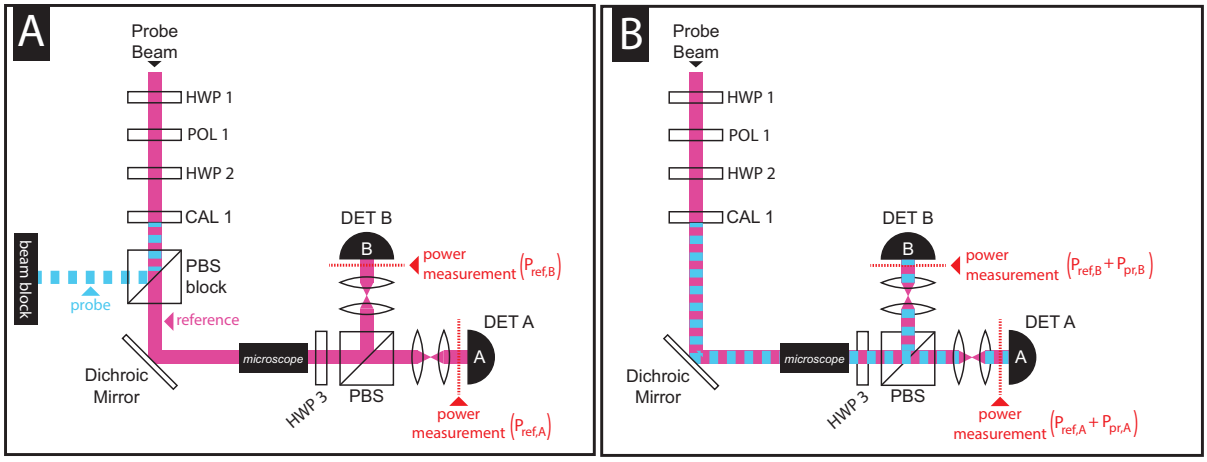

Figure A.4: (A) This was the setup for the first power measurement made. The probe pulse was redirected by a PBS after CAL 1 and HWP 3 was oriented to maximize the power of the reference pulse on DET A. (B) This was the setup for the second power measurement made; both the reference and probe pulses were allowed to transmit through the system. Power was again measured directly before DET A and and DET B.

Then a power measurement was made with the PBS block removed. Here both the reference and probe pulses transmitted through the microscope and onto the detectors. The orientation of

HWP 3 was not adjusted from the previous measurement. The measured power values for setup B were $P_{\mathrm{ref,A}} + P_{\mathrm{pr,A}} = 0.44\ \mathrm{mW}$ and $P_{\mathrm{ref,B}} + P_{\mathrm{pr,B}} = 0.37\ \mathrm{mW}$. To determine θ_{pr} the power levels measured in this geometry must first subtract the reference power levels.

Using the geometry of the beamsplitter, we can determine the ellipticity of the reference polarization where the p-polarized axis of the detection PBS is aligned to the major axis of the polarization, but there is a directional ambiguity as to whether the angle θ_{ref} should be denoted as cw or ccw with respect to the PBS axis. Figure A.5 shows relationship between the reference and probe pulses and the s- and p- axes of the PBS for the HWP 3 position.

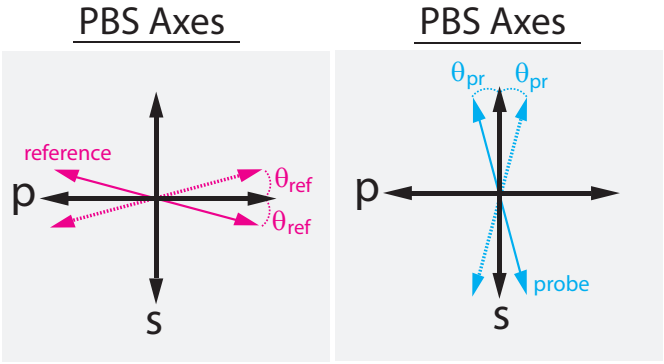

Figure A.5: Ambiguity on the sign of θ_{ref} and θ_{pr} arises since both negative and positive signs contribute equal power to the opposing detector.

To calculate θ_{ref} and determine projections onto the s- and p- detectors for the reference pulse we can use the trigonometric relationships

$$\frac{\cos\theta_{\mathrm{ref}}}{\cos\theta_{\mathrm{ref}} + \sin\theta_{\mathrm{ref}}} = \frac{P_{\mathrm{ref,A}}}{P_{\mathrm{ref,A}} + P_{\mathrm{ref,B}}} = \frac{0.37\ \mathrm{mW}}{0.37\ \mathrm{mW} + 0.02\ \mathrm{mW}} = 0.9487 \tag{A.2}$$

$$\cos\theta_{\mathrm{ref}} = 0.9487(\cos\theta_{\mathrm{ref}} + \sin\theta_{\mathrm{ref}}) \tag{A.3}$$

$$\frac{\sin\theta_{\mathrm{ref}}}{\cos\theta_{\mathrm{ref}} + \sin\theta_{\mathrm{ref}}} = \frac{P_{\mathrm{ref,B}}}{P_{\mathrm{ref,A}} + P_{\mathrm{ref,B}}} = \frac{0.02\ \mathrm{mW}}{0.37\ \mathrm{mW} + 0.02\ \mathrm{mW}} = 0.0512 \tag{A.4}$$

$$\sin\theta_{\mathrm{ref}} = 0.0512(\cos\theta_{\mathrm{ref}} + \sin\theta_{\mathrm{ref}}) \tag{A.5}$$

$$\frac{\sin\theta_{\text{ref}}}{0.0512} = \frac{\cos\theta_{\text{ref}}}{0.9487} \tag{A.6}$$

$$\tan\theta_{\text{ref}} = \frac{0.0512}{0.9487} = 0.0540 \tag{A.7}$$

$$\theta_{\text{ref}} = 0.0539\ \text{rad} = 3.0892^\circ \tag{A.8}$$

We can also show that the ellipticity factor $e_{\text{ref}} = \sqrt{\frac{P_{\min}}{P_{\max}}} = \sqrt{\frac{P_{\text{ref,B}}}{P_{\text{ref,A}}}} = \sqrt{\frac{0.02\text{mW}}{0.37mW}} = 0.2325$. Similarly we can determine θ_{pr} but taking into account the subtraction of power contributed by the reference pulse to the measurement in B; thus, $P_{\text{pr,A}} = 0.44\ \text{mW} - \text{P}_{\text{ref,A}} = 0.07\ \text{mW}$ and $P_{\text{pr,B}} = 0.37\ \text{mW} - \text{P}_{\text{ref,B}} = 0.35\ \text{mW}$.

$$\frac{\cos\theta_{\text{pr}}}{\cos\theta_{\text{pr}} + \sin\theta_{\text{pr}}} = \frac{P_{\text{pr,B}}}{P_{\text{pr,A}} + P_{\text{pr,B}}} = \frac{0.35\ \text{mW}}{0.35\ \text{mW} + 0.07\ \text{mW}} = 0.8333 \tag{A.9}$$

$$\cos\theta_{\text{pr}} = 0.8333(\cos\theta_{\text{pr}} + \sin\theta_{\text{pr}}) \tag{A.10}$$

$$\frac{\sin\theta_{\text{pr}}}{\cos\theta_{\text{pr}} + \sin\theta_{\text{pr}}} = \frac{P_{\text{pr,A}}}{P_{\text{pr,A}} + P_{\text{pr,B}}} = \frac{0.07\ \text{mW}}{0.35\ \text{mW} + 0.07\ \text{mW}} = 0.1666 \tag{A.11}$$

$$\sin\theta_{\text{pr}} = 0.1666(\cos\theta_{\text{pr}} + \sin\theta_{\text{pr}}) \tag{A.12}$$

$$\frac{\sin\theta_{\text{pr}}}{0.1666} = \frac{\cos\theta_{\text{pr}}}{0.8333} \tag{A.13}$$

$$\tan\theta_{\text{pr}} = \frac{0.1666}{0.8333} = 0.1999 \tag{A.14}$$

$$\theta_{\text{pr}} = 0.1973\ \text{rad} = 11.3056^\circ \tag{A.15}$$

The ellipticity factor for the probe is $e_{\text{pr}} = \sqrt{\frac{P_{\min}}{P_{\max}}} = \sqrt{\frac{P_{\text{pr,A}}}{P_{\text{pr,B}}}} = \sqrt{\frac{0.07\text{mW}}{0.35mW}} = 0.4472$. Since the signs of both θ_{ref} and θ_{ref} suffer from ambiguity, the overall angle Ψ could be one of four values:

$$\Psi = 90^\circ + 11.3056^\circ + 3.0892^\circ = 104.4^\circ \tag{A.16}$$

$$\Psi = 90^\circ + 11.3056^\circ - 3.0892^\circ = 98.2^\circ \tag{A.17}$$

$$\Psi = 90^\circ - 11.3056^\circ + 3.0892^\circ = 81.8^\circ \tag{A.18}$$

$$\Psi = 90^\circ - 11.3056^\circ - 3.0892^\circ = 75.6^\circ \tag{A.19}$$

In order to find similar model and measurement overlap with each of these values of Ψ, the diattenuation terms were adjusted manually until good model/measurement overlap occurred. Figure A.6 shows a comparison of these curves. The resulting diattenuation and polarization aberration value pairs are shown in Table A.2.

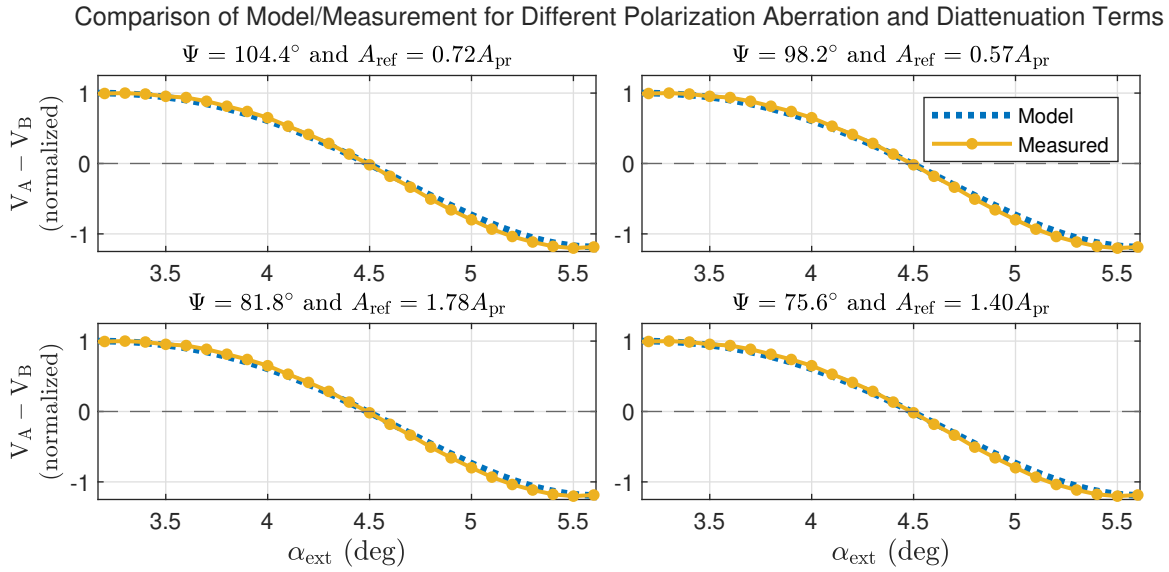

Figure A.6: Corresponding model/measurement curves to accompany the value pairs shown in Table A.2.

Table A.2: A comparison of values of Ψ to the diattenuation terms required for good model/measurement overlap.

Polarization Aberration Term	Diattenuation Term
$\Psi = 104.4^\circ$	$A_{\text{ref}} = 0.72A_{\text{pr}}$
$\Psi = 98.2^\circ$	$A_{\text{ref}} = 0.57A_{\text{pr}}$
$\Psi = 81.8^\circ$	$A_{\text{ref}} = 1.78A_{\text{pr}}$
$\Psi = 75.6^\circ$	$A_{\text{ref}} = 1.40A_{\text{pr}}$

As a reminder, a measurement of the probe and reference powers revealed a diattenuation term of $A_{\text{ref}} = 0.93A_{\text{pr}}$. However, if we compare the model with the measured terms $\Psi = 104.4^\circ$ and $A_{\text{ref}} = 0.93A_{\text{pr}}$ to the measured data, the fit is poor. Comparatively, an adjustment of the

diattenuation term to $A_{\text{ref}} = 0.72A_{\text{pr}}$ shows a good fit. Figure A.7 shows a comparison of these two models to the measured data.

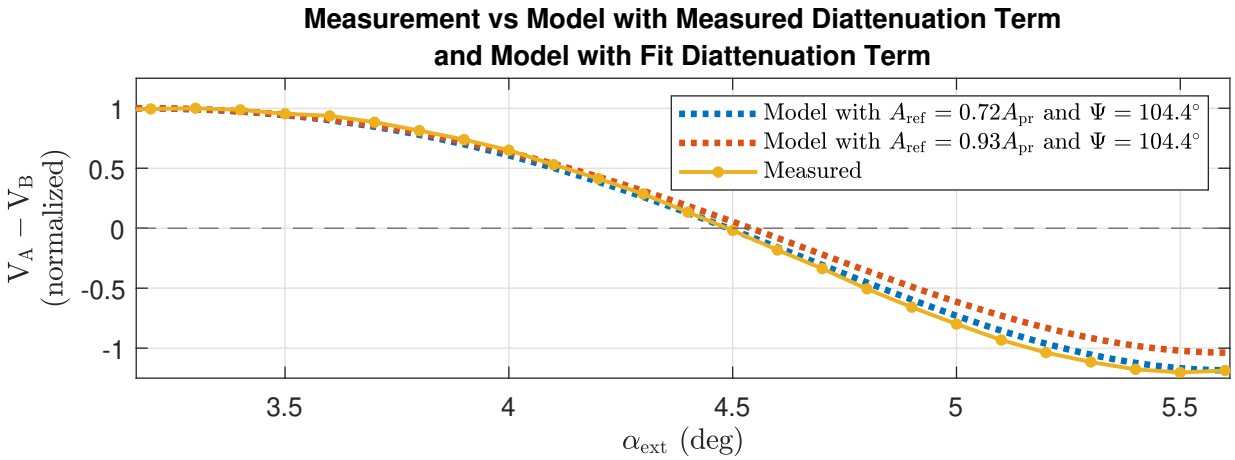

Figure A.7: A comparison of the model with measured parameters $\Psi = 104.4°$ and $A_{ref} = 0.93A_{pr}$ versus the model with measured parameter $\Psi = 104.4°$ and fit parameter $A_{\text{ref}} = 0.72A_{\text{pr}}$ to the measured data.

In conclusion, there is a mismatch between the model and the measured data regarding the diattenuation term; this could be due to spectral phase interference effects or there could be a different factor not accounted for in this model. However, the good overlap between the measured data and the model with the measured Ψ value and a fit diattenuation term suggests that diattenuation and polarization aberration could be contributing to SNR decreases in the TΦM signal on the order of 45%. Excluding the results of the polarization modeling, there is clearly an SNR decrease experienced (see page 56) in the TΦM signal that is due to polarization-dependent spectral phase picked up at the dichroic mirror. It is possible that the dichroic mirror is also contributing polarization aberration to the probe and reference pulses by changing the linear polarization to elliptical polarization [2]. The best course of action to mitigate any SNR affects by the dichroic mirror would be to swap out the dichroic for an optic such as a 50/50 beam splitter. While this would reduce power by 50%, it would not contribute polarization-dependent aberrations to the reference and probe pulses. Additionally, the 50% power cut would be insignificant for our research purposes

since we have been using only several milliwatts of power at the focus; overall, the probe arm has several hundred mW of power available and the pump arm has over a watt of power available.

Bibliography

[1] Marcos A. De Araújo, Rubens Silva, Emerson De Lima, Daniel P. Pereira, and Paulo C. De Oliveira. Measurement of gaussian laser beam radius using the knife-edge technique: improvement on data analysis. *Applied Optics*, 48(2):393, January 2009.

[2] Sawyer Miller, Linan Jiang, and Stanley Pau. Birefringent coating to remove polarization aberrations. *Opt. Express*, 30(12):20629–20646, Jun 2022.

Appendix B

Protocols for a Cantilevered Fiber Optic Scanning Microscope

B.1 Operating the V3.3 System

B.1.1 Startup

Make sure you have the correct protective laser eyewear for the wavelength of light and power you are using. As of 7/14/22 the 785nm laser diode is in use.

Step	Image
1. Flip a light switch to illuminate the LASER ON sign outside of the lab door	
2. Turn ON the power supply for the high voltage amplifier. Voltage should read 12.3V, current 0.03A.	

3. Turn ON the power supply for the position sensitive detector. The voltage should read 5V.	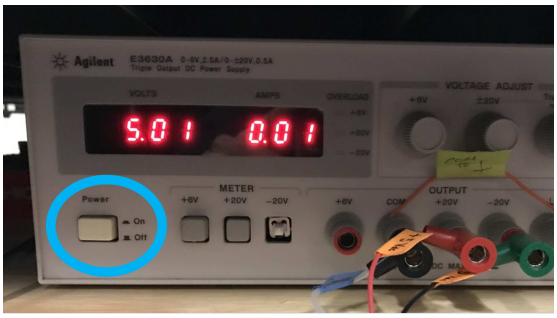
4. Turn ON the photodiode.	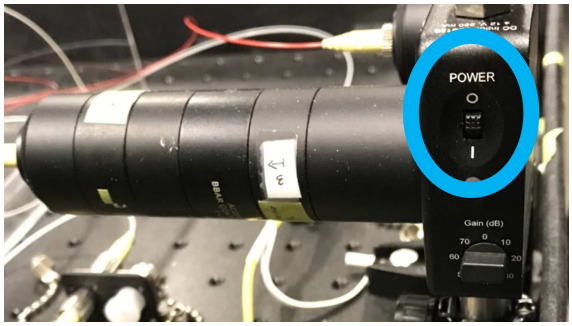
5. Turn ON the power for the laser diode driver by selecting the power switch on the back of the driver unit.	
6. Turn ON the TEC for the laser diode driver from the touch screen. The temperature should be rise to settle at 25C.	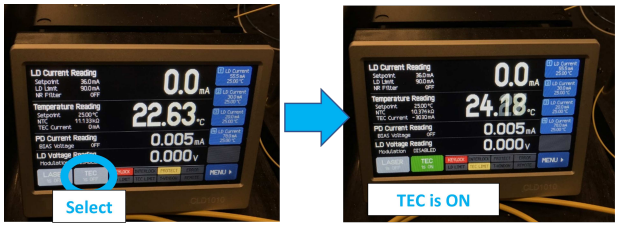

7. Rotate the safety KEYLOCK on the back panel from LOCKED to UNLOCKED. The red keylock light on the front of the driver will turn off when the key is rotated to the unlocked position. This is a safety mechanism to make sure the laser is not accidentally turned on when touching the screen.	
8. Select the LASER button the screen to turn the laser output ON. The current should be set to 36mA (but really should be set so that it is below the max limit on the measured current vs max output power curve.	

B.1.2 Shutdown

1. Turn OFF the Laser
2. Rotate the Keylock from the UNLOCKED position to LOCKED
3. Turn OFF the TEC
4. Power OFF the laser diode driver
5. Turn OFF the photodiode

6. Turn OFF the power supply for the position sensitive detector

7. Turn OFF the power supply for the high votlage amplifier

8. Switch off the light switch for the laser safety sign outside the lab door

B.1.3 Imaging

Code for acquiring and plotting continuous imaging data can be found at **FiberScanner > ImagingCode >** ContinuousDataAcquisitionCode_CNC_2023Oct12.m from [1]. Another file in this folder titled ContinuousDataAcquisitionCode_CNC_2023Oct12_WithLPSparseInpainting.m will plot both the raw image data as well as a low pass image to help bridge the gaps for sparsely sampled images when real-time feedback is needed.

B.2 Aligning the 4f Imaging Lenses inside Lens Tubing

For this process you will need three plano-convex lenses; L1 and L2 associated with your 4f-imaging setup where the focal lengths of L1 and L2 are f1 and f2, respectively. You will also need a third plano convex lens, preferably with a focal length similar to L1/L2 if you are short on table space. You will also need and iris and a slip on post collar to set and save the height of the post, two separate post holders, and an optical rail that can be attached to the table and that is atleast longer than 2*f1 + 2*f2, but ideally as long as possible (this helps with checking collimation).

1. Begin with the housing holding the fiber bolted to the optics table. Adjust the fiber until it is visually as level to the plane of the table as possible. It can be helpful to place a magnetic ruler on the opposite side of the fiber optic so you can gauge the levelness of the cantilever base to the fiber tip. This is a crucial step – it will be very difficult to properly align the lenses if the fiber is angled with respect to the plane of the table; especially if the lenses have longer focal lengths.

2. To initially set the height of the iris, pick two locations near and far to the fiber tip within the diameter of the iris and set the iris height for the far location. You will want to screw down

a post holder at the near point and far point where the iris is centered. If the iris height is not the same for the two points then your fiber cantilever is not level; return to step one and utilize the near and far point iris to help you narrow in on a flat fiber.

3. Press the optical rail up against the base of each post (avoiding the table clamp) so that the optical rail defines a straight line along the path of the posts. Secure.

4. The easiest way to determine if a lens is at its focal length from the previous plane is to check the collimation. We will start by adding in the external lens, L3, to create collimated light from the diverging light exiting the fiber tip. First, remove the two posts that were secured to the table in Step 2 and add in a post with L3 mounted. Move the other two posts downstream to use for the iris; make sure the locations chosen have the post base touching the optical rail similarly to their previous position. This will ensure that all the optics are aligned along a defined line.

5. Set the height of L3 by checking the vertical positioning on the downstream iris at two locations. Once the vertical position is centered at both locations then the L3 post is at the correct height.

6. Check the collimation by closing down the iris until it is just around the diameter of the beam (visible with the IR viewer for our wavelength of 785nm), then move the iris post to the other post holder and determine if the beam diameter has changed. If it has then either move L3 closer or farther from the fiber tip until the collimation is perfect. This can easily be done by sliding the base along the optical rail secured in Step 3.

7. Finally set the angle of L3 by checking for the back reflection on the fiber, using the IR viewer this backreflection should be centered on the piezotube.

8. Next, add in L1. The distance from L3 does not matter; start by setting the post height of L1 using the same method in Step 5 with two downstream iris locations.

9. Then set the angle of L1 by again checking the back reflection on L3 and on the piezotube, making sure the back reflections are centered.

10. Now add in L2; if L2 is in a lens tube connected to L2 the distance from L1 can initially be approximated and checked by checking the collimation on the downstream iris at two locations. The angle and height should automatically be set.

11. Remove L3 and set the distance of L1 from the fiber tip by checking the downstream collimation. If L1 is connected to the fiber optic housing with a lens tube, then again the angle and height are automatically set.

B.3 Measuring the Resolution of a Fiber Cantilever

After collecting the following data manually, utilize the matlab file **FiberScanner > ResolutionMeasurements >** DetermineRayleighRangeandBeamWaistFromAxialandLateralPSFMeasurements.m from [1]. You will need to fit your acquired data to the functions outlined in the Chapter 3 > Characterization > Resolution section.

B.3.1 Lateral PSF Measurement

Utilizing the large square reflective resolution target (or a square mirror), start by finding the focus of the beam with the target normal to the fiber scanner. The target should be mounted on both a Z translation stage (for finding the focus) and an X translation stage (for moving laterally across the focus). Starting near the edge of the target but with the beam still fully reflected back, measure changes in position versus the measured steady state reflected intensity. You will need to take steps $\leq$ 0.5um.

B.3.2 Axial PSF Measurement

For the axial measurement you do not need to have a lateral translation stage; just a stage in Z. Start with the stage in front of the focus (if you are far enough out of the focus, the measured intensity will not change if you change the axial position slightly). Then measure the reflected

steady state intensity as a function of position on the translation stage as you move the reflective target backwards through the focus until you have reached a point that is again out of the focus.

B.4 Measuring the Frequency Response of a Fiber Cantilever

Using the matlab file found at **FiberScanner > ResonantFrequency >** ScannerSystem_ ResonanceFinder.m from [1], start by setting the range of frequencies you wish to sweep through and the step frequency. For this code you must only drive the X or Y channel and then re-run the script to acquire data for the other channel. The position sensitive detector (PSD) should be placed at the beam focus.

The resonant frequency is dependent on the driving voltage and can be acquired at various driving voltages. See Figure 3.17 from Chapter 3. A single-axis sinusoid is output to the piezotube for one second before stepping to the next frequency and the fiber displacement is measured by the PSD.

Then utilize the matlab file **FiberScanner > ResonantFrequency >** ProcessFrequencySweepData.m from [1] to load each one second trace, calculate the PSD X axis and Y axis displacement and plot the resulting maximum displacements versus frequency for the two axes.

B.5 Selecting the Optimal Driving Frequencies of a Lissajous-Scanning Fiber Cantilever

Once the resonant frequency sweep has been conducted and there is a clear peak in the data, move on to selecting the optimal driving frequencies. The frequencies selected for driving a lissajous pattern in this section will follow a semi-resonant selection; thus the actual resonant frequency will not be chosen to drive the fiber, rather a pair of frequencies straddling the peak will be selected. Generally, the higher the resonant frequency, the faster the available frame rates there are to choose from. The frame rate depends on the greatest common factor between the two frequencies that are selected.

The goal is to select a frequency pair that is as close to the peak resonant frequency as possible (this will control the maximum fiber displacement available), but also select a pair that is separated enough to allow for the highest GCF (this will control frame rate).

Driving Freq (Hz)	Rx (Vpp)	Ry (Vpp)
797.5	1.01	1.07
798.0	1.12	1.13
798.5	1.15	1.20
799.0	1.26	1.27
799.5	1.34	1.37
800.0	1.42	1.44
800.5	1.52	1.54
801.0	1.69	1.68
801.5	1.79	1.79
802.0	1.98	1.91
802.5	2.10	2.06
803.0	2.27	2.23
803.5	2.41	2.34
804.0	2.52	2.37
804.5	2.58	2.33
805.0	**2.61**	2.40
805.5	2.59	2.45
806.0	2.57	**2.48**
806.5	2.56	2.46
807.0	2.02	2.43
807.5	1.75	2.43
808.0	1.58	1.64
808.5	1.47	1.48
809.0	1.39	1.38
809.5	1.31	1.29
810.0	1.19	1.23
810.5	1.12	1.11
811.0	1.09	1.10
811.5	1.02	1.03

(a)

Range Calculations

	Rx	Ry
Resonant	805 Hz | 2.61 Vpp	806 Hz | 2.48 Vpp
Top 10%	2.35 - 2.61 Vpp	2.23 - 2.48 Vpp
10-20%	2.08 - 2.35 Vpp	1.99 - 2.23 Vpp
20-30%	1.82 - 2.08 Vpp	1.74 - 1.99 Vpp
30-40%	1.56 - 1.82 Vpp	1.49 - 1.74 Vpp
40-50%	1.30 - 1.56 Vpp	1.24 - 1.49 Vpp
50-60%	1.04 - 1.30 Vpp	0.99-1.24 Vpp

Frame Rate Combinations

3 Frames/Second	
Possible Frequency Pairs	798Hz, 801Hz, 804Hz, 807Hz
Optimal Frequency Pair	(804Hz, 807Hz)
Fiber Response	(2.52 Vpp, 2.43 Vpp)
6 Frames/Second	
Possible Frequency Pairs	798Hz, 804Hz, 810Hz
Optimal Frequency Pair	(810Hz, 798Hz)
Fiber Response	(1.19 Vpp, 1.13 Vpp)

(b)

Figure B.1: Table (a) is color coded based the voltage value as related to the maximum value (shown with white text); it shows driving frequency (col. 1) versus measured X and Y voltage peak-to-peak signal (i.e. an indicator of fiber displacement). The decile-based color-coding legend in (b, upper) shows different voltage ranges depending on the X versus Y measurements. The frame rate combinations table in (b, lower) shows possible frequency pairs, optimal frequency pairs once considering displacement and the associated voltage response for two frame rates.

I typically start by loading the portion of data around the resonant peak into a table and separating those frequencies which fall into the upper 20 percent of the maximum displacement (peak resonance). The widths of the resonance peaks for the X axis may differ from those for the Y axis.

Starting with the a GCF of 2 and working up until you hit the maximum GCF allowed within the top 20 percent range, list out all the possible frequency pairs. Figure B.1 shows a visual of this process.

Figure B.2 visualizes the table shown in Figure B.1 so that it is easier to see the roll off of fiber displacement as one moves away from resonance to select a larger GCF.

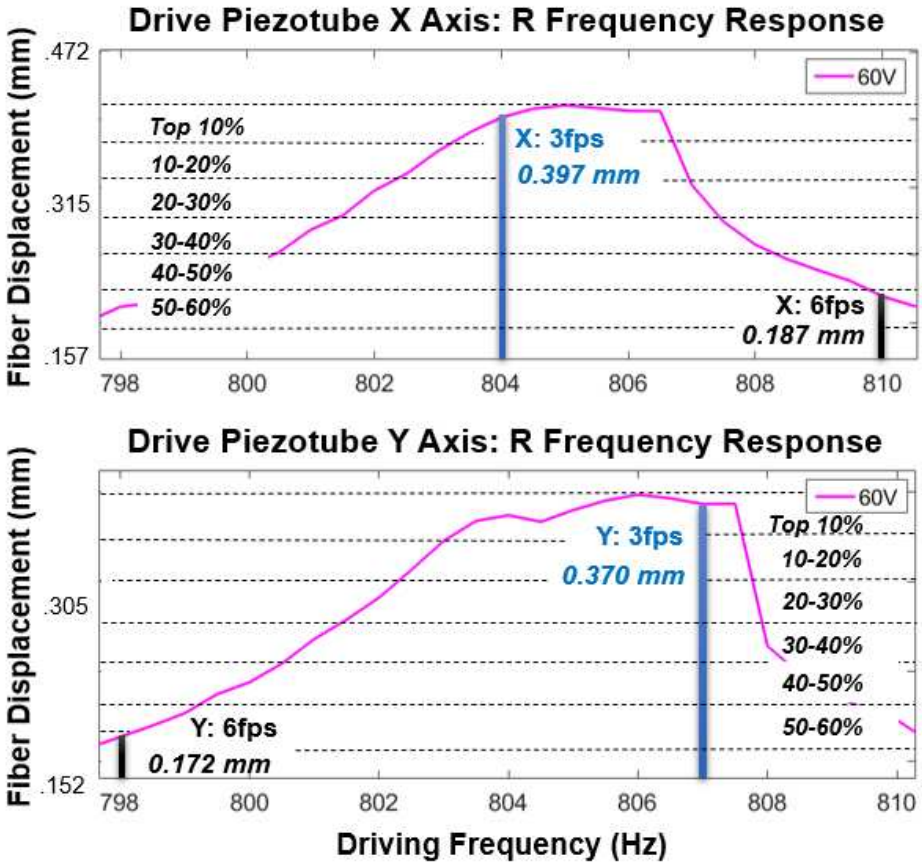

(a)

3 Frames/s	6 Frames/s
Freq Pair (Hz)	Freq Pair (Hz)
(804, 807)	(810, 798)
Displacement (mm)	Displacement (mm)
(0.397, 0.370)	(0.187, 0.172)

(b)

Figure B.2: Visual of the tradeoffs between fiber displacement and frame rate when selecting a frequency pair.

The frequencies selected for a particular instrument version will have to optimize the most important parameters for its intended application. In this scenario, fiber displacement was valued more than fiber displacement. A general rule of thumb is that the longer the fiber cantilever the lower the resonant frequency will be and thus the slower the available frame rates; the shorter the fiber cantilever the higher the resonant frequency, the higher the available frame rates. This is an important design consideration that can play into the earlier construction and cleaving of the fiber optic.

B.6 Finding and Applying Eigen-Transformations to Correct for Non-Ideal Lissajous Scan Patterns with a Fiber Cantilever

Start by placing the position sensitive detector (PSD) at the focal plane. The PSD will measure the displacement of the fiber.

Starting with the X axis driving frequency, use the matlab code **FiberScanner > EigenaxisIdentification >** SendOutputWaveformsforMeasuringEigenaxisResponse.m from [1] to send a single axis sinusoidal waveform rotated through 180 degrees. The rotation occurs in 1 degree steps and acquires the PSD signal at each angle for 1 second. After acquiring data for the X axis driving frequency, the script will collect the fiber response at the Y axis driving frequency. Do this first for the smallest driving voltage that will be applied to the piezotube, and then repeat for the largest driving voltage. In addition to being sensitive to frequency, the eigenaxes of the fiber optic are also sensitive to driving voltage.

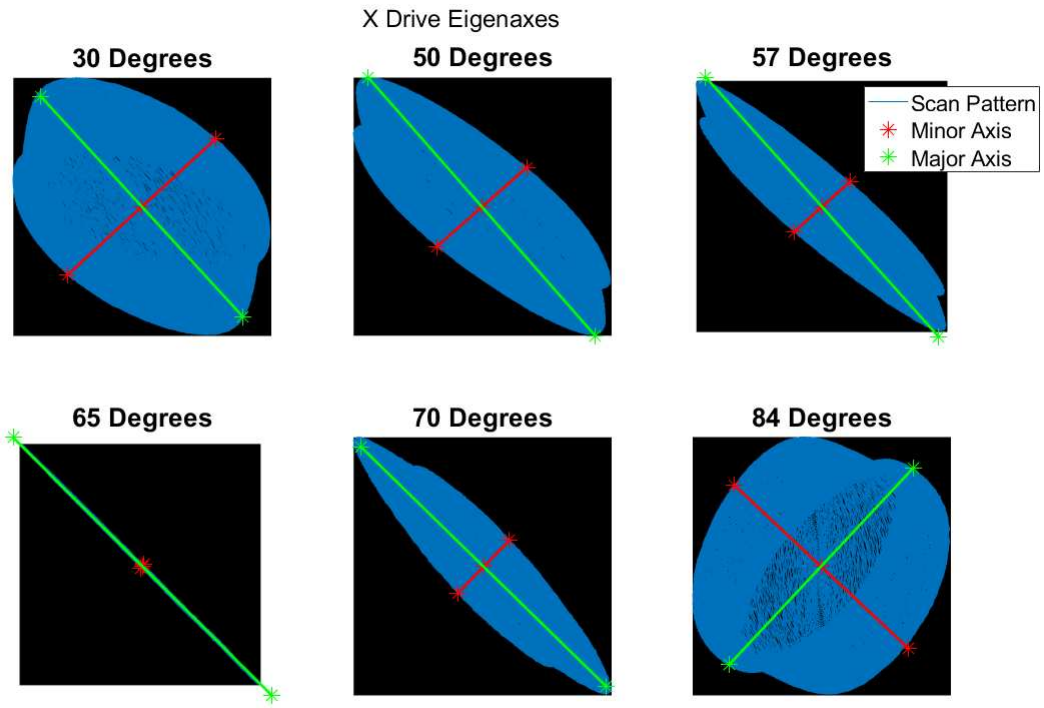

Figure B.3: Measured beam path trajectories (ellipses) for driving a 12V 804Hz single axis sinusoidal waveform through various input angle rotations. The major and minor axis chords are shown on each beam outline, corresponding to the plotted chord length in Figure B.6.

After the data has been acquired load each 1s datafile, utilize the matlab file **FiberScanner > EigenaxisIdentification >** ProcessEigenaxisDataandDetermineOptimalEigenangles.m from [1] to plot it and compute the minor and major axis of the measured ellipse. Make sure this file is in the same folder as the functions calculate_major_minor_axes_final.m and calculate_subplots_axes.m. The angles where the major axis is at a maximum and the minor axis a minimum correspond to eigenangles for the drive frequency applied.

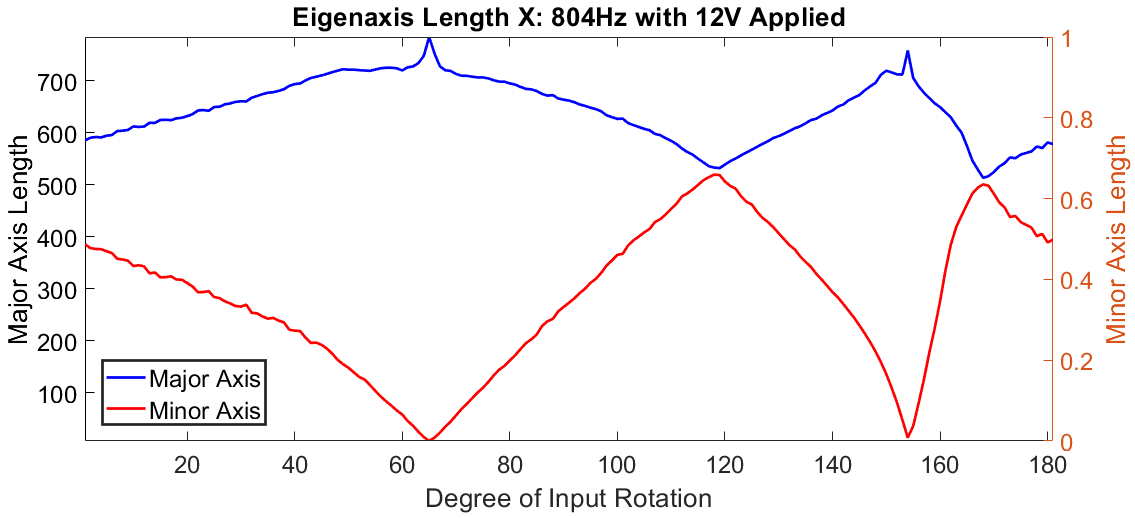

Figure B.4: For a 12V drive voltage with a driving frequency for the X axis of 804Hz, these are the measured major and minor ellipse axes. The major axis length is shown in blue with the left hand axis; the minor axis length is shown in red with the right hand axis. The two eigenaxes occur at 65 degrees and 154 degrees for 804Hz.

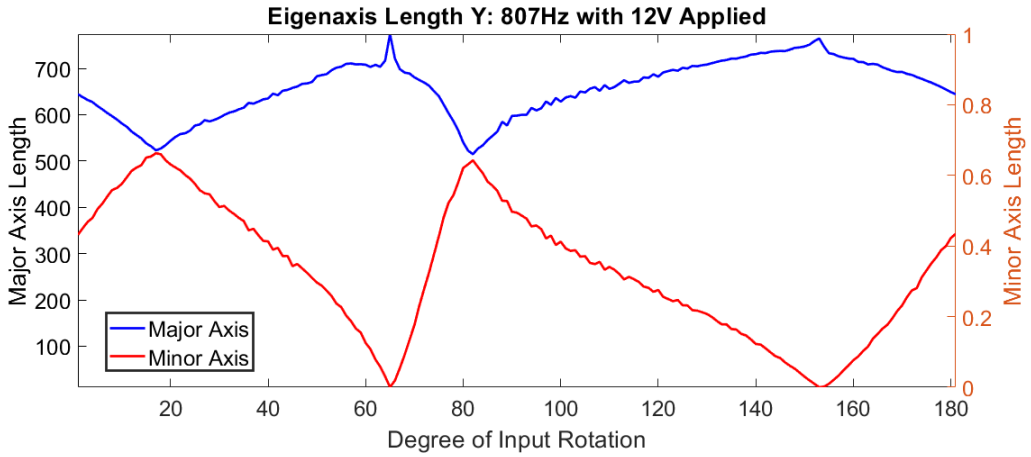

Figure B.5: For a 12V drive voltage with a driving frequency for the X axis of 804Hz, these are the measured major and minor ellipse axes. The major axis length is shown in blue with the left hand axis; the minor axis length is shown in red with the right hand axis. The two eigenaxes occur at 65 degrees and 153 degrees for 807Hz.

With 90V applied the eigenaxes for 804Hz are at 67 and 149 degrees and for 807Hz are at 68 and 149 degrees. Note that these are different from applying 12V (804Hz: 65, 154 deg | 807Hz:

65, 154 deg). Thus the eigenaxes are sensitive to both driving frequency and driving voltage where nonlinear mechanical distortions can shift things significantly.

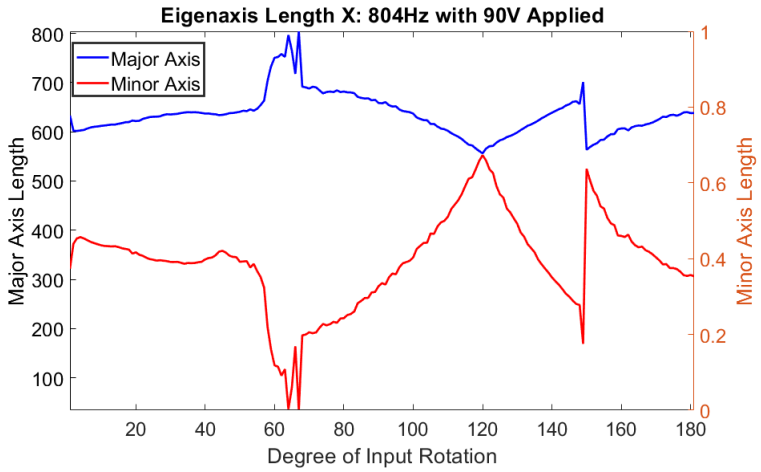

Figure B.6: For a 90V drive voltage with a driving frequency for the X axis of 804Hz, these are the measured major and minor ellipse axes. The major axis length is shown in blue with the left hand axis; the minor axis length is shown in red with the right hand axis. The two eigenaxes occur at 65 degrees and 153 degrees for 807Hz.

B.6.1 Build Tutorial for Version 3

Table B.2: List of components for V3.3 Scanner Build.

Component	Source
(1) Ferrule	Thorlabs: CF128-10
(2) Fiber Optic Patch Cable	Thorlabs: P1-780A-FC-5
(3) 900um Furcation Tubing	Thorlabs: FT900Y
(4) 1" Flange to Lens Adapter	Thorlabs: SM1F2
(5) Piezotube	PiezoDrive: TB2005
(6) Conn Junct 2POS Poke-in 18-26AWG	Digikey: 478-8728-ND
(7) 4-40 Screws & Hex Nuts	Ace Hardware
(8) Ferrule Holder	Machined out of plastic
(9) Buffer Holder	Machined out of plastic
(10) Piezo Holder	3D Printed
(11) External Housing (2 pieces)	3D Printed

This tutorial provides step-by-step instructions for how to build Version 3.3 of the fiber scanner. CAD files with dimensions can be found in my public github repository at [1] under Dissertation > FiberScanner > CADFiles.

Step-by-Step Instuctions

1. Start by attatching the piezo holder and the flange-to-lens tube adapter together. You will need the piezo holder, the 4-40 screws and hex nuts and four small springs that fit over the 4-40 screws.

    (a) Add a hex nut to each 4-40 screw and rotate until it is snug against the screw head. Then, add a screw to each corner of the flange-to-lens tube adapter with the the screw head and the lens tube threads on the same side. After sliding the screws through, each screw should have a spring slipped over it between the adapter face and the front face of the piezo holder. The cylindrical tube of the piezo holder sits inside the cutout on the adapter. On the exiting side of the piezo holder, add a 4-40 hex nut to the end of each screw and UV glue the hex nut to the piezo holder so it does not rotate (only the screw can rotate through it).

2. Next mount the assembly from (1) into the larger external housing, using the vertical and horizontal pairs of screws and springs.

    (a) With the external housing piece that has a large cutout, place a spring inside each of the two rectangular cutouts on the inside of the edging. Then, while holding the piezo holder centric inside the cutout, slide a screw through each opposing hole on the external housing and into the groove on the outside of the piezo holder. Adjust the screw lengths and spring positions until the piezo holder is held snugly inside the cutout.

3. Screw in the high voltage connector to the back side of the external housing piece used in (2).

4. Add in the push-release wire connectors. UV glue to an out of the way location inside of the housing used in (2).

5. Connect the high voltage wires to the push-release connectors.

6. Add in the buffer holder. UV glue the front or the back side to the outer housing.

7. Mount the piezotube into the piezo holder. The wires should slide all the way through and fit around the buffer holder to the inside of the housing. You can slightly tug onthese wires to help adjust the position of the piezotube. Make sure the piezotube is perpendicular to the external housing front plane before curing the glue at the base.

8. Add in the wires from the piezotube to the push-connectors.

9. Remove about 5 inches of jacket from the patch cable. Slide a piece of buffer ($\sim$8-9 inches) into the jacket leaving enough space at the tip of the buffer so that the fiber is not coming out.

10. Slide the buffer through the hole for the jacket in the back of the external housing and into the buffer holder. Then slide the jacket up the buffer all the way to the slot on the external housing, making sure the kevlar fibers stay short and out of the way.

11. Push the buffer into the jacket and allow some of the fiber to come out of the end of the piezotube (several inches). Remove the fiber coating using the heated coating remover and cut the end of the fiber using the fiber cleaver.

12. Use gloved hands to slide the fiber into a ferrule with a bore hole atleast 2 microns larger than the recommended size (I used a ferrule with a bore hole of 128um instead of 126um).

13. Add fiber epoxy to the ferrule and allow it to wick up.

14. Slip fit the ferrule into the ferrule holder.

15. Pull buffer out of the jacket to pull the fiber tip assembly into the front of the piezotube. Here I used loctite epoxy EA E-00CL to glue the ferrule holder into the piezotube. (A previous student did studies on off-gassing of different epoxies and found this was the only one that wouldn't coat and ruin the fiber optics while curing).

16. Construction is complete.

Bibliography

[1] cncoleal. Dissertation. https://github.com/cncoleal/Dissertation, 2023. Accessed: 2023-09-19.

Appendix C

Protocols for FIFFR

C.1 Parameter Optimization

There are four variables to optimize when running FIFFR. A brief exploration found that the order in which these four variables is optimized does matter; first the minimum threshold L is to be optimized, then the maximum threshold U, then the sigmoid slope a and finally the sigmoid shift s from Algorithm 1. These values can be optimized for varying levels of sparsity using a simulated sparsely sampled image and computing the SSIM to the original fully sampled image.

Minimum Threshold In order to optimize the minimum threshold, the following values were present until they could also be optimized: $U = 20e-2$, $a = 1$, $s = 0$. L is swept from values of $0.1e-4$ to $1e-2$. Matlab code to run this optimization can be found at **FIFFR > NAoptimize_minthresh.m** from [1].

Maximum Threshold After the optimal L value is found, then U is swept from $0.1e{-}2$ to $90e{-}2$ with L equal to its new optimal value, $a = 1$ and $s = 0$. Matlab code to run this optimization can be found at **FIFFR > NAoptimize_maxthresh.m** from [1].

Sigmoid Slope Next, a is swept from 0.05 to 0.025 with L and U equal to their optimal values, and $s = 0$. Matlab code to run this optimization can be found at **FIFFR > NAoptimize_a.m** from [1].

Sigmoid Shift The threshold function in matlab is fed a vector ranging from -10 to 10 which is scaled for the number of iterations after the Next, a is swept from 0.05 to 0.025 with L and U equal to their optimal values, and $s = 0$. Matlab code to run this optimization can be found at **FIFFR > NAoptimize_a.m** from [1].

C.2 Static FIFFR Algorithm

Code to run the FIFFR algorithm on simulated data is available in [1] at **FIFFR > static-FIFFRAlgorithm.m** where the simulated dataset is titled **SparseSampledButterflyData.mat**.

Bibliography

[1] cncoleal. Dissertation. https://github.com/cncoleal/Dissertation, 2023. Accessed: 2023-09-19.

Appendix D

License

Colorado State University LaTeX Thesis Template

by Elliott Forney – 2017

This is free and unencumbered software released into the public domain.

Anyone is free to copy, modify, publish, use, compile, sell, or distribute this software, either in source code form or as a compiled binary, for any purpose, commercial or non-commercial, and by any means.

In jurisdictions that recognize copyright laws, the author or authors of this software dedicate any and all copyright interest in the software to the public domain. We make this dedication for the benefit of the public at large and to the detriment of our heirs and successors. We intend this dedication to be an overt act of relinquishment in perpetuity of all present and future rights to this software under copyright law.

THE SOFTWARE IS PROVIDED "AS IS", WITHOUT WARRANTY OF ANY KIND, EXPRESS OR IMPLIED, INCLUDING BUT NOT LIMITED TO THE WARRANTIES OF MERCHANTABILITY, FITNESS FOR A PARTICULAR PURPOSE AND NONINFRINGEMENT. IN NO EVENT SHALL THE AUTHORS BE LIABLE FOR ANY CLAIM, DAMAGES OR OTHER LIABILITY, WHETHER IN AN ACTION OF CONTRACT, TORT OR OTHERWISE, ARISING FROM, OUT OF OR IN CONNECTION WITH THE SOFTWARE OR THE USE OR OTHER DEALINGS IN THE SOFTWARE.